UNIVERSIDAD NACIONAL AUTÓNOMA DE MÉXICO

POSGRADO EN CIENCIAS DE LA TIERRA

CENTRO DE GEOCIENCIAS

CARTOGRAFÍA, ANATOMÍA Y FACIES DE LA IGNIMBRITA XÁLTIPAN ASOCIADA AL COLAPSO DE LA CALDERA DE LOS HUMEROS (PUEBLA); EVIDENCIAS DE LA MAYOR ERUPCIÓN DE LA FAJA VOLCÁNICA TRANS-MEXICANA E IMPLICACIONES GEOTÉRMICAS

TESIS

QUE PARA OPTAR POR EL GRADO DE

DOCTOR EN CIENCIAS DE LA TIERRA

PRESENTA:

JAIME ALBERTO CAVAZOS ÁLVAREZ

DIRECTOR DE TESIS:

DR. GERARDO CARRASCO NÚÑEZ
POSGRADO EN CIENCIAS DE LA TIERRA

Juriquilla, Querétaro
Noviembre, 2020

Declaración de ética

Declaro conocer el Código de Ética de la Universidad Nacional Autónoma de México, plasmado en la Legislación Universitaria. Con base en las definiciones de integridad y honestidad ahí especificadas, aseguro mediante mi firma al calce que el presente trabajo es original y enteramente de mi autoría. Todas las citas de, o referencias a, las obras de otros autores aparecen debida y adecuadamente señaladas, así como acreditadas mediante los recursos editoriales convencionales.

Jaime Alberto Cavazos Álvarez

Esta tesis se la dedico a mi esposa Cinthia y al clan Cavazos Álvarez

Agradecimientos

He logrado alcanzar esta meta profesional guiado por un académico con grandes fortalezas intelectuales y sólidos valores personales, quien me encausó en este proceso de formación y aprendizaje de manera respetuosa, empática y motivadora, orientándome con su amplio conocimiento y experiencia. Doctor Gerardo Carrasco, el ejemplo que me ha modelado me compromete a respetar y disfrutar la investigación geológica, y compartirla con la generosidad y sencillez que lo caracterizan. Para Usted mi eterno agradecimiento.

A mi comité tutor, los Doctores Gerardo Aguirre Díaz y Pablo Dávila, quienes más allá de guiarme con su valiosa y constante asesoría durante esta tesis, también me otorgaron su amistad. Particularmente, al Dr. Gerardo Aguirre le agradezco permitirme compartir con él excelentes e interesantes discusiones en el campo y por invitarme a seguir desarrollando mi carrera docente. Por otro lado, le reconozco al Dr. Pablo Dávila su valiosa colaboración en uno de los artículos incluidos en esta tesis.

A los miembros del jurado de esta tesis, los Doctores Pablo Dávila, Guido Giordano, Penélope López y José Luis Macías, por su valiosa revisión de esta tesis, así como por su participación en el proceso de revisión y edición de los artículos que conforman esta tesis.

A la Universidad Nacional Autónoma de México, particularmente al Centro de Geociencias, por permitirme formar parte de esta grandiosa casa de estudios, en donde encontré todos los recursos y el apoyo necesario para la realización de este proyecto. A los responsables del Posgrado del Centro de Geociencias Mariano Cerca, Carlos Mendoza y Alex Correa, y a sus asistentes Marta Pereda, Armando Ramírez y Blanca Rendón, por el apoyo brindado en la gestión administrativa. Además, agradezco el apoyo económico facilitado en múltiples ocasiones, con motivo de compartir este proyecto en congresos internacionales, así como la organización de excursiones geológicas.

A Juan Vázquez y a Bartolo Rodríguez, por la asesoría técnica durante la realización de láminas delgadas y tamizado de muestras, respectivamente. Así mismo, también agradezco a María Mercedes Zavala, por su apoyo en la realización de los análisis de picnometría y permeometría de gas en el Instituto Potosino de Investigación Científica y Tecnológica.

Al Consejo Nacional de Ciencia y Tecnología (CONACyT) por la beca doctoral otorgada [No. 504993]. Al Centro Mexicano de Innovación en Energía Geotérmica (CeMIEGeo) [No. 2007032, Proyecto P05 (México)], por el valioso financiamiento otorgado en la fase inicial de este proyecto. Así mismo, agradezco al Consorcio Unión Europea – México GEMEX, financiado por el Fondo de Sustentabilidad Energética SENER-CONACyT [No. 2015-04-268074, Proyecto 4.5], por su significativo financiamiento, particularmente en la última etapa de este proyecto.

A la Comisión Federal de Electricidad por su continua colaboración durante la realización de este proyecto, así como por proporcionar muestras de los pozos del campo geotérmico Los Humeros que fueron fundamentales para cumplir los objetivos de este proyecto.

A mis amigos y colegas del proyecto Los Humeros. A Javier Hernández, Francisco Fernández, Adrián Jáquez, Daniela Peña, Steven Barrios, Héctor Cid y Dante Arteaga, con quienes compartí excelentes campañas de trabajo en campo y laboratorio, y con quienes entablé interesantes discusiones que enaltecieron este trabajo. Particularmente agradezco a Héctor Cid y a Dante Arteaga quienes con su experiencia me apoyaron en la realización de los análisis de microtomografía de rayos-X en el laboratorio LUMIR del Centro de Geociencias. Aprovecho para reconocer a la Lic. Ana María, quien siempre con total amabilidad y profesionalismo, ha apoyado a este equipo de trabajo con los trámites del proyecto.

A mis padres Lorenzo y Gloria, por apoyarme incondicional y totalmente en esta y todas las etapas de mi vida. A Ustedes les agradezco el haber sembrado en mí la sed y el gusto por el conocimiento, así como el compromiso que este conlleva para servir a la sociedad.

A mi esposa Cinthia, por siempre acompañarme y apoyarme incondicionalmente en esta etapa y todas las etapas de nuestras vidas; gracias por ser mi mayor inspiración y motivación.

ÍNDICE

Resumen

La ignimbrita Xáltipan en el Complejo Volcánico Los Humeros (CVLH) es un caso ejemplar para el estudio de grandes erupciones formadoras de calderas. Esta ignimbrita representa un evento esencial en la evolución de este complejo volcánico ya que marca un periodo de actividad explosiva relacionado con la conformación del campo geotérmico Los Humeros. En esta tesis, se presenta un estudio detallado de la ignimbrita Xáltipan a partir de una metodología que integra técnicas convencionales (trabajo de campo, petrografía, geoquímica) y modernas (microtomografía computarizada de rayos-X, picnometría con gas). Los resultados se presentan en tres partes principales: 1) la cartografía de la ignimbrita Xáltipan; 2) su historia eruptiva a partir del estudio de su anatomía (distribución, estratigrafía y magnitud); y 3) el estudio de sus facies.

En la primera parte se describe el trabajo cartográfico de la ignimbrita, para el cual se desarrolló una metodología innovadora que integra mediciones de campo, proyecciones geométricas, secciones geológicas y la aplicación de un conjunto de herramientas de Sistemas de Información Geográfica. Se hace especial énfasis en la aplicación de esta metodología para resolver los problemas durante el mapeo como son los la erosión, enterramiento y las variaciones en el soldamiento. Como resultado se presenta un mapa de la ignimbrita disponible en diferentes formatos (2D estático, 2D interactivo y 3D interactivo).

La segunda parte aborda la historia eruptiva de esta ignimbrita. Para esto, se hizo un análisis estratigráfico de los depósitos de flujos piroclásticos fuera de la caldera. La estratigrafía se construyó a partir de dos *secciones estratotipo* que muestran la distribución de las unidades internas de la ignimbrita y su relación con las condiciones de emplazamiento. Con la estratigrafía, se interpretó una erupción continua, dividida en cuatro fases: La erupción inicia con una fase Pliniana efímera (fase 1) que generó una columna sostenida y el depósito de caída de pómez basal (BPF), la cual eventualmente colapsó formando depósitos de corrientes piroclásticas de densidad (CPD). La erupción evolucionó a su fase culminante tipo *boiling-over* (fase 2), marcada por la generación masiva de CPD que formaron la unidad de flujo inferior (LFU) y en donde ocurrió el colapso de la caldera Los Humeros. Esta fase terminó con el declive de la erupción y el cese en la generación de CPD. Posteriormente ocurrió una

segunda fase Pliniana (fase 3) al oeste de la caldera formando un depósito de caída intermedio (IPF). La erupción finaliza con el colapso de la columna eruptiva y la generación de CPD de la unidad de flujo superior (UFU). Además, se presenta un cálculo de la magnitud eruptiva a partir del volumen y masa de la ignimbrita. Para esto, se implementó una metodología *ad hoc* que considera la distribución, espesor, densidad y el volumen erosionado de la ignimbrita Xáltipan. La magnitud resultante es de *ca.* 290 km^3 de roca densa equivalente y una masa de 1.1x10^{12} kg, lo que indica que se trata de la mayor erupción explosiva registrada en la Faja Volcánica Trans-Mexicana (Índice de Explosividad Volcánica 6 – 7). Este nuevo cálculo de la magnitud eruptiva apunta a una fuente magmática mucho mayor a la convencionalmente utilizada para el modelo geotérmico de Los Humeros (115 km^3), lo cual podría implicar la existencia de condiciones geotérmicas aún más favorables que las previamente consideradas.

En la tercera parte se presenta una caracterización de las facies de la ignimbrita. Esto a partir de una serie de análisis petrofísicos y geoquímicos en muestras de los flujos piroclásticos y de los depósitos intracaldera. A partir de los resultados petrofísicos, se identificó una asociación de tres facies, la cual puede ser correlacionada entre ambos ambientes: 1) La facies basal, caracterizada por alto grado de soldamiento, baja porosidad (dominada por vesículas) y condiciones de impermeabilidad (<0.01 – 0.05 mD) causadas por efectos de soldamiento y reducción de poros por minerales secundarios. 2) La facies intermedia, en donde el soldamiento es moderado y la porosidad es mayor; esta última conformada por espacios interesquirlas, vesículas y fracturas. En esta facies, la mineralización es un factor reductor de porosidad importante. No obstante, las condiciones son permeables (6.11 – 46.38 mD). 3) La facies superior, la cual está conformada por los depósitos con nulo a bajo grado de soldamiento, y en donde las condiciones de porosidad y permeabilidad son altas (310.72 – 1,557.26 mD). Dentro del campo geotérmico, el desarrollo de esta asociación de facies petrofísicas está directamente controlada por el espesor de la ignimbrita. En donde el espesor es mayor a 400 m, se desarrolla la asociación de facies completa, mientras que donde es menor se desarrollan solamente las facies intermedia y superior. Esto significa que, en donde el espesor de la ignimbrita es mayor a 400 m, es probable que se hayan desarrollado condiciones impermeables en su base (facies basal), lo cual puede servir como un sello para el paso de fluidos hidrotermales. Además, se identificó la presencia de brechas líticas co-ignimbríticas intercaladas en la ignimbrita intracaldera que no habían sido previamente

reportadas y que son interpretadas como resultado del proceso del colapso de la caldera Los Humeros. Geoquímicamente, la ignimbrita presenta zonamiento composicional que va de riolítico en la base (LFU) a traquítico-riolítico hacia la cima (IPF y UFU). Este zonamiento se interpreta como el resultado de una cámara magmática composicionalmente heterogénea. Finalmente, la correlación positiva entre las asociaciones de facies entre los depósitos de flujos piroclásticos y los depósitos intracaldera sugiere un sistema análogo sin precedentes. Por lo tanto los flujos fuera de la caldera pueden funcionar como un referente para entender las condiciones de porosidad y permeabilidad de la ignimbrita en el campo geotérmico.

Palabras clave: **Complejo Volcánico Los Humeros; estratigrafía de ignimbritas; facies de ignimbritas; cartografía volcánica; Corrientes Piroclásticas de Densidad; magnitud eruptiva; erupciones formadoras de calderas**

Abstract

The Xáltipan ignimbrite at the Los Humeros Volcanic Complex (CVLH) is a model case for studying large caldera-forming eruptions. This ignimbrite represents the main event in the evolution and configuration of this volcanic complex since it marks a period of explosive activity related to the onset of the Los Humeros geothermal field. In this thesis, a detailed study of the Xáltipan ignimbrite is presented based on a methodology that integrates conventional (fieldwork, petrography, geochemistry) and modern techniques (computerized X-ray microtomography, gas pycnometry). The results are presented in three main parts: 1) the mapping of the Xáltipan ignimbrite; 2) its eruptive history from the study of its anatomy (distribution, stratigraphy, and magnitude); and 3) the study of its facies.

In the first part, the ignimbrite cartographic work is described, for which an innovative methodology was developed integrating field measurements, geometric projections, geological sections, and a set of Geographic Information Systems tools. Particular emphasis is placed applying this methodology to solve problems while mapping the ignimbrite, such as erosion, burial, and welding variations. As a result, a detailed map of the ignimbrite is presented in different formats (static 2D, interactive 2D, and interactive 3D).

The second part deals with the eruptive history of this ignimbrite. For this, a robust stratigraphic analysis was made on the outflows. The stratigraphy was built from two stratotype sections showing the ignimbrite's internal units and their relationship with the emplacement conditions. From the ignimbrite's stratigraphy, a continuous eruption was interpreted, divided into four phases: The eruption begins with an ephemeral Plinian phase (phase 1) that generated a sustained column and the basal pumice deposit (BPF), which eventually collapsed forming pyroclastic density current (PDC). The eruption evolved directly into its boiling-over type climatic phase (phase 2), marked by the massive generation of PDC that formed the lower flow unit (LFU) and where the collapse of the Los Humeros caldera occurred. This phase ends with an eruption waning and the interruption of PDC generation. Subsequently, a Plinian phase (phase 3) occurred in the western sector of the caldera, forming an intermediate fall deposit (IPF). The eruption ends with the collapse of the eruptive column and the generation of the upper flow unit (UFU). Furthermore, a

calculation of the eruptive magnitude from the volume and mass of the ignimbrite is presented. For this calculation, an *ad hoc* methodology was implemented that considers the distribution, thickness, density, and the eroded volume of the Xáltipan ignimbrite. The resulting magnitude is *ca.* 290 km^3 of dense rock equivalent and a mass of 1.1x10^{12} kg, indicating that it is the largest explosive eruption recorded in the Trans-Mexican Volcanic Belt (6 – 7 Volcanic Explosive Index). This new calculation of the eruptive magnitude points to a much larger magmatic source than the conventionally used for the Los Humeros geothermal model (115 km^3), which could imply the existence of even more favorable geothermal conditions than previously thought.

The third part presents a facies characterization of the ignimbrite. For this, a series of petrophysical and geochemical analyzes were applied to samples of pyroclastic flows and intracaldera deposits. From the petrophysical results, a three-facies association was identified which can be correlated between both environments. 1) The basal facies, characterized by high welding degree, low porosity (dominated by vesicles), and conditions of impermeability (<0.01 – 0.05 mD) caused by effects of welding and reduction of pores by secondary minerals. 2) The intermediate facies, where welding is moderate, and porosity is higher, this last being made up of intershard spaces, vesicles, and fractures. In this facies, mineralization is an important pore reducing factor. However, conditions are permeable (6.11 - 46.38 mD). 3) The upper facies, which is made up of non-to-poorly welded deposits, and where the conditions of porosity and permeability are high (310.72 - 1,557.26 mD), being incipiently reduced due to the effects of welding and secondary mineralization. Into the geothermal field, the occurrence of this facies association is directly controlled by the ignimbrite's thickness. Where the thickness is larger than 400 m, the complete facies association develops, while where it is thinner, only the intermediate and upper facies develop. This means that where the ignimbrite is thicker than 400 m, the development of impermeable conditions at the base (basal facies) is more likely, serving as a caprock for hydrothermal fluids' circulation. Moreover, several unprecedented coarse co-ignimbritic lithic breccias were identified into the intracaldera ignimbrite, which are interpreted to derive from the caldera collapse event. Geochemically, the ignimbrite presents compositional zoning that goes from rhyolitic at the base (LFU) to trachytic-rhyolitic towards the top (IPF and UFU). This zoning is interpreted as the result of a subtle compositionally heterogeneous magmatic chamber. Finally, the

positive correlation between facies associations between pyroclastic flow deposits and intra-caldera deposits suggests an unprecedented analogous system. Therefore the outflows could serve as a reference to understand the ignimbrite's porosity and permeability conditions into the geothermal field.

Keywords: **Los Humeros Volcanic Complex; ignimbrites stratigraphy; ignimbrites facies; volcanic mapping; Pyroclastic Density Currents; eruptive magnitude; caldera-forming eruptions**

1. Introducción

Las ignimbritas asociadas a las calderas de colapso evidencian los eventos volcánicos más explosivos y catastróficos de la Tierra. Estas ignimbritas se forman a partir del emplazamiento de grandes volúmenes de Corrientes Piroclásticas de Densidad (CPD), que son corrientes más densas que la atmósfera y altamente móviles impulsadas por la energía eruptiva y gravitacional. Debido a la naturaleza móvil y densa de las CPD, las ignimbritas tienden a cubrir grandes extensiones alrededor de su fuente volcánica superando barreras topográficas, rellenando valles y nivelando el terreno. Estas características hacen de las ignimbritas depósitos muy variables en su anatomía, es decir, en su distribución, tamaño y estratigrafía, así como en sus facies. Es por esto que la anatomía y facies de las ignimbritas aportan información valiosa para interpretar su historia eruptiva, misma que es crucial para entender la evolución del sistema volcánico que las alberga. Además, el estudio de las facies de las ignimbritas permite conocer los mecanismos de sedimentación de sus CPD y los procesos fisicoquímicos que han actuado durante y después de su emplazamiento. Adicionalmente, debido a que las calderas son ambientes de formación de sistemas geotérmicos, las ignimbritas suelen ser unidades clave para la conformación y el funcionamiento de importantes campos geotérmicos.

La ignimbrita Xáltipan (IX) representa la erupción formadora de caldera más importante en la evolución del Complejo Volcánico de Los Humeros (CVLH), el sistema caldérico más grande de la Faja Volcánica Trans-Mexicana (FVTM) (Fig. 1). Además, de acuerdo al volumen estimado en este trabajo de *ca.* 290 km^3 de roca densa equivalente (RDE), esta erupción representa el evento explosivo de mayor magnitud de la FVTM, durante el cual ocurrió el colapso de la caldera Los Humeros (Ferriz y Mahood, 1984; Willcox, 2011). Por otro lado, esta erupción también marca el inicio de un periodo de actividad explosiva en el CVLH hace 164±4.2 ka, en el que se registran al menos tres fases explosivas principales; dos de ellas asociadas a la formación de calderas y CPD (ignimbrita Xáltipan - caldera de los Humeros; ignimbrita Zaragoza - caldera de Los Potreros), y una fase de tipo Pliniana, formadora de depósitos de caída de pómez (toba Faby) (Ferriz y Mahood, 1984). El piso y relleno volcánico de este sistema de calderas alberga al campo geotérmico Los Humeros, uno de los principales campos productores de energía eléctrica en México (*ca.* 95 MW, de acuerdo con Romo-Jones et al., 2017). Dentro de este sistema, la IX es una unidad clave ya que sobreyace directamente a las unidades reservorio. Por lo tanto, las propiedades de porosidad y permeabilidad de la IX son fundamentales en las trayectorias de los fluidos hidrotermales. Todos estos atributos hacen de la IX un caso de estudio ejemplar a nivel mundial para mejorar el entendimiento de los procesos asociados a erupciones formadoras de calderas, el emplazamiento de ignimbritas de gran volumen y las variaciones de sus facies, las cuales son de gran relevancia para determinar las condiciones de permeabilidad de los sistemas geotérmicos.

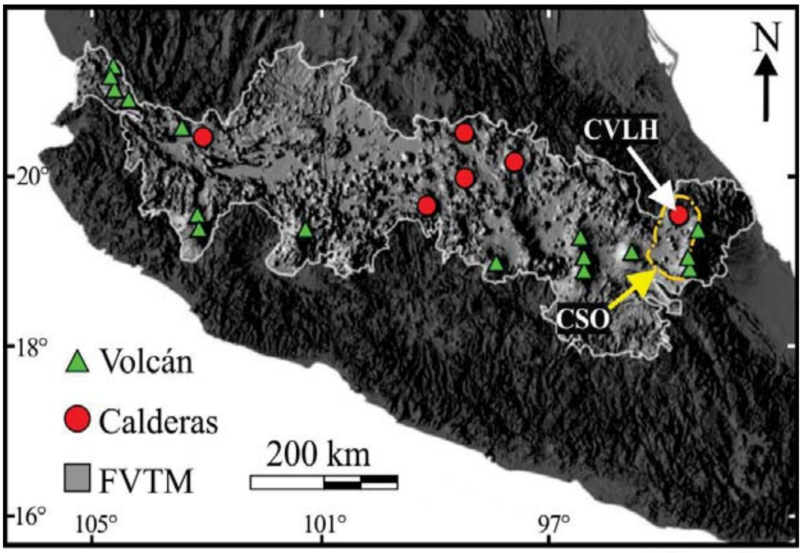

Fig. 1. Ubicación del Complejo Volcánico de Los Humeros (CVLH) y la Cuenca Serdán Oriental (CSO) en el límite este de la Faja Volcánica Trans-Mexicana (FVTM). Modificado de Carrasco-Núñez et al. (2018)

En este trabajo se presenta una caracterización detallada de la IX que incluye su anatomía y facies, esto a partir de una metodología que integra técnicas convencionales (trabajo de campo, petrografía, geoquímica cuantitativa) y modernas (microtomografía computarizada de rayos-X, picnometría de gas). Los resultados obtenidos durante el desarrollo de este trabajo se expresan en forma de tres artículos científicos, los cuales son el sustento para proponer la historia de esta gran erupción, cuya magnitud, aquí recalculada, la posiciona como la más grande de la FVTM. Además, se presenta un estudio detallado de las facies que describe a los depósitos que se emplazaron fuera y dentro de la caldera Los Humeros. Este modelo de facies provee una caracterización robusta de las propiedades de porosidad y permeabilidad de la ignimbrita en sus diferentes niveles estratigráficos, por lo que puede ser aplicada directamente al modelo del campo geotérmico. Finalmente, aunque esta tesis se desarrolló utilizando de diversas metodologías convencionalmente empleadas para el estudio de ignimbritas, también se presenta el desarrollo de metodologías innovadoras que tienen el potencial de ser aplicadas en otros estudios de ignimbritas a nivel global.

1.1 Justificación

Aunque el CVLH representa uno de los campos volcánicos más estudiados en México, aún se conoce poco acerca de su principal erupción, la cual derivó en la formación de la IX y en el colapso de la caldera Los Humeros. Esta erupción podría considerarse como la más importante del CVLH por diversas razones: 1) Se trata de la erupción explosiva de mayor magnitud del CVLH, y posiblemente de la FVTM con un volumen de 115 km^3 de RDE (reportado previo a este trabajo por Ferriz y Mahood, 1984); 2) Durante esta erupción ocurrió el colapso de la caldera Los Humeros, la estructura principal que alberga al actual sistema geotérmico (Ferriz y Mahood, 1984; Willcox, 2011); 3) Esta erupción marca el inicio de la etapa caldérica hace 164±4.2 ka (Carrasco-Núñez, et al., 2018), conformada por al menos tres erupciones explosivas, la formación de un sistema de calderas anidadas y el emplazamiento de potentes depósitos piroclásticos dentro y fuera del sistema caldérico; 4) Dentro de la caldera, la IX sobreyace directamente al basamento volcánico, el cual está compuesto por una secuencia de lavas andesíticas altamente fracturadas y que funciona como la unidad reservorio del actual campo geotérmico. Esto significa que, dependiendo de sus propiedades de porosidad y permeabilidad, la IX puede funcionar como una unidad sello.

Estas características hacen de la IX un caso de estudio ejemplar para mejorar el entendimiento de estas grandes erupciones formadoras de calderas a partir de sus depósitos. Por estos motivos es necesario desarrollar un estudio geológico integral y detallado de la IX que permita reconstruir la historia de esta erupción, así como reevaluar la magnitud eruptiva a partir de su anatomía (distribución, tamaño y estratigrafía). Adicionalmente, es necesario hacer una caracterización detallada de las facies de la ignimbrita a partir de sus propiedades petrofísicas y geoquímicas. Esto último con el objetivo de entender los procesos fisicoquímicos que han actuado desde la erupción hasta después de su emplazamiento, así como para explicar las variaciones de permeabilidad que tiene la ignimbrita en el campo geotérmico.

1.2 Hipótesis

La caracterización geológica detallada de la IX, que incluya su anatomía y facies, aportará nueva información que mejorará el entendimiento de la evolución volcánica del CVLH, los mecanismos de emplazamiento de grandes ignimbritas y los procesos fisicoquímicos que las forman y modifican. El estudio de las variaciones de facies puede asociarse a cambios en las propiedades de porosidad y permeabilidad de las rocas en el subsuelo del campo geotérmico, lo que permitirá explicar la variabilidad de la permeabilidad en el subsuelo.

1.3 Objetivos

Objetivo general

Realizar una caracterización geológica de la IX, que incluya su distribución, estratigrafía y facies, a partir de técnicas convencionales (trabajo de campo, petrografía, geoquímica) y modernas (microtomografía computarizada de rayos-X, picnometría con gas), que permita interpretar su historia eruptiva y proponer un modelo de facies aplicable al campo geotérmico Los Humeros.

Objetivos particulares

- Elaborar un mapa de la IX que muestre su distribución original y actual.
- Calcular los parámetros de la ignimbrita que permitan estimar su magnitud eruptiva.
- Reconstruir la historia eruptiva de la IX a partir de su anatomía, es decir, de su tamaño, distribución y estratigrafía.
- Identificar y clasificar las diferentes facies de la ignimbrita a partir de sus características petrofísicas y geoquímicas.
- Proponer un modelo de facies que pueda ser utilizado para fines de exploración y explotación de campo geotérmico de Los Humeros.

2. Marco teórico

En esta sección se describen los principales conceptos utilizados para la descripción de las ignimbritas, mismos que son utilizados en esta tesis para describir y discutir los atributos de la IX.

2.1 Ignimbritas

Las ignimbritas son un tipo de depósito de las CPD caracterizadas por ser ricas en material pumicítico. Estas pueden presentar una gran variedad de tamaños, formas y facies. Generalmente, están compuestas por una mezcla pobremente seleccionada de pómez y líticos accidentales tamaño lapilli a bloque, soportados en una matriz de ceniza pumicítica y cristalina, que se depositan en facies de toba o toba-lapilli, y que puede o no presentar soldamiento.

2.2 Modelos de emplazamiento de las ignimbritas

La primera propuesta que explica el emplazamiento de las ignimbritas es el modelo *en masse* (Freundt y Schmincke, 1986; Sheridan, 1979; Sparks et al., 1973; Sparks, 1976; Wright y Walker, 1981). Este modelo sostiene que las corrientes piroclásticas se transportan como un flujo granular denso, altamente concentrado y con una anatomía bien definida que se emplaza de manera súbita, y cuyo depósito refleja la estructura (o parte de) su flujo padre. Por lo tanto, los depósitos de estos flujos tienden a seguir una anatomía genérica denominada unidad estándar de flujo ignimbrítico. Además, este modelo propone que los depósitos reflejan el espesor y las estructuras del flujo justo antes de su depósito. Una descripción detallada de la anatomía de la unidad de flujo ignimbrítico estándar, y el significado de cada una de sus partes se presenta en Sparks et al. (1973).

El modelo *en masse* fue posteriormente cuestionado en los trabajos magistrales de Branney y Kokelaar (1992; 2002) quienes proponen que la anatomía de las ignimbritas no es para nada genérica, por el contrario, que estas son el resultado de un proceso de sedimentación gradual que ocurre en la zona límite entre la base de la CPD y el sustrato, denominado agradación progresiva. Este mecanismo fue primeramente propuesto por

(Fisher, 1966), y establece que dentro de las CPD existe una zona de interfase entre la base de la corriente y la parte superior del depósito denominada zona límite de flujo (ZLF). En esta zona ocurre la sedimentación gradual de las partículas transportadas en la parte basal del flujo. Por lo tanto, bajo condiciones de sedimentación en la ZLF el depósito incrementa su espesor. Esto significa que la construcción vertical de los depósitos registra los cambios temporales en la ZLF, y no la estructura del flujo al momento de su emplazamiento, como se había propuesto en el modelo *en masse*.

No obstante la gran diferencia que existe en ambos modelos para explicar el mecanismo de emplazamiento de las CPD, en la literatura es común encontrar ignimbritas que presentan evidencias que soportan ambos modelos. Por ejemplo, estructuras como frentes (*levees*) abruptos o lobados en las facies terminales de los flujos (p.e., Iverson y Vallance, 2001; Miyabuchi, 1999; Rowley, 1981) reflejan condiciones de alta resistencia interna de los flujos (Sparks, 1976), la cual es una característica del modelo *en masse*. Por otro lado, en muchos otros casos, la ocurrencia de grandes espesores de ignimbritas masivas, en donde no se identifican los componentes de la unidad de flujo estándar, evidencian el modelo de agradación progresiva (Bursik y Woods, 1996; Dade y Huppert, 1996). Otra evidencia que soporta fuertemente al modelo de agradación progresiva es el zonamiento composicional del material juvenil en ignimbritas, el cual refleja un cambio temporal en la fuente magmática (Branney y Kokelaar, 1992, 1997; Carrasco-Núñez y Branney, 2005).

2.3 Distribución y volumen de los depósitos

Las ignimbritas pueden presentarse en una amplia variedad de formas y tamaños (Fig. 2). Una característica general de las ignimbritas poco voluminosas que se emplazan en terrenos altamente accidentados, es que estas tienden a rellenar parcialmente las depresiones topográficas y por lo tanto adoptan su morfología canalizada. Por otro lado, las ignimbritas de gran volumen suelen cubrir totalmente el terreno, resultando en una morfología radial con una superficie suavizada. Un caso particular es el de las erupciones dirigidas como la del Monte Santa Helena en 1980, en donde las CPD se emplazan hacia el flanco de la erupción en forma de abanico.

El área cubierta por las ignimbritas puede variar ampliamente del orden de algunos cientos de metros cuadrados hasta cerca de 45,000 km^2 (Freudnt et al., 2000). El área de dispersión suele ser mayor mientras más grande es el volumen eyectado, la fluidez de la CPD y la uniformidad topográfica del terreno pre-eruptivo. Esto significa que, la forma y extensión final de una ignimbrita está directamente relacionada con el volumen de material piroclástico eyectado durante la erupción, así como con las condiciones de emplazamiento de sus CPD.

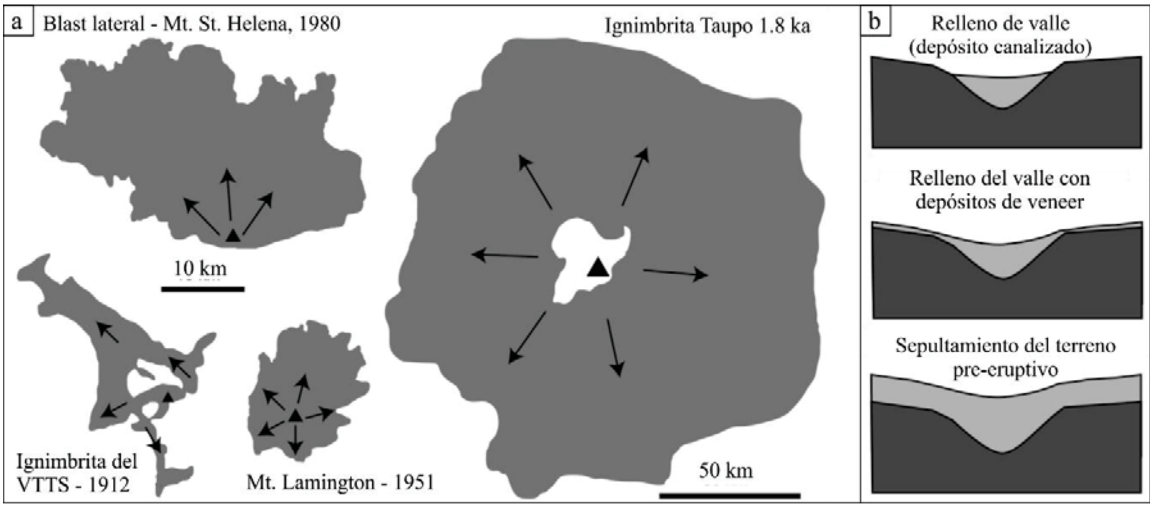

Fig. 2. a) Mapas de distribución de ignimbritas mostrando diferentes morfologías. b) Sección transversal de un canal o valle con relleno de depósitos piroclásticos (modificado de Brown y Andrews, 2015).

El volumen de las ignimbritas puede variar hasta en seis órdenes de magnitud (0.001 - >1000 km^3 - RDE) (Brown y Andrews, 2015). En el caso de las ignimbritas de gran volumen, estas suelen estar relacionadas con eventos catastróficos en donde ocurre la formación de calderas de colapso. Por ejemplo, la ignimbrita Toba (74 ka), con un volumen de ≥30,000 m^3 (Rose y Chesner, 1987), estuvo a punto de causar la extinción del *Homo Sapiens* (Rampino y Self, 1993).

Considerando que el volumen de las ignimbritas puede ser muy variable, su cálculo representa una tarea desafiante, particularmente en el caso de ignimbritas de gran tamaño que han sido modificadas por procesos como la erosión o que están sepultadas por otros depósitos más jóvenes. Es por esto que se han realizado diversos trabajos enfocados al cálculo de la volumétrico de ignimbritas, el cual tiene la finalidad de estimar la magnitud de las erupciones que las generaron (p.e., Best et al., 2013; Cook et al., 2016; Folkes et al., 2011; Giordano et al., 2010). De manera concreta, la magnitud representa la cantidad de material eyectado durante una erupción, la cual se puede medir a partir del volumen de sus depósitos o de la masa magmática eyectada (Pyle, 2015). En el caso del volumen, éste representa, en términos de espacio, el tamaño de la ignimbrita. Existen dos maneras de reportar este volumen: el primero es el volumen no compactado, el cual representa el espacio real que ocupa la ignimbrita ya depositada y que considera los factores de fragmentación y porosidad intrínsecos en estos depósitos. Regularmente para este cálculo solamente se utilizan datos de área de dispersión y de espesor de los depósitos. El segundo es el volumen de RDE, el cual considera el volumen magmático eyectado durante la erupción. Para esto, es necesario conocer el volumen no compactado para luego corregirlo en función de la densidad magmática, es decir, no fragmentada ni porosa. En cuanto al cálculo de la magnitud a partir de su masa, esta se mide en kilogramos y se representa con una escala logarítmica (Ecuación 1).

Ecuación 1): $\text{Magnitud} = \log_{10}(\text{masa eyectada, kg}) - 7$

Otro parámetro comúnmente utilizado para estimar el poder explosivo de una erupción es a partir de su intensidad, que mide la tasa de descarga de la erupción (Ecuación 2). Por lo tanto, la intensidad se puede traducir como la relación entre la magnitud de la erupción en función del tiempo (kg/s).

Ecuación 2): $\text{intensidad} = -\log_{10}(\text{tasa de masa eyectada, kg/s}) + 3$

No obstante, no es posible calcular este parámetro en casos de erupciones explosivas en donde se desconozca la duración del evento.

El Índice de Explosividad Volcánica (IEV) es una de las medidas más ampliamente utilizadas para representar las erupciones volcánicas explosivas (Newhall y Self, 1982). Este cálculo establece una escala logarítmica del 0 al 8 que describe con un valor el tamaño, duración y explosividad de una erupción, antigua o actual. Para esto, el IEV combina los parámetros de volumen de ceniza producida, la altura de la pluma y la duración de la erupción. Sin embargo, en el caso de que algunos de estos parámetros no puedan ser medidos, es posible utilizar el resto para determinar el IEV de una erupción.

En el caso de erupciones antiguas, el cálculo del IEV se basa únicamente en el volumen de los depósitos, del cual es posible inferir la intensidad. En erupciones observadas, la altura de la columna es la base para determinar la intensidad del evento. Aunque es imposible determinar con precisión la dimensión de la columna de erupciones antiguas es posible aproximar este valor si se conoce la dispersión de los piroclastos derivados de la erupción.

2.4 Ignimbritas de relleno de valle y tipo *veneer*

Se puede concluir que la fluidización de las CPD y el terreno sobre el cual se depositan son factores determinantes para la morfología final de las ignimbritas. A partir de los trabajos realizados en la ignimbrita Taupo (Nueva Zelanda) (Walker, 1980; Walker et al., 1981) es posible clasificar dos tipos de ignimbritas en función de su movilidad y los terrenos en donde se emplazan: las ignimbritas de relleno de valle y las ignimbritas tipo *veneer* (Fig. 3).

Las ignimbritas de relleno de valle se caracterizan por el emplazamiento de las CPD en depresiones topográficas. Estos depósitos, los cuales se interpretan como el resultado de CPD altamente concentradas y de baja movilidad, suelen ser de gran espesor y masivos (p.e., Miyabuchi, 1999). En valles donde la acumulación de piroclastos es suficientemente alta, el relleno forma nueva topografía con una superficie relativamente plana. Mientras que de no ser suficiente, estas rellenan parcialmente los valles dejando expuestos los altos topográficos (Fig. 2b). Un proceso típico en las ignimbritas que se emplazan en valles hidrológicamente activos es la erosión, la cual tiende a incidir preferencialmente en las zonas donde la ignimbrita está no consolidada. Regularmente, estas incisiones por erosión, son las principales ventanas que permiten determinar el espesor y estructuras del depósito.

Las ignimbritas tipo *veneer*, al contrario de las de relleno de valle, se caracterizan por cubrir de manera más uniforme el terreno, incluyendo las zonas topográficamente altas. Estas están asociadas a CPD altamente móviles y diluidas, y son formados por la interacción de la parte superior y más veloz de la corriente con la topografía. Los principales rasgos que caracterizan a estos depósitos, y que los distinguen de las ignimbritas de relleno de valle, son que estos cubren la topografía de manera semicontinua, con una capacidad de depositarse en pendientes de hasta 30º con una superficie paralela al terreno. Además, es común que presenten estratificación. El espesor de estos depósitos se caracteriza por ser muy variable, adelgazándose hacia la cima y aumentando hacia los flancos. No obstante, el espesor es mucho menor que el de las ignimbritas de relleno de valle, regularmente del orden de centímetros a unos cuantos metros. En muchos casos estos depósitos no se observan en el registro ignimbrítico debido a que son fácilmente erosionados por su espesor relativamente bajo y pobre a nula consolidación.

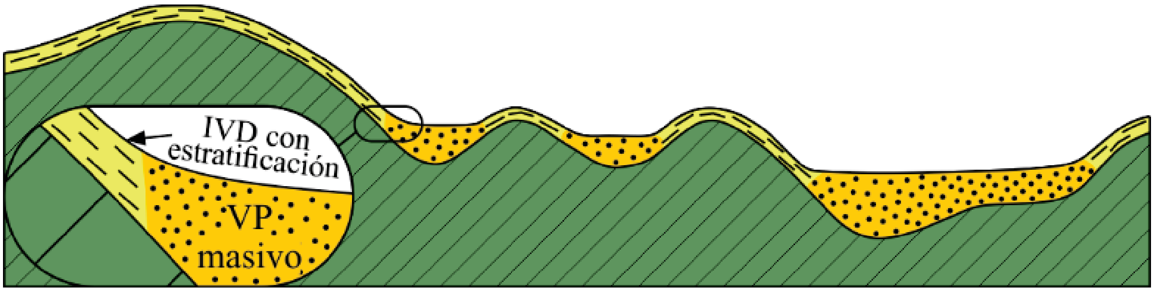

Fig. 3. Sección transversal de la ignimbrita Taupo (Nueva Zelanda) mostrando los depósitos tipo *veneer* (IVD) y de relleno de valle (VP) (modificado de Walker et al. 1981).

2.5 Componentes y composición

Las ignimbritas son una mezcla heterogénea de material piroclástico juvenil (pómez y escoria en la fracción lapilli, esquirlas de vidrio y cristales en la fracción de ceniza), líticos accidentales incorporados durante el ascenso por los conductos y durante su emplazamiento sobre la superficie, e incluso restos de vegetación y suelo atrapado por la corriente. Por lo tanto, la materia sólida dentro de una CPD tiene un amplio rango de propiedades físicas, como densidad, tamaño y forma. Por ejemplo, la fracción de pómez tiene una densidad de 200-1000 kg/m^3, mientras que los clastos líticos son típicamente >2000 kg/m^3 (Brown y Andrews, 2015).

El material juvenil de las ignimbritas es generalmente de composición ácida (riolítica a dacítica), debido a la relación que existe entre la viscosidad de los magmas ácidos y la alta acumulación de volátiles, lo que deriva en erupciones de carácter explosivo. No obstante, se han reportado ignimbritas, regularmente de menor volumen, que son de composición intermedia a básica [p.e., Masaya en Nicaragua (Williams, 1983), Tanna en el Archipiélago Vanuatu (Robin et al., 1994), o el campo volcánico Garrotxa en la Península Ibérica (Martí et al., 2017)]. Por otro lado, la mayoría de las ignimbritas, particularmente las de gran volumen, presentan zonamiento composicional del material juvenil. Este zonamiento composicional resulta de variaciones composicionales de la fuente magmática y/o por modificaciones del conducto durante la erupción. Los procesos más comunes incluyen la estratificación composicional por diferenciación de la fuente magmática, mezcla de magmas, inyecciones de magmas composicionalmente diversos y cambios en el conducto por el colapso del techo parcial o total del techo de la cámara magmática (Bacon y Druitt, 1988; Briggs et al., 1993; Cole et al., 2005; Fedele et al., 2016). Por otro lado, estudios recientes han explicado la formación de ignimbritas composicionalmente zonificadas por la interacción de cuerpos ricos en cristales (*crystal mush zones*) con zonas ricas en fundidos (*high-melt* zones) en sistemas magmáticos física y composicionalmente heterogéneos (Bachmann y Bergantz, 2004, 2008; Cashman y Giordano, 2014).

2.6 Facies de las ignimbritas

El término facies aplicado para las ignimbritas se puede definir como el conjunto de características físicas y composicionales, de una parte o todo el depósito, que la distingue de su entorno, y que son el resultado de varios procesos que actúan desde la erupción, durante la sedimentación y después del emplazamiento (p.e., Branney y Kokelaar, 2002; Brown y Branney, 2004; Druitt, 1998; McPhie et al., 1993; Quane y Russell, 2005; Wilson y Walker, 1982). Aun cuando el término facies es estrictamente descriptivo, esta descripción es la base para interpretar los procesos volcánicos formadores de las ignimbritas. Sin embargo, para la caracterización de las facies de una ignimbrita es indispensable conocer la estratigrafía y arquitectura de sus depósitos. Esto debido a que las ignimbritas comúnmente exhiben múltiples facies, las cuales pueden variar espacialmente de manera gradual a abrupta y a distintas escalas (dentro de unidades de flujo hasta sucesiones de ignimbritas).

Es posible hacer estudios de facies en ignimbritas desde diferentes perspectivas, que pueden ser sedimentarias, petrofísicas o composicionales. Los estudios con enfoques sedimentarios son aquellos que comprenden la descripción de las estructuras sedimentarias o ausencia de ellas, la relación y contenido de componentes y fábrica de sus depósitos. Estas características son la base para interpretar la evolución temporal del emplazamiento de las ignimbritas así como su historia eruptiva (Branney y Kokelaar, 2002). Desde el punto de vista petrofísico, es posible hacer una clasificación de facies basada en las propiedades físicas del depósito, principalmente en el tipo de medio poroso y su relación con la fracción sólida (Couves et al., 2016; Grunder y Russell, 2005; Quane y Russell, 2005; Streck y Grunder, 1995), e incluso basada en su respuesta a factores físico mecánicos (p.e., Bernard et al., 2007; Flint y Selker, 2003; Langella et al., 2017).

Por otro lado, el zonamiento composicional de las ignimbritas también es un criterio para la distinción de facies. Esto debido a que este zonamiento revela cambios temporales en el suministro del magma fuente de las ignimbritas. Una inspección detallada de estas variaciones tiene el potencial de revelar los procesos magmáticos que actuaron durante la erupción, así como posibles cambios del conducto. Además, las facies composicionales pueden ser utilizadas como marcadores estratigráficos usados en la correlación de ignimbritas.

2.7 Brechas líticas co-ignimbríticas

Las facies ricas en líticos son elementos típicos en las ignimbritas que se desarrollan principalmente en las zonas proximales a medias en forma de brechas líticas (Allen y Cas, 1998; Branney y Acocella, 2015; Branney y Kokelaar, 1992; Druitt y Bacon, 1986; Druitt y Sparks, 1982; Lipman, 1976, 1984). Particularmente, es común encontrar brechas líticas cerca de la fuente que se forman por la erosión del conducto y ventila volcánica, originalmente referidas como “depósitos de caída de rezago co-ignimbrítico” (*co-ignimbritic lag-fall deposit*) (Wright y Walker, 1977), posteriormente referidas como “brechas de rezago” (*lag breccias*) (Druitt y Sparks, 1982), o simplemente como “brechas líticas gruesas” (*coarse lithic breccias*) (Walker, 1985). La interpretación del origen de este tipo de facies presentada por Walker (1985), sostiene que estas se depositan en las áreas proximales a la fuente, cerca de la zona de deflación de la columna eruptiva. Se trata de depósitos crudamente estratificados y que se acumulan progresivamente capa por capa, sin mostrar evidencias de acumulación por caída piroclástica. Por otro lado, el engrosamiento de sus depósitos en las depresiones topográficas y estructuras de estratificación muestran que estas han pasado por transporte lateral. Comúnmente se encuentran en la base e interestratificadas con las ignimbritas. Por lo tanto, esta interpretación sostiene que estos depósitos de brechas líticas reflejan fluctuaciones de la intensidad de la columna eruptiva o pulsos en donde se fragmentan las paredes del conducto o roca encajonante de la fuente magmática, o alternativamente evidencian un proceso de colapso de caldera. Un ejemplo de este tipo de brechas líticas formadas durante la subsidencia de las calderas de colapso, ocurre dentro de la ignimbrita Zaragoza en el CVLH (Fig. 4). Aquí, al menos dos pulsos son registrados en un mismo afloramiento en forma de brechas líticas heterolitológicas (Willcox, 2011).

Otro tipo de brecha lítica formada durante el colapso de las calderas son las “brechas de derrumbe” (*landslide breccias*), descritas por Lipman (1976). Estas brechas se han interpretado como resultado de la acumulación de fragmentos líticos desprendidos de la pared interna de la caldera, así como de las paredes de grandes bloques del piso (Fig. 5). De manera similar a las brechas líticas gruesas (o brechas de rezago), las brechas de derrumbe suelen

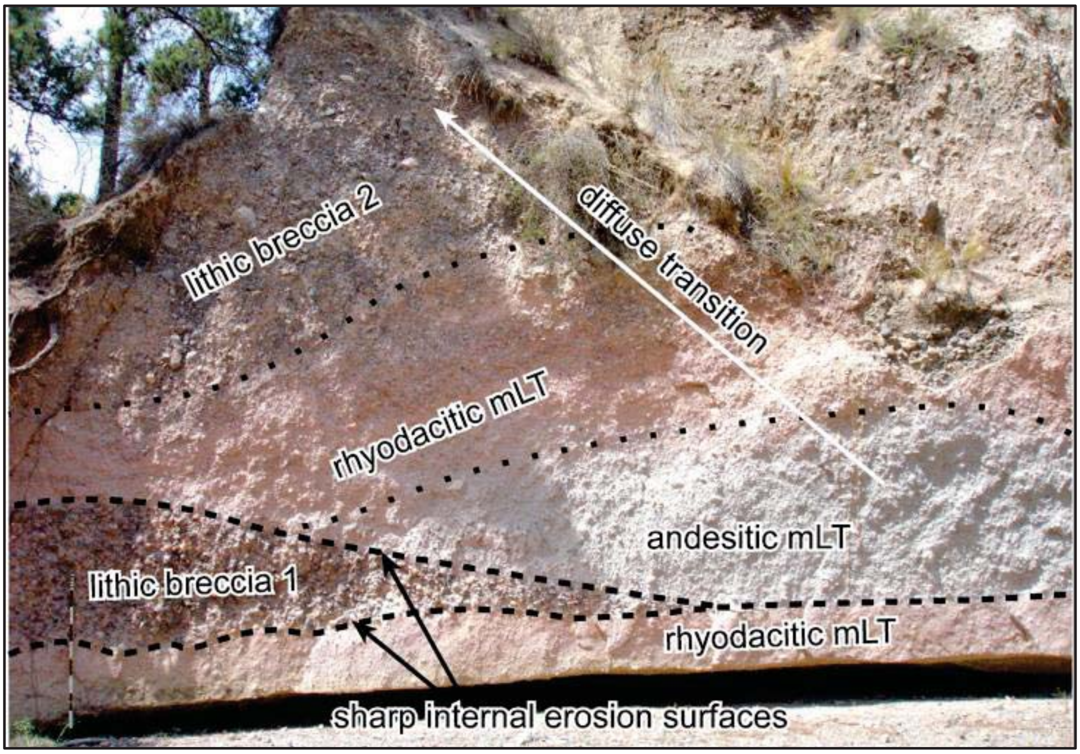

Fig. 4. Fotografía de la ignimbrita Zaragoza mostrando la presencia de al menos dos brechas líticas heterolitológicas. Cada brecha indica un posible pulso durante el colapso de la caldera Los Potreros. La división de escala está en decenas de centímetros (fotografía tomada de Willcox, 2011).

formarse durante la fase culminante de la erupción, que es cuando ocurren los principales pulsos de colapso y la fragmentación de las paredes. Durante estos pulsos, los fragmentos líticos son incorporados a las CPD y depositados en las facies proximales intercalados en la ignimbrita fuera y dentro de la caldera. En la mayoría de los casos de erupciones formadoras de calderas, la distinción del origen de las brechas líticas co-ignimbríticas en las facies proximales resulta poco factible, aunque es altamente probable que estas brechas resulten de una combinación de ambos procesos; la erosión del conducto y ventila volcánica y el desprendimiento de fragmentos de las paredes inestables del borde y piso de la caldera.

Fig. 5. Fotografía de una ignimbrita en el Monte Pinatubo (Filipinas), mostrando cerca de su cima una brecha proximal que registra la fase culminante de la erupción relacionada con la formación de una caldera de colapso. Nótese a la persona como escala (tomada de Branney y Acocella, 2015).

2.8 Efectos térmicos

El material magmático eyectado durante las erupciones ignimbríticas tiene una temperatura inicial de entre 800 y 1000 °C, llegando a temperaturas de emplazamiento de entre 200 y 600 °C (Brown y Andrews, 2015). Debido a que el vidrio que compone a las ignimbritas es un material metaestable, la exposición a altas temperaturas y la interacción con fluidos hidrotermales, deriva en procesos que modifican su textura y propiedades físicas y químicas, tal como la desvitrificación, en donde el material vítreo amorfo cambia su estructura para formar redes cristalinas silicatadas.

2.9 Soldamiento

El principal cambio físico en las ignimbritas emplazadas a alta temperatura es el soldamiento. El soldamiento involucra un conjunto de procesos que derivan en la deformación, cohesión y eventual coalescencia de los piroclastos juveniles (pómez, escoria y esquirlas de vidrio) cuando estos están sometidos a alta temperatura y presión (Grunder y Russell, 2005 y referencias en el mismo). Estas condiciones tornan a los piroclastos en materiales plásticos con el potencial de deformarse en estado dúctil. Para que esto ocurra, la temperatura debe superar la temperatura de transición de vidrio (500 y 750°C) (p.e., Gottsmann et al., 2002; Porreca et al., 2014; Quane et al., 2009; Wright et al., 2011), y debe estar sometido a un esfuerzo diferencial, los cuales son la fuerza gravitacional (en forma de peso litostático) y la inercia del flujo piroclástico. La temperatura requerida para que ocurra soldamiento varía de acuerdo a las propiedades físicas y químicas de la masa ignimbrítica, aunque esta regularmente debe superar los 500ºC. Por otro lado, entre mayor sea el peso litoestático ejercido mayor será la intensidad del soldamiento. Sin embargo, en casos extremos en donde las partículas son muy fluidas (poco viscosas), el soldamiento es casi instantáneo al emplazamiento y puede ocurrir independientemente del peso litoestático, a este proceso se le denomina aglutinación.

Las principales evidencias de soldamiento están registradas en cambios texturales y en las propiedades físicas de la ignimbrita, principalmente el aplastamiento y fábrica de los clastos de pómez y vitroclastos; además de cambios en las propiedades físicas del depósito, tales como la reducción de volumen y porosidad y el aumento de la densidad (McPhie et al., 1993; Quane y Russell, 2005).

El soldamiento generalmente desarrolla un conjunto de características texturales denominado textura *eutaxítica* (Fig. 6a). Esta se caracteriza por desarrollar un arreglo interno en donde los piroclastos se han aplanado y alineado en una dirección perpendicular a la dirección del esfuerzo principal (Fig. 6b). Los clastos pumicíticos que muestran esta deformación se les denomina *fiammes* y son excelentes marcadores de la posición original de la ignimbrita. Esto debido a que su eje corto es paralelo a la dirección del esfuerzo deformante, habitualmente la dirección vertical por presión litoestática. Además, los *fiammes* son útiles para cuantificar el grado de soldamiento, esto a partir de su grado de compactación (referido en la literatura como *oblateness*). Esta medida representa la relación del eje mayor entre el eje menor de un clasto de pómez (Ecuación 3), asumiendo que estos originalmente eran objetos esféricos que al compactarse resultan en un elipsoide (Quane y Russell, 2005).

Ecuación 3): Aplastamiento (oblateness) = $1 - c/a$

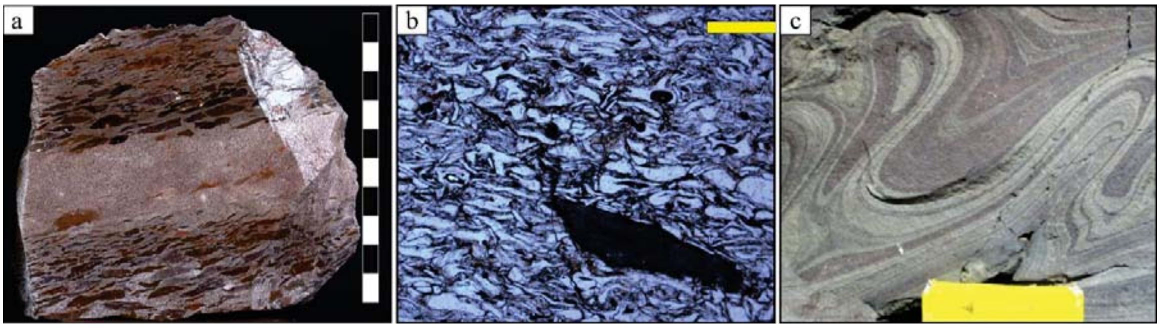

Fig. 6. Ignimbritas soldadas. a) Textura eutaxítica marcada por la formación de fiammes (clastos obscuros) en una ignimbrita moderadamente soldada (fotografía cortesía de Alexis del Pilar). Cada división en la escala representa un centímetro. b) Microfotografía de la ignimbrita Xáltipan altamente soldada, en donde se observa un clasto de pómez colapsado con aspecto de obsidiana dentro de una matriz totalmente compactada y con foliación. c) Ignimbrita reomórfica con alto grado de soldamiento mostrando deformación dúctil (tomada de Brown y Andrews, 2015).

En donde *c* representa el eje menor o compactado y *a* el eje mayor o alargado.

El nivel de soldamiento de las ignimbritas puede presentarse en un amplio rango (Fig. 7 y Tabla 1). Adoptando el esquema de clasificación de Quane y Russell (2005), el rango I es aquel en donde los clastos de pómez no están deformados y la matriz no presenta evidencias de compactación. A este tipo de ignimbrita también se le denomina ignimbrita no soldada.

En el caso extremo, el rango VI representa aquellas ignimbritas con un alto grado de soldamiento, las cuales pueden presentar deformación dúctil, ocultando su textura eutaxítica. Estas últimas comúnmente pueden ser confundidas con lavas riolíticas con textura de flujo (Fig. 6c).

Generalmente el soldamiento suele desarrollarse en las partes centrales y base de los depósitos donde la combinación de las condiciones de conservación térmica y presión litoestática es óptima. Esto ocurre aproximadamente entre el 25-33% de la distancia de la base hacia la cima (Brown y Andrews, 2015). En este sentido, el soldamiento está ausente cerca del contacto con el sustrato, ya que en esta zona la dispersión térmica enfría sustancialmente a la ignimbrita, inhibiendo el desarrollo de soldamiento. Mientras que hacia la cima, el decremento de presión litoestática y la pérdida de calor por el contacto con la atmósfera impide el soldamiento.

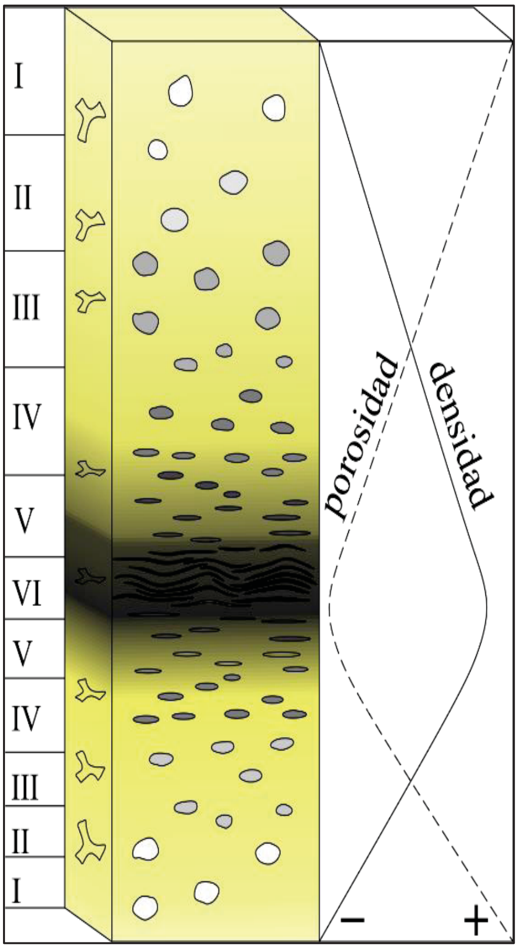

Fig. 7. Esquema de clasificación de soldamiento en ignimbritas mostrando los seis rangos de soldamiento y los efectos que estos tienen en la textura del depósito. Nótese el aumento en la densidad y disminución de la porosidad al incrementar el soldamiento (modificado de Quane y Russell, 2005).

2.10 Desvitrificación y cristalización por fase de vapor

La desvitrificación involucra la transformación de material vítreo (vidrio volcánico juvenil) a material cristalizado (Lofgren, 1971; Marshall, 1961; McPhie et al., 1993; Zheng et al., 2018). Aunque el término en el sentido estricto puede aplicarse en cuerpos magmáticos que nuclean y desarrollan cristales a profundidad; en las rocas volcánicas este término involucra el desarrollo de ciertos cuerpos cristalinos a partir del vidrio volcánico solidificado, el cuál es un material metaestable. Particularmente esto ocurre sobre los piroclastos juveniles que han sido expuestos a procesos de soldamiento, es decir, que conservaron un grado de temperatura relativamente alto por un periodo de tiempo (McPhie et al., 1993). Una de las principales asociaciones minerales de desvitrificación a alta temperatura son las esferulitas (Fig. 8a). Otro tipo de desvitrificación es el desarrollo de perlita, que se forma debido a la hidratación y expansión del vidrio (Fig. 8b). En otros casos en donde la ignimbrita disminuye lentamente su temperatura se forman la cristobalita y el feldespato alcalino.

La cristalización por fase de vapor es un proceso que ocurre posterior al emplazamiento de una ignimbrita. Se caracteriza por el desarrollo de minerales de grano fino entre los intersticios de la matriz, que pueden ser poros primarios o secundarios. Comúnmente la cristalización ocurre en vesículas no colapsadas de clastos de pómez o en fracturas secundarias (Fig. 8c). El grado de cristalización puede variar desde ligero hasta penetrativo. Al igual que durante los procesos de soldamiento y desvitrificación, este proceso involucra la liberación de material volátil, mismo que es la materia prima para formar especies minerales, por ejemplo la fase de litofisas (*litophysae)*.

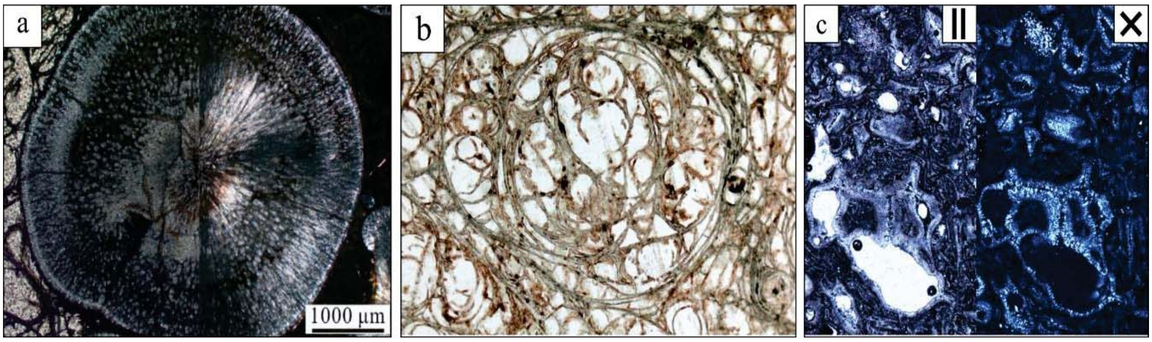

Fig. 8. Principales estructuras formadas por efectos térmicos en ignimbritas. a) esferulitas dentro de una matriz vítrea (fotografía tomada de Zheng, 2018). b) Fracturas concéntricas perlíticas formadas en un clasto de obsidiana (fotografía tomada de Shelley, 1992). c) Precipitación secundaria de cuarzo alrededor de las paredes porosas de la matriz vitroclástica de la ignimbrita Xáltipan, moderadamente soldada, en luz natural (izquierda) y polarizada (derecha) (este trabajo).

Tabla 1. Características petrográficas usadas para definir los rangos de soldamiento (tomada de Quane y Russel, 2005).

Rango	Matriz de ceniza	Pómez lapilli
I	No consolidada[1], no coherente[4], ligeramente compactada[2], con poca o nula adhesión entre esquirlas[3]	Falta de deformación[3], orientación aleatoria[2]
II	Coherente[4], cierta adherencia entre las esquirlas[3], sin coalescencia del material vítreo[3]	Orientación aleatoria[2], sin deformación[3], sin textura eutaxítica[4], se presenta fracturamiento alrededor y no en los clastos de pómez[1]
III	Altamente porosa y suave[4], lustre opaco y fracturamiento irregular[1], esquirlas con forma de burbuja originalmente esféricas ligeramente elipsoidales[3], cierta coalescencia del material vítreo[3]	Incipiente[1] a ligeramente[3] aplanadas[4] (colapsadas), se presenta fracturamiento que corta a las pómez[1]
IV	Relativamente suave[4], moderadamente foliada[5] pero las esquirlas de vidrio ligeramente deformadas[3], con incremento en el área de contacto entre esquirlas[5] y clastos moderadamente adheridos entre sí[3]	Foliación orientada a la textura eutaxítica[4] con pómez moderada a completamente colapsadas en forma de *fiammes* [3,5]
V	Esquirlas fuertemente foliadas[5], fuertemente adheridas entre sí[3] y moderadamente deformadas[3]	Foliación en una textura eutaxítica bien desarrollada[4], colapso de clastos en forma de *fiammes* [3] que presentan aspecto de obsidiana, aunque es posible observar algunas trazas de vesículas primarias[1]
VI	Vitrófiro tipo obisidiana[1,3], esquirlas fuertemente colapsadas[1,3] y completamente adheridas entre sí[3]	Textura eutaxítica y *fiammes* con aspecto de obsidiana apenas visibles[1] o difícilmente detectables[3]

[1]Smith 1960; [2]Sheridan y Ragan 1972, [3]Streck y Grunder 1995; [4]Wilson y Hildreth 2003; [5]Quane y Russel, 2005

3. Marco geológico

3.1 Contexto vulcano-tectónico

El complejo volcánico de Los Humeros (CVLH) se encuentra en el límite oriental del Faja Volcánica Trans-Mexicana (FVTM) (Fig. 1). La FVTM es un arco continental del Mioceno con más de 1,000 km de largo y 20-150 km de ancho cuya construcción resulta de un prolongado periodo de actividad volcánica, asociada a la subducción de las placas Cocos y Rivera por debajo de la placa Norteamericana a través de la trinchera Meso Americana (Demant, 1978; Ferrari et al., 2012). El CVLH se desarrolló dentro de la cuenca Serdán-Oriental, una depresión cerrada del Plioceno-Holoceno caracterizado por un vulcanismo de tipo bimodal, principalmente monogenético, en donde se han construido conos cineríticos, domos riolíticos, y *maars* basálticos y riolíticos (Carrasco-Núñez et al., 2010; Negendank et al., 1985; Siebe et al., 1995).

3.2 Basamento del CVLH

El CVLH descansa sobre un potente basamento pre-volcánico (Fig. 9) compuesto en la base por un complejo metamórfico Paleozoico asociado al macizo Teziutlán (246 – 231 Ma, Yáñez-García y García-Durán, 1982). Este macizo está cubierto por una sucesión sedimentaria marina Mesozoica compuesta por rocas sedimentarias terrígenas y carbonatadas de las formaciones Pimienta (Jurásico Tardío) y Tamaulipas Inferior (Cretácico Temprano), fuertemente deformada durante el Cretácico tardío – Eoceno por una fase orogénica asociada a la formación del Cinturón de Pliegues y Cabalgaduras Mexicano (Fitz-Díaz et al., 2018, y referencias en el mismo). Esta secuencia sedimentaria es cortada por intrusiones graníticas y sieníticas que datan del Eoceno-Oligoceno (14.5 – 31 Ma, K/Ar) que cortan a las rocas carbonatadas, que causan metamorfismo local a mármol, *hornfels* y skarn (Ferriz y Mahood, 1984; Gutiérrez-Negrín y Izquierdo-Montalvo, 2010; Yáñez-García y García-Durán, 1982). La cima de este basamento está compuesta por un periodo intenso de actividad volcánica efusiva que integra a la formación Teziutlán, la cual está compuesta por grandes campos de lavas andesíticas porfídicas recientemente fechadas entre 2.6 a 1.4 Ma. Esta unidad representa el basamento volcánico sobre el que se desarrolló el CVLH, mismo que, debido a sus alto grado de fracturamiento, sirve como el reservorio de los fluidos hidrotermales del campo geotérmico (Carrasco-Núñez et al., 2017b).

3.3 Cronoestratigrafía del CVLH

A partir de la revisión cronoestratigráfica más reciente del CVLH, es posible dividir su evolución en tres etapas: 1) etapa Precaldera; 2) etapa de Caldera; y 3) etapa Postcaldera (Carrasco-Núñez et al., 2018) (Fig. 9).

La etapa Precaldera incluye la formación de domos y flujos de lavas riolíticas que se desarrollaron en lo que actualmente es el límite occidental de la caldera Los Humeros. Fechamientos $^{40}Ar/39^{Ar}$ y U/Th de las lavas riolíticas indican que estas se emplazaron entre 693 ± 1.9 y 270 ± 17 ka. Estas unidades representan la actividad volcánica más joven previa a la fase explosiva del CVLH.

La etapa de Caldera comprende tres principales eventos explosivos. El primer y más grande evento está definido por la erupción de la IX hace 164±4.2 (U-Th en circón y $^{40}Ar/39^{Ar}$ en plagioclasa – Carrasco-Núñez et al., 2018), asociado al colapso de la caldera Los Humeros, una caldera sub-circular de 17-18 km de diámetro (Norini., 2019). El único dato reportado del volumen de esta erupción (hasta este trabajo), indica que se eyectó un total de 115 km^3 de RDE (Ferriz y Mahood, 1984).

Posteriormente, un segundo periodo de actividad explosiva representado por la formación de una secuencia de depósitos de caída separados por paleosuelos hace 70±23 ka, la cual se ha agrupado y denominado como la toba Faby (Ferriz y Mahood, 1984; Willcox, 2011). Hasta el momento no se han identificado depósitos de CPD o la formación de estructuras caldéricas asociadas a esta secuencia. La distribución de esta unidad es amplia, aunque es más evidente en la porción oriental del CVLH, en donde se ha inferido que está su fuente magmática (Ferriz y Mahood, 1984). El material juvenil de la toba Faby presenta un zonamiento composicional que va de félsica a básica además de un aumento en el contenido de fenocristales (Ferriz y Mahood, 1984).

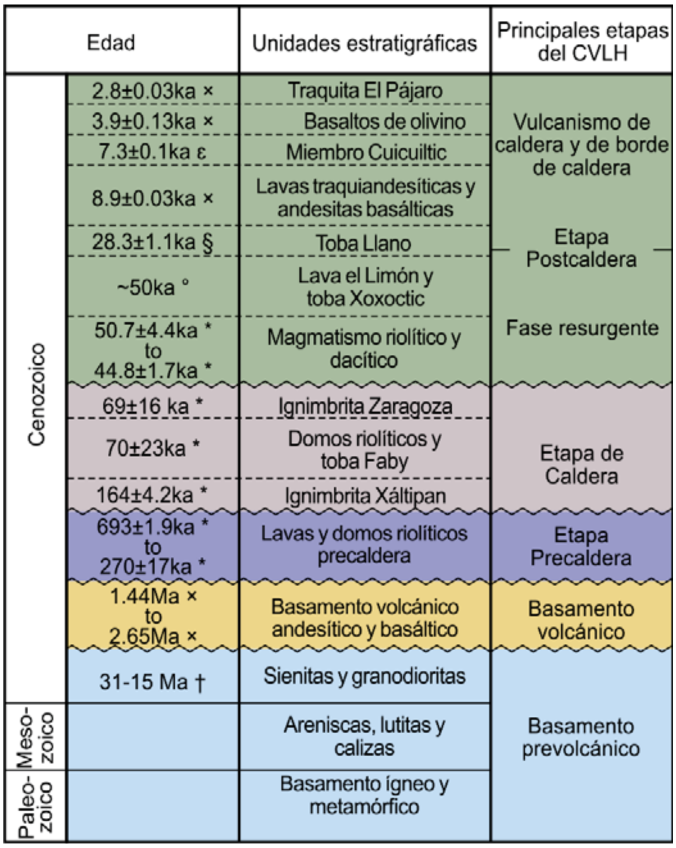

	Edad	Unidades estratigráficas	Principales etapas del CVLH
Cenozoico	2.8±0.03ka ×	Traquita El Pájaro	Vulcanismo de caldera y de borde de caldera
	3.9±0.13ka ×	Basaltos de olivino	
	7.3±0.1ka ε	Miembro Cuicuiltic	
	8.9±0.03ka ×	Lavas traquiandesíticas y andesitas basálticas	
	28.3±1.1ka §	Toba Llano	Etapa Postcaldera
	~50ka °	Lava el Limón y toba Xoxoctic	
	50.7±4.4ka * to 44.8±1.7ka *	Magmatismo riolítico y dacítico	Fase resurgente
	69±16 ka *	Ignimbrita Zaragoza	Etapa de Caldera
	70±23ka *	Domos riolíticos y toba Faby	
	164±4.2ka *	Ignimbrita Xáltipan	
	693±1.9ka * to 270±17ka *	Lavas y domos riolíticos precaldera	Etapa Precaldera
	1.44Ma × to 2.65Ma ×	Basamento volcánico andesítico y basáltico	Basamento volcánico
	31-15 Ma †	Sienitas y granodioritas	Basamento prevolcánico
Meso-zoico		Areniscas, lutitas y calizas	
Paleo-zoico		Basamento ígneo y metamórfico	

Fig. 9. Síntesis estratigráfica del CVLH mostrando las principales unidades propuestas por Norini et al. (2015). La información cronoestratigráfica está compuesta por diversos trabajos: [* - Carrasco-Núñez et al. (2018); ×- Carrasco-Núñez et al. (2017b); §- Rojas-Ortega (2016); ε - Dávila-Harris y Carrasco-Núñez (2014); °- Ferriz y Mahood (1984); † - Yáñez-García y García-Durán (1982)].

Posterior al emplazamiento de la Toba Faby, ocurre un segundo episodio eruptivo que resultó en el colapso de la caldera Los Potreros y en la generación de la ignimbrita Zaragoza y depósitos de caída asociados, que en conjunto forman la toba Zaragoza fechada entre los 0.1 – 0.06 Ma (Carrasco-Núñez y Branney, 2005; Willcox, 2011). Fechamientos recientes de la ignimbrita Zaragoza proporcionan una edad de 69±16 ka (Carrasco-Núñez et al., 2018). Esta ignimbrita tiene un volumen de ~15km^3, el cual es mucho menor comparado con el de la IX. Esta ignimbrita se caracteriza por un doble zonamiento composicional (riodacita – andesita – riodacita) (Carrasco-Núñez y Branney, 2005), y representa la última actividad explosiva formadora de una caldera. La caldera Los Potreros, con un diámetro de aproximadamente 10 km, se encuentra anidada dentro de la caldera Los Humeros y registra un colapso de cerca de 200 m (Carrasco-Núñez y Branney, 2005).

La etapa Postcaldérica está caracterizada por un vulcanismo bimodal y de borde de caldera, así como un proceso de resurgencia en el centro de la caldera Los Humeros. La fase de resurgencia está definida por actividad magmática riolítica-dacítica dentro de la caldera (44.8 ka), y por el emplazamiento de domos riolíticos en el borde norte (50.7±4.4 ka) (Carrasco-Núñez et al., 2018). Mientras que la actividad bimodal está conformada por diversos eventos explosivos formadores de depósitos de caída (toba Xoxoctic ~50 ka) y flujos piroclásticos y breccias (toba Llano (Carrasco-Núñez et al., 2018; Ferriz y Mahood, 1984;

Willcox, 2011). Durante el Holoceno, la etapa Postcaldera está definida por actividad volcánica en el sector sur de la caldera, formando múltiples flujos de lava, así como actividad explosiva bimodal (miembro Cuicuiltic) (Dávila-Harris y Carrasco-Núñez, 2014). La actividad volcánica más reciente está marcada por la formación de flujos de lava en la parte central y periférica de la caldera Los Humeros, datados en 2.8±0.003 ka (Carrasco-Núñez et al., 2017a).

3.4 Ignimbrita Xáltipan

Antes de este trabajo, la IX había sido descrita e interpretada principalmente durante los trabajos pioneros de Yáñez-Garcia y García-Durán (1982), Ferriz y Mahood (1984) y posteriormente por Willcox (2011), siendo estos últimos dos los únicos que presentan una caracterización de la estratigrafía de la IX. A pesar de que en estos trabajos la IX fue descrita en localidades diferentes y bajo modelos estratigráficos diferentes (Fig. 10), es posible presentar una descripción general de sus depósitos. Cabe mencionar que esta descripción se muestra como antecedente de los datos encontrados en esta tesis.

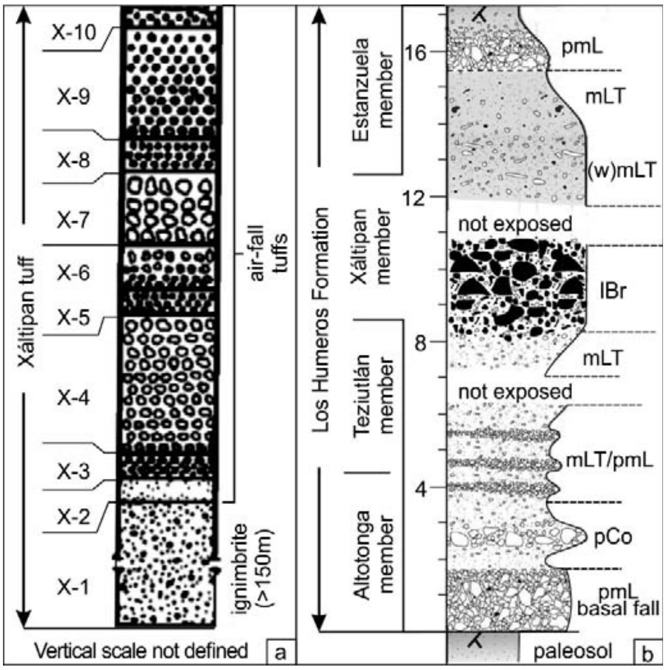

Fig. 10. Estratigrafía previamente propuesta para la ignimbrita Xáltipan. a) Columna estratigráfica modificada de la toba Xáltipan propuesta por Ferriz y Mahood (1984), mostrando en la base el cuerpo de la ignimbrita y por encima las nueve unidades de caída. b) Columna estratigráfica modificada del miembro Xáltipan propuesto por Willcox (2011), usando las abreviaciones de facies presentadas en Branney y Kokelaar (2002).

La primera estimación del tamaño de la IX por Ferriz y Mahood (1984) indica que esta tiene una cobertura de ~3,500 km^2 y un volumen de 115km^3 de RDE, mismos datos que han sido ampliamente aceptados y considerados en otros trabajos asociados al CVLH, y que han sido los únicos hasta este trabajo. La distribución propuesta por Ferriz y Mahood (1984) indica que los flujos de esta unidad descendieron hasta 1,900 m por cerca de 50 km a través de cañones con dirección hacia el Noreste, hasta depositarse en zonas que corresponden a la provincia de la Planicie Costera del Golfo (Fig. 11a). Hacia el Oeste, sus depósitos se encauzaron a través de los principales sistemas hidrológicos activos como el río Apulco. Hacia el Sur, los flujos se han identificado como depósitos de relleno topográfico sobre un terreno más plano, creando nueva topografía (López-Hernández, 1995). Hacia el Este, los flujos de la IX remontaron el flanco occidental del volcán Cofre de Perote, escalando hasta 600 m sobre las planicies del CVLH emplazándose hasta la ciudad de Xalapa (Ferriz y Mahood, 1984; López-Hernández, 1995). Hacia el Suroeste su dispersión fue obstruida por la Sierra de Tlaxco, aunque se han documentado algunos afloramientos en localidades que actualmente están a aproximadamente 100 m de altura (Ferriz y Mahood, 1984). La localidad tipo de esta ignimbrita originalmente se ubicó en el poblado Xáltipan, el cual está cimentado sobre los afloramientos de esta unidad (Yáñez-García y García-Durán, 1982), aunque más recientemente se ha propuesto su reubicación en Tenextepec (Willcox, 2011). Esta primera propuesta de la distribución de la IX por Ferriz y Mahood (1984) representa un trabajo de exploración amplio con la identificación de muchas localidades en donde aflora la ignimbrita, sin embargo es posible observar que los depósitos inferidos están pobremente desacoplados con la topografía (Fig. 11b). Este desacoplamiento es más evidente en las zonas de los valles, en donde el trazo de la ignimbrita corta de forma oblicua a perpendicular a los valles.

La estratigrafía propuesta por (Ferriz y Mahood, 1984), incluye un conjunto de 10 sub-unidades que en conjunto forman la toba Xáltipan. La base de esta toba Xáltipan está conformada por el cuerpo principal de la ignimbrita, sobre el cual descansa un estrato delgado de ceniza interpretado como coignimbrítica. Sobre estos ocurren otros ocho depósitos de caída en contacto concordante (Fig. 10a). Estos autores sugieren que esta secuencia de depósitos de caída muestra una transición gradual a composiciones más básicas hacia la cima, desde riodacitas a andesitas, lo que se ha interpretado como resultado de una cámara magmática zonificada previamente a la erupción formadora de la caldera hace *ca.* 460 ka. Una observación importante de esta reconstrucción estratigráfica es que las ocho subunidades que sobreyacen al cuerpo de la ignimbrita se reconocieron y muestrearon en un solo afloramiento por estos autores.

Por otro lado, Willcox (2011) agrupa a la IX con dos depósitos de caída asociados por debajo y por encima, y nombra a esta secuencia como Miembro Xáltipan (Fig. 10b). Este miembro comprende, en la base, un depósito de caída de pómez riolítica, en medio, el cuerpo de la IX y en la cima, un depósito de caída de pómez dacítica. Esta reconstrucción estratigráfica integra las observaciones en diferentes localidades. Por ejemplo, el depósito de caída inferior es descrito en solo una localidad ~6 km al este de la caldera en forma de un estrato masivo de 1.35 m. Esta capa es interpretada por Willcox (2011) como la primera etapa de caída de una columna eruptiva Pliniana sostenida. Esta interpretación también se aplica para el depósito de caída superior. La descripción general de la IX la hace en la localidad tipo en Tenextepec, con un espesor aproximado de 7.5 m, en donde aflora de manera masiva. Adicionalmente, Willcox (2011) presenta una descripción más detallada de la base a partir de unos afloramientos en la zona de Teziutlán y cerca de Vista Hermosa, mientras que la parte superior es descrita a partir de un afloramiento ~7 km al este de la caldera.

La IX es un depósito piroclástico que varía de riolítico a traquítico (67 a 76.2% SiO_2), soportado por matriz, pobremente seleccionado, color gris en depósito fresco y que tiene un color de alteración naranja a rosa, presentándose en facies de toba lapilli masiva a toba masiva (Ferriz y Mahood, 1984; Willcox, 2011). La matriz de ceniza está compuesta principalmente por vidrio con un bajo contenido de cristales, líticos y obsidiana como un componente característico. Se han identificado diferentes clastos de pómez lapilli con diferentes texturas y formas, que van de

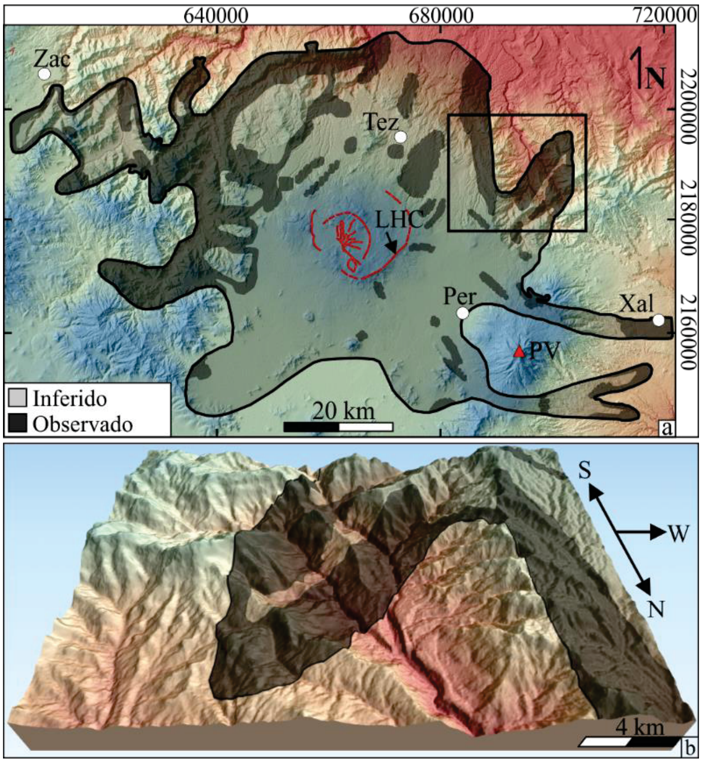

Fig. 11. a) Mapa de distribución de la ignimbrita Xáltipan (IX) propuesto por Ferriz y Mahood (1984). El recuadro muestra la ubicación del valle Las Minas. b) Proyección 3D de los depósitos de la IX sobre el valle de Las Minas propuesto por Ferriz y Mahood (1984). Nótese la disparidad entre la traza de la IX y la topografía. Exageración vertical de 1.5.

redondeadas a angulares en forma tabular, y con vesiculación esponjosa a fibrosa, siendo estas pómez principalmente afíricas y en algunos casos ricas en biotita (Willcox, 2011). El contenido cristalino está compuesto principalmente por plagioclasa, feldespato potásico, biotita y piroxeno. Los líticos accidentales son principalmente clastos volcánicos de andesita del basamento volcánico, aunque también es común encontrar fragmentos del basamento sedimentario. Finalmente, la IX está caracterizada por presentar zonas de alteración hidrotermal que le otorga su color naranja-rosáceo característico. Además, en las zonas donde la ignimbrita no está consolidada es común encontrar vetas induradas subhorizontales así como intemperismo en forma de panal.

4. Metodología

Los resultados de esta tesis se obtuvieron aplicando una metodología que comprende cuatro etapas: 1) organización de datos, 2) trabajo de campo, 3) laboratorio analítico, y 4) reducción e interpretación de datos.

4.1 Organización de datos

La primera etapa de este proyecto consistió en la compilación de los datos bibliográficos referentes a la descripción de ignimbritas asociadas a sistemas caldéricos y geotérmicos, así como una revisión de las metodologías convencionales y modernas utilizadas para su estudio. Simultáneamente, se examinaron todos los trabajos previos en donde se presentan caracterizaciones de la IX en sus depósitos de flujos piroclásticos, así como de relleno de caldera. En el caso de los depósitos de flujos, los trabajos más representativos son los publicados por Ferriz y Mahood (1984) y por Willcox (2011), los cuales presentan descripciones cronoestratigráficas, petrológicas, y geoquímicas, así como interpretaciones de su historia eruptiva. De estos trabajos, se extrajo la ubicación de los afloramientos que serían posteriormente visitados durante la etapa de trabajo de campo. En el caso de los depósitos intracaldera, se inspeccionaron todos los reportes de pozos del campo geotérmico de Los Humeros, enfatizando aquellos en donde se describen ignimbritas del grupo caldérico. En estos casos, se examinaron las muestras disponibles, así como sus correspondientes láminas delgadas, descripciones petrográficas y análisis geoquímicos de elementos mayores y trazas.

Toda la información cartográfica preexistente de la IX fue integrada a una base de datos digital, creada con el programa de acceso libre Quantum GIS (QGIS). Para esta base de datos se estableció un espacio de trabajo de 120 x 100 km. Se utilizó un modelo digital de elevación (MDE) SRTM de 30 m de resolución por pixel como base. Se estableció un Sistema de Coordenadas de Referencia (SCR) y proyección WGS 84 – UTM para esta base de datos, mismo que se utilizó en el GPS utilizado para capturar la ubicación de los datos en campo.

Esta base de datos digital sirvió inicialmente como el medio para organizar las campañas de exploración del trabajo de campo, y posteriormente fue el medio para la cartografía digital de la IX.

4.2 Trabajo de campo

El trabajo de campo consistió en ocho campañas de exploración sobre y alrededor de la caldera de Los Humeros, durante las cuales se levantaron registros estratigráficos, registrando el espesor del depósito y la descripción de sus facies, y en ciertas localidades, se colectaron muestras de la ignimbrita para los análisis de laboratorio. Durante las primeras dos campañas, se visitaron las localidades reportadas por Ferriz y Mahood (1984) y por Willcox (2011), con la finalidad de examinar la estratigrafía propuesta por estos autores. Las campañas subsiguientes tuvieron como objetivo principal explorar nuevas áreas sin reportes precedentes de la IX. En total se identificaron más de 216 localidades en donde aflora la IX. En cada localidad se levantó una columna estratigráfica local, y en ciertos casos, se colectaron muestras para diversos análisis de laboratorio. De manera general, se utilizaron dos técnicas de muestreo en función del grado de consolidación de la ignimbrita. En las condiciones no consolidadas, se seleccionó un área del afloramiento de aproximadamente 50 x 50 cm, de la cual se extrajo el material suelto utilizando un azadón o pala (Fig. 12a). Durante este proceso se procuró que el área fuera lo más representativa posible del afloramiento en general. En el caso de la ignimbrita consolidada, se colectaron fragmentos de mano, en la mayoría de los casos, con su orientación de campo. Los datos de campo, que incluyen descripciones estratigráficas y de facies, así como el registro del muestreo, se digitalizaron en hojas de trabajo Excel, para posteriormente ser trasladados a la base de datos digital en QGIS.

4.3 Laboratorio

Preparación de muestras

La preparación de las muestras para los análisis de laboratorio se realizó en función de su grado de compactación y tamaño. En el caso de las muestras consolidadas de los flujos de la ignimbrita se extrajeron fragmentos para la elaboración de láminas delgadas y para análisis petrofísicos (Fig. 12b). Para las láminas delgadas, se extrajeron dos bloques orientados, uno a la horizontal y el otro a la vertical, respecto a la posición en campo. Por otro lado, para los análisis petrofísicos se extrajeron núcleos de 2.54 cm de diámetro y un largo variable de 2.54 a 5.08 cm. Cabe mencionar que la extracción de estos núcleos se realizó en el Laboratorio de Petrofísica y Geología Aplicada del Instituto Potosino de Investigación Científica y Tecnológica (IPICyT). Para las muestras no consolidadas se llevó a cabo un cuarteo, dejando un mínimo de 200 gr como testigo. Del resto de la muestra, una fracción se asignó para la elaboración de láminas delgadas, otra para conteos de componentes y otra para la selección de pómez para los análisis geoquímicos. En el caso de las muestras intracaldera, se utilizaron las láminas delgadas previamente elaboradas por colegas que han realizado trabajos de descripción petrográfica de los pozos del campo geotérmico, así como las descripciones de reportes petrográficos provistos por la Comisión Federal de Electricidad (Carrasco-Núñez et al., 2017b, y referencias en el mismo). Por otro lado, para los análisis petrofísicos, se seleccionaron los fragmentos más grandes y frescos de cada nivel muestreado.

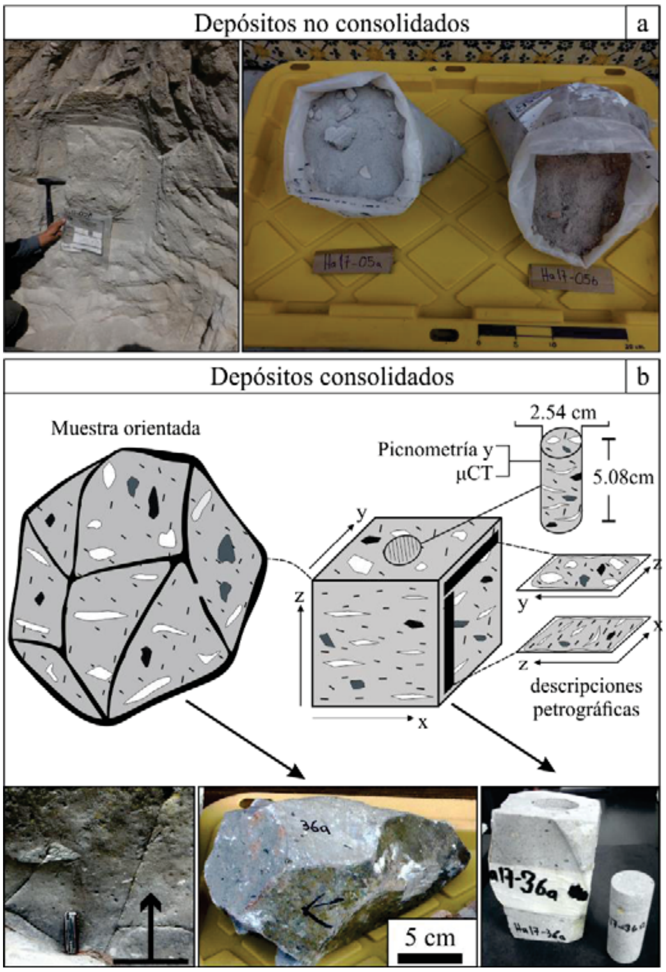

Fig. 12. Tipo de muestreo y preparación de las muestras para los diferentes análisis de laboratorio. a) Muestras no consolidadas obtenidas en un área de aproximadamente de 50 x 50 cm. b) Secuencia de preparación para las muestras consolidadas y orientadas.

Petrografía

Las láminas delgadas se analizaron por medio de un microscopio petrográfico. Las muestras no consolidadas fueron previamente impregnadas con resina, con la finalidad de endurecer el material y llevar a cabo la técnica convencional de laminación, la cual se realizó también para las muestras consolidadas. En todos los casos, las observaciones petrográficas se enfocaron en describir la fábrica, textura y la mineralogía primaria y secundaria de la ignimbrita. En el caso de que las muestras presentaran un grado de soldamiento de bajo a alto, se hicieron descripciones de sus láminas delgadas en ambas orientaciones respecto a su orientación en campo. Esta visualización en dos planos permitió medir los principales rasgos de la textura eutaxítica, mismos que serían la base para evaluar el grado de soldamiento de la muestra. Los principales rasgos medidos fueron el grado de compactación de la matriz de ceniza, foliación, deformación de las esquirlas de vidrio y grado de compactación de los clastos de pómez (referido en la bibliografía como *oblateness*). En los casos en donde fue necesario hacer cuantificación de componentes o hacer mediciones con mayor precisión, se utilizó el programa ImagePro.

Microtomografía computarizada de rayos-X (µCT)

Con el objetivo de realizar una caracterización tridimensional de alta resolución de las muestras consolidadas de los flujos e intracaldera, se seleccionaron conjuntos de muestras representativas para ser analizadas por microtomografía computarizada de rayos-X (µCT). Estos análisis se realizaron en el Laboratorio Universitario de Microtomografía de rayos-X (LUMIR) de Centro de Geociencias (CGEO), usando un tomógrafo Xradia Versa-510. En el caso de las muestras de los flujos, los núcleos se montaron en un portamuestras de acuerdo a su orientación original en campo. En estos casos, las tomografías se tomaron cubriendo un espacio de 1000 x 1000 x 700 mm a una resolución constante de 14.55 nm/voxel. Por otro lado, los fragmentos de pozos fueron montados con una orientación aleatoria. Debido a que estos fragmentos tenían un tamaño y forma variable, para cada uno de ellos el espacio analizado y resolución fue variable. Sin embargo, en todos los casos se procuró abarcar el mayor espacio posible. Las tomografías fueron reconstruidas en forma de imágenes 3D usando el programa *Scout-And-Scan Control System and Reconstruction*, para luego ser procesadas usando el programa AVIZO 2019.4.

Durante la etapa de procesamiento se aplicó una serie de filtros con el objetivo de disminuir el ruido y los artefactos (*artifacts*) que no son propios de la muestra. Posteriormente, se realizó un proceso de segmentación de los componentes de la muestra en donde se separan tres fases: 1) las fracciones sólidas, 2) la fase porosa, y 3) una fase intermedia que incluye los poros que están debajo de la resolución del análisis (microporosidad) (Fig. 13). Para la segmentación se utilizó la metodología propuesta por Cid et al. (2017). Adicionalmente, en el caso de las muestras que se analizaron para medir los efectos del soldamiento en la ignimbrita, se implementó una metodología que discrimina la porosidad vesicular de la porosidad total. Esta metodología consiste en filtrar los poros usando ciertos parámetros geométricos, tales como tamaño, esfericidad, y superficie específica. Los detalles de esta metodología se encuentran en la sección 5.3.

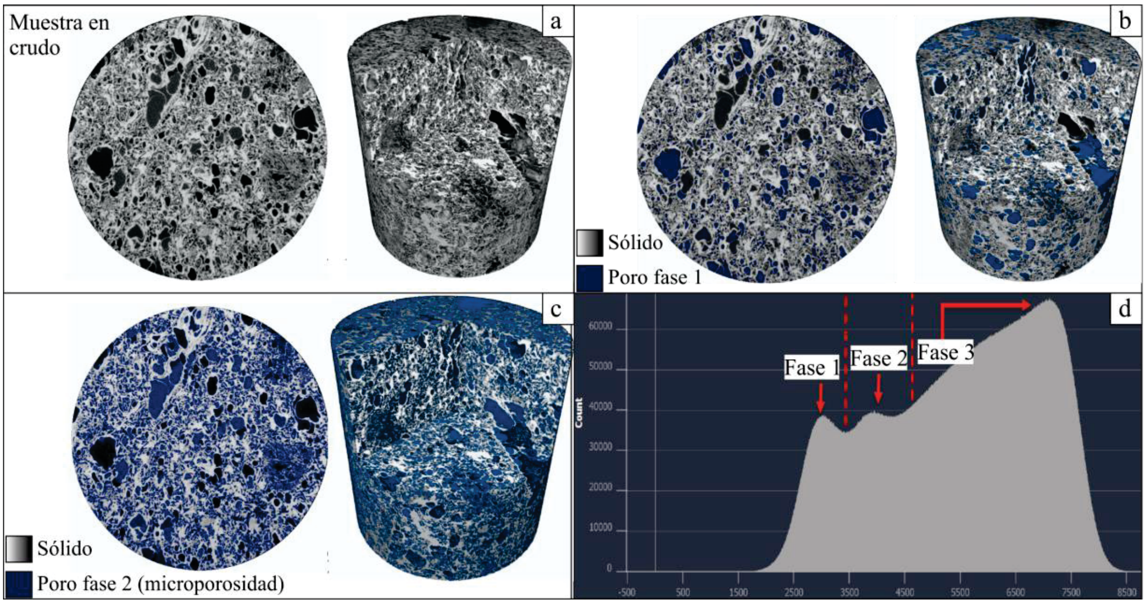

Fig. 13. Imágenes de microtomografía de rayos-X de una muestra de la ignimbrita Xáltipan. a) Muestra en escala de grises, el extremo de gris con tonos obscuros representan el material menos denso, mientras que los más claros el material más denso. b) Misma muestra mostrando en color azul el material menos denso (fase 1), interpretado como el medio poroso, mientras que el material en escala de grises corresponde a la fracción sólida. c) En azul, la fase 2, que corresponde al medio poroso que está por debajo de la resolución del análisis, y que es interpretado como un medio con microporosidad. d) Histograma que muestra el valor en escala de grises (X), contra el conteo de los pixeles (Y). Nótese que la curva de distribución presenta tres modas, cada una correspondiente a una fase.

Picnometría con gas

Los análisis de picnometría por gas se realizaron en muestras representativas de los flujos de la ignimbrita soldada. Para esto, las muestras de mano fueron enviadas al Laboratorio de Petrofísica y Geología Aplicada del Instituto Potosino de Investigación Científica y Tecnológica (IPICyT). Aquí, se extrajeron los núcleos para el experimento, los cuales fueron primero secados en horno, para luego ser pulidos en su superficie. Posteriormente, se aplicó el procedimiento de rutina, que incluye una primera medición de la porosidad y permeabilidad con un picnómetro de Helio Coretest PHI-220, a una presión de confinamiento constante de 240 PSI. Posteriormente, se midieron los parámetros de porosidad y permeabilidad con gas utilizando un Porosímetro-Perméometro Coretest AP608. Los resultados de este experimento incluyen la medición del peso y volumen de los núcleos, por lo que es posible conocer la densidad de las muestras. No obstante, hay que considerar que esta última medición tiene un factor de error, debido al contenido de líticos accidentales que, por lo general, son más densos que el material magmático, es decir, el vidrio y cristales primarios.

Inmersión en agua

Para el cálculo de la densidad de las muestras no consolidadas y los fragmentos intracaldera, se utilizó el método de inmersión en agua sustentado en el principio de Arquímedes. Para las muestras no consolidadas, primero se pesaron porciones de muestra total (vidrio, cristales y líticos accidentales) de aproximadamente 50 gr, utilizando una báscula de alta precisión. Posteriormente, se extrajeron todos los líticos accidentales utilizando el microscopio binocular. Estos líticos también fueron pesados en la báscula. Luego, la muestra libre de líticos fue sumergida en una probeta con agua, de la cual se midió el nivel de agua antes y después de la inmersión de la muestra. El cambio en el nivel de agua se traduce directamente como el volumen de la muestra sumergida. Posteriormente, se incorporaron los líticos a la probeta con la muestra y se midió el cambio en el volumen de la muestra. Como resultado, se obtuvo el volumen de las muestras con y sin líticos accidentales, y conociendo el peso de cada uno de estos componentes, fue posible determinar la densidad de ambos. En el caso de las muestras intracaldera, se pesaron y sumergieron un conjunto de fragmentos de cada nivel muestreado, representativos de la roca total. La estimación de los líticos en el caso de las muestras no consolidadas sirvieron como referente para la corrección en las muestras intracaldera.

Geoquímica

Se realizaron análisis químicos de elementos mayores y trazas en pómez de los flujos de la ignimbrita. Para esto, las muestras fueron preparadas en el Laboratorio de Vulcanología del CGEO, iniciando con la separación de los clastos de pómez más limpios de cada muestra. Las pómez fueron lavadas con agua desionizada y en el limpiador ultrasónico, y posteriormente bajo el microscopio binocular para detectar y remover posibles zonas con alteraciones y contenido de líticos. Las pómez fueron pulverizadas con un sistema de discos de alúmina hasta que alcanzaron una fracción granulométrica menor a 4 phi (<0.088 mm). El polvo resultante fue enviado a los laboratorios de geoquímica para análisis de elementos mayores y trazas. Los elementos mayores se midieron por fluorescencia de rayos X en el Laboratorio Universitario de Geoquímica Isotópica del Instituto de Geología (LUGIS – UNAM), mientras que los elementos traza se midieron por espectrometría de masas con fuente de plasma (ICP-MS) en el Laboratorio de Estudios Isotópicos (LEI) del CGEO (UNAM). Los detalles metodológicos para el análisis de los elementos mayores y trazas pueden encontrarse en Lozano y Bernal (2005) y en Mori (2007), respectivamente.

4.4 Reducción e interpretación de datos

Se utilizaron diferentes medios para el manejo, reducción y presentación de los datos obtenidos en cada etapa metodológica. Para los resultados analíticos, como los de picnometría con gas, μCT y geoquímica, se utilizaron hojas de trabajo de Excel. Con este programa, se hicieron las gráficas y tablas que posteriormente fueron parte de los resultados presentados en los artículos científicos. Por otro lado, para la elaboración de figuras cartográficas, tales como el mapa de la ignimbrita y las secciones geológicas, se usó el programa QGIS. Estas figuras fueron posteriormente editadas y preparadas con el programa CorelDraw X7 para su publicación.

4.5 Cálculo del volumen erosionado

Una aportación importante de esta tesis, es la implementación de una metodología para calcular el volumen erosionado de depósitos ignimbríticos que se han emplazado en cuencas bien definidas, en este caso, aplicado a los casos en donde la IX se emplazó en zonas de valles. Esta metodología se desarrolló utilizando herramientas instaladas por defecto en el programa QGIS, y que se encuentran disponibles en cualquier otro Sistema de Información Geográfica (SIG). De manera general, esta metodología consiste en proyectar los polígonos que representan el área en superficie de un depósito, sobre un MDE. Posteriormente, para cada polígono, se genera un plano interpolado a partir de su contorno. Este plano interpolado representa la superficie previa a la erosión, la cual se asume es relativamente horizontal y suavizada. Finalmente, se hace una resta aritmética de la altitud del plano interpolado menos la topografía actual, lo que resulta en el valor vertical que ha sido erosionado. Esta metodología se explica a detalle en el artículo correspondiente a la sección 5.1. En este trabajo, esta metodología sirvió para el mapeo efectivo de la IX, no obstante, tiene el potencial de ser aplicada en otras ignimbritas del mundo, así como en otro tipo de depósitos controlados por gravedad.

4.6 Cálculo de la magnitud eruptiva

La metodología para el cálculo del tamaño de la ignimbrita en términos de área, volumen y magnitud, forma parte fundamental de esta tesis. En el caso del área, esta fue calculada utilizando una función por defecto del programa QGIS, que permite conocer el área de polígonos que estén referenciados a un sistema de coordenadas. Para el volumen, se dividió el área de la ignimbrita en sectores. Para cada sector se calculó un espesor promedio de la ignimbrita, esto considerando el espesor medido en campo más el espesor erosionado. Para cada sector se calculó el volumen de la ignimbrita multiplicando su área por el espesor. Es importante mencionar que el volumen calculado incluye una corrección por el contenido de líticos, mismos que fueron estimados aplicando la metodología de inmersión de agua. Finalmente, la magnitud eruptiva se calculó a partir de los valores de densidad de la ignimbrita. En este trabajo se utilizaron dos valores de densidad en función del grado de soldamiento, medidos a partir de las mediciones de densidad por picnometría de gas y por inmersión de agua. En las condiciones de soldamiento nulo a moderado se calculó una densidad de 1,700 kg/m^3, mientras que en las condiciones de soldamiento alto 2,200 kg/cm^3. Para corregir el factor de equivalencia de densidad con respecto a rocas no fragmentadas, se utilizó una densidad de magmas riolíticos de 2,350 kg/m^3, mismo que es utilizado ampliamente para este tipo de cálculos (Folkes et al., 2011; Mason et al., 2004).

4.7 Estructura de los resultados

Los resultados de este trabajo se presentan en el Capítulo 3, expresados en tres apartados. Cada uno de ellos corresponde a un artículo científico publicado en revistas internacionales especializadas en el área de las Geociencias.

En el primer apartado (5.1), se presenta el trabajo cartográfico de la IX. En él se aborda la resolución de los principales problemas para el mapeo de la IX, que son su heterogeneidad en las facies de soldamiento y los procesos de enterramiento y erosión. Para esto, se presenta una metodología innovadora que integra mediciones tomadas durante el trabajo de campo, proyecciones geométricas convencionales, la construcción de secciones geológicas y un conjunto de herramientas de Sistemas de Información Geográfica. El resultado principal es un mapa digital de la IX presentado en un formato interactivo en donde se pueden consultar sus rasgos principales. Este mapa es la base para la caracterización de la anatomía de la ignimbrita, que incluye su estratigrafía y tamaño.

En el segundo apartado (5.2) se describe la anatomía de la IX, la cual es el sustento para proponer su historia eruptiva. Para esto, se realizó una reconstrucción de la estratigrafía de la ignimbrita en diferentes zonas alrededor de la caldera Los Humeros y ambientes de emplazamiento contrastantes. Como resultado, se construyeron dos columnas compuestas que tipifican la estratigrafía de la ignimbrita en las diferentes condiciones de emplazamiento. En estas columnas se identificaron las unidades que componen a la ignimbrita y que sustentan que esta deriva de una erupción continua con múltiples fases explosivas, en donde se generaron CPD y depósitos de caída asociados. El reconocimiento de estas unidades y su distribución espacial, son la base para el análisis de facies posterior. Adicionalmente, en este artículo se presenta un cálculo del volumen de la ignimbrita a partir de una metodología integral. El volumen aquí calculado permite confirmar que la IX representa la erupción explosiva de mayor magnitud reportada para la FVTM.

El tercer apartado (5.3) está enfocado en la caracterización de las facies de la IX, así como en su distribución y variaciones espaciales. Para lograrlo, se hizo una combinación de técnicas analíticas petrofísicas y geoquímicas que permitieron identificar una asociación de facies, que es sistemática y correlacionable entre los depósitos de flujos y de relleno de caldera. A partir de estas facies, es posible invocar a cambios en la fuente magmática durante la erupción de la IX, que pueden asociarse a una cámara magmática composicionalmente heterogénea. Además, desde el punto de vista petrofísico, es posible identificar zonas impermeables en la ignimbrita, las cuales tienen fuertes implicaciones para los propósitos de explotación del campo geotérmico. Los resultados obtenidos muestran una gran variabilidad en el grado de soldamiento y de mineralización secundaria a diferentes niveles estratigráficos registrados en los pozos del campo geotérmico, lo cual permite explicar la variación de la permeabilidad de la IX en el sistema geotérmico. Este resultado tiene el potencial de ser considerado en las las acciones de exploración del campo geotérmico, con el objetivo de optimizar su explotación.

5. Resultados

5.1 Mapeo efectivo de grandes ignimbritas utilizando una metodología basada en SIG; caso de la ignimbrita Xáltipan en la caldera Los Humeros, México.

Artículo: *Effective mapping of large ignimbrites by using a GIS-based methodology; case of the Xáltipan ignimbrite from Los Humeros caldera, México/Mapeo efectivo de grandes ignimbritas utilizando una metodología basada en SIG; caso de la ignimbrita Xáltipan en la caldera Los Humeros, México*.

Autores: Cavazos-Álvarez, J. A., y Carrasco-Núñez, G., (2019).

Revista: Terra Digitalis, vol. 3(2), p. 1-8.

DOI: 10.22201/igg.25940694.2019.2.65.

Received: 2 Aug. 2019, **Accepted:** 15 Oct. 2019
Published online: 31 Oct. 2019
DOI: 10.22201/igg.25940694.2019.2.65.142 **Volume:** 3, **Issue:** 2, **Pages:** 1-8

terra digitalis
international e-journal of maps

Effective mapping of large ignimbrites by using a GIS-based methodology; case of the Xáltipan ignimbrite from Los Humeros caldera, Mexico. ☆

Mapeo efectivo de grandes ignimbritas utilizando una metodología basada en SIG; caso de la ignimbrita Xáltipan en la caldera de Los Humeros, Mexico

Jaime Alberto Cavazos Álvarez*[a], Gerardo Carrasco-Núñez[a]

[a]*Centro de Geociencias, Universidad Nacional Autónoma de México, Blvd. Juriquilla 3001, Campus UNAM-Juriquilla, Querétaro, 76230, México.*

Abstract

The Xáltipan ignimbrite records the largest single-eruption of the Trans-Mexican Volcanic Belt up to date (≥344 km^3 uncompacted volume). As most large ignimbrites, this ignimbrite presents common challenges when mapping. These are abrupt welding variations, burial by younger units near other volcanic sources, and highly eroded deposits in active-water valleys. In this work, we deal with these issues by integrating classical cartographic techniques such as field measurements, geometric projections of energy lines and construction of geologic cross-sections, with a GIS-based methodology that quantifies the eroded bulk. As a result, we obtained a map with the main ignimbrite features that is presented in an interactive format. Furthermore, we describe the resources used for the map construction and how the results may contribute to the interpretation of the eruptive processes. These contributions include: 1) the energy lines point to a low-height pyroclastic density currents source, typical of caldera-forming, boiling-over eruptions; 2) the landscape formed by the ignimbrite, coupled with the geologic sections, indicate that in the proximal facies the ignimbrite filled a volcanic field, leaving a radially shaped and even distribution, while in the distal facies it channelized into a steep mountainous ground; and 3) the geologic sections in the valley areas, where the active rivers highly eroded the original deposits, revealed the preferential development of welded zones along channel centers.

Keywords: Los Humeros Volcanic Complex; PDC emplacement; energy line, ignimbrite mapping, geographic information systems, ignimbrite geometry

Resumen

La ignimbrita Xáltipan registra la erupción más grande del Cinturón Volcánico Trans-Mexicano reportado hasta la fecha (≥ 344 km^3 volumen no compactado). Esta ignimbrita, como la mayoría de las ignimbritas de gran volumen, presenta problemas comunes al momento de mapearla. Estos obstáculos incluyen variaciones abruptas en el grado de soldamiento, sepultamiento por otras unidades volcánicas más recientes cerca de otras fuentes volcánicas, y depósitos altamente erosionados en zonas de valles activos. En este trabajo, estos problemas son atendidos mediante la integración de técnicas cartográficas clásicas que incluyen mediciones de campo, proyecciones geométricas de líneas de energía y construcción de secciones geológicas con una metodología basada en Sistemas de Información Geográfica para la cuantificación de la masa erosionada. Como resultado, obtuvimos un mapa, que se presenta en un formato interactivo que contiene las principales características de esta ignimbrita. Además, describimos los recursos utilizados para la construcción del mapa y cómo los resultados contribuyeron a la interpretación de la historia eruptiva. Estas contribuciones incluyen: 1) las líneas de energía apuntan a una fuente somera de corrientes piroclasticas densas, lo cual es típico en erupciones tipo boiling-over asociadas a la formación de calderas; 2) el terreno formado por la ignimbrita, junto con la información de las secciones geológicas, indican que en las facies proximales la ignimbrita rellenó por completo un campo volcánico, depositándose con una distribución en forma radial y con una superficie plana, mientras que en las facies distales se canalizó en un terreno montañoso; y 3) las secciones geológicas en las áreas del valle, donde los ríos activos han erosionado profundamente los depósitos originales, revelan el desarrollo preferencial de zonas soldadas a lo largo de los centros de los canales.

Palabras clave: Complejo Volcánico de Los Humeros; emplazamiento de CPD; línea de energía; mapeo de ignimbritas; sistemas de información geográfica; geometría de ignimbritas

---

1. Introduction

Caldera-forming eruptions are extremely violent events that generates massive pumice-rich, concentrated pyroclastic density currents (PDCs), called ignimbrites. Ignimbrite mapping is a key tool to interpret the eruptive history of their volcanic source and to assess the volcanic hazards. Because of this, many maps of large volume ignimbrites have been published focusing on different aspects, such as their internal architecture (Aldiss and Ghazali, 1984; Cook et al., 2016; Walker et al., 1980; Wilson et al., 1995), sedimentation processes (Cas et al., 2011; Giordano and Doronzo, 2017), and the interpretation of the eruptive evolution of large volcanic fields (Aguirre-Díaz, 1996; Brown and Branney, 2004; Self et al., 1984; Suñe-Puchol et al., 2018). Nevertheless, common challenges arise while mapping large ignimbrites. Three of the most common are: 1) they typically present lithofacies variations (texture, internal structures, componentry, and composition) that change their aspect drastically; 2) they are commonly buried by younger volcanic and epiclastic units near other volcanic sources; and 3) non-welded ignimbrites that deposited in active water-running valleys are rapidly eroded away. These three conditions occur in the Xáltipan ignimbrite (XI) at Los Humeros Volcanic Complex (LHVC), which is the largest ignimbrite in the Trans-Mexican Volcanic Belt (TMVB). This unit is characterized by being mostly buried under younger volcanic and epiclastic units from the LHVC and adjacent volcanic sources. In the areas where it is exposed, the deposits are highly eroded and present abrupt welding variations that range from rank I to V (Quane and Russell, 2005). This work describes the construction of the XI map by applying a GIS-based methodology. This methodology integrates conventional cartographic techniques such as field measurements, geometric projections of energy lines, construction of geologic sections, as well as an innovative method to estimate the eroded volumes in valley areas. Special attention is paid to how the mapping challenges were solved with this methodology and how the cartographic results contributed to interpreting the eruptive history.

2. Geologic setting

The XI is associated with the first caldera-forming event of the LHVC, located in the eastern sector of the TMVB (Figure 1). The LHVC forms the northern boundary of the Serdán-Oriental basin, where a characteristic bimodal, mostly monogenetic volcanism is present (Carrasco-Núñez et al., 2010, 1997; Negendank et al., 1985; Siebe et al., 1995). The pre-volcanic basement is made of Paleozoic plutonic and metasedimentary rocks and by a Mesozoic sedimentary succession deformed during the Laramide orogeny (Ferriz and Mahood, 1984; Gómez-Tuena et al., 2003; Viniegra, 1965). An intense volcanic activity was developed during Miocene (8.9-10.5 Ma: Yáñez-Garcia and García-Durán, 1982) and Pliocene times (1.45-2.6 Ma: Carrasco-Núñez et al., 2017b; 3.5-5 Ma: Yáñez-Garcia and García-Durán, 1982), producing a large andesitic lava flow field, which is mainly buried by the LHVC volcanism. In the last decades, the LHVC has been widely studied because it hosts the Los Humeros geothermal system, the third most productive geothermal field in Mexico (Carrasco-Núñez et al., 2018, and references therein). The evolution of the LHVC can be summarized into three main stages (Carrasco-Núñez et al., 2018); 1) pre-caldera stage, with the emplacement of multiple lava domes of rhyolitic composition, 2) caldera-stage, marked by the formation of a nested-caldera system that started with the Los Humeros caldera (LHC) collapse and the XI emplacement at 164 ± 4.2 ka, followed by a period of Plinian activity at 70 ± 23 ka that formed a thick sequence of pumice-fallout layers referred as the Faby tuff (Ferriz and Mahood, 1984), and that concluded 69 ± 16 ka ago with a second caldera-forming eruption that deposited the Zaragoza ignimbrite; and 3) post-caldera stage, characterized by resurgence and ring-fracture, and bimodal style volcanism, which now covers most of the LHVC area.

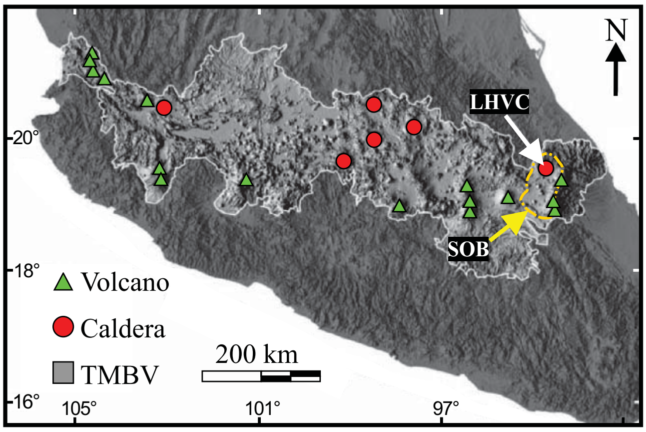

Figure 1: Location of Los Humeros Volcanic Complex (LHVC) and the Serdán Oriental Basin (SOB) in the eastern limit of the TMVB. Modified from Carrasco-Núñez et al. (2018) / Figura 1. Ubicación del Complejo Volcánico de Los Humeros (LHVC) y la Cuenca Serdán Oriental (SOB) en el límite este de la Faja Volcánica Trans-Mexicana (TMVB). Modificado de Carrasco-Núñez et al. (2018)

The first distribution map of the XI was made by Ferriz and Mahood (1984), who estimated a volume of 115 km^3 Dense Rock Equivalent (DRE) over a 3,500 km^2 area (Figure 2a). However, a detailed insight of this map reveals that in some places the inferred area contour is inconsistent with the topography. This is most evident in the mountainous terrains, where the proposed ignimbrite distribution suggests that the PDCs passed undisturbed over rough ground, instead of channelizing through the topographic depressions (Figure 2b). As part of a current

---

**E-mail address:* `jcavazos@geociencias.unam.mx` detailed stratigraphic and volumetric analysis of the XI (Cavazos and Carrasco-Núñez, in press), an updated map was constructed. The main result from this work pointed to a single, multi - phase, boiling - over type eruption with two flow-units, bounded by a basal and an intercalated pumice fallout layer. As a result of this work we have estimated a significative larger uncompacted volume of 344 km^3 (291 km^3 - DRE) over a 4,620 km^2 coverage area. These results were obtained by the remapping of the XI, which is based on extensive fieldwork and GIS analyses described in this work.

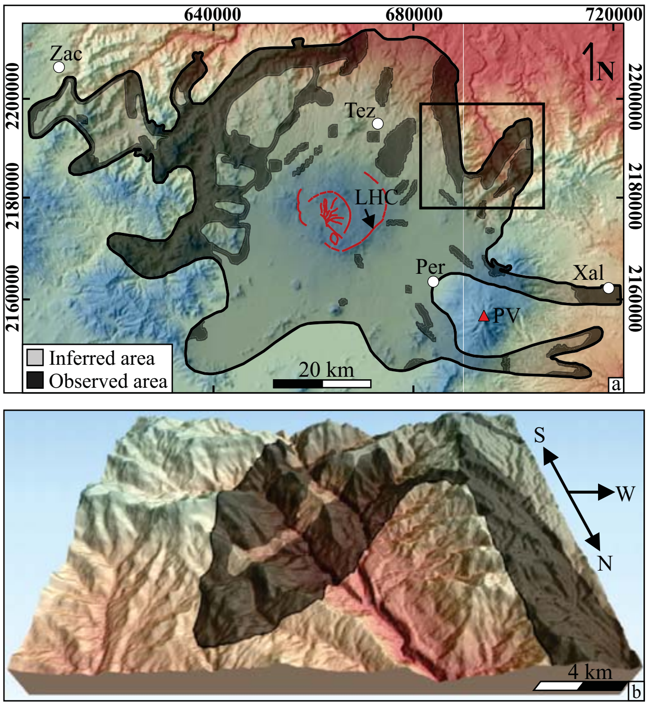

Figure 2: a) Distribution map of the Xáltipan ignimbrite (XI) as proposed by Ferriz and Mahood (1984). The inset box is showing the location of the Las Minas valley. b) 3D projection of the XI deposits over Las Minas valley as proposed by Ferriz and Mahood, (1984). Note the disparity between the XI trace and the topographic setting. Vertical exaggeration of 1.5 / Figura 2. a) Mapa de distribución de la ignimbrita Xáltipan (IX) propuesto por Ferriz y Mahood (1984). El recuadro muestra la ubicación del valle Las Minas. b) Proyección 3D de los depósitos de la IX sobre el valle de Las Minas propuesto por Ferriz y Mahood (1984). Nótese la disparidad entre la traza de la IX y la topografía. Exageración vertical de 1.5

3. Methods

The cartographic work is based on the integration of fieldwork campaigns, digital mapping, and image edition. During fieldwork, up to 216 checkpoints of the XI were located and described (Table 1, supplementary material). These checkpoints include both the exposed outcrops and water wells where the XI was identified. Simultaneous to fieldwork, digital mapping and graphic edition were carried out with QGIS and CorelDraw software, respectively. This work allowed to present the following features: a) the observed deposits, where the XI is presently exposed; b) the inferred deposits which represent the XI original distribution before burial and erosion based on 12 sections where the Energy Line concept (Hsu, 1975) was applied; c) four geologic cross-sections; and d) the areas where the eroded bulk of the ignimbrite was calculated. The methodology to construct each feature is presented in the following section.

3.1. Observed deposits

The observed deposits represent the areas where the XI is presently exposed at the surface. These areas are based on the location of the checkpoints where the presence of the ignimbrite was confirmed. At those sites, the contour of the observed deposits was traced by using the highest checkpoints as the reference of the maximum height. In the case of areas with scarce checkpoints, the contour was traced following a decreasing altitude away from the source.

3.2. Inferred deposits

The inferred deposits area was delimited by using the Energy Line concept (Hsu, 1975). This is an effective method to determine the lateral extent of a gravity-driven rock-mass such as PDCs where the topography and location of observed deposits are known. Another application of this method is that the intersection of the energy lines with the source provides an approximation of the height where the PDCs were generated (Beget and Limke, 1988). A total of 12 energy lines where constructed radially from the LHC by using the QGIS Profile tool (Table 2, supplementary material). The profiles with the location of the observed deposits were exported to CorelDraw. In each profile, the energy line was projected from the furthest observed deposit to the LHC rim, which is inferred as the source of the ignimbrite. For each energy line, the slope and the height above the source were measured. In the case where the topographic highs were intersected by the energy lines, these were interpreted as barriers not surmounted by the PDCs.

3.3. Geologic cross-sections

Seven geologic sections were constructed by using the Profile tool in QGIS (Table 2 supplementary material) and later edited in CorelDraw X7. Four of them were traced from the LHC rim to the distal areas, while three were constructed perpendicular to the valleys in the distal area to show a cross-view of the filled channels with the XI. The sections integrate surficial and subsurface lithological information of the most updated geologic map from of the LHVC (Carrasco-Núñez et al., 2017a), and show the location of the welded zones along the channel centers.

3.4. Eroded bulk

The eroded space from the observed deposits at the valley-pond sectors was calculated by using a methodology that consists of simple operations using QGIS tools and a worksheet, summarized here. A shapefile with the polygons of the observed deposits and a DEM raster file was loaded to the QGIS workspace. Because the volume of each polygon is calculated independently, the polygons were saved as individual shapefiles (Figure 3a). The individual polygon was then converted to a point shapefile, where the points are along the contour of the original polygon. The altitude value from the DEM is assigned to each point. By interpolating these points, a plane approximating the original surface of the ignimbrite before erosion was constructed (Figure 3b). Subsequently, the present altitude values from the DEM were subtracted from the newly created surface, generating a raster file with height values that represent the eroded thickness. This raster image was converted to a vector layer, in the form of a pixel grid that contain information of the area and eroded height for each pixel (Figure 3c).

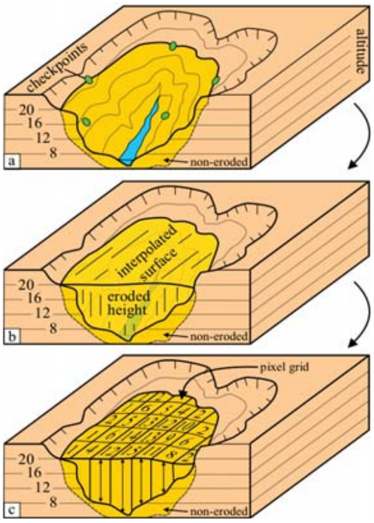

Figure 3: Sketch showing the methodology to calculate the eroded bulk in a valley area: a) plotting of the observed deposits polygon over a Digital Elevation Model (DEM) based on the checkpoints identified in the field, b) interpolation of the surface that resembles the deposit prior to eruption, and c) the construction of a pixel grid where with individual eroded thicknesses / Figura 3. Esquema que muestra la metodología para calcular el volumen erosionado en una area de valle: a) trazo de un polígono de depósitos observados sobre el modelo digital de elevación basado en los puntos de control identificados en campo, b) superficie interpolada que semeja el depósito previo a la erosión, y c) construcción de un mallado de pixeles con el espesor erosionado en cada uno

These values were exported and filtered into a worksheet where the volume for each pixel was calculated. The sum of the individual volumes represents the total eroded bulk (Table 3 supplementary material). A detailed explanation of this method is presented as part of the supplementary material.

4. Results

The XI map is plotted at a 30 m resolution, using a 120 x 100 km DEM from the Shuttle Radar Topography Mission, and projected in UTM (WGS84) coordinates (Plate1). The features included in the map are checkpoints, observed and inferred deposits areas, energy lines and geologic sections, photographs of the outcrops, and the areas where the eroded bulk was calculated. Every feature includes additional information (Table 1) that can be consulted on the interactive map available at the journal website and served to solve the mapping challenges of the XI.

The highly-welded zones were traced by using the checkpoints where these lithofacies were identified and the longitudinal and perpendicular geologic sections along the valleys. The geologic sections show that welding preferentially developed in the valleys' centers, and that is absent near the contact with the valley slopes (Figure 4).

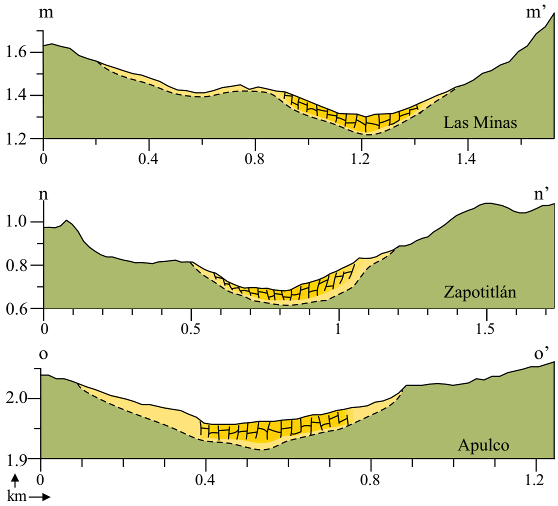

Figure 4: Perpendicular cross-sections in the valley areas showing the welding zones in the center of the valleys and non-welded zones where the ignimbrite is in contact with the basement rocks and where is not ponded. The location of the sections is indicated in Plate 1 / Figura 4. Secciones perpendiculares a los valles mostando el desarrollo de zonas de soldamiento en la parte central de los valles y las zonas no soldadas cerca del contacto de la ignimbrita con las rocas del basamento y en donde no se depositó en forma de relleno de valle. La ubicación de las secciones está indicada en la Lámina 1.

In the proximal area, the thickness of the partially buried deposits was obtained by direct observation and water wells information. Here, these deposits were plotted in the geologic sections with a tabular shape. The eroded volume was adequately calculated in the valley areas by integrating the information of the observed deposits with the present topography showed in the DEM. This calculation provides, with high accuracy, the eroded ignimbrite volume in this type of environment. Nevertheless, the resulting volume by using this method should be considered as a minimum value because it is based on the observed deposits of a highly eroded ignimbrite, instead of the inferred deposits.

Xáltipan ignimbrite map at Los Humeros Volcanic Complex, México.

Jaime Alberto Cavazos Álvarez[a], Gerardo Carrasco-Núñez[a]

[a]Centro de Geociencias, Universidad Nacional Autónoma de México, Juriquilla, Qro.

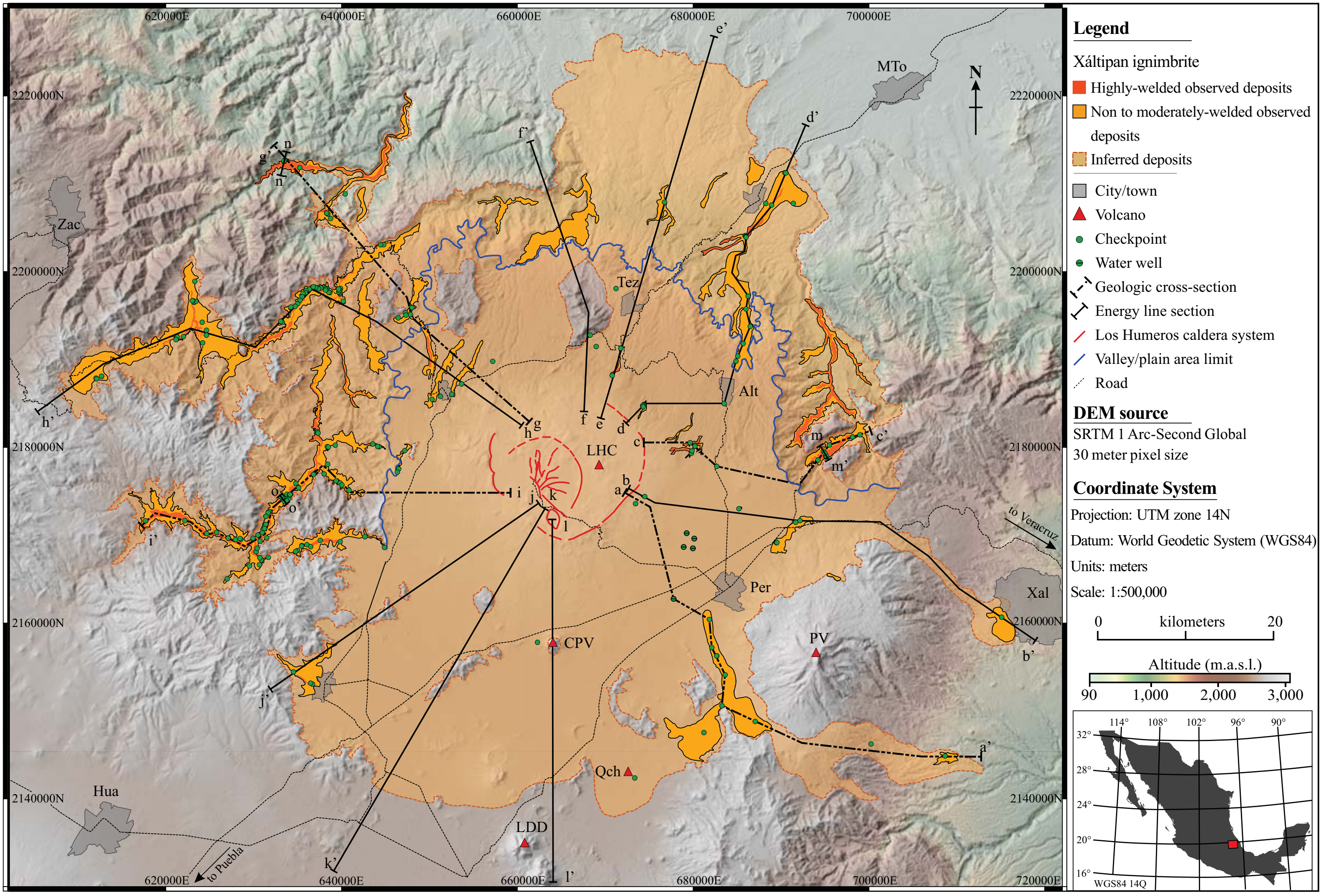

Plate 1. Map showing the inferred and observed (non-to-moderately and highly-welded facies) deposits of the Xáltipan ignimbrite. The map is plotted over a color graded and shaded 30 m resolution DEM. The location of the checkpoints (green circles) and profiles used for the energy lines (solid and dashed lines) and geologic sections (dashed lines) are indicated. Location of the main volcanoes are shown in red triangles (LDD – Las Derrumbadas; Qch – Quechulac tuff ring; CPV – Cerro Pizarro volcano; PV – Perote volcano; LHV – Los Humeros caldera). Main towns and cities in gray areas (Per – Perote; Tez – Teziutlán; Xal – Xalapa; Zac – Zacatlán; MTo – Martínez de la Torre). Main roads indicated as fine dashed lines. / Lámina 1. Mapa que muestra los depósitos inferidos y observados (facies no a moderadamente y altamente soldadas) de la ignimbrita Xáltipan. El mapa está trazado sobre un modelo digital de elevación de 30 m de resolución. La ubicación de los puntos de control (círculos verdes) y perfiles usados para las líneas de energía (lineas sólidas y punteadas) y secciones geológicas (líneas punteadas) están señalados. La ubicación de los principales volcanes están mostrados en triángulos rojos. Principales ciudades y pueblos en áreas grises. Principales carreteras indicadas en lineas punteadas delgadas.

Table 1. Features in the Xáltipan ignimbrite map / Tabla 1. Rasgos del mapa de la ignimbrita Xáltipan

Features	**Description**	**Included data**
Checkpoints	Locations where the XI was located and described. Includes the location of five water wells where the ignimbrite was logged	- Checkpoint number - Coordinates - Welding facies
Observed deposits	Areas where the XI is exposed. It is subdivided into non- to moderately and highly-welded facies	- Area of the polygon
Inferred deposits	The area originally covered by the ignimbrite prior to burial and erosion, with a coverage of ca. 4,600 km^2	- Area of the polygon
Energy lines	12 topographic sections traced radially from the Los Humeros caldera, covering all the studied area. These sections, coupled with the observed deposits information are the base to trace the inferred deposits polygon	- Figure of the section
Geologic sections	Seven geologic sections that integrate surficial and subsurface lithological information of the most updated geologic map from of the LHVC. From these, four are traced from the Los Humeros caldera rim to the distal areas, and three perpendicular to the valleys in the distal area	- Figure of the geologic section
Eroded bulk	15 polygons in the valley areas where the eroded bulk was calculated. The total eroded volume sums 14.6 km^3	- 3D model showing the valley prior to erosion - Eroded bulk volume (m^3)
Photographs	207 photographs of the outcrops and panoramic views of the Xáltipan ignimbrite and related deposits	- Photo name - Coordinates and altitude - Direction view (azimuth) - Brief description of the photo

5. Contributions to interpreting the XI eruption

5.1. PDC source and type of eruption

The projections from the energy lines pointed to a low-altitude PDC generation zone, which is typical in boiling-over, caldera-forming eruptions. This is supported by the consistent geometry with low slopes of the energy lines along the study area (Table 2). These values vary from 0.9 to 3.6°, with a shallow height of the PDC source that goes from 0 to 395 m, except for the three energy lines of the SE and E zone. Here, the energy lines present a higher slope (4 to 6.5°) and source height (1,900 to 3,500 m). Nevertheless, these atypical geometries can be explained by the topological aspect ratio concept (Giordano and Doronzo, 2017), where currents can change their emplacement conditions. In this case, the current passed from a forced condition to an inertia-driven current when entering steep terrains. This change is observed in profiles a-a' and b-b', where the PDC surmounted the 510 m high Cerro Pizarro volcano flanks and later descended through a steep open ramp, reaching runout distances of >40 km (Figure 5a). This can be also observed in profile c-c', where the PDC confined into the deep Las Minas valley, reducing the runout distance to <30 km (Figure 5b).

5.2. Changes in the landscape

Although in the proximal area the XI is poorly exposed, the evidence provided by the water wells indicates a 151 m thickness for the ignimbrite sheet. In this proximal area, the geologic sections show that the XI filled the pre-caldera volcanic field with a radial shape and flat surface. Further, in the distal facies to the southeast, thickness decreased where the PDC entered to open terrain and surmounted the Cofre de Perote topographic high. In this southern area, even if no outcrops of the XI where identified, the occurrence of consolidated fragments of the XI into the phreatomagmatic sequence from the

Table 2. Energy lines information / Tabla 2. Información de las líneas de energía

Profile	**Direction (azimuth)**	**Height (H) (m)**	**Lenght (L) (m)**	**H/L**	**Slope (°)**	**Intersection height (m)**	**Zone**
a-a'	135	5,000	48,037	0.1041	5.9	3,530	E-SE
b-b'	110	3,300	46,150	0.0715	4.1	1,930	
c-c'	90	3,274	27,560	0.1188	6.8	1,900	
d-d'	30	2,380	35,600	0.0669	3.8	93	NE-N-NW
e-e'	15	2,332	40,400	0.0577	3.3	50	
f-f'	348	1,490	22,800	0.0654	3.7	0	
g.g'	318	2,280	39,030	0.0584	3.3	395	
h-h'	270	495	51,000	0.0097	0.6	0	W
i-i'	270	685	41,400	0.0165	0.9	161	
j-j'	235	504	32,450	0.0155	0.9	0	
k-k'	215	560	34,900	0.0160	0.9	0	SW-S
l-l'	180	471	27,500	0.0171	1.0	0	

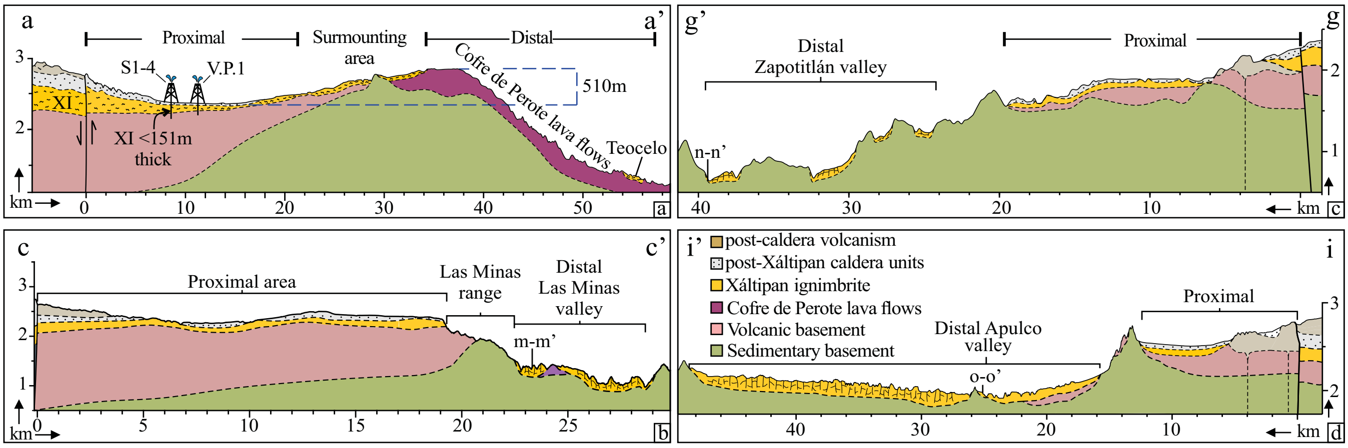

Figure 5: Selected geologic sections showing the inferred XI architecture over the pre-eruption topography. a) a-a' profile showing the location of the water wells and the surmounting of the XI over the Cofre de Perote lava flows. b) c-c' profile showing the Las Minas valley. c) g-g' profile showing the distal Zapotitlán valley. d) profile i-i' showing the distal Apulco valley. The location of the sections is indicated in Plate 1 / Figura 5. Secciones geológicas que muestran la arquitectura inferida de la IX sobre la topografía pre-eruptiva. a) Perfíl a-a' mostrando la ubicación de los pozos de agua y el remontamiento de la IX sobre los flujos de lava del Cofre de Perote. b) Perfil c-c' mostrando el valle de Las Minas. c) Perfil g-g' mostrando el valle distal de Zapotitlán. d) Perfil i-i' mostrando el valle distal de Apulco. La ubicación de las secciones está indicada en la Lámina 1.

younger Quechulac tuff ring, and into the collapse breccia deposits from the Cerro Pizarro dome (location in Figure 6), point to the presence of the XI, covered by a thick sequence of volcanic, phreatomagmatic, and epiclastic rocks from the Serdán Oriental Basin. Nevertheless, the subsurface position and thickness of the deposits in this area are unknown.

In the distal facies, particularly in the northern sector of the map, the paleotopographic features are more evident. Here, the XI flowed and deposited over the highly-deformed Mesozoic basement. Even where the XI filled this zone, the drainage system rapidly eroded the deposits exposing the welded ignimbrite on steep walls (Figure 7). The total eroded bulk in these areas reaches 14.6 km^3 .

5.3. *Application of the eroded bulk methodology in other ignimbrites*

Ignimbrite volume calculations are based on the area, thickness, and density of its deposits. Nevertheless, these issues

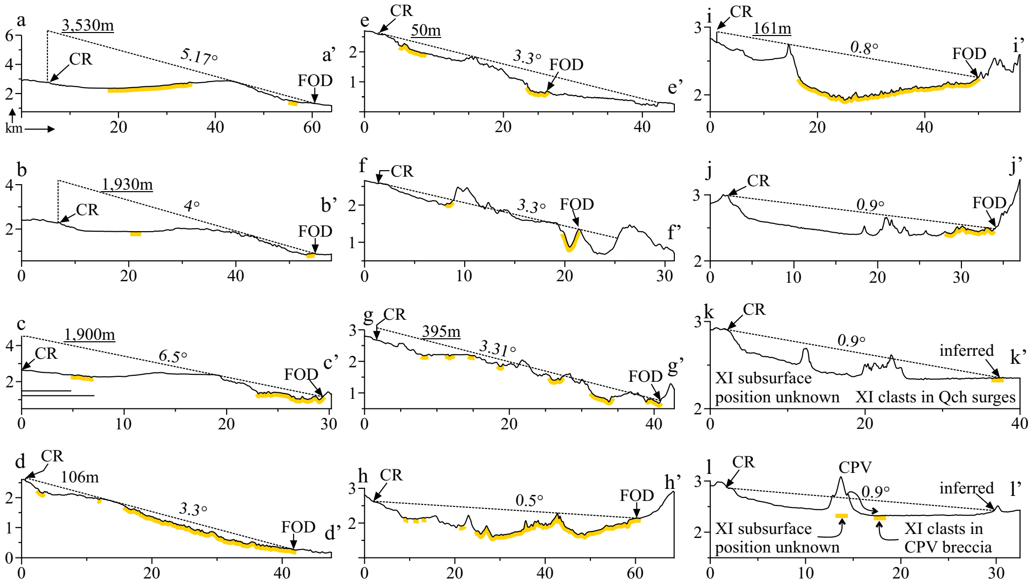

Figure 6: Profiles with the energy lines. Each profile shows the slope of the projected line, the intersection height with the Los Humeros caldera rim (CR), and the position of the observed deposits (yellow line) where the furthest is indicated (FOD). The location of the profiles is indicated in Plate 1 / Figura 6. Perfiles de las líneas de energía. Cada perfil muestra la pendiente de la línea proyectada, la altura de intersección con el borde la caldera Los Humeros (CR), y la posición de los depósitos observados (línea amarilla) en donde el más lejano está indicado (FOD). La ubicación del perfil está indicada en la Lámina 1.

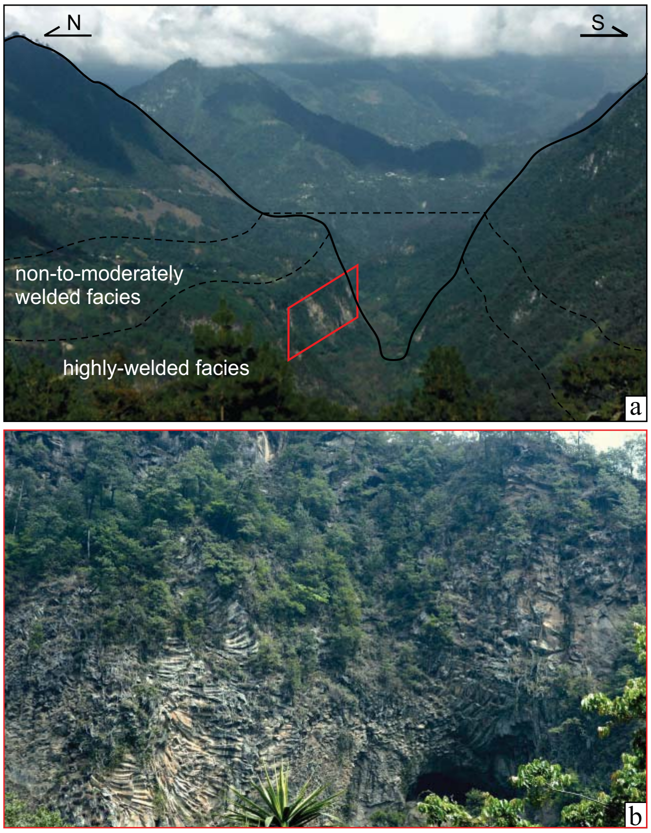

Figure 7: a) North view of the Las Minas valley showing the eroded space and the approximate position of the XI in the different welding facies that changes from highly-welded in the base to non-to-moderately welded through the top. Inset box in red square shows, b) a >110 m thick wall of the XI in highly-welded facies with spectacular columnar jointing development / Figura 7. Vista al norte del valle de Las Minas mostrando el espacio erosionado y la ubicación aproximada de la IX en las diferentes facies de soldamiento que va de altamente soldada en la base a no a moderadamente soldada hacia la cima. El recuadro en rojo muestra, b) una pared de >110 m compuesta por la IX en facies altamente soldadas y mostrando un desarrollo espectacular de columnas de enfriamiento.

commonly present high uncertainties caused, among other processes, by erosion. Two recent works exemplify this situation. The first occurs in the Otowi Member at the Valles Caldera, where the erosion of the outflow sheet is estimated based on erosion rates of another unit, resulting in the most significant uncertainty of the total volume calculation (Cook et al. 2016). The second is observed in the Cerro Galán ignimbrites, where the erosion is calculated at different zones by using thickness observations in individual valley zones and corrected by using correction factors that range from 1 (non-eroded) to 2 (half-eroded) with a ± 0.25 uncertainty (Folkes et al., 2011). The methodology to calculate the eroded bulk presented in this work estimates the erosion effect with no uncertainty. This because the method requires only two data, the area where ignimbrite is exposed at surface and a DEM that covers such area. Therefore, the method has the potential to be easily applied in ignimbrites that have been already mapped, as the two examples previously mentioned.

6. Conclusions

The XI exemplifies three common situations that complicate ignimbrite mapping. These includes lithofacies variations, burial by younger rocks, and high-rates of erosion. In these cases, the integration of conventional cartographic techniques, such as field mapping, energy lines, and geologic sections, with GIS tools, allowed to trace the original and present distribution of the deposits. These cartographic results revealed three essential features of the eruption and emplacement process: 1) The energy lines projections point to a low altitude PCDs source, typical in boiling-over, caldera-forming eruptions; 2) The inferred distribution area shows a combination of radial and valley-filling shapes that respond to the topography before the eruption. In the proximal facies, the radial shape forms due to the relatively flattened pre-caldera lava field, while in the distal southern area the PDC showed a higher fluidization surmounting topographic barriers such as the Cerro Pizarro volcano, and in the distal facies the PDCs channelized into the steep valleys of the pre-volcanic basement; 3) Geologic sections, parallel and perpendicular to the ignimbrite-filled valleys, reveal that the highly-welded facies of the XI focus within channel centers and that these facies are exposed due to erosion processes.

Software

The map was constructed using the Quantum GIS (QGIS) V.2.8.4-Wien with SAGA plugins installed. Besides the default QGIS tools, the plugins used where: Profile tool and qgis2threejs. Figures were drawn with CorelDraw X7.

Acknowledgments

We acknowledge the financial support given by the Consortium GEMEX European Union-Mexico [No. 2015-04-268074] and by the Centro Mexicano de Inovación en Energía Geotérmica from the Fondo de Sustentabilidad Energética SENER-CONACyT [No. 2007032], and to CONACyT-Mexico, who provided financing to the first author in the form of doctoral grant [No. 504993]. We are grateful to Francisco Fernández and Javier Hernández for their valuable help and discussions during fieldwork, to Mario Navarro for his technical assistance during the data processing in QGIS, and Javier Osorno Covarrubias for the design and implementation of the interactive map. Special thanks to Penélope López-Quiroz, who greatly enhanced this work with cartographic advices and editorial support. We also thank the valuable comments of two anonymous reviewers. Finally, we thank the Centro de Geociencias (UNAM), who provided vehicles and infrastructure to support this work.

References

Aguirre-Díaz, G. J., 1996. Volcanic stratigraphy of the Amealco caldera and vicinity, central Mexican Volcanic Belt. Rev. Mex. Ciencias Geol. 13, 10–51.

Aldiss, D. T., Ghazali, S. A., May 1984. The regional geology and evolution of the Toba volcano-tectonic depression, Indonesia. Journal of the Geological Society 141 (3), 487–500, https://doi.org/10.1144/gsjgs.141.3.0487.

Beget, J. E., Limke, A. J., Jun. 1988. Two-dimensional kinematic and rheological modeling of the 1912 pyroclastic flow, Katmai, Alaska. Bulletin of Volcanology 50 (3), 148–160, https://doi.org/10.1007/BF01079679.

Brown, R. J., Branney, M. J., Jul. 2004. Event-stratigraphy of a caldera-forming ignimbrite eruption on Tenerife: the 273 ka Poris Formation. Bulletin of Volcanology 66 (5), 392–416, https://doi.org/10.1007/s00445-003-0321-y.

Carrasco-Núñez, G., Bernal, J. P., Dávila, P., Jicha, B., Giordano, G., Hernández, J., 2018. Reappraisal of Los Humeros Volcanic Complex by New U/Th Zircon and 40ar/39ar Dating: Implications for Greater Geothermal Potential. Geochemistry, Geophysics, Geosystems 19 (1), 132–149, https://doi.org/10.1002/2017GC007044.

Carrasco-Núñez, G., Gómez-Tuena, A., Laura, L. V., 1997. Geologic map of Cerro Grande volcano and surrounding area, Central México. Geol. Soc. Am.

Carrasco-Núñez, G., Hernández, J., León, L. D., Dávila, P., Norini, G., Bernal, J. P., Jicha, B., Navarro, M., López-Quiroz, P., Oct. 2017a. Geologic Map of Los Humeros volcanic complex and geothermal field, eastern Trans-Mexican Volcanic Belt. Terra Digitalis 1 (2), https://doi.org/10.22201/igg.terradigitalis.2017.2.24.

Carrasco-Núñez, G., López-Martínez, M., Hernández, J., Vargas, V., May 2017b. Subsurface stratigraphy and its correlation with the surficial geology at Los Humeros geothermal field, eastern Trans-Mexican Volcanic Belt. Geothermics 67, 1–17, https://doi.org/10.1016/j.geothermics.2017.01.001.

Carrasco-Núñez, G., Siebert, L., Díaz-Castellón, R., Vázquez-Selem, L., Capra, L., Nov. 2010. Evolution and hazards of a long-quiescent compound shield-like volcano: Cofre de Perote, Eastern Trans-Mexican Volcanic Belt. Journal of Volcanology and Geothermal Research 197 (1), 209–224, https://doi.org/10.1016/j.jvolgeores.2009.08.010.

Cas, R. A. F., Wright, H. M. N., Folkes, C. B., Lesti, C., Porreca, M., Giordano, G., Viramonte, J. G., Dec. 2011. The flow dynamics of an extremely large volume pyroclastic flow, the 2.08-Ma Cerro Galán Ignimbrite, NW Argentina, and comparison with other flow types. Bulletin of Volcanology 73 (10), 1583–1609, https://doi.org/10.1007/s00445-011-0564-y.

Cavazos, J., Carrasco-Núñez, G., ???? Anatomy of the Xáltipan ignimbrite at Los Humeros Volcanic Complex; the largest eruption of the Trans-Mexican Volcanic Belt. J. Volcanol. Geotherm. Res.

Cook, G. W., Wolff, J. A., Self, S., Feb. 2016. Estimating the eruptive volume of a large pyroclastic body: the Otowi Member of the Bandelier Tuff, Valles caldera, New Mexico. Bulletin of Volcanology 78 (2), 10, https://doi.org/10.1007/s00445-016-1000-0.

Ferriz, H., Mahood, G. A., 1984. Eruption rates and compositional trends at Los Humeros Volcanic Center, Puebla, Mexico. Journal of Geophysical Research: Solid Earth 89 (B10), 8511–8524, https://doi.org/10.1029/JB089iB10p08511.

Folkes, C. B., Wright, H. M., Cas, R. A. F., de Silva, S. L., Lesti, C., Viramonte, J. G., Dec. 2011. A re-appraisal of the stratigraphy and volcanology of the Cerro Galán volcanic system, NW Argentina. Bulletin of Volcanology 73 (10), 1427–1454, https://doi.org/10.1007/s00445-011-0459-y.

Giordano, G., Doronzo, D. M., Jun. 2017. Sedimentation and mobility of PDCs: a reappraisal of ignimbrites' aspect ratio. Scientific Reports 7 (1), 1–7, https://doi.org/10.1038/s41598-017-04880-6.

Gómez-Tuena, A., LaGatta, A. B., Langmuir, C. H., Goldstein, S. L., Ortega-Gutiérrez, F., Carrasco-Núñez, G., 2003. Temporal control of subduction magmatism in the eastern Trans-Mexican Volcanic Belt: Mantle sources, slab contributions, and crustal contamination. Geochemistry, Geophysics, Geosystems 4 (8), https://doi.org/10.1029/2003GC000524.

Hsü, K. J., Jan. 1975. Catastrophic Debris Streams (Sturzstroms) Generated by Rockfalls. GSA Bulletin 86 (1), 129–140, https://doi.org/10.1130/0016-7606(1975)86<129:CDSSGB>2.0.CO;2.

Negendank, J., Emmermann, R., Krawczyk, R., Mooser, F., Tobschall, H., Werle, D., 1985. Geological and geochemical investigations on the eastern Trans-Mexican Volcanic Belt. Geofísica Int. 24, 477–575.

Quane, S. L., Russell, J. K., Feb. 2005. Ranking welding intensity in pyroclastic deposits. Bulletin of Volcanology 67 (2), 129–143, https://doi.org/10.1007/s00445-004-0367-5.

Self, S., Rampino, M. R., Newton, M. S., Wolff, J. A., Nov. 1984. Volcanological study of the great Tambora eruption of 1815. Geology 12 (11), 659–663, https://doi.org/10.1130/0091-7613(1984)12<659:VSOTGT>2.0.CO;2.

Siebe, C., Macías, J. L., Abrams, M. J., Rodríguez, S., Castro, R., Delgado Granados, H., 1995. Quaternary explosive volcanism and pyroclastic deposits in east central Mexico: implications for future hazards. Guided. Geol. excursions conjunction with Annu. Meet. Geol. Soc. Am. New Orleans, Louisiana, Nov. 6-9, 1–48.

Suñe-Puchol, I., Aguirre-Díaz, G. J., Dávila-Harris, P., Miggins, D. P., Pedrazzi, D., Costa, A., Ortega-Obregón, C., Lacan, P., Hernández, W., Gutiérrez, E., Feb. 2019. The Ilopango caldera complex, El Salvador: Origin and early ignimbrite-forming eruptions of a graben/pull-apart caldera structure. Journal of Volcanology and Geothermal Research 371, 1–19, https://doi.org/10.1016/j.jvolgeores.2018.12.004.

Viniegra, F., 1965. Geología del macizo de Teziutlán y de la cuenca cenozoica de Veracruz. Boletín la Asoc. Mex. Geólogos Pet. 17, 100–135.

Walker, G. P. L., Heming, R. F., Wilson, C. J. N., Jan. 1980. Low-aspect ratio ignimbrites. Nature 283 (5744), 286–287, https://doi.org/10.1038/283286a0.

Wilson, C. J. N., Houghton, B. F., Kampt, P. J. J., McWilliamst, M. O., Dec. 1995. An exceptionally widespread ignimbrite with implications for pyroclastic flow emplacement. Nature 378 (6557), 605–607, https://doi.org/10.1038/378605a0.

Yáñez-Garcia, C., García-Durán, S., 1982. Exploración de la región geotérmica Los Humeros–Las Derrumbadas, Estados de Puebla y Veracruz. Comisión Federal de Electricidad. Mexico, D. F.

This article accompanies the following material:

HTML:	DOI:10.22201/igg.25940694.2019.2.65.139
Static Map:	DOI:10.22201/igg.25940694.2019.2.65.145
2D Interactive Map:	DOI:10.22201/igg.25940694.2019.2.65.140
3D Interactive Map:	DOI:10.22201/igg.25940694.2019.2.65.141
Supplementary material 1:	DOI:10.22201/igg.25940694.2019.2.65.143
Supplementary material 2:	DOI:10.22201/igg.25940694.2019.2.65.144

5.2 Anatomía de la ignimbrita Xáltipan; historia de la mayor erupción explosiva de la Faja Volcánica Trans-Mexicana.

Artículo: *Anatomy of the Xáltipan ignimbrite at Los Humeros Volcanic Complex; the largest eruption of the Trans-Mexican Volcanic Belt.*

Autores: Cavazos-Álvarez, J. A., y Carrasco-Núñez, G., (2020).

Revista: Journal of Volcanology and Geothermal Research, vol. 392, p. 1-18.

DOI:10.1016/j.jvolgeores.2019.106755

Journal of Volcanology and Geothermal Research 392 (2020) 106755

Contents lists available at ScienceDirect

Journal of Volcanology and Geothermal Research

journal homepage: www.elsevier.com/locate/jvolgeores

Anatomy of the Xáltipan ignimbrite at Los Humeros Volcanic Complex; the largest eruption of the Trans-Mexican Volcanic Belt

Jaime Alberto Cavazos-Álvarez *, Gerardo Carrasco-Núñez

Centro de Geociencias, Universidad Nacional Autónoma de México, Blvd. Juriquilla 3001, Campus UNAM-Juriquilla, Querétaro 76230, Mexico

ARTICLE INFO

Article history:
Received 7 May 2019
Received in revised form 9 December 2019
Accepted 12 December 2019
Available online 23 December 2019

Keywords:
Ignimbrite stratigraphy
DRE volume
Welding lithofacies
Caldera-forming eruption
Los Humeros caldera
Trans-Mexican Volcanic Belt

ABSTRACT

The Xáltipan ignimbrite (*ca.* 290 km^3 DRE) represents the major explosive event from Los Humeros Volcanic Complex (LHVC) that can be ranked as the largest caldera-forming eruption of the Trans-Mexican Volcanic Belt (TMVB). This eruption marked the onset of an explosive period of LHVC producing the collapse of the main Los Humeros caldera at 164 ± 4.2 ka. This paper provides a detailed characterization of the Xáltipan ignimbrite anatomy and eruptive chronology that records a multi-phase, single eruption. This eruption resulted in more complex architecture and lithofacies variations of the ignimbrite than previously reported. To support these findings, we present two representative composite Xáltipan stratigraphic columns based on two regional reference sections, together with a welding lithofacies map, digital mapping, energy line projections, geologic sections and high-resolution petrophysical characterization (micro-CT, He-pycnometry). Additionally, we have reevaluated the magnitude (DRE volume), and the total erupted mass of the deposit by taking into account critical primary and post-emplacement processes such as lithic concentration, welding grade, and bulk loss due to erosion. The internal architecture of the Xáltipan ignimbrite is composed of two flow units and two pumice fallout deposits (a basal one and an intercalated layer), which formed as a result of a voluminous and sequential eruption that can be resumed in four eruptive phases. The initial stage of the eruption produced a basal pumice fallout (BPF) (phase 1) derived from a buoyant plume that eventually collapsed, generating pyroclastic density current (PDC) deposits with intra-ignimbrite pumice fallout beds. This event was followed by the climactic, caldera-forming, boiling over-type eruptive phase (phase 2) that generated voluminous PDCs of the lower flow unit (LFU). As the eruption waned, a brief eruptive hiatus occurred, immediately followed by a second explosive event in the western rim of the caldera with a boiling-over type eruptive column depositing a discrete pumice fallout layer (IPF) (phase 3), which later collapsed depositing less voluminous PDC (UFU) in the western flank of the Los Humeros caldera (phase 4). The anatomy of the deposits shows that the Xáltipan ignimbrite was emplaced in different behaviors: radially in the proximal parts and channelized and confined in the distal parts, showing significant welding variations that range from non-to-highly welded conditions (welding ranks I-VI) controlled mainly by the paleotopography. The size calculations indicate that the deposits have an aerial extent of *ca.* 4600 km^2, an ejected bulk volume of *ca.* 330 km^3 with a DRE volume of *ca.* 290 km^3, and an ejected mass of 1.1×10^{12} kg, which points out to a paroxysmal eruption (VEI 6-7).

1. Introduction

Calderas are large volcanoes usually associated with a long-term and complex volcanic evolution (Cashman and Giordano, 2014; Druitt and Sparks, 1984; Gottsman and Martí, 2008; Lipman, 1997, 2000; Smith and Bailey, 1968; Suñe-Puchol et al., 2018). Large volume caldera-related ignimbrites (>100 km^3) provide valuable insights into the evolution of these big volcanic systems. Detailed stratigraphic studies that define the eruptive history of how the ignimbrites are assembled, including the vertical and lateral variations in lithofacies (Brown and Branney, 2004; Cas et al., 2011; Pacheco-Hoyos et al., 2018; Wilson et al., 1995; Wilson and Hildreth, 1997, 2003; Wilson and Walker, 1982). In addition to these studies, the eruptive magnitude estimation is critical to understand the size of the eruption and its implications to the magmatic system (Mason et al., 2004). Nevertheless, the volume calculation of large ignimbrites in volcanic complexes is often a difficult task that requires a detailed mapping of its deposits coupled with thickness and rock density data, and that usually is determined with high uncertainties (*e.g.*, Scott et al. (1996). In the case of ancient, highly eroded, and buried ignimbrites, this task is even more challenging. Different

---

* Corresponding author.
E-mail address: jcavazos@geociencias.unam.mx (J.A. Cavazos-Álvarez).

https://doi.org/10.1016/j.jvolgeores.2019.106755
0377-0273/

techniques have been applied to estimate the volume of ignimbrites based on their particular conditions and pre-eruptive topography (Best et al., 2013; Cook et al., 2016; Folkes et al., 2011; Giordano et al., 2010).

In this paper, we document the largest caldera-forming eruption of the Trans-Mexican Volcanic Belt (TMVB) recorded at Los Humeros Volcanic Complex (LHVC) (Fig. 1) during the Pleistocene, which caused the collapse of Los Humeros caldera (LH caldera) and the emplacement of the voluminous Xáltipan ignimbrite. This event is the leading eruption of the LHVC, marking the onset of an explosive activity period that derived in the formation of a nested-caldera system and the emplacement of a thick pyroclastic sequence. We provide a detailed characterization of the lithostratigraphic features and variations of the Xáltipan ignimbrite and apply a simple but effective methodology to calculate with a high degree of accuracy the size of this large ignimbrite in terms of area, magnitude (inflated and DRE volume) and total ejected bulk during the eruption (Walker, 1980).

Despite the importance of this caldera-forming eruption in the LHVC evolution, only two works have described the stratigraphy of its deposits (Ferriz and Mahood, 1984; Willcox, 2011), which in both cases present generalized stratigraphic reconstructions of the Xáltipan ignimbrite based on relatively few outcrops. Noteworthy that in both works, the proposed stratigraphic models are significantly divergent and classify the ignimbrite in different lithostratigraphic categories without describing significant lithofacies variations. However, recent fieldwork and petrophysical analysis of both, subsurface intracaldera samples within the geothermal field and the surficial outcrops, reveal that the ignimbrite has a different stratigraphic succession as well as marked vertical and lateral lithofacies variations related to the stratigraphic position and emplacement conditions (Cavazos and Carrasco-Núñez, 2017).

In this paper, we present a detailed stratigraphic reconstruction of the ignimbrite outflow sheets (OS) deposits, lithofacies variations, and an estimate of the total erupted volume, by integrating fieldwork, digital mapping, and laboratory analysis. The volume estimation is built on fieldwork and digital mapping combined with petrophysical analysis, considering the different emplacement environments and post-emplacement processes that modify the original deposit, such as erosion and welding. These results provide a more realistic interpretation of the eruptive history, PDC emplacement conditions, and magnitude of the leading eruption of LHVC. Furthermore, the reevaluation of the eruptive magnitude is key for assessing the conductive model of the Los Humeros geothermal system, the fourth most productive geothermal field in Mexico (93 MW power).

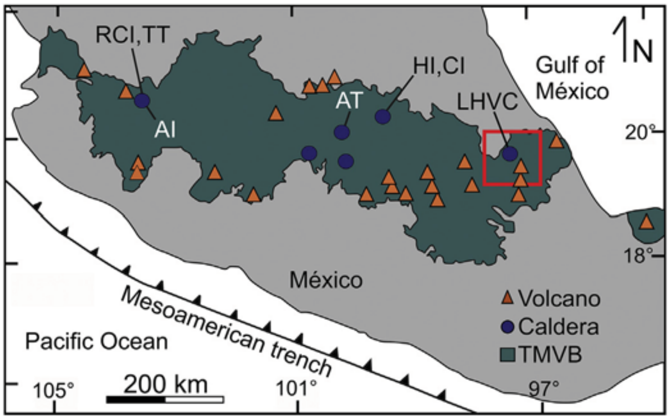

Fig. 1. Location of Los Humeros Volcanic Complex (LHVC) in the eastern sector of the Trans-Mexican Volcanic Belt (TMBV) (red square) (modified from Carrasco-Núñez et al. (2017b). Location of the main volcanoes is indicated in the legend.

2. Geological background

2.1. Regional geologic setting

LHVC is one of the most studied volcanic fields in Mexico because of its intriguing geologic evolution and because it hosts a geothermal field currently producing *ca.* 93 MW (Romo-Jones et al., 2017). It is located in the eastern boundary of the TMVB, a continental volcanic arc active since Miocene times, with an extension >1000 km long and 20–150 km width (Fig. 1), which resulted from volcanic activity associated with the subduction of the Cocos and Rivera plate under the North American plate (Demant, 1978; Ferrari et al., 2012). This volcanic province is distributed transversely in a rough west-east orientation, oblique from the Pacific trench near the Puerto Vallarta coast up to the Veracruz coast in the Gulf of Mexico, and constructed by large andesitic stratovolcanoes, silicic calderas, domes, and monogenetic volcanic fields. During the Pliocene-Holocene, the eastern sector of the TMVB was characterized by a diverse volcanic activity and regional faulting that formed the Serdán-Oriental Basin (SOB) (Ferrari et al., 2012). The SOB records a critical period of regional volcanic activity formed by a dominant bimodal monogenetic volcanism including maar structures, cones, domes, and lava flows, bounded by polygenetic volcanism such as the nested-caldera-system of LHVC, stratovolcanoes chains and compound volcanoes (Carrasco-Núñez et al., 2007; Negendank et al., 1985; Siebe et al., 1995).

2.2. Geologic setting of the LHVC

LHVC has been built over a pre-volcanic basement and an extensive andesitic volcanic sequence (Fig. 2). The evolution of LHVC can be divided into three main stages based on the type of volcanic activity and eruptive styles: 1) pre-caldera stage; 2) a caldera stage, divided into

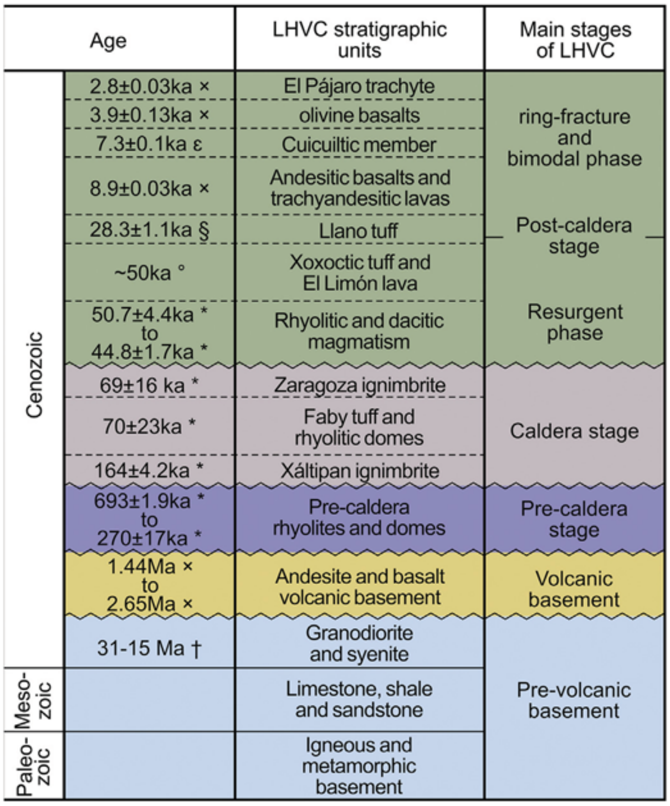

	Age	LHVC stratigraphic units	Main stages of LHVC
Cenozoic	2.8±0.03ka ×	El Pájaro trachyte	ring-fracture and bimodal phase
	3.9±0.13ka ×	olivine basalts	
	7.3±0.1ka ε	Cuicuiltic member	
	8.9±0.03ka ×	Andesitic basalts and trachyandesitic lavas	
	28.3±1.1ka §	Llano tuff	Post-caldera stage
	~50ka °	Xoxoctic tuff and El Limón lava	
	50.7±4.4ka * to 44.8±1.7ka *	Rhyolitic and dacitic magmatism	Resurgent phase
	69±16 ka *	Zaragoza ignimbrite	Caldera stage
	70±23ka *	Faby tuff and rhyolitic domes	
	164±4.2ka *	Xáltipan ignimbrite	
	693±1.9ka * to 270±17ka *	Pre-caldera rhyolites and domes	Pre-caldera stage
	1.44Ma × to 2.65Ma ×	Andesite and basalt volcanic basement	Volcanic basement
	31-15 Ma †	Granodiorite and syenite	Pre-volcanic basement
Meso-zoic		Limestone, shale and sandstone	
Paleo-zoic		Igneous and metamorphic basement	

Fig. 2. Stratigraphic summary of LHVC showing the main stratigraphic units as proposed by Norini et al. (2015). Chronological data is compiled from several works: [* - Carrasco-Núñez et al., 2018; × - Carrasco-Núñez et al., 2017b; § - Rojas-Ortega, 2016; ε - Dávila-Harris and Carrasco-Núñez, 2014; ° - Ferriz and Mahood, 1984; † - Yáñez-Garcia and García-Duran (1982)].

three eruptive events; and 3) a post-caldera stage, which is subdivided into a resurgent phase and a ring-fracture and bimodal phase (Carrasco-Núñez et al., 2017a, 2018).

The regional basement is made up of a late Paleozoic plutonic and the metasedimentary sequence of the Teziutlán Massif (Ferriz and Mahood, 1984; Gómez-Tuena et al., 2003; Viniegra, 1965). Over this basement, rests a thick Mesozoic sedimentary succession of carbonated and terrigenous rocks of the Sierra Madre Oriental, which is highly deformed by the Laramide orogeny; and Eocene-Oligocene granitic and syenitic intrusions that caused local metamorphism of the limestones (Yáñez-Garcia and García-Durán, 1982; Ferriz and Mahood, 1984). Over the pre-volcanic basement occurs a thick Pliocene sequence (>1500 m) of lava flows made of highly-fractured pyroxene-bearing andesite of the Teziutlán formation (Cedillo, 1997; Ferriz and Mahood, 1984; Yáñez-Garcia and García-Durán, 1982). This unit has been recently dated at 2.6–1.4 Ma, and due to its high permeability, wide distribution, and stratigraphic position serves as the reservoir rock of the geothermal system (Carrasco-Núñez et al., 2017b).

The pre-caldera stage includes the formation of rhyolitic lava domes in the south and particularly the west sides of LH caldera. Recent chronostratigraphic studies based on ^{40}Ar/^{39}Ar and U/Th dating, indicate that the rhyolitic lavas emplaced between 693 ± 1.9 and 270 ± 17 ka (Carrasco-Núñez et al., 2018). This activity is the earliest silicic volcanic activity preceding the LHVC explosive phase.

The caldera stage comprises three explosive events. The first and largest one resulted in the collapse of Los Humeros caldera, associated with the emplacement of the Xáltipan ignimbrite with an initially estimated volume of 115 km^3 DRE (Ferriz and Mahood, 1984). This eruption has been recently dated in 164 ± 4.2 ka, based on a combination of ^{40}Ar/^{39}Ar (plagioclase) and U/Th (zircon) dating (Carrasco-Núñez et al., 2018). The second event comprises a succession of Plinian eruptions occurred 70 ± 23 ka, characterized by multiple rhyodacitic pumice fallout layers separated by paleosols grouped as the Faby tuff formation (Carrasco-Núñez et al., 2018; Ferriz and Mahood, 1984; Willcox, 2011). No caldera structure has been recognized during this eruption. The third explosive event resulted in the Los Potreros caldera-forming eruption that deposited the Zaragoza ignimbrite. This ignimbrite is smaller in volume (~15 km^3 DRE) and shows a marked double compositional zonation (rhyodacitic - andesitic - rhyodacitic) (Carrasco-Núñez and Branney, 2005) and an ^{40}Ar/^{39}Ar and U/Th age of 69 ± 16 ka (Carrasco-Núñez et al., 2018). This latter date is in agreement with the field relations, as the Zaragoza ignimbrite is overlaying a rhyolitic lava dated at 74.2 ± 4.5 ka.

The caldera stage was followed by the post-caldera activity characterized by ring-fracture and bimodal volcanism, and by with the development of the resurgent phase in the central part of the LH caldera. The resurgent phase is composed by rhyolitic and dacitic magmatism inside the caldera (44.8 ± ka) and by the emplacement of a rhyolitic dome north the caldera (50.7 ± 4.4 ka) (Carrasco-Núñez et al., 2018). Furthermore, explosive activity derived in the formation of various fallout deposits (Xoxoctic tuff ~50 ka), and pyroclastic flows and breccias (Llano tuff) (Ferriz and Mahood, 1984; Willcox, 2011; Carrasco-Núñez et al., 2018), with a maximum age of ~28 ka (Rojas-Ortega, 2016). During the Holocene, the volcanic activity focused mainly along the southern caldera rim in the form of lava flows (andesitic - basaltic andesite), with contemporaneous explosive eruptions of bimodal composition (basaltic and rhyodacitic), forming the 7.3 ka Cuicuiltic member (Dávila-Harris and Carrasco-Núñez, 2014). The most recent volcanism of LHVC includes olivine-rich basalt flows that outcrop both in the central portion and the periphery of Los Humeros caldera (~4 ka), as well as basaltic andesite and trachytic lava flows dated at 2.8 ± 0.03 ka (Carrasco-Núñez et al., 2017a).

2.3. Xáltipan ignimbrite previous works

The stratigraphic and petrologic description of the Xáltipan ignimbrite was first reported by Ferriz and Mahood (1984), and later by Willcox (2011) (Fig. 3). Both describe it as a discrete, massive, mainly non-consolidated, vitric tuff. The pumice is of rhyolitic composition, and mainly aphyric with rarely porphyritic biotite rhyodacitic pumice. Nevertheless, both works propose different stratigraphic models and situate the ignimbrite in different stratigraphic groups. Ferriz and Mahood (1984), group these deposits as the "Xáltipan tuff" describing it as sequence made by the ignimbrite body at the base covered by a co-ignimbrite ash-fall deposit, and concordantly overlaid atop by eight air-fall lapilli tuffs with a gradual andesite-to-rhyodacite upward transition (Fig. 3a). The Xáltipan air-fall units described by (Ferriz and Mahood, 1984) are defined in one locality ~2 km SE from the caldera rim, and the ignimbrite body in six different locations. Nevertheless, in the recent fieldwork, these overlaying fallout deposits were not found in the reported locality nor on the rest of the study area.

Alternatively, Willcox (2011), presents a different stratigraphic scheme, proposing the "Los Humeros formation," which includes the Xáltipan member (Fig. 3b). According to Willcox (2011), this member comprises a rhyolitic pumice fallout deposit in the base, the ignimbrite body in the middle, and a dacitic pumice fallout to the top. The fall layers are described in three different localities by Willcox (2011), who interpreted them as a result of a sustained Plinian column. He provided a general description of the ignimbrite body based in a locality near Tenextepec, with an average thickness of 7.5 m. In both cases, the stratigraphic reconstructions are established by a restricted quantity of localities, resulting in a generalized and incomplete representation for such a voluminous ignimbrite.

On the other hand, the conventional geothermic model of Los Humeros describes the intracaldera ignimbrite as a texturally homogeneous and impermeable unit that acts as an aquitard in the geothermal system (Cedillo, 1999). Nevertheless, more recent descriptions from well-samples show significant lateral and vertical lithofacies heterogeneities (Carrasco-Núñez et al., 2017b; Fernández-Maya, 2017; Huerta-Luna, 2018; Jáquez-Domínguez, 2018; Peña-Rodrigez, 2018). These observations suggest that the intracaldera ignimbrite features an irregular lithofacies distribution that can affect its permeable properties. Recent textural studies suggest that these variations are critical in the

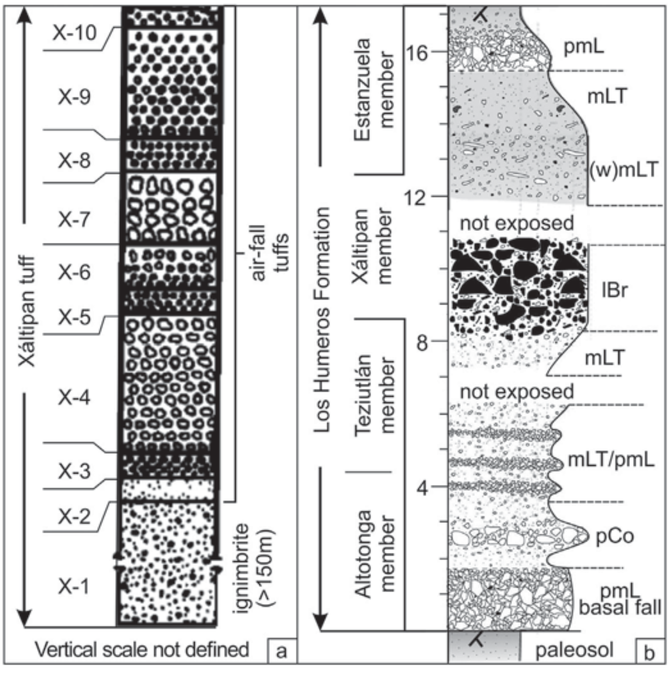

Fig. 3. Previous stratigraphic columns for the Xáltipan ignimbrite. (a) Modified stratigraphic column of the Xáltipan tuff as proposed by Ferriz and Mahood (1984). b) Modified stratigraphic column of the Xáltipan member within Los Humeros formation as proposed by Willcox (2011), with abbreviations adopted from those described by Branney and Kokelaar (2002).

exploitation of the geothermal resource (Cavazos and Carrasco-Núñez, 2017) and thus, must be carefully examined and characterized through petrophysical analysis to enhance the Los Humeros geothermal model.

The age of the ignimbrite was first reported in 460 ka by Ferriz and Mahood (1984) by K/Ar dating on plagioclase and biotite crystals. Recently, a chronostratigraphic reappraisal of LHVC by Carrasco-Núñez et al. (2018) proposes a significantly younger age of 164 ± 4.2 ka, based on combining $^{40}Ar/^{39}Ar$ and U/Th dating on plagioclase and zircon, respectively. These new findings support that the first and largest caldera collapse stage occurred much younger than previously proposed and provide an entirely new eruptive reconstruction of LHVC.

A distribution map and volume estimation of the ignimbrite was first reported by Ferriz and Mahood (1984), who estimate an extent of 3500 km^2 with a DRE volume of 115 km^3 (Fig. 4a). Nevertheless, although these results derive from a pioneer cartographic and stratigraphic work, we observed that the distribution map is somewhat poorly coupled with topographic features. This decoupling is mainly observed in the valley and range terrains, where the ignimbrite deposits do not follow the topographic depressions, and instead, are traced linearly over the highly deformed basement. Additionally, there is no information about the thickness values nor density calculations that are fundamental to support the volume estimation and DRE correction.

3. Methods

The methodology consisted of three main work stages: fieldwork coupled with digital mapping, laboratory techniques, and data processing.

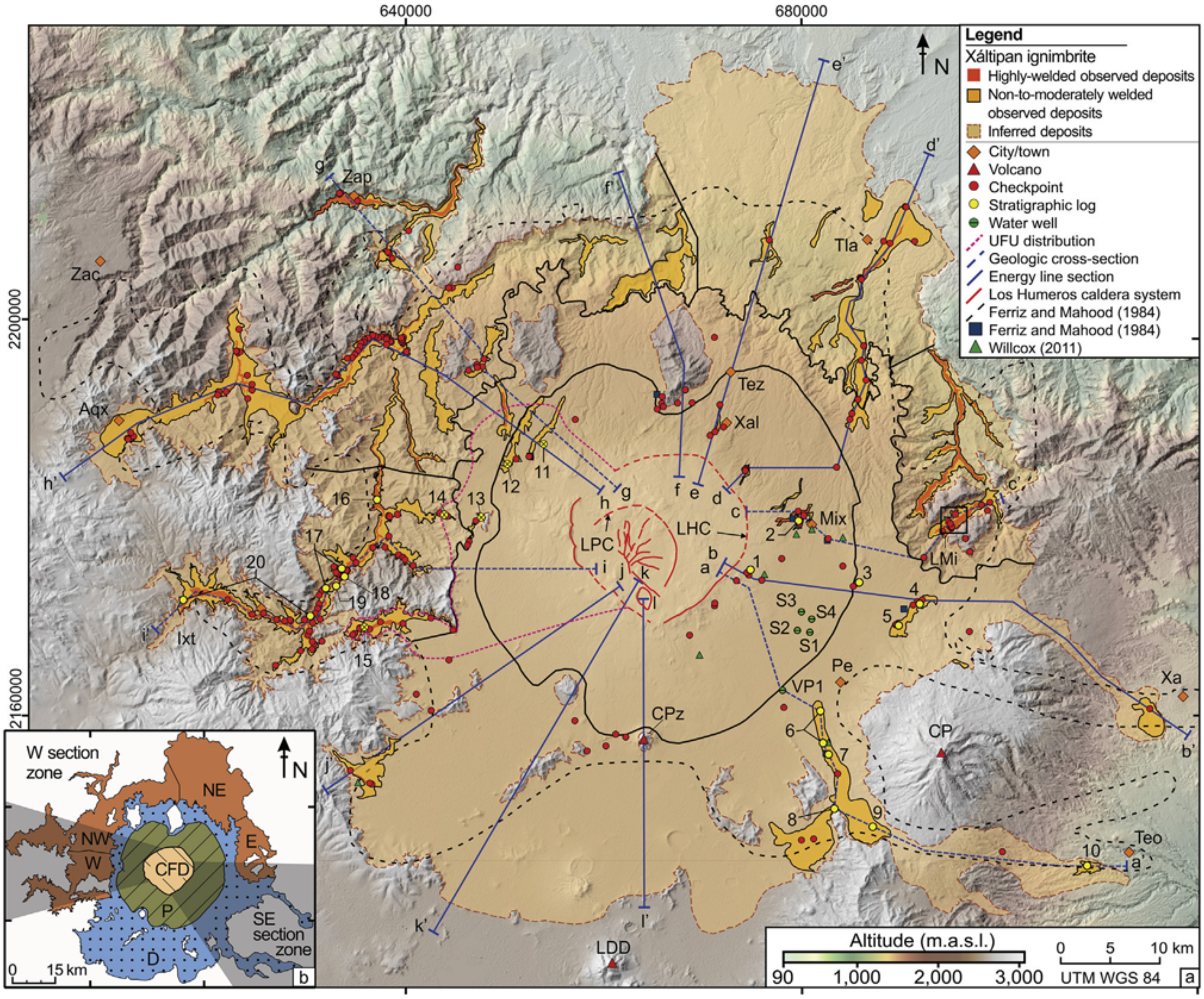

Fig. 4. Color graded Digital Elevation Model of LHVC area (blue is the highest; red is the lowest) showing the distribution of the observed deposits (OD) of the Xáltipan ignimbrite with its welding lithofacies variations (non-to-moderately welded in yellow, and highly welded in orange), and the inferred deposits (ID) (transparent pale yellow). Also showing the location of stratigraphic logs (yellow dots), which include the localities of the intercalated fallout layer and upper flow unit (yellow dots with cross), and the upper flow unit (UFU) distribution (pink dashed line); location of water wells (green dots); Los Humeros (LHC) and Los Potreros (LPC) caldera structures (red lines); Cofre de Perote (CP), Cerro Pizarro (CPz), and Las Derrumbadas (LDD) volcanoes (red triangles); energy lines sections (blue lines), including the four selected sections of the geologic sections (dashed blue lines); cities and towns in orange diamonds (Xa-Xalapa, Teo-Teocelo, Pe-Perote, Tez-Teziutlán, Xal-Xáltipan, Tla-Tlapacoyan, Ixt-Ixtacamaxtitlán, Aqx-Aquixtla, Zap-Zapotitlán, Zac-Zacatlán de las Manzanas). The previous distribution of the Xáltipan ignimbrite as proposed by Ferriz and Mahood (1984) is marked in the black dashed line. The localities with stratigraphic descriptions reported by Ferriz and Mahood (1984) and by Willcox (2011) are pointed in green triangles and blue squares, respectively; and the localities where the Xáltipan ignimbrite was reported and described during this work in red circles. Inset box (b) show a sketch distribution map of the Xáltipan ignimbrite showing the location of the different emplacement environments and sectors (CFD – Caldera-fill deposits; P – Proximal; D – Distal; VP – Valley-pond zones divided into; E – East; NE – Northeast; NW – Northwest; W – West), and the stratigraphic sections zones (grey shadow).

3.1. Fieldwork and digital mapping

Fieldwork includes eight weeks of exploration and cartography during seven different campaigns around Los Humeros caldera, aiming to collect stratigraphic data, mapping, and sampling the ignimbrite outflow sheets in its different lithofacies. The field data were digitalized on the Quantum GIS software and projected over a 30 m resolution DEM (SRTM at 1 Arc-Second). A detailed description of the GIS methodology used for the construction of this map is presented by Cavazos-Álvarez and Carrasco-Núñez (2019). A distribution map was constructed using this database and the information of 223 local descriptions, showing the exposed and inferred deposits (Fig. 4a). The criteria for delimiting both areas are presented below.

The observed deposits comprise the zones where the ignimbrite is exposed on the surface. The contour of this area was traced by field observations, satellite images photointerpretation, and by using the DEM as the ground base. The observed deposits are subdivided into two welding grade lithofacies based on their density and porosity and by considering the welding rank scheme proposed by Quane and Russell (2005): the non-to-moderately welded facies (rank I–IV), and the highly welded facies (rank V–VI). This petrophysical information is critical for the estimation of the DRE volume and erupted mass.

The inferred deposits area is constructed based on the observed deposits. We assume it represents the best approximation of the original distribution of the ignimbrite. This area shows that the Xáltipan ignimbrite is mostly not exposed due to two post-emplacement processes: 1) high erosion rates, particularly in the non-consolidated lithofacies and in the valley-pond areas where the hydrologic systems have worked for *ca.* 165 ky, and 2) burial by younger deposits of the post-Xáltipan volcanic activity, including thick caldera-related pyroclastic deposits (*e.g.*, Faby tuff, Zaragoza ignimbrite, Cuicuiltic tuff), as well as multiple lava flows related with caldera-rim effusive activity. In the caldera area, the Xáltipan ignimbrite is entirely buried by a thick package of younger eruptive units; therefore, the information is obtained from the well-logs of the geothermal field. Burial of the outflows is observed at the southern sector, where the ignimbrite is partially buried by a thick sequence of pyroclastic and minor epiclastic deposits associated with the phreatomagmatic and magmatic activity of the SOB, and also by the epiclastic deposits of the Cofre de Perote-Citlaltépetl volcanic chain (Carrasco-Núñez et al., 2010). The original deposits area was traced by projecting 12 sections by using the Energy Line concept (Hsu, 1975) (Fig. 4a). The energy lines integrate the actual topographic setting coupled with the estimated runout distance and the location of the furthest observed deposits, leading to the projection of the inferred deposits area. This method also allows the projection of rock-mass and pyroclastic flows over the topographic setting using the location of the observed deposits, and favor the estimation of the eruptive column collapse's height (Beget and Limke, 1988). Nevertheless, this last approximation should be treated carefully for caldera-forming eruptions where the eruptive column height can be temporarily and spatially highly variable (Trolese et al., 2019; Druitt and Sparks, 1984; Druitt and Bacon, 1986; Todesco et al., 2006).

The stratigraphic and cartographic results presented in this work are based on 223 verification points at different localities identified during this study and previous works (Ferriz and Mahood, 1984; Willcox, 2011) (Fig. 4a). Also, four geologic sections were built at different orientations from the Los Humeros caldera to show the architecture of the ignimbrite and its relation with the paleotopographic setting (Fig. 4a). Because the type section of the ignimbrite is not fully exhibited in a single locality, the stratigraphy was constructed by combining two geologic sections in the form of *section stratotypes*, (North American Commission on Stratigraphic Nomenclature, 2005). Each *section stratotype* consists of ten multiple local stratigraphic logs of different stratigraphic levels that were later integrated as composite stratigraphic columns. These sections include the most representative lithofacies in the different topographic environments where the ignimbrite was deposited. The Southeastern section represents the location where the pyroclastic density currents (PDC) surmounted the Cofre de Perote (CP) lava flows, and deposited as ignimbrite veneer deposit (IVD), and flowed downwards through the eastern flank of CP volcano distal deposits. The Western section shows the PDC surmounting the Zautla-Contla range and the confining along the Apulco river as valley-pond ignimbrite. The lithological units distinct from the Xáltipan ignimbrite and structural features are based on the most updated geologic map for LHVC made by Carrasco-Núñez et al. (2017a).

3.2. Laboratory: density and welding measurements

The methodology used for the density and welding measurements depends on the degree of consolidation of the samples. For the outflows non-consolidated samples, we applied the Archimedean immersion method, where a whole-rock portion of the sample was weighted in a high-precision scale and then submerged in a graduated test tube, resulting in a whole-rock density value (Bouvet de Maisonneuve et al., 2009) (see Supplementary data for density estimation procedure). The process was repeated with a lithic-free sample to obtain the magmatic density. On the other hand, the lithic fraction into the −1 to −4 Phi fractions was measured manually by component counting. The components were separated and weighted as juvenile and accidental clasts.

The welding grade of the consolidated samples was measured by using petrographic descriptions, computerized microtomography (micro-CT), and He-pycnometry analysis (Fig. 5). The methodologic sequence is depicted in Fig. 5 and summarized as follows: an oriented decimeter-scale cube of the collected sample was extracted, from which thin-sections were cut horizontally and vertically relative to the *in-situ* orientation. This, to have a three-dimensional perspective of the textural features associated with welding compaction. From this, *fiammae* aspect ratios and eutaxitic textures of the vitroclastic matrix were measured, as well as an estimation of the lithic content proportions. Subsequently, we extracted a cylindrical core of 2.54 × 5.08 cm, oriented perpendicularly to the in-field horizontal plane to consider the vesiculation and eutaxitic texture influence in the experiments. For the micro-CT, the cores were analyzed in an Xradia Zeiss Versa 510 microtomograph in the University Laboratory of X-Ray Microtomography (LUMIR) at the Geosciences Center, UNAM, with a 5–16 μm/pixel resolution. The resulting data were processed with the (AVIZO software to obtain 3D images, which allowed the reconstruction, visualization, and numerical quantification of high-resolution images following the methods described by Cid et al. (2017). We used the micro-CT as the primary tool for visualizing the samples' internal texture and for quantifying its different components (pores, vitric matrix, crystals, and lithics), as it is a non-invasive and non-destructive technique. The density of the consolidated samples was measured in a Helium-Porosimeter PHI-220, and in an Automatized Porosimeter-Permeometer AP608 in the Applied Geology and Petrophysics Laboratory, of the IPICyT, S.L.P., México. The experiments were calibrated at

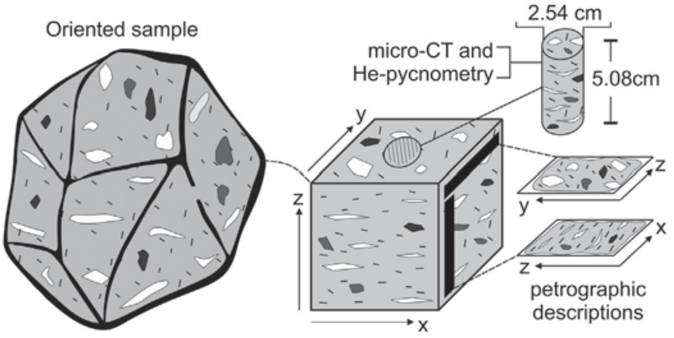

Fig. 5. Sketch showing the methodological sequence of the different analyses for the consolidated (welded) samples. See details in text.

confining pressure of 1.72 MPa, with an estimated pore resolution of 2 nm. This analysis is non-invasive and non-destructive, allowing the use of the same sample for further micro-CT analysis. In the case of the consolidated and smaller chips of the intracaldera deposits, these were analyzed only by micro-CT.

3.3. Data processing: geometry and size of the deposits

One of the principal goals of this work is to estimate the ignimbrite size, which includes its distribution, inflated volume (actual density state), DRE volume (pre-eruption magmatic density), and erupted mass. For this estimation, we revised different techniques (Best et al., 2013; Cook et al., 2016; Folkes et al., 2011; Giordano et al., 2010). We finally adopted the approach proposed by Cook et al. (2016) as the most convenient for this study, where the area covered by the ignimbrite is partitioned in different sectors according to their topographic and geologic characteristics. These sectors include the intracaldera deposits (CFD) and the outflow sheets (OS). For the latter, three emplacement environments were classified based on its topographic setting: Proximal (P), Distal (D), and Valley-pond (VP) deposits, being the last one subdivided into four zones in order to have a better control of the thickness in the different areas (E, NE, NW, and W) (Fig. 4b). For the OS, the observed and inferred deposits were calculated individually, while for the CFD, the calculation is presented as single values because the post-emplacement processes inside the caldera do not modify the buried bulk mass. The distribution area was calculated with the Field Calculator Tool of the Quantum GIS software. For the CFD deposits, we consider the rim-faults traced in the LHVC geologic map from Carrasco-Núñez et al. (2017a) as the structural boundaries of the caldera, while for the OS area the dividing criterion was primarily the actual topographic setting and the deposit thickness.

An important factor in estimating the OS total volume and erupted mass is the thickness reduction due to erosion. Consequently, the eroded bulk was calculated on the observed deposits by interpolating a hypothetical surface that represents the original height of the deposit (Fig. 6). This surface was constructed by using the contour altitude values of the observed deposits polygons, which allowed us to determinate the eroded thickness for each pixel by subtracting the DEM altitude from the plane altitude. Subsequently, the total thickness was calculated by adding the eroded thickness values with the non-eroded thickness measured during fieldwork. Finally, this information was used to estimate the mean thickness in each sector, and thus to calculate its corresponding volume. For the CFD the mean thickness values, and therefore, the inflated volume was calculated by using the lithostratigraphic information from 13 well logs from the geothermal field (Carrasco-Núñez et al., 2017b; Fernández-Maya, 2017; Huerta-Luna, 2018; Jáquez-Domínguez, 2018; Peña-Rodrigez, 2018). In the proximal sector, the thickness was determined with the information of five hydrologic-wells located ~12 km SE from the caldera rim, ranging from 50 to 150 m deep (Table 1). Another correction factor is related to the lithic content. This value was calculated from petrographic analyses in the case of the consolidated samples and sieved component counting for the non-consolidated material. A mean 8% of the lithic volume was derived from both analyses (see Supplementary data).

The DRE volume was calculated by using the average density of each welding grade lithofacies measured from the laboratory analysis (Appendix A). For the CFD, the average density resulted in 2200 kg/m^3, while for the OS in the non-to-moderately and highly-welded grade resulted in 1700 and 2200 kg/m^3, respectively. Subsequently, we calculated an average magmatic density of 2, 350 kg/m^3 for the erupted mass, which is in the range of reported values elsewhere (Folkes et al., 2011; Mason et al., 2004).

4. Results

4.1. Stratigraphy

The Xáltipan ignimbrite is composed of two flow units separated by a pumice fallout layer and a basal pumice fallout. These units are referred from base to top as basal pumice fallout (BPF), lower flow unit (LFU), intermediate pumice fallout (IPF), and upper flow unit (UFU). These units in the Southeastern and Western zones are shown along the stratotype sections (Fig. 7) and in the form of composite stratigraphic columns (Fig. 8). Each reference section represents a different topographic domain where the PDCs were emplaced. A detailed description of the recognized units and characteristic lithofacies is presented below, following Branney and Kokelaar (2002) classification scheme.

This basal layer (BPF) is described in localities 1 and 2 (see Fig. 4a for location). It is composed of a 50 cm-thick, well-sorted, clast-supported, massive rhyolitic pumice lapilli (mpL) layer. It is composed of fresh aphyric, white to light-brown, angular pumice lapilli with maximum clast size of 5 cm, mafic lithics (scoria and non-vesiculated mafic lavas) and black obsidian (logs 1 and 2 in Fig. 7a). The distribution of the BPF is restricted to the proximal areas of the southeastern sector of the caldera. In the nearest locality 1, layer BPF is overlying a volcanic sequence made of spatter-type scoria agglomerate (mscAg) and a

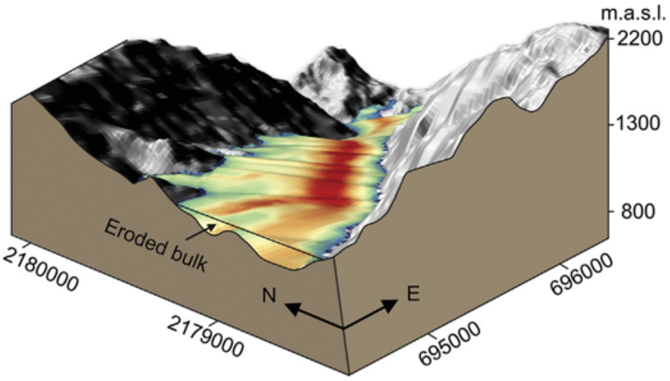

Fig. 6. Three-dimensional projection of a portion of Las Minas' valley, showing the actual surface (grey-scale) and the hypothetical surface of observed deposit (color scale), see location in Fig. 2a. Colors indicate the height difference between the hypothetical surface and the actual ground elevation (red - higher, blue - shallower). Note that the eroded material is concentrated in the center of the valley and thins towards the valley walls.

Table 1
Thickness values measured from log-well information in the intra-caldera geothermal field and hydrologic wells in the outflows.

	Well	X	Y	Thickness (m)
Intracaldera geothermal field well-logs	H-20	663330	2177486	90
	H-8	661582	2176392	110
	H-5	660540	2175950	140
	H-10	662081	2176381	140
	H-19	662881	2176643	150
	H-50	663536	2173024	150
	H-25	666396	2176169	200
	H-42	663320	2173500	200
	H-55	663314	2177721	310
	H-43	661240	2178060	350
	H-26	663133	2175459	400
	H-63	661155	2178053	675
	H-59	661574	2178239	880
Water wells	VP1	677830	2162837	50
	S1	680161	2167233	140
	S2	679486	2167700	151
	S3	680545	2169086	106
	S4	680969	2168133	142

Coordinates in UTM WGS84 system (zone 14Q).

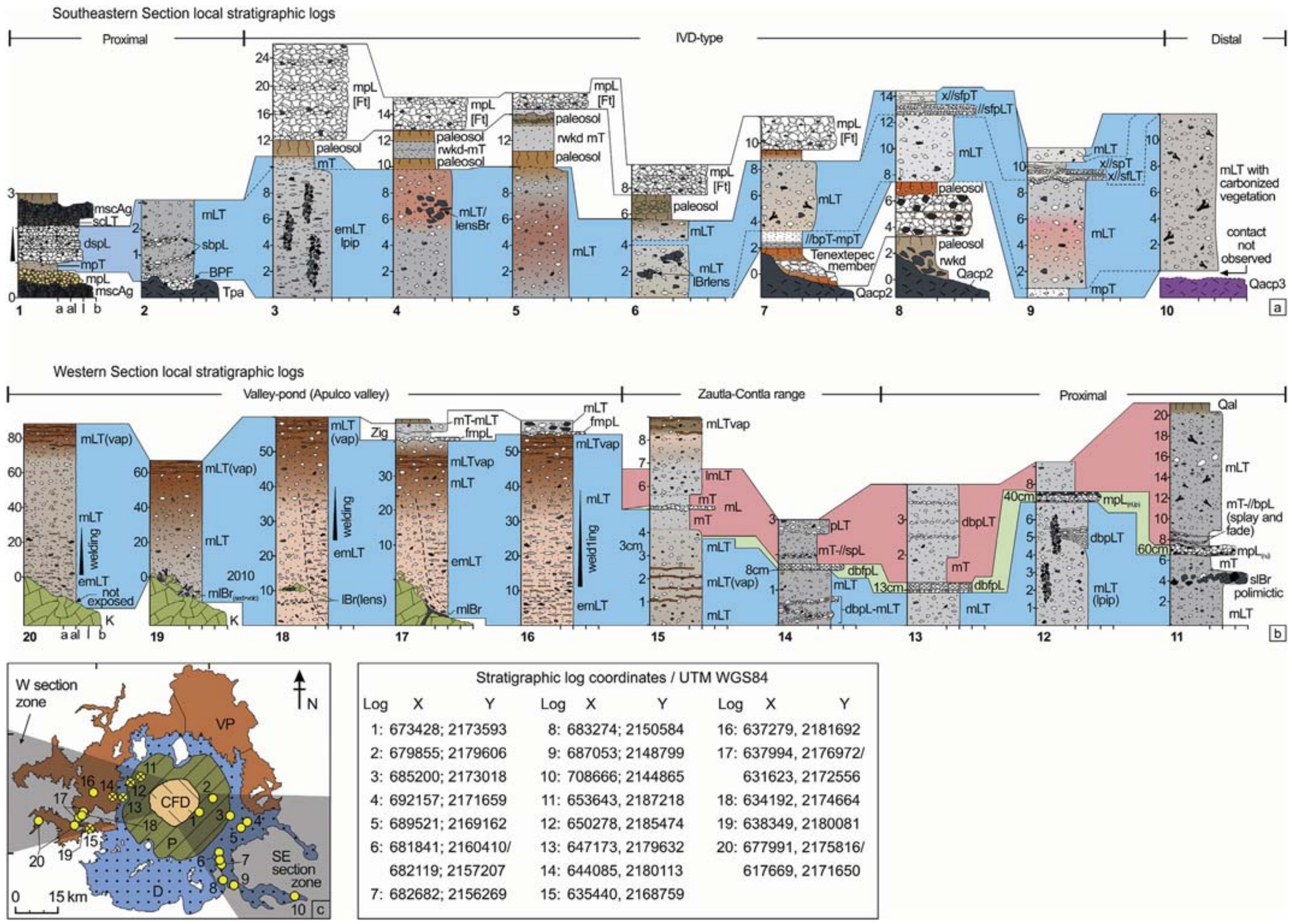

Stratigraphic log coordinates / UTM WGS84

Log	X	Y	Log	X	Y	Log	X	Y
1:	673428;	2173593	8:	683274;	2150584	16:	637279,	2181692
2:	679855;	2179606	9:	687053;	2148799	17:	637994,	2176972/
3:	685200;	2173018	10:	708666;	2144865		631623,	2172556
4:	692157;	2171659	11:	653643,	2187218	18:	634192,	2174664
5:	689521;	2169162	12:	650278,	2185474	19:	638349,	2180081
6:	681841;	2160410/	13:	647173,	2179632	20:	677991,	2175816/
	682119;	2157207	14:	644085,	2180113		617669,	2171650
7:	682682;	2156269	15:	635440,	2168759			

Fig. 7. Correlation of the selected stratigraphic logs of the Xáltipan ignimbrite. a) Southern logs are showing the basal pumice fallout (BPF) and the lower flow unit (LFU – blue); b) Western logs show the correlation of two flow units and an intercalated fallout deposit are correlated (LFU - blue, IPF, green, UFU - pink). Lithofacies nomenclature [adopted from Branney and Kokelaar, 2002]. c) Sketch of the distribution map showing the localities where the stratigraphic logs were described. UTM coordinates of the localities.

fallout layer of light brown mpL. Here, the contact between the BPF and the volcanic sequence is bounded by a 5-cm thick massive pumice tuff (mpT) with subordinate obsidian and volcanic lithic clasts interpreted as a surge-like deposit. Upwards, the BPF discordantly overlies a volcanic sequence made of spatter-type mscAg and mafic mpL fallout layers. In locality 2, the UPF directly overlies the andesitic lavas belonging to the Teziutlán formation in a discordant contact, while the contact between the BPF with the LFU is marked by a sharp and uneven surface. In both localities, the Xáltipan ignimbrite-related deposits underlie the mpL fallout sequence of the Faby tuff.

The LFU is the most widespread and voluminous unit of the ignimbrite. In general, it is composed of a poorly sorted, massive lapilli tuff (mLT), with shard-rich pumice, obsidian, and lithic clasts within the ashy matrix. The deposits show strong variations in thickness (0–180 m) and welding (rank I–V), being highly welded in the center of the valleys, and non-welded near the base contact. In topographic highs and valley flanks, the LFU is in unconformable contact with the volcanic and sedimentary basement. In the valley flanks, the basal contact is characterized by <2-m thick, matrix-supported, massive lithic breccia (mlBr) layers composed of local clasts. The main body of the ignimbrite presents important component and welding variations in the mLT lithofacies, as well as argillic alteration horizons that develop the characteristic pink to orange colour and sub-horizontal indurated alteration veins. The top of this unit is scarcely observed because it is mostly eroded. Nevertheless, in the proximal western localities (11 and 15; see Fig. 7), the upper contact is observed with the overlying IPF. Here, the top of the LFU presents a 1.5 m thick mT, which is in concordant contact with the overlying unit IPF.

The IPF unit is exposed on the western side of the LH caldera at localities 11–15, thinning systematically away from the source (60–0 cm). It is composed of a well-sorted, clast-supported, massive to diffuse bedded, fine white pumice lapilli (dbfpL to mpL) with subordinated obsidian and lithic clasts. In the proximal localities (11 and 12), it features diffuse inverse to normal grain size grading, and normal lithic and inverse pumice grading ($mpL_{(i,n)}$). Unit IPF is directly overlying the LFU, and underlies the UFU, both in concordant contacts. An inferred distribution of this unit is traced based on the localities where it is exposed (see location in Fig. 4a).

The uppermost UFU is also shown on the western side of LH caldera, in the same localities as the IPF. This flow unit is considerably thinner than LFU (<12 m) and consists of a shard-rich mT. Near the base, it presents component variations such as mLT with subhorizontal parallel beds of pumice-rich lapilli (//bpL) with splay-and-fade structures, centimeter-scale vertical lithic-rich elutriation pipes (mLT-pip), and carbonized vegetation. In all the localities where this unit was described, no upper contact with other units were observed.

4.1.1. Southeastern section

The base of the deposit is recorded in the Southeastern section (Fig. 9a), where the BPF and the LFU are exposed over a well-sorted,

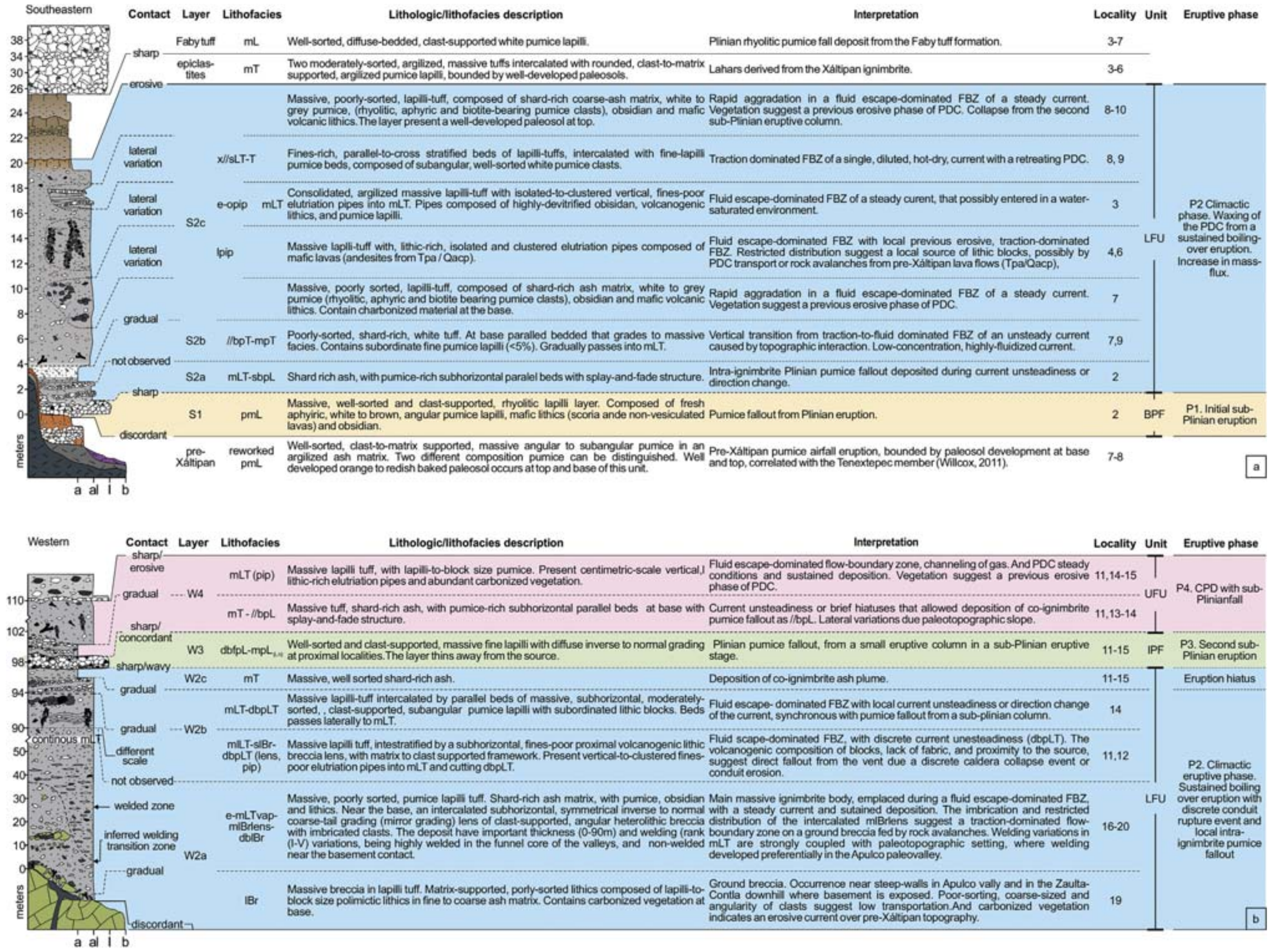

Contact	Layer	Lithofacies	Lithologic/lithofacies description	Interpretation	Locality	Unit	Eruptive phase
	Faby tuff	mL	Well-sorted, diffuse-bedded, clast-supported white pumice lapilli.	Plinian rhyolitic pumice fall deposit from the Faby tuff formation.	3-7		
sharp	epiclas-tites	mT	Two moderately-sorted, argilized, massive tuffs intercalated with rounded, clast-to-matrix supported, argilized pumice lapilli, bounded by well-developed paleosols.	Lahars derived from the Xáltipan ignimbrite.	3-6		
erosive	S2c		Massive, poorly-sorted, lapilli-tuff, composed of shard-rich coarse-ash matrix, white to grey pumice, (rhyolitic, aphyric and biotite-bearing pumice clasts), obsidian and mafic volcanic lithics. The layer present a well-developed paleosol at top.	Rapid aggradation in a fluid escape-dominated FBZ of a steady current. Vegetation suggest a previous erosive phase of PDC. Collapse from the second sub-Plinian eruptive column.	8-10	LFU	P2 Climactic phase. Waxing of the PDC from a sustained boiling-over eruption. Increase in mass-flux.
lateral variation		x//sLT-T	Fines-rich, parallel-to-cross stratified beds of lapilli-tuffs, intercalated with fine-lapilli pumice beds, composed of subangular, well-sorted white pumice clasts.	Traction dominated FBZ of a single, diluted, hot-dry, current with a retreating PDC.	8, 9		
lateral variation		e-opip mLT	Consolidated, argilized massive lapilli-tuff with isolated-to-clustered vertical, fines-poor elutriation pipes into mLT. Pipes composed of highly-devitrified obisidan, volcanogenic lithics, and pumice lapilli.	Fluid escape-dominated FBZ of a steady curent, that possibly entered in a water-saturated environment.	3		
lateral variation		lpip	Massive lapilli-tuff with, lithic-rich, isolated and clustered elutriation pipes composed of mafic lavas (andesites from Tpa / Qacp).	Fluid escape-dominated FBZ with local previous erosive, traction-dominated FBZ. Restricted distribution suggest a local source of lithic blocks, possibly by PDC transport or rock avalanches from pre-Xáltipan lava flows (Tpa/Qacp),	4,6		
			Massive, poorly sorted, lapilli-tuff, composed of shard-rich ash matrix, white to grey pumice (rhyolitic, aphyric and biotite bearing pumice clasts), obsidian and mafic volcanic lithics. Contain charbonized material at the base.	Rapid aggradation in a fluid escape-dominated FBZ of a steady current. Vegetation suggest a previous erosive phase of PDC.	7		
gradual	S2b	//bpT-mpT	Poorly-sorted, shard-rich, white tuff. At base paralled bedded that grades to massive facies. Contains subordinate fine pumice lapilli (<5%). Gradually passes into mLT.	Vertical transition from traction-to-fluid dominated FBZ of an unsteady current caused by topographic interaction. Low-concentration, highly-fluidized current.	7,9		
not observed	S2a	mLT-sbpL	Shard rich ash, with pumice-rich subhorizontal paralel beds with splay-and-fade structure.	Intra-ignimbrite Plinian pumice fallout deposited during current unsteadiness or direction change.	2		
sharp	S1	pmL	Massive, well-sorted and clast-supported, rhyolitic lapilli layer. Composed of fresh aphyiric, white to brown, angular pumice lapilli, mafic lithics (scoria ande non-vesiculated lavas) and obsidian.	Pumice fallout from Plinian eruption.	2	BPF	P1. Initial sub-Plinian eruption
discordant	pre-Xáltipan	reworked pmL	Well-sorted, clast-to-matrix supported, massive angular to subangular pumice in an argilized ash matrix. Two different composition pumice can be distinguished. Well developed orange to redish baked paleosol occurs at top and base of this unit.	Pre-Xáltipan pumice airfall eruption, bounded by paleosol development at base and top, correlated with the Tenextepec member (Willcox, 2011).	7-8		

Contact	Layer	Lithofacies	Lithologic/lithofacies description	Interpretation	Locality	Unit	Eruptive phase
sharp/ erosive	W4	mLT (pip)	Massive lapilli tuff, with lapilli-to-block size pumice. Present centimetric-scale vertical,l lithic-rich elutriation pipes and abundant carbonized vegetation.	Fluid escape-dominated flow-boundary zone, channeling of gas. And PDC steady conditions and sustained deposition. Vegetation suggest a previous erosive phase of PDC.	11,14-15	UFU	P4. CPD with sub-Plinianfall
gradual		mT - //bpL	Massive tuff, shard-rich ash, with pumice-rich subhorizontal parallel beds at base with splay-and-fade structure.	Current unsteadiness or brief hiatuses that allowed deposition of co-ignimbrite pumice fallout as //bpL. Lateral variations due paleotopographic slope.	11,13-14		
sharp/ concordant	W3	dbfpL-mpL$_{(i-n)}$	Well-sorted and clast-supported, massive fine lapilli with diffuse inverse to normal grading at proximal localities. The layer thins away from the source.	Plinian pumice fallout, from a small eruptive column in a sub-Plinian eruptive stage.	11-15	IPF	P3. Second sub-Plinian eruption
sharp/wavy	W2c	mT	Massive, well sorted shard-rich ash.	Deposition of co-ignimbrite ash plume.	11-15	LFU	Eruption hiatus
gradual	W2b	mLT-dbpLT	Massive lapilli-tuff intercalated by parallel beds of massive, subhorizontal, moderately-sorted, , clast-supported, subangular pumice lapilli with subordinated lithic blocks. Beds passes laterally to mLT.	Fluid escape- dominated FBZ with local current unsteadiness or direction change of the current, synchronous with pumice fallout from a sub-plinian column.	14		P2. Climactic eruptive phase. Sustained boiling over eruption with discrete conduit rupture event and local intra-ignimbrite pumice fallout
gradual		mlLT-slBr-dbpLT (lens, pip)	Massive lapilli tuff, intestratified by a subhorizontal, fines-poor proximal volcanogenic lithic breccia lens, with matrix to clast supported framework. Present vertical-to-clustered fines-poor elutriation pipes into mLT and cutting dbpLT.	Fluid scape-dominated FBZ, with discrete current unesteadiness (dbpLT). The volcanogenic composition of blocks, lack of fabric, and proximity to the source, suggest direct fallout from the vent due a discrete caldera collapse event or conduit erosion.	11,12		
not observed	W2a	e-mLTvap-mlBrlens-dblBr	Massive, poorly sorted, pumice lapilli tuff. Shard-rich ash matrix, with pumice, obsidian and lithics. Near the base, an intercalated subhorizontal, symmetrical inverse to normal coarse-tail grading (mirror grading) lens of clast-supported, angular heterolithic breccia with imbricated clasts. The deposit have important thickness (0-90m) and welding (rank (I-V) variations, being highly welded in the funnel core of the valleys, and non-welded near the basement contact.	Main massive ignimbrite body, emplaced during a fluid escape-dominated FBZ, with a steady current and sutained deposition. The imbrication and restricted distribution of the intercalated mlBrlens suggest a traction-dominated flow-boundary zone on a ground breccia fed by rock avalanches. Welding variations in mLT are strongly coupled with paleotopographic setting, where welding developed preferentially in the Apulco paleovalley.	16-20		
gradual discordant		lBr	Massive breccia in lapilli tuff. Matrix-supported, porly-sorted lithics composed of lapilli-to-block size polimictic lithics in fine to coarse ash matrix. Contains carbonized vegetation at base.	Ground breccia. Occurrence near steep-walls in Apulco vally and in the Zaulta-Contla downhill where basement is exposed. Poor-sorting, coarse-sized and angularity of clasts suggest low transportation.And carbonized vegetation indicates an erosive current over pre-Xáltipan topography.	19		

Fig. 8. Composite representative lithostratigraphic columns showing a summary of the lithologic description of the identified layers with its type of contact, lithofacies nomenclature [adopted from Branney and Kokelaar, 2002], locality, summarized interpretation of the individual layer, proposed eruptive phases, and flow unit type for Southeastern (a) and Western sections (b).

clast-supported, layer (mpL) (logs 7, 8 in Fig. 7a), previously described as the Tenextepec member (Willcox, 2011) and lava flows from the volcanic basement. At the locality 2 the BPF unit is represented by layer S1 (Figs. 7a and 8a), which is a 1-m thick pmL composed of well-sorted, clast-supported, coarse white pumice lapilli with subordinate fine lapilli volcanic lithics that overlies the Teziutlán andesite lava flows (Tpa), and locally overlies a well-developed brown paleosol. This layer can be correlated with the basal fallout reported in a nearby outcrop by Willcox (2011), judging by their similar lithologic characteristics. In the same locality occurs layer S2a, which represents the basal lithofacies of LFU. This is a 2.3-m thick, poorly sorted, shard-rich mLT layer, with intercalated beds of well-sorted, clast-supported, stratified, white pumice lapilli (sbpL). A coeval unit to layer S2a is exposed ~1.4 km SE from the caldera rim at locality 1, where the base of the ignimbrite is overlaying in sharp and unconformable contact the volcanic basement. In this locality, layer S2a is composed of a cyclic sequence of highly vesiculated mscAg, intercalated with concordant layers of well-sorted, clast-supported, beige and black mpL. Here, the ignimbrite is defined by a thin (11–20 cm), poorly-sorted, mpT, overlaid by a 1 m diffusely stratified pumice-rich lapilli (dspL) fallout layer. The basal tuff is composed of coarse-to-fine, shard-rich ash with subordinate biotite, obsidian, and lithic components. The fallout is composed of three diffuse beds of clast-supported, well-sorted white pumice lapilli layers with subordinated fine-lapilli to coarse-ash obsidian and volcanic lithics with normal grading. At the top of this layer appears a paleosol that, in turn, is overlaid discordantly by a younger sequence of scoria agglomerates with pumice lapilli beds.

A lateral variation of the basal part of the LFU is exposed in the IVD-type localities as layer S2b (logs 3–9 in Fig. 7a). Here, the ignimbrite overlies the CP lava flows and the Tenextepec member (Willcox, 2011). Layer S2b is characterized in the base by a 50–100 cm, well-sorted, shard-rich, white mpT (Fig. 9b). The basal contact of this layer with the CP is observed in log 7, showing at the base a 5-cm thick horizon with parallel bedding structures that grades upwards to a massive tuff (//bpT-mpT). This layer is also observed in log 9 (Fig. 7a), although the basal contact is not observed.

Layer S2b grades upwards into layer S2c, which is the LFU main layer (logs 3–10 in Fig. 7a). This layer is a >15-m thick, mLT composed of a poorly sorted, massive, grey (fresh) to pink (weathered) shard-rich ash matrix, with white-to-grey, fine to coarse pumice lapilli (aphyric and biotite bearing), obsidian and mafic volcanic lithics (Fig. 9c). Three lateral lithofacies variations of layer S2b are identified at different stratigraphic levels. Near the base at logs 4 and 6, layer S2b exhibits coarse-rich facies in the form of isolated and clustered-elutriation pipes composed of mafic lavas (lpip-mLT) (Fig. 9d). An incipiently welded mLT features the middle part of log 3, with abundant isolated and clustered vertical elutriation pipes (opip-emLT) composed of black and black-and-green mingled, highly-devitrified obsidian, and mafic volcanic lithics (Fig. 9e, f). Near the top, at logs 8 and 9, it presents a zone with intercalated fines-rich beds in the form of cross-to-parallel stratified lapilli tuff (x//sfLT) into the mLT (Fig. 9g). A well-developed paleosol marks the upper contact of the ignimbrite with the post-Xáltipan epiclastic units and with the younger pumicitic air-fall layers derived from the Faby tuff.

4.1.2. Western section

The Western section is divided into three domains with different topographic features (Fig. 7b): 1) Proximal, where the ignimbrite was emplaced mainly over the volcanic basement (localities 11–13); 2) Zautla-Contla range, where the ignimbrite surmounted and emplaced over the steep slope of the highly folded sedimentary basement (locality l4); and 3) Valley-pond, where the ignimbrite confined

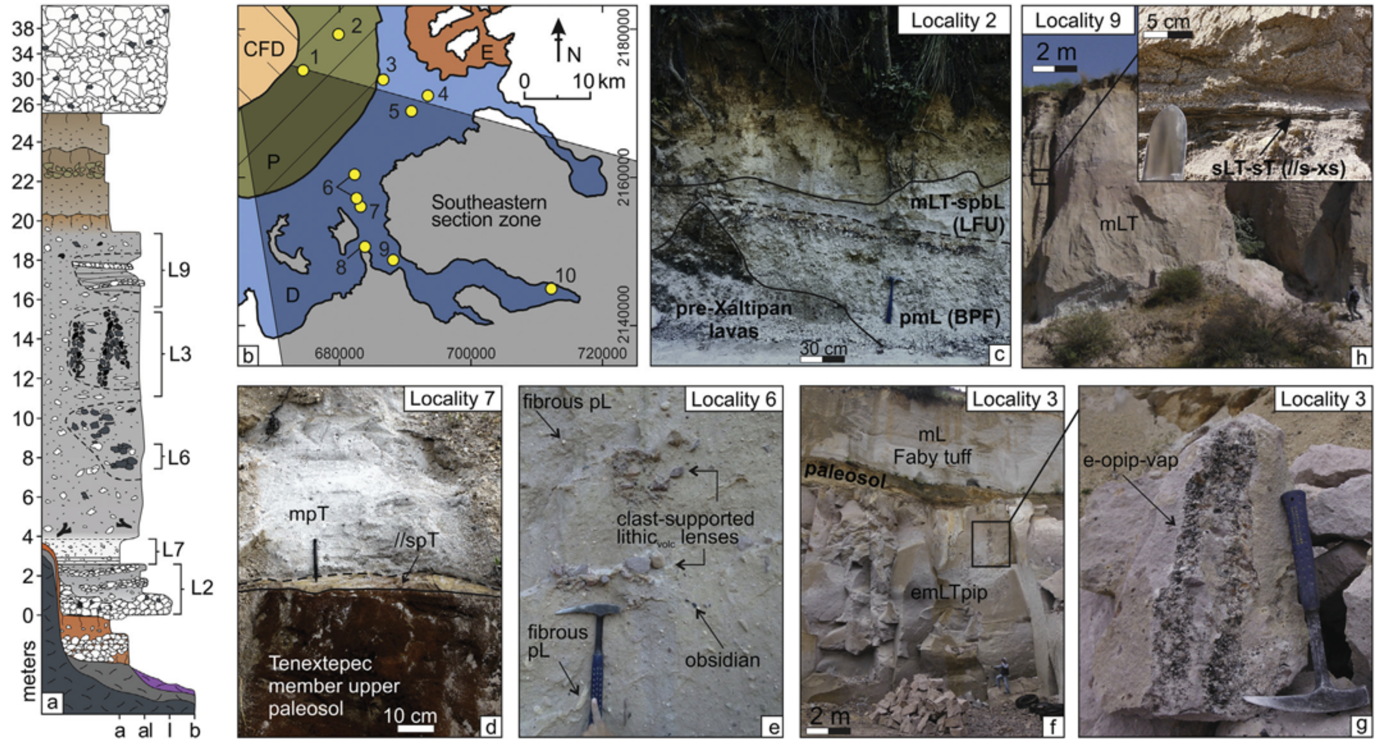

Fig. 9. Photographs of the Southeastern section zone at different stratigraphic levels. a) The stratigraphic column showing the approximate location of the photographs. b) Simplified map of the Southeastern section showing the localities with stratigraphic descriptions. c) Basal pumice fallout (BFP) over the andesite lava flows from the volcanic basement. Upwards turns into the lowermost PDC emplacement deposit from the lower flow unit (LFU) as mLT with intercalated intra-ignimbrite fallout deposits from (BPF). d) Contact of Tenextepec member with the base of the LFU in //spT facies which grades upwards into a mpT. e) Intra mLT lithic facies in the form of lithic lenses and isolated pods. f–g) Moderately welded lithofacies with vapor phase alteration and high development of obsidian-rich vertical and clustered elutriation pipes. h) Body of the LFU in a mLT lithofacies. Note the zoned alteration zone (pink) in the middle part of the deposit, and the sedimentary structures near the top of the ignimbrite body. See the zoom photo showing the layered structures intercalated into the dominating mLT facies.

into the Apulco valley (localities 15–20). Here, the stratigraphy records the LFU and UFU, separated by the IPF layer (Fig. 10a). The LFU is exposed through all the Western section, showing considerable thickness (~80 m) and welding variations, which are mainly controlled by the paleotopography. In contrast, the IPF and UFU are considerably smaller deposits restricted to the Proximal and Zautla-Contla range domains. A rough distribution area is proposed for the IPF and UFU based on the localities where they were identified (Fig. 10b).

The voluminous layer W2a represents the lowermost part of LFU (Fig. 10c). This layer is a very thick (>90 m) mLT that shows notable welding variations, being non-welded near the valley walls and near the top of the deposit, and moderately to highly welded towards the valley center. Near to the base (logs 17 and 19 in Fig. 7b), is a 3-m thick, matrix-supported, mlBr, layer composed of poorly sorted, subangular, lapilli-to-block sedimentary and volcanic clasts, accompanied with scarce carbonized vegetation fragments (Fig. 10d). Intercalated with W2a, occurs a sub-horizontal, symmetrical, inverse-to-normal coarse tail grading (mirror grading), moderately-sorted, clast-supported, heterolithic breccia lens (lBrlrens) showing angular and imbricated clasts (log18 in Fig. 7) (Fig. 10e).

The upper portion of the LFU (W2b) is observed at the proximal localities (logs 11–15, Fig. 7b). Even though this portion shows lateral lithofacies variations, its position is known due to its stratigraphic relation with the overlaying IPF unit. In the most proximal locality (log 11), W2b shows a mLT with an intercalated layer of volcanogenic lithic breccia (slBr) that shows a lateral variation from matrix-to-clast supported (Fig. 10f). The slBr is composed mainly of black and mingled (brown and black) obsidian blocks (>35 cm), and fresh aphyric rhyolite and andesite angular blocks (>45 cm). In a nearby outcrop (log 12), W2b lithofacies are characterized by a mLT with abundant vertical and clustered, fines-poor, elutriation pipes that cut local diffuse bedded pumice lapilli-tuff horizons (mLTlpip-dbpLT) (Fig. 10g). At a more distant outcrop (log 14), W2b layer is defined by a mLT lithofacies with intercalated, sub-horizontal, laterally discontinuous, well-sorted, sub-angular, diffuse-bedded, pumice lapilli layer that laterally passes to mLT (dbpL-mLT) (Fig. 10h). This facies layer transitionally turns into the uppermost part of LFU (logs 11 and 15) defined by an 80 cm thick, well-sorted, shard-rich, mT composed of matrix-supported fine-pumice lapilli, obsidian, and lithics (Fig. 10i). Concordantly overlaying the LFU is the IPF unit. This unit is a well-sorted, clast-supported, pumice lapilli mainly massive (mpL) near the source (logs 11 and 12) and diffusely bedded (dbfpL) at distant localities (logs 12–15) (Fig. 10 g–i). It exhibits inverse-to-normal grain size grading, and normal and inverse grading of lithics and pumice, respectively (Fig. 10g). The layer presents a systematic thinning away from Los Humeros caldera, ranging from 60 to 3 cm (logs 11 to 15).

Concordantly overlying IPF outcrops the upper flow unit (UPF) (logs 11–15). The lower portion of UFU occurs as a mT with intercalated horizontal //bpL, and with lateral thickness variations (8–0 cm) passing *via* splay-and-fade into mLT (Fig. 10j). This lithofacies gradually turns upwards to a <10 m thick mLT layer (logs 11, 15), with local batches of abundant carbonized vegetation (Fig. 10k). This layer is the uppermost

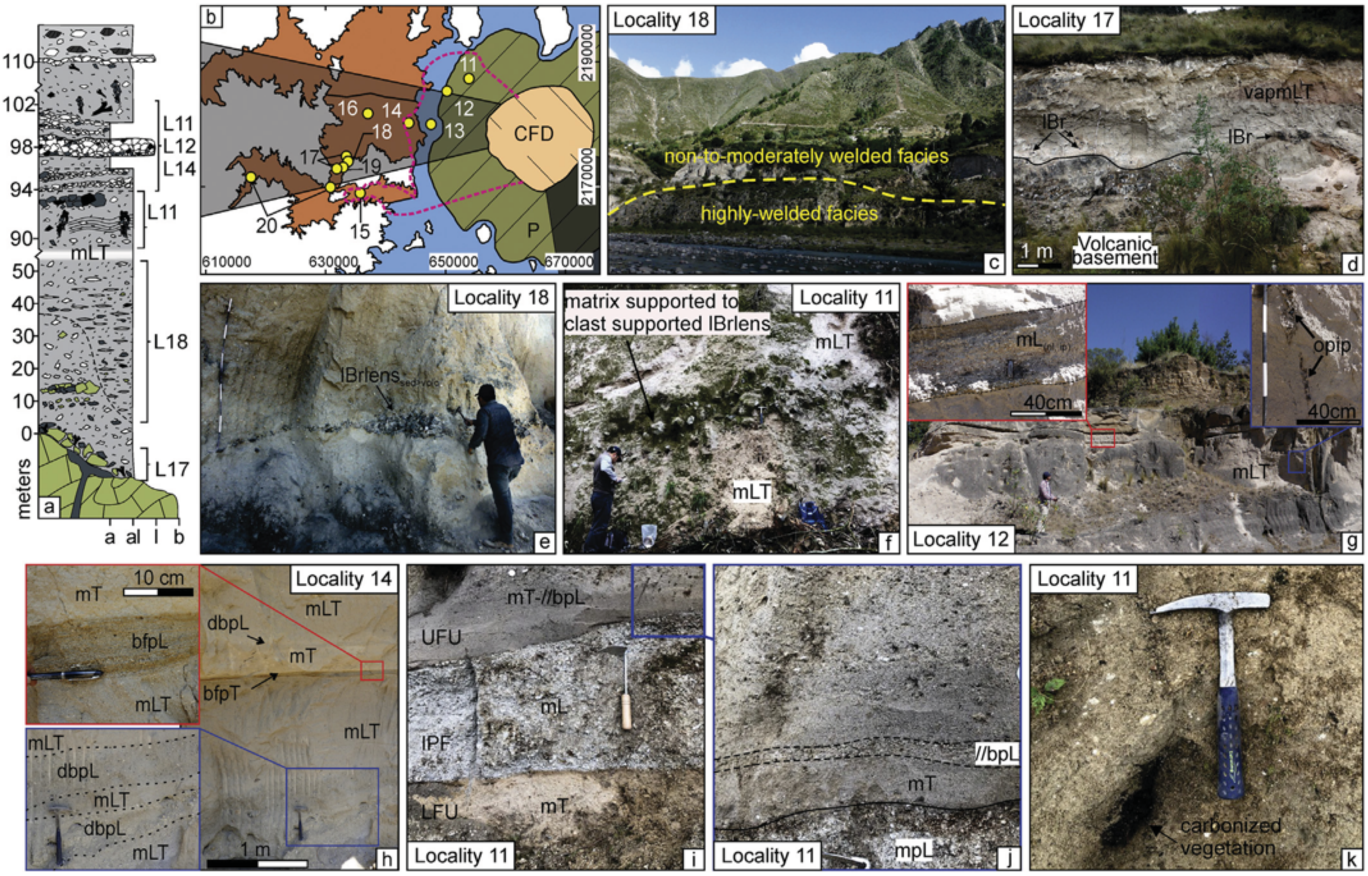

Fig. 10. Photographs of the Western section zone at different stratigraphic levels. a) The stratigraphic column is showing the approximate location of the photographs. b) Simplified map of the Western section showing the localities with stratigraphic descriptions. c) Ignimbrite exposure in the Apulco valley showing the characteristic vertical welding variations. The deposit has a minimum thickness of 60 m. d) Contact of the ignimbrite over the sedimentary basement, showing the lithic breccia clasts embedded into the mLT. e) mLT facies and the intercalated lBrlens of the lower flow unit LFU. f) lBrlens facies intercalated near the top of LFU. g) Lower and upper flow units separated by the upper pumice fallout unit, inset show the characteristic fines-poor elutriation pipes. h) Vertical lithofacies variations in the upper portion of LFU. i–j) Contact of the upper pumice fallout unit and the flow units in locality 11, at the base UFU shows //spL with splay and fade structure. k) Fragment of carbonized vegetation in the upper flow unit (UFU).

of the Xáltipan ignimbrite identified in the western sector. Although the upper contact is not observed, the angular unconformity with the Zaragoza ignimbrite at logs 16 and 17 (Fig. 7) suggests the direct deposition of this unit over Xáltipan ignimbrite. Here, the Zaragoza ignimbrite shows at the base a laterally continuous, well-sorted, clast-supported, fine pumice lapilli, related with the lower pumice fall layer, overlaid by a massive layer of two-composition pumice lapilli, which can be correlated with the main Zaragoza ignimbrite body (Carrasco-Núñez and Branney, 2005).

4.2. Distribution map and geologic sections

Preliminary geologic mapping suggested that the Xáltipan ignimbrite has a more extensive distribution than previously reported, and therefore it needed to be reevaluated. Outside the caldera, the ignimbrite outflows are widely exposed, while the intra-caldera deposits are entirely buried by younger volcanic units. Nevertheless, multiple analysis from well-log samples of the active geothermal field of Los Humeros provides an excellent thickness control of the unit within the caldera, showing a very variable thickness ranging from 90 to 880 m (Table 1) (Carrasco-Núñez et al., 2017b; Fernández-Maya, 2017; Huerta-Luna, 2018; Jáquez-Domínguez, 2018; Peña-Rodrigez, 2018). Although the well-samples show some degree of hydrothermal alteration and are obtained in the form of small chips, we can still recognize features of the original deposit. Outside the caldera, the OS shows a radially to channelized distribution along contrasting topographic conditions, with runout distances exceeding 55 km from the rim (Fig. 4a). In the Proximal and Distal sectors, the ignimbrite is scarcely exposed because it is buried by younger deposits or because it is highly eroded. In these sectors, the ignimbrite partially outcrops in the order of ones to tens of meters, not showing its basal contact. On the other hand, at the valleys, the ignimbrite is better exposed, showing its basal contact and welding variations in the form of terraces with steep walls of >150 m thick.

4.2.1. Energy lines

The distribution map shows two main areas: the *inferred deposits* area, which resembles the distribution of the ignimbrite before erosion and burial, and the *observed deposits*, which exhibit the observed ignimbrite over the surface (Fig. 4a). The inferred deposits area shows a combined landform that goes from radially-shaped in the proximal parts to valley-fill-shaped at the distal sectors. In general, the energy lines used to construct the inferred deposits area present a consistent geometry (Fig. 11, Table 2). These energy lines have minimum slopes that range from 0.9 to 3.6° and small heights when intersected with the caldera rim ranging from 0 to 395 m. An exception occurs in the SE-E zone (profiles a-a′, b-b′ and c-c′, in Fig. 11), where the slope range increases to 4–6.-5° and an intersection height between 1900 and 3500 m. In particular, the energy lines to the SE shows a maximum linear runout distance of >40 km in open terrain, indicating that the PDC surmounted a 510 m barrier formed by the CP lava flows. In the NE-N-NW zone (profiles d-d′, e-e′, f-f′, and g-g′), the PDC descended into a topographic depression with a 3.3° a slope. Here, the projections suggest a low eruptive column collapse height lower than 395 m. Furthermore, section j-j′ shows a significant topographic barrier that impeded the pyroclastic cloud continuity straight north, which in turn channelized it to the west and east to the more extended k-k′ and i-i′ sections. The W zone (profile h-h′, i-i′, and j-j′ in Fig. 11) show a smoother slope of 0.5–0.9°, with projected lines suggesting collapse-height lower than 161 m. Also, it reveals the largest linear runout distance with 51 km from the caldera rim (section l-l′ in Fig. 11). Zones SW-S (sections k-k′, l-l′ in Fig. 11) also shows distinctive low-slope energy lines (0.9°) that intersects with the actual caldera-rim altitude, having a maximum runout distance of ~35 km. The highly-welded lithofacies are mainly concentrated at the valley-pond and proximal sectors, while they are practically absent in the distal sector. Nevertheless, the absence of welded deposits in this area could be due to burial effects.

4.2.2. Geologic sections

Geologic section a-a′ (Fig. 12a) is 59 km long and runs from the southeastern caldera rim, passing through the water wells, the CP volcano, reaching up to the furthest observed deposit near Teocelo town. This section indicates that the PDCs traveled at least 48.5 km, surmounting the CP lava flows, as previously reported by Ferriz and Mahood (1984). The section can be divided into three topographic domains (Fig. 12a): 1) Proximal, including the localities where the ignimbrite emplaced over the volcanic basement (logs 1 and 2); 2) IVD-type, where the ignimbrite emplaced as non-consolidated lithofacies and surmounted the CP lava flows (logs 3–9); and 3) Distal, where the ignimbrite emplaced over the CP eastern flank. In the proximal part of the section, the topography is relatively flat, and the ignimbrite is scarcely exposed in local quarries because it is mainly covered by younger units. In this area, five water-well logs were used to estimate its thickness, ranging from 50 to 151 m (Table 1, Fig. 4a). At the Distal facies (>30 km), the topography is marked by a steep ramp of the CP eastern flank.

The 30 km-long geologic section c-c′ is projected to the east, where the ignimbrite emplaced over two different paleotopographic settings (Fig. 12b). In the proximal area, the ignimbrite deposited over the volcanic basement (0 to 20 km) and is mostly buried by younger units and scarcely exposed in local paleochannels as at the type locality near the Xáltipan town and near Mixquiapan where the thicknesses reach up to 60 m. In the last place, the ignimbrite directly overlies the Teziutlán andesite. Over Las Minas' range, there are no outcrops of the ignimbrite, while at the distal facies (>20 km), the PDC channelized into Las Minas' valley as valley-pond fills, reaching a linear runout of 26 km. Here, the ignimbrite rests discordantly over sedimentary Mesozoic limestones and shales and locally on Tertiary granite intrusions.

The geologic g-g′ section is 41 km-long and projected to the northwest (Fig. 12c). In proximal facies (<20 km), the pre-Xáltipan topography displays a relatively flat surface possibly controlled by the pre-caldera Tezitulán andesitic flows, which in turn emplaced over an uneven Mesozoic sedimentary basement (K/J). These contacts are not directly observed but inferred by the subsurface stratigraphy from the geothermal wells inside the Los Humeros caldera (Carrasco-Núñez et al., 2017b). In distal facies, the ignimbrite emplaced in valley-pond conditions over a highly uneven terrain controlled by the Mesozoic basement, forming isolated patches divided by topographic highs. The furthest exposed outcrop is located near Zapotitlán City, indicating a 39 km linear runout distance.

The western area is represented by the 49 km-long section i-i′ (Fig. 12d), which displays two topographic domains; a relatively flat terrain in the proximal sector (0 to 12 km), and a Valley-pond type in the Distal sector (12 to 50 km) corresponding to the Apulco valley. These domains are bounded by a 400-m topographic high at ~12 km, from the exhumed sedimentary basement. The furthest outcrop to the west of the caldera is exposed near the Ixtacamaxtitlán locality, suggesting a 41 km linear runout distance of the ignimbrite. In this sector, the exposed ignimbrite is 80 m thick and has an inferred thickness of 50 m.

4.3. Ignimbrite volume and erupted mass

The observed and inferred deposits of the ignimbrite were measured individually. Nevertheless, in this work, we consider that the inferred deposits accurately represent a minimum estimation of the original ignimbrite size, since they are constructed directly from the observed deposits (Fig. 13 and Table 3). A total inferred area of 4620 km^2 was calculated. From this, 222 km^2 correspond to the CFD of Los Humeros caldera, and 4398 km^2 to the OS inferred deposits. For the CFD, a mean thickness of 290 m was calculated from well-logs (Table 1), resulting in an inflated volume of 64.4 km^3. Thickness values for the observed and inferred deposits in each OS sector were considered. In the proximal sector, thickness ranges from 70 m, as reported in the Xáltipan quarry, up to a mean thickness of 135 m calculated from the water wells

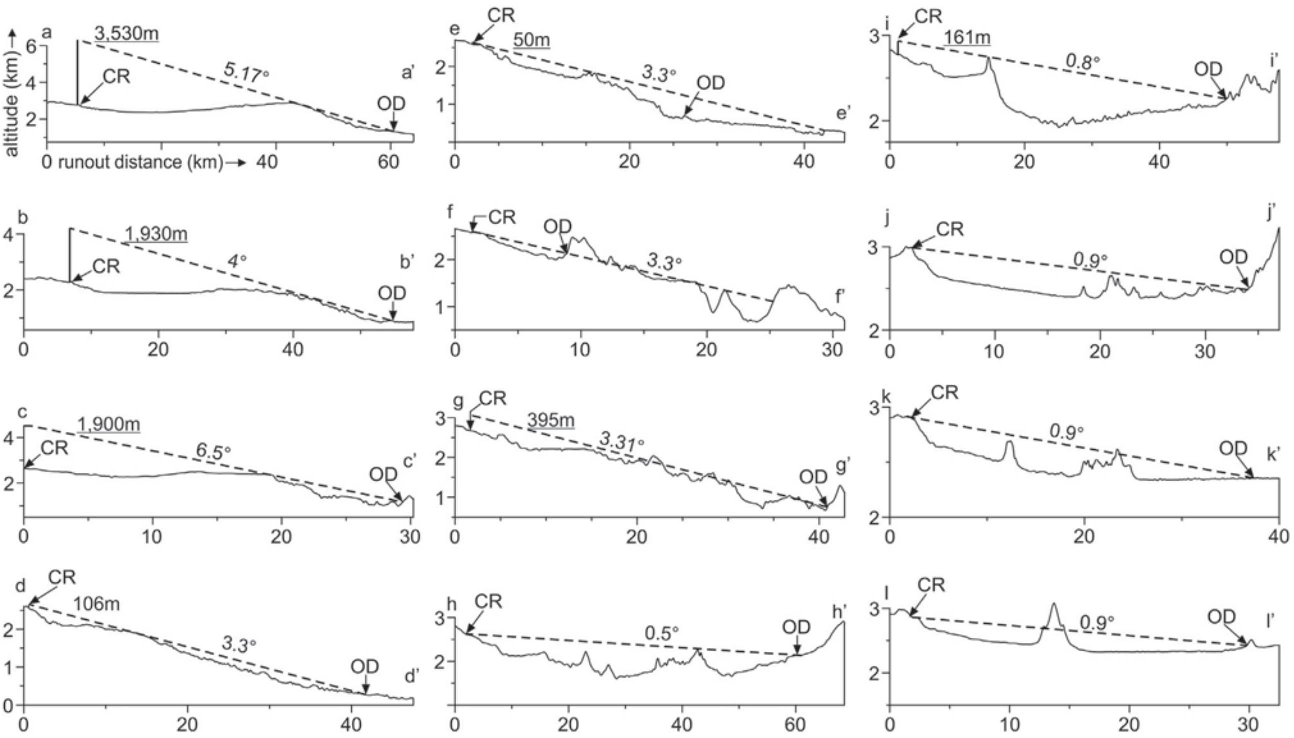

Fig. 11. Energy line profiles, indicating furthest observed deposit (OD), slope, runout distance, and intersection height with the caldera rim (CR). Vertical and lateral scale in kilometers. The traces of the energy lines are shown in Fig. 2a.

S1-S4. In the Distal sector, the observed deposits represent a minimum measured thickness of 40 m, and a mean thickness of 75 m is considered for the inferred deposits. This last value is obtained by examining a linear thinning of the deposit and by using a maximum thickness of 151 m measured in well S2. In the Valley-pond sectors, the thickness increases abruptly. This increase is observed in the E sector representing the thickest, highly-welded, lava-like, ignimbrite deposits with a mean measured thickness of 180 m. Here, the ignimbrite shows spectacular columnar joints exposed by erosion at the valley centers (Fig. 14). Away from the valley's centers, a 60 m inferred mean thickness is considered. The NE sector shows a measured thickness of 80 m as measured in the Tlapacoyan valley, while an inferred thickness of 50 m is estimated for the rest of the sector. The NW sector is the largest valley-pond sector, presenting highly-welded ignimbrite exposures of >160 m. Here, the thickness of the inferred deposits is calculated at a mean value of 60 m. The W sector is defined by the Apulco hydrologic system, where 80-m-thick ignimbrite's walls were measured. The inferred deposits are calculated with a mean thickness of 50 m. An uncompacted-rock volume of 344 km^3 was calculated using these thickness values. For the DRE, a density and lithic content correction were applied. The density correction was made by using the mean density calculated for each welding lithofacies, which are non-to-moderately (1700 kg/m^3) and highly-welded (2200 kg/m^3), and a theoretical average solid rock density of 2350 kg/m^3 (Appendix A). For the lithic content correction, we used the calculated 8% mean volume measured in the laboratory experiments. The DRE volume resulted in a total of 291 km^3 (*ca.* 290 km^3), corresponding 59 km^3 to the CFD, and 231 km^3 to the OS. Finally, the total erupted mass is computed in 1.1 × 10^{12} kg, where 1.3 × 10^{11} kg corresponds to the CFD deposits and 9.8 × 10^{11} kg to the OS.

Table 2
Synthesis of the energy lines geometries divided by sectors. Each sector presents a particular slope, column collapse, and linear runout distance range.

Zones	Profiles	Slope	CR intersection height (m)	Lineal runout (m)
SE, E	a-a′, b-b′, c-c′	4–6.5°	1900–3530	55,250
NE, N, NW	d-d′, e-e′, f-f′, g-g′	3.3–3.6°	0–395	41,050
W	h-h′, i-i′, j-j′	0.5–0.9°	0–161	59,240
SW-S	k-k′, l-l′	0.9°	0	35,670

5. Discussion

5.1. Pre-Xáltipan landscape and ignimbrite assemble

The proximal sector is characterized by a relatively flat topography and scarce outcrops of the Xáltipan ignimbrite restricted to material quarries and water-well logs. In this sector, the Xáltipan ignimbrite settled over a thick and irregular lava flow field dominated by the Teziutlán andesite (Tpa) and by several isolated rhyolitic domes, the last being particularly exposed in the western rim of LH caldera. Nevertheless, the significant thickness variations ranging from 151 m (water well S2) to a few-meters suggest that the ignimbrite filled a highly irregular surface, smoothing the terrain, and leading to a radially-shaped distribution.

Further away from the proximal sector, the ignimbrite shows a channelized-like distribution instead. To the southeastern, the PDC passed over the slopes of CP and emplaced until 47 to 51 km away in linear runout near Xalapa city and Teocelo town (see location in Fig. 4a), for which the flow required to surmount up to 510 m high as proposed by Ferriz and Mahood (1984) (Fig. 12a). Nevertheless, the energy lines of these sections showed an anomalous high-slope concerning the general low-slope in the rest of the sections. Here, it is interpreted that the pyroclastic flow had a highly-fluidized behavior that allowed the surmounting and latter inertial-driven current transport (Giordano and Doronzo, 2017).

In the distal northern hemisphere, the ignimbrite emplaced into the highly deformed Mesozoic sedimentary basement as a valley-pond type ignimbrite. Here, the ignimbrite confined into the valleys and surrounded the topographic highs revealing the irregular pre-eruption

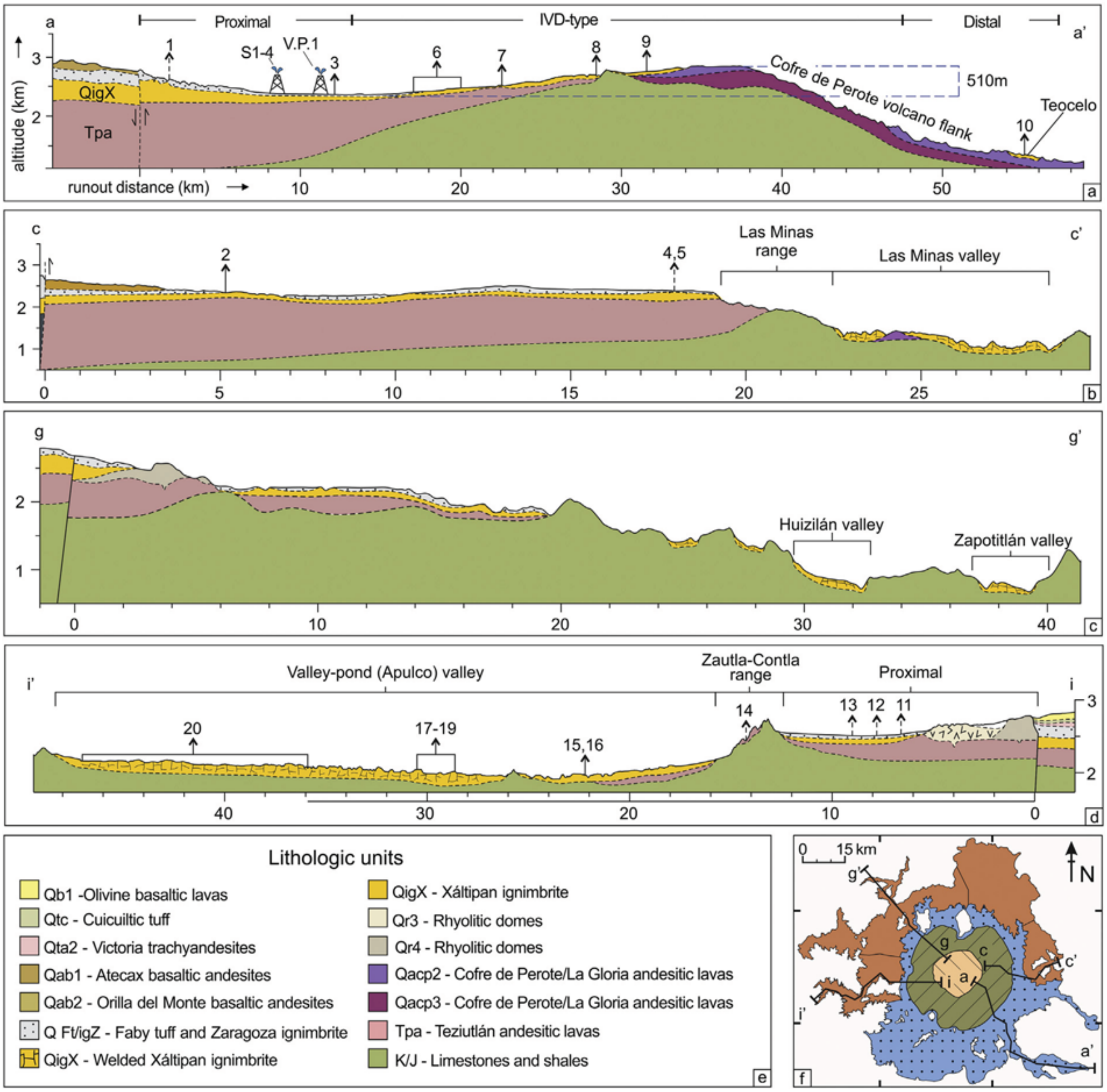

Fig. 12. a–d) Selected geologic sections showing the lateral ignimbrite distribution over the pre-volcanic and volcanic basement. Arrows indicate the accurate (solid) and approximate (dashed) location of water wells and localities with stratigraphic descriptions. e) Sketch of the distribution map showing the trace of the geologic sections. Legend for the lithologic units as proposed by Carrasco-Núñez et al., 2017a).

configuration. This is well exposed at Las Minas' locality, where the ignimbrite shows a 180 m thick wall measured in the center of the valley, thinning systematically through the valley flanks of the sedimentary basement. Nevertheless, in this valley, the ignimbrite shows a relatively low runout distance (25–30 km), probably because the PDC flowed over a meandered channel system, leading to a preferential lateral filling and

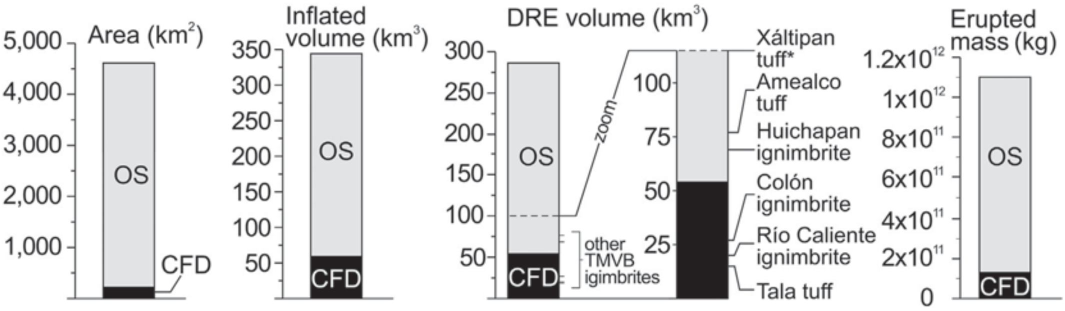

Fig. 13. Bar graphs showing the area, volume (inflated and DRE), and erupted mass of the Xáltipan ignimbrite in the Caldera-fill deposits (CFD), and Outflow sheets (OS) environments. The data is based on the inferred deposits, which represent the most accurate estimation. Note the comparison of the DRE volume with other important ignimbrites of the TMVB and the previously reported for the Xáltipan tuff by Ferriz and Mahood, 1994 (*).

Table 3
Computed calculations of the area, volume, and erupted mass of the Xáltipan ignimbrite.

Sectors		Caldera-fill deposits (CFD)	Outflow sheets (OS) sectors												Observed deposits	Inferred deposits
			Proximal (P)		Distal (D)		Valley-pond (VP)									
							Eastern (E)		Northeast (NE)		Northwest (NW)		Western (W)			
Welding rank		V–VI	I–IV	V–VI	I–IV	V–VI	I–IV	V–VI	I–IV	V–VI	I–IV	V–VI	I–IV	V–VI	–	–
Mean density (gr/cm^3)		2200	1700	2200	1700	2200	1700	2200	1700	2200	1700	2200	1700	2200	–	–
Mean thickness (m)	Obs	290	70		75		180		80		160		80		–	–
	Inf		135		40		60		50		60		50		–	–
Area (km^2)	Obs	222	12	1	77	1	21	11	46	3	136	15	63	15	625	4620
	Inf		1132		1531		205		615		625		290			
Inflated volume (km^3)	Obs	59.2	0.8	0.1	5.3	0.1	3.5	1.9	3.4	0.2	20.0	2.2	4.7	1.1	102	344
	Inf		140.6		56.3		11.3		28.3		34.5		13.3			
DRE volume (km^3)	Obs	55.4	0.6	0.1	3.8	0.1	2.5	1.8	2.5	0.2	14.5	2.0	3.4	1.0	88	291
	Inf		116.7		46.8		9.4		23.5		28.6		11.1			
Erupted mass (kg)	Obs	1.3×10^{11}	1.3×10^9	2.1×10^8	9×10^9	1.6×10^8	5.9×10^9	4.2×10^6	5.8×10^9	4.7×10^8	3.4×10^{10}	4.8×10^9	7.9×10^9	2.4×10^9	2.1×10^{11}	
	Inf		5.48×10^{11}		2.2×10^{11}		4.41×10^{10}		1.1×10^{11}		1.35×10^{11}		5.2×10^{10}			1.1×10^{12}

A measured 8% of the lithic volume is used for the volume and erupted mass correction.
A magmatic density value of 2350 kg/m^3 is used for the DRE and erupted mass correction.
Welding rank adopted from the proposed by Quane and Russell (2005).

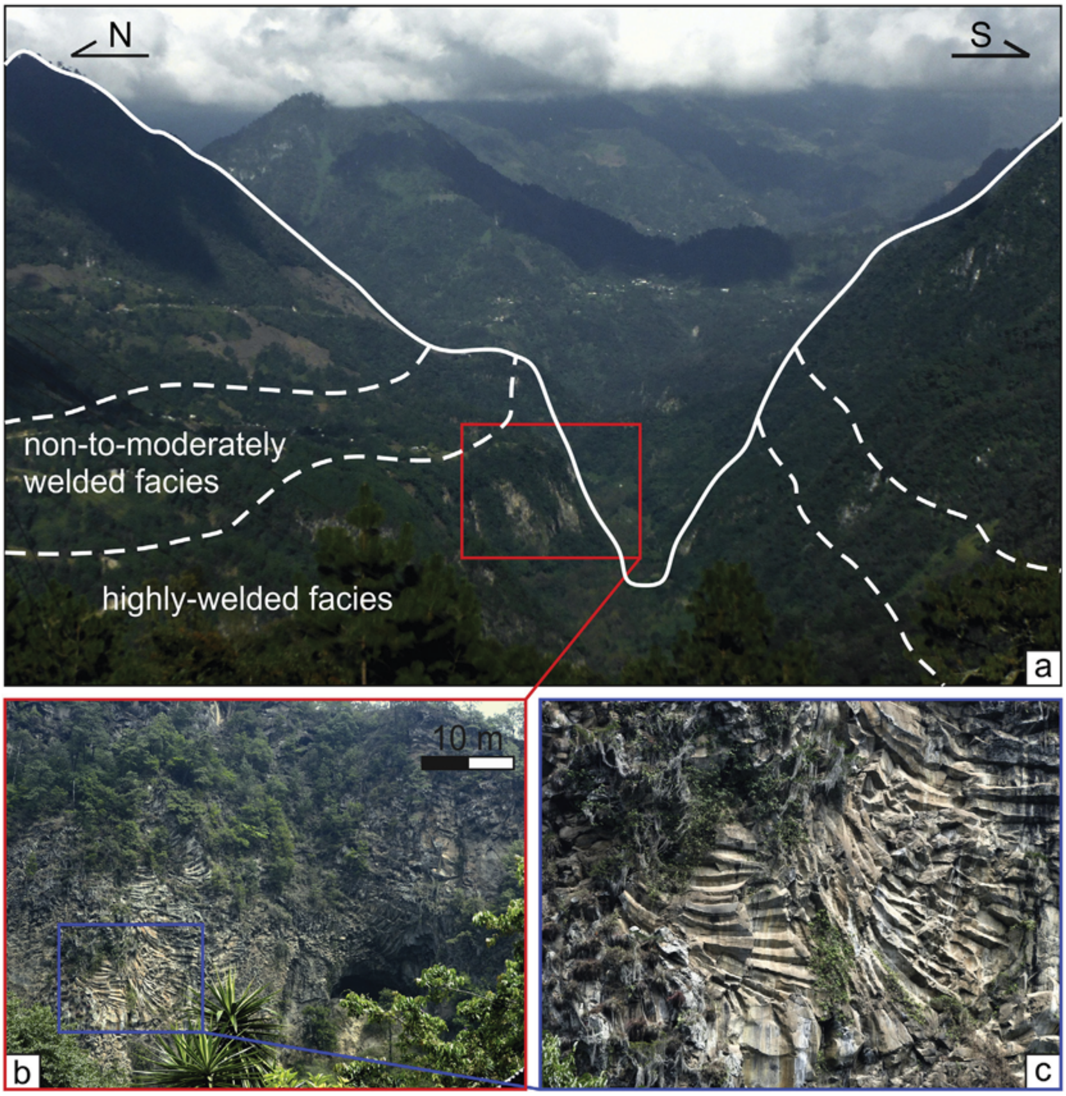

Fig. 14. Photographs showing: a) panoramic view of Las Minas' valley, showing the Xáltipan ignimbrite valley-pond type deposit in its two different welding lithofacies (dashed lines). b) Partial view of a 180 m thick exposure, showing the lava-like columnar joints of the highly welded lithofacies; c) Zoomed area (blue box) indicated in figure (b) showing a well-developed irregular columnar joints distribution.

energy depletion of the current. The same occurred at the NW sector near Zapotitlán, where the ignimbrite channelized in a narrow valley system, with perpendicular paleochannels, where the current waned while emplaced laterally to the west.

In contrast, the western channel systems are preferentially oriented along the flow direction, recording the furthest runout distances of the ignimbrite in the Valley-pond facies with 45–50 km up to the Ixtacamaxtitlán and Aquixtla towns. Thus, it is observed that the orientation of the pre-existing channels strongly controls the resulting runout distance.

5.2. Eruptive history

Based on its stratigraphic features, the Xáltipan ignimbrite records two flow units and two fallout layers, all related to a single eruptive event. Based on this, four main phases can be recognized, which constitute the eruptive history of this single, but voluminous eruption (Fig. 15).

The onset of the eruptive activity is defined by an explosive eruption with a relatively low eruptive column (phase 1), forming the BPF (Fig. 15a). This unit is limited to a meter-scale exposure in a single outcrop at the proximal facies and is absent in the distal sectors. This indicates a small and short-lived eruptive column with limited dispersion of pyroclastic material carried by prevailing winds coming from the west (layer S1). This initial low eruptive column was possibly not so energetic and difficult to sustain itself for a long time. Thus, it rapidly collapsed, forming the LFU (phase 2), which started with the PDC generation synchronously with the pumice fallout deposition from the eruptive column. In the proximal localities, the base of the LFU unit underlies the coarse pumice lapilli fall layers of the BPF. However, away from the vent, they were are deposited as intra-ignimbrite pumice fallout (layer S2a), indicating a simultaneous deposition of both layers. At distal locations, the PDC that formed the LFU traveled as a low-concentration, highly-fluidized PDC, with a traction-dominated flow boundary zone (FBZ). The current evolved to a fluid-scape-dominated FBZ by waxing in the current velocity, leading the inhibition of shear-induced segregation (//bpT), and permitting the continuous aggradation of the mT lithofacies. This part of the LFU mantled and surmounted the topographic barriers up to 510 m as occurred over the CP. The eruption evolved gradually, reaching its climactic eruptive episode in the form of a boiling-over eruption (Fig. 15b), characterized by an eruption waxing, conduit widening, increase in the mass-flux, and massive PDC generation, that formed steady currents with rapid aggradation in a fluid escape-dominated FBZ. This whole phase is probably the longer-lived in the eruptive history of Los Humeros and during which most of the pyroclastic material erupted, forming the main ignimbrite body that surmounted and filled the distal valley-pond sectors, and that settled the landscape to the actual a radial-shape flattened zone in the proximal sector (layers S2c and W2a). The welding zonation in the core of the valley-pond type ignimbrite suggests that the pyroclastic current emplaced at high-temperature and cooled rapidly near the basement-ignimbrite and atmosphere-ignimbrite interphases. The lithic breccia near the base of the LFU (mlBrlens in layer W2a and lpip in layer S2c) evidences deposition near the basal contact with the sedimentary basement, where the poor sorting, matrix-support, and clasts angularity of the lithic clasts points to a local ground breccia fed by loose basement clasts during and erosive current-ground interaction. Instead, the intercalated lithic lBrlens with angular clasts and restricted distribution points to a local lithic source, possibly from nearby brecciated deposits. Even though no evidence of massive lithic breccias was found in the field, the lithic breccia found in the proximal locality 11 (see location in Fig. 4a), and that lithic breccia reported by Willcox (2011) support the idea that the Los Humeros caldera collapsed during this phase in multiple but discrete caldera pulses. The collapse events could occur during this phase through intracaldera fissure vents. In this case, the ejected lithic breccias could be incorporated within the PDC and buried into the intracaldera deposits and in the lower stratigraphic level of the ignimbrite body in the proximal sector. This phase progressed with an eruption waning and current retreat, that produced the deposition of diluted, hot-dry deposits in the top of the main massive lapilli tuffs. After this, a short hiatus is recorded, where a co-ignimbrite ash layer deposited as a thin massive tuff atop the lower flow unit (layer W2c) (Fig. 15c). Subsequently, a short-lived eruptive column (phase 3) was resumed in the western caldera rim, accompanied by the deposition of a well-defined pumice fallout layer (IPF) dispersed to the west (layer W3) (Fig. 15d). The lack of basal or upper paleosols and the sharp and wavy contact with the bonding layers suggest immediate phase transitions. The collapse of this second eruptive column (phase 4) is marked by a PDC generation that flowed to the west depositing the UFU, which is considerably smaller than the LFU, reaching up to ~22 km to the W-SW (Fig. 15e). This pyroclastic flow unit records a brief eruptive pulse, marked at the base by a low-concentration, highly-fluidized, ground surge current that gradually passed through a massive PDC.

5.3. Volume implications

The *ca.* 290 km^3 DRE volume calculated in this work for the Xáltipan ignimbrite exceeds by far the volume of 115 km^3 previously reported by Ferriz and Mahood (1984). Moreover, when compared with other reported caldera-related ignimbrites of the TMBV (Aguirre-Díaz, 1996; Aguirre-Díaz and López-Martínez, 2001; Mahood, 1980; Pacheco-Hoyos et al., 2018; Wright, 1981; Wright and Walker, 1977), the Xáltipan ignimbrite ranks as the largest single explosive eruption of the TMVB (Table 4) with a VEI scale of 6–7 (Newhall and Self, 1982) (Fig. 13). Beyond the area and thickness parameters commonly used to estimate volumes of lithological units, this calculation considers other various essential elements that affect the resulting value, such as welding-related density variations, eroded bulk, and lithic content. Nevertheless, this estimation should be considered as conservative because it does not take on count the distally deposited co-ignimbrite fine-ash that theoretically accompanied the main PDC, and that may represent a substantial proportion of the total ejected material (Sparks and Walker, 1977).

The new DRE volume reported here for the Xáltipan ignimbrite may have important implications for the LHVC geothermal field, particularly in assessing the conductive model, which is determined in function of the age, timing and rejuvenation of the volcanic activity, as well as in the size of the magmatic reservoir (Carrasco-Núñez et al., 2018; Duffield and Sass, 2003; Smith and Shaw, 1975). Here, the magmatic reservoir volume is calculated in *ca.* 2900 km^3, by assuming a previously established 1/10 relation between the erupted volume (*ca.* 290 km^3) with the magmatic chamber (Smith and Shaw, 1975; Smith, 1979). This estimation is much larger than that proposed by Verma et al. (2011) of 1000 to 1400 km^3. This together with the recent geochronological reappraisal of the LHVC by Carrasco-Núñez et al. (2018), where a much younger age of the Xáltipan eruption (164 ± 4.2 ka) was obtained, strongly support more favorable geothermal conditions than previously assumed.

6. Conclusions

In this work, we present a detailed description of the stratigraphy, and lithofacies of the Xáltipan ignimbrite outflow deposits as well as an accurate estimation of its geometrical dimensions based on fieldwork, digital mapping processing, and petrophysical analysis. These results help to unravel the anatomy of the largest ignimbrite reported so far at the TMVB and provide a comprehensive reconstruction of the eruptive history of the main volcanic event of LHVC, which is critical in understanding its volcanic evolution and also for geothermal implications. We summarized the main results derived from this study in the following topics:

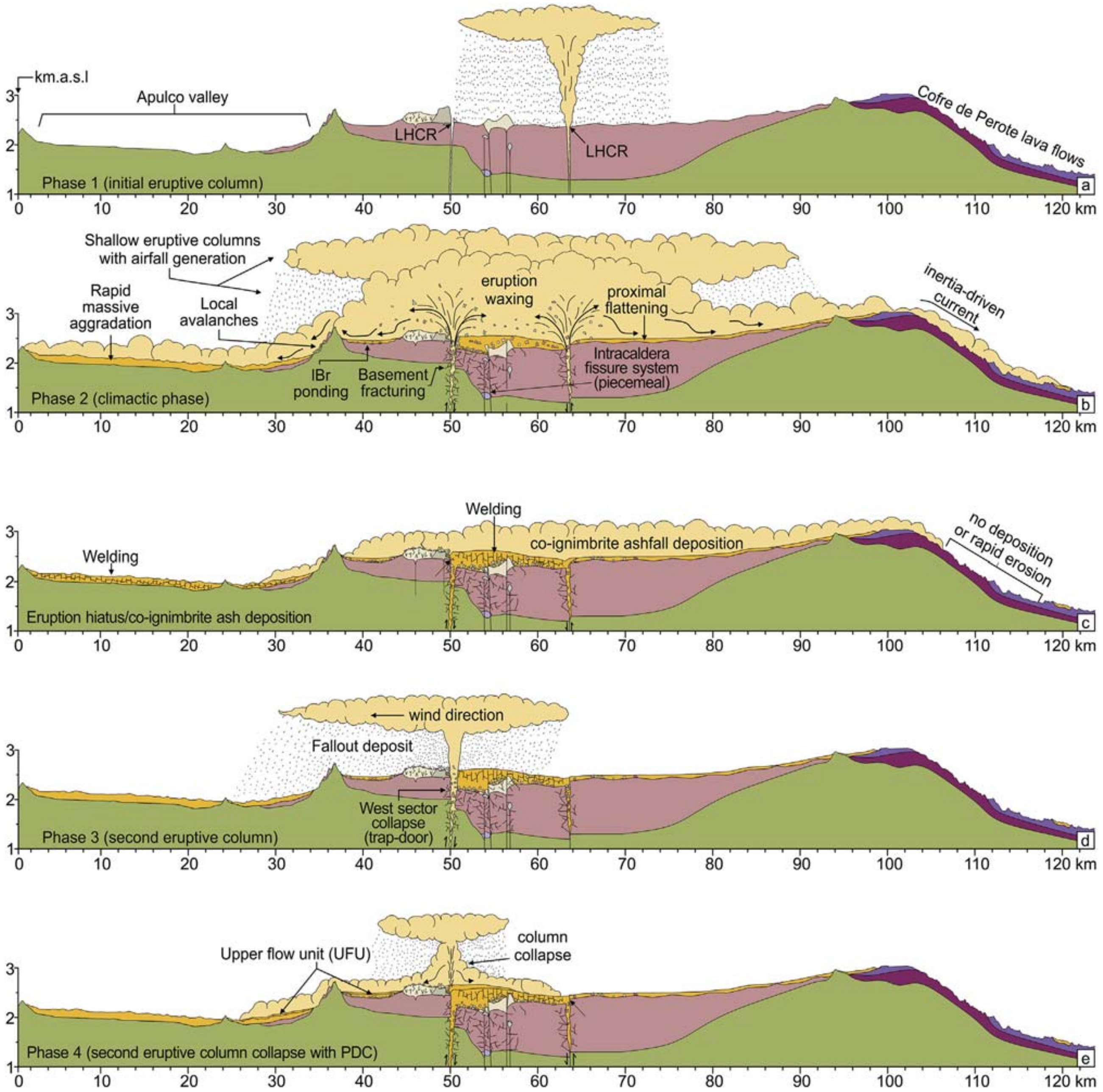

Fig. 15. Schematic representation of the eruptive evolution in four phases producing the Xáltipan ignimbrite. a) Phase 1: Initial, ephemeral, short-lived, eruptive column depositing the basal pumice fallout deposit (BPF). b) Phase 2: Climactic phase with the onset of the caldera collapse, producing the massive lower flow unit (LFU). c) Brief eruption hiatus with the deposition of a co-ignimbrite ash fall. d) Phase 3: Formation of a second short-lived eruptive column dispersed to the west forming the intermediate pumice fallout (IPF). e) Phase 4: Collapse of the second eruptive column forming the upper flow unit (UFU). The topographic and lithologic information is based on the geologic sections a-a' and i-i' and from the geologic map of Carrasco-Núñez et al. (2017).

Stratigraphy and eruptive history

The Xáltipan ignimbrite resulted from a voluminous and continuous eruption that can be divided into four eruptive phases: The eruptive activity started with an explosive eruption that deposited a basal pumice fallout (BPF) (phase 1). This short-lived, ephemeral eruptive column eventually collapsed, evolving to the climactic, caldera-forming, boiling-over eruption that generated massive PDC that deposited as the main body of the ignimbrite (LFU) (phase 2). After the eruption waning, and a brief eruptive hiatus, a second explosive event (phase 3) occurred in the western limit of the caldera with the formation of a short-lived eruptive column that deposited a second pumice fallout (IPF), which immediately collapsed (phase 4) generating PDC that

Table 4
New volume of the Xáltipan ignimbrite (*ca.* 290 km^3) compared with of ignimbrites of the Trans-Mexican Volcanic Belt.

Ignimbrite	DRE volume (km^3)	Work
Acatlán ignimbrite	3	Wright and Walker (1977)
Tala tuff	20	Mahood (1980)
Río Caliente ignimbrite	18.5	Wright (1981)
Amealco tuff	77	Aguirre-Díaz (1996)
Colón ignimbrite	27.5	Aguirre-Díaz and López-Martínez (2001)
Huichapan ignimbrite	69	Pacheco-Hoyos et al. (2018)
Xáltipan tuff	115	Ferriz and Mahood (1984)
Xáltipan ignimbrite	290	This paper

deposited a minor flow unit (UFU) confined to the western flank of the LH caldera.

Architecture and emplacement

The ignimbrite shows a relatively complex distribution controlled by the paleotopography. In the proximal areas, the deposit shows a predominantly radial-shaped distribution that covers the preexisting volcanic field with topographic unevenness that ranges from at least 151 m. Nevertheless, the pyroclastic flows were able to level the irregular paleotopography and form a large, roughly subhorizontal, plateau. In the distal localities, the PDC channelized and confined as a valley-pond type deposit, adopting the shape of the hydrologic pattern (paleochannels). The energy lines, except for the east and southeast sections, show a shallow source height $>$ 400 m of the eruptive column, with large runout distances $<$52 km, which points to a boiling-over eruption. The anomalous energy lines of the east and southeast sections are explained by an inertia-controlled PDC when overpassing the CP topographic barrier. The ignimbrite shows significant welding variations that range from non-to-highly welded conditions (welding ranks I-VI), firmly controlled by the paleotopography. Welding developed preferentially in the valley central parts and is mostly non-welded near the ground/current and atmosphere/current interphase.

Volume and erupted mass

The Xáltipan ignimbrite records a paroxysmal eruption with an aerial extent of *ca.* 4600 km^2, an inflated volume of *ca.* 340 km^3, DRE volume of *ca.* 290 km^3, and an erupted mass of 1.1×10^{12} kg, and that can be ranked as 6–7 in the VEI. The volume estimation (*ca.* 290 km^3) can be considered as a minimum estimation (without considering the co-ignimbrite ash cloud's volume) but is much larger than the previously reported for the Xáltipan ignimbrite (115 km^3) and in fact, place it as the largest eruption reported so far in the TMVB. This new estimation involves a larger magmatic heat source for LHVC, which has important implications for geothermal purposes.

Author statement

Cavazos Jaime: Conceptualization, Methodology, Investigation, Writing – Original Draft, Visualization, Project administration. Carrasco-Núñez Gerardo: Conceptualization, Resources, Writing – Review & Editing, Supervision, Funding acquisition.

Declaration of competing interest

None.

Acknowledgments

We want to thank the reviewers Dr. Adelina Geyer, Dr. Guido Giordano, and the associated editor Dr. José Luis Macías, who greatly enhanced this work with their constructive comments and suggestions. We are grateful to the Comisión Federal de Electricidad (CFE) for continuous support during this project. Also, we would like to thank Juan Vázquez and Dante Arteaga, who helped and supervised with great enthusiasm during the thin-section elaboration and the microCT analysis, respectively. We thank María Mercedes Zavala for the assistance with the Helium pycnometry and permeability analysis. Special thanks to our colleagues Javier Hernández and Francisco Fernandez, who inverted valuable weeks of fieldwork and contributed with meaningful comments during all the stages of this work. G. Carrasco-Núñez is grateful to the PASPA-DGAPA program (UNAM) for support during his sabbatical stay at the University of Roma Tre (Rome, Italy).

Funding

During the early stages of this study, partial funding was provided by the Consortium Centro Mexicano de Innovación en Energía Geotérmica (CeMIEGeo) sponsored by the Fondo de Sustentabilidad Energética SENER-CONACYT [No. 2007032, project P05 (Mexico)]. Additionally, this work was supported by the Consortium GEMEX European Union-Mexico [No. 2015-04-268074]. Finally, necessary funding was provided by CONACYT-Mexico in the form of a doctoral scholarship grant to the first author.

Appendix A. Supplementary data

Supplementary data to this article can be found online at https://doi.org/10.1016/j.jvolgeores.2019.106755.

References

Aguirre-Díaz, G.J., 1996. Volcanic stratigraphy of the Amealco caldera and vicinity, central Mexican Volcanic Belt. Rev. Mex. Ciencias Geol. 13, 10–51.

Aguirre-Díaz, G.J., López-Martínez, M., 2001. The Amazcala caldera, Queretaro, Mexico. Geology and geochronology. J. Volcanol. Geotherm. Res. 111, 203–218. https://doi.org/10.1016/S0377-0273(01)00227-X.

Beget, J.E., Limke, A.J., 1988. Two-dimensional kinematic and rheological modeling of the 1912 pyroclastic flow, Katmai, Alaska. Bull. Volcanol. 50, 148–160. https://doi.org/10.1007/BF01079679.

Best, M.G., Christiansen, E.H., Deino, A.L., Gromme, S., Hart, G.L., Tingey, D.G., 2013. The 36–18 Ma Indian Peak-Caliente ignimbrite field and calderas, southeastern Great Basin, USA: multicyclic super-eruptions. Geosphere 9, 864–950. https://doi.org/10.1130/GES00902.1.

Bouvet de Maisonneuve, C., Bachmann, O., Burgisser, A., 2009. Characterization of juvenile pyroclasts from the Kos Plateau Tuff (Aegean Arc): insights into the eruptive dynamics of a large rhyolitic eruption. Bull. Volcanol. https://doi.org/10.1007/s00445-008-0250-x.

Branney, M.J., Kokelaar, P., 2002. Pyroclastic density currents and the sedimentation of ignimbrites. Geol. Soc. London 27, 152.

Brown, R.J., Branney, M.J., 2004. Event-stratigraphy of a caldera-forming ignimbrite eruption on Tenerife: the 273 ka Poris Formation. Bull. Volcanol. 66, 392–416. https://doi.org/10.1007/s00445-003-0321-y.

Carrasco-Núñez, G., Branney, M.J., 2005. Progressive assembly of a massive layer of ignimbrite with a normal-to-reverse compositional zoning: the Zaragoza ignimbrite of central Mexico. Bull. Volcanol. 68, 3–20. https://doi.org/10.1007/s00445-005-0416-8.

Carrasco-Núñez, G., Ort, M.H., Romero, C., 2007. Evolution and hydrological conditions of a maar volcano (Atexcac crater, Eastern Mexico). J. Volcanol. Geotherm. Res. 159, 179–197. https://doi.org/10.1016/j.jvolgeores.2006.07.001.

Carrasco-Núñez, G., Siebert, L., Díaz-Castellón, R., Vázquez-Selem, L., Capra, L., 2010. Evolution and hazards of a long-quiescent compound shield-like volcano: Cofre de Perote, Eastern Trans-Mexican Volcanic Belt. J. Volcanol. Geotherm. Res. 197, 209–224. https://doi.org/10.1016/j.jvolgeores.2009.08.010.

Carrasco-Núñez, G., Hernández, J., De León, L., Dávila-Harris, P., Norini, G., Bernal, J.P., Jicha, B., Navarro, M., López-Quiroz, P., 2017a. Geologic Map of Los Humeros volcanic complex and geothermal field, eastern Trans-Mexican Volcanic Belt Mapa geológico del complejo volcánico Los Humeros y campo geotérmico, sector oriental del Cinturón Volcánico Trans-Mexicano. Terra Digit 1, 1–11. https://doi.org/10.22201/igg.terradigitalis.2017.2.24.78.

Carrasco-Núñez, G., López-Martínez, M., Hernández, J., Vargas, V., 2017b. Subsurface stratigraphy and its correlation with the surficial geology at Los Humeros geothermal field, eastern Trans-Mexican Volcanic Belt. Geothermics 67, 1–17. https://doi.org/10.1016/j.geothermics.2017.01.001.

Carrasco-Núñez, G., Bernal, J.P., Dávila, P., Jicha, B., Giordano, G., Hernández, J., 2018. Reappraisal of Los Humeros volcanic complex by new U/Th zircon and 40Ar/39Ar dating: implications for greater geothermal potential. Geochemistry, Geophys. Geosystems 19, 132–149. https://doi.org/10.1002/2017GC007044.

Cas, R.A.F., Wright, H.M., Folkes, C.B., Lesti, C., Porreca, M., Giordano, G., Viramonte, J.G., 2011. The flow dynamics of an extremely large volume pyroclastic flow, the 2.08-Ma Cerro Galán Ignimbrite, NW Argentina, and comparison with other flow types. Bull. Volcanol. 73, 1583–1609. https://doi.org/10.1007/s00445-011-0564-y.

Cashman, K.V., Giordano, G., 2014. Calderas and magma reservoirs. J. Volcanol. Geotherm. Res. https://doi.org/10.1016/j.jvolgeores.2014.09.007.

Cavazos, J.A., Carrasco-Núñez, G., 2017. Vertical and Lateral Lithofacies Variations of a Caldera-Related Ignimbrite and Their Implications in an Active Geothermal System: The Case of Los Humeros Geothermal Field, Mexico. IAVCEI, Portland, Oregon.

Cavazos-Álvarez, J.A., & Carrasco-Núñez, G., 2019. Effective mapping of large ignimbrites by using a GIS-based methodology; case of the Xaltipan ignimbrite from Los Humeros caldera, Mexico/Mapeo efectivo de grandes ignimbritas utilizando una metodología basada en SIG; caso de la ignimbrita Xáltipan en la caldera Los Humeros, México. Terra Digit. 3, 78–97. https://doi.org/10.22201/igg.25940694.2019.2.65.

Cedillo, F., 1997. Geología del subsuelo del campo geotérmico de Los Humeros, Puebla, México. Gerencia de Proyectos Geotermoeléctricos, Residencia Los Humeros.

Cedillo, F., 1999. Modelo Hidrogeológico de los Yacimientos Geotérmicos de Los Humeros, Pue., México (Los Humeros, Puebla).

Cid, H.E., Carrasco-Núñez, G., Manea, V.C., 2017. Improved method for effective rock microporosity estimation using X-ray microtomography. Micron 97, 11–21. https://doi.org/10.1016/j.micron.2017.01.003.

Cook, G.W., Wolff, J.A., Self, S., 2016. Estimating the eruptive volume of a large pyroclastic body: the Otowi Member of the Bandelier Tuff, Valles caldera, New Mexico. Bull. Volcanol. 78, 1–11. https://doi.org/10.1007/s00445-016-1000-0.

Dávila-Harris, P., Carrasco-Núñez, G., 2014. An unusual syn-eruptive bimodal eruption: the Holocene Cuicuiltic Member at Los Humeros caldera, Mexico. J. Volcanol. Geotherm. Res. 271, 24–42. https://doi.org/10.1016/j.jvolgeores.2013.11.020.

Demant, A., 1978. Características del Eje Neovolcánico Transmexicano y sus problemas de interpretación.

Druitt, T.H., Bacon, C.R., 1986. Lithic breccia and ignimbrite erupted during the collapse of Crater Lake Caldera, Oregon. J. Volcanol. Geotherm. Res. 29, 1–32. https://doi.org/10.1016/0377-0273(86)90038-7.

Druitt, T.H., Sparks, R.S.J., 1984. On the formation of calderas during ignimbrite eruptions. Nature 310, 679–681. https://doi.org/10.1038/310679a0.

Duffield, W.A., Sass, J.H., 2003. Geothermal energy: Clean power from the earth's heat. U. S. Geol. Surv. Circ. https://doi.org/10.3133/cir1249.

Fernández-Maya, F.O., 2017. Caracterización petrográfica y geoquímica del pozo H-26 en el campo geotérmico de los Humeros, Puebla. Instituto Tecnológico de Ciudad Madero.

Ferrari, L., Orozco-Esquivel, T., Manea, V., Manea, M., 2012. The dynamic history of the Trans-Mexican Volcanic Belt and the Mexico subduction zone. Tectonophysics 522–523, 122–149. https://doi.org/10.1016/j.tecto.2011.09.018.

Ferriz, H., Mahood, G.A., 1984. Eruption rates and compositional trends at Los Humeros Caldera, Puebla, Mexico. J. Geophys. Res. Solid Earth 89, 8511–8524.

Folkes, C.B., Wright, H.M., Cas, R.A.F., de Silva, S.L., Lesti, C., Viramonte, J.G., 2011. A re-appraisal of the stratigraphy and volcanology of the Cerro Galán volcanic system, NW Argentina. Bull. Volcanol. 73, 1427–1454. https://doi.org/10.1007/s00445-011-0459-y.

Giordano, G., Doronzo, D.M., 2017. Sedimentation and mobility of PDCs: a reappraisal of ignimbrites' aspect ratio. Sci. Rep. 7, 1–7. https://doi.org/10.1038/s41598-017-04880-6.

Giordano, G., Mattei, M., Funiciello, R., 2010. Geological map of the Colli Albani volcano. In: Funiciello, R., Giordano, G. (Eds.), The Colli Albani Volcano. Geological Society of London, pp. 43–98.

Gómez-Tuena, A., LaGatta, A.B., Langmuir, C.H., Goldstein, S.L., Ortega-Gutiérrez, F., Carrasco-Núñez, G., 2003. Temporal control of subduction magmatism in the eastern Trans-Mexican Volcanic Belt: mantle sources, slab contributions, and crustal contamination. Geochemistry, Geophys. Geosystems 4. https://doi.org/10.1029/2003GC000524.

Gottsman, J., Martí, J., 2008. Caldera Volcanism: Analysis, Modelling and Response, Developments in Volcanology. Elsevier https://doi.org/10.1016/S1871-644X(07)00011-3.

Hsu, K.J., 1975. Catastrophic debris streams (Sturzstroms) generated by rockfalls. Geol. Soc. Am. Bull. 86, 129. https://doi.org/10.1130/0016-7606(1975)86<129:CDSSGB>2.0.CO;2.

Huerta-Luna, G., 2018. Caracterización geológica y geoquímica de subsuelo del campo geotérmico Los Humeros, Puebla, México: caso de estudio, Pozo H-50. Instituto Politécnico Nacional.

Jáquez-Domínguez, J.A., 2018. Caracterización petrográfica y geoquímica del pozo H-59 del campo geotérmico Los Humeros, Puebla. Universidad Autónoma de Zacatecas.

Lipman, P.W., 1997. Subsidence of ash-flow calderas: relation to caldera size and magma-chamber geometry. Bull. Volcanol. 59, 198–218. https://doi.org/10.1007/s004450050186.

Lipman, P.W., 2000. Calderas. Encycl. Volcanoes, pp. 643–662.

Mahood, G.A., 1980. Geological Evolution of a Pleistocene Rhyolitic Center Sierra La Primavera, Jalisco, México. J. Volcanol. Geotherm. Res. 8, 199–230. https://doi.org/10.1016/0377-0273(80)90105-5.

Mason, B.G., Pyle, D.M., Oppenheimer, C., 2004. The size and frequency of the largest explosive eruptions on Earth. Bull. Volcanol. 66, 735–748. https://doi.org/10.1007/s00445-004-0355-9.

Negendank, J., Emmermann, R., Krawczyk, R., Mooser, F., Tobschall, H., Werle, D., 1985. Geological and geochemical investigations on the eastern Trans-Mexican Volcanic Belt. Geofis. Int. 24, 477–575.

Newhall, C.G., Self, S., 1982. The volcanic explosivity index (VEI) an estimate of explosive magnitude for historical volcanism. J. Geophys. Res. 87, 1231. https://doi.org/10.1029/JC087iC02p01231.

Norini, G., Groppelli, G., Sulpizio, R., Carrasco-Núñez, G., Dávila-Harris, P., Pellicioli, C., Zucca, F., De Franco, R., 2015. Structural analysis and thermal remote sensing of the Los Humeros Volcanic Complex: implications for volcano structure and geothermal exploration. J. Volcanol. Geotherm. Res. 301, 221–237. https://doi.org/10.1016/j.jvolgeores.2015.05.014.

North American Commission on Stratigraphic Nomenclature, 2005. North American stratigraphic code. Am. Assoc. Pet. Geol. Bull. https://doi.org/10.1306/07050504129.

Pacheco-Hoyos, J.G., Aguirre-Díaz, G.J., Dávila-Harris, P., 2018. Boiling-over dense pyroclastic density currents during the formation of the ~100 km^3 Huichapan ignimbrite in Central Mexico: Stratigraphic and lithofacies analysis. J. Volcanol. Geotherm. Res. 349, 268–282. https://doi.org/10.1016/j.jvolgeores.2017.11.007.

Peña-Rodrigez, D., 2018. Caracterización petrográfica y geoquímica de una sección del subsuelo del campo geotérmico de Los Humeros, Puebla: caso de estudio del pozo H10. Instituto Tecnológico de Ciudad Madero.

Quane, S.L., Russell, J.K., 2005. Ranking welding intensity in pyroclastic deposits. Bull. Volcanol. 67, 129–143. https://doi.org/10.1007/s00445-004-0367-5.

Rojas-Ortega, E., 2016. Litoestratigrafía, petrografía y geoquímica de la toba Llano, y su relación con el cráter el Xalapazco, Caldera de Los Humeros, Puebla. Instituto Potosino de Investigación Científica y Tecnológica.

Romo-Jones, J.M., Gutiérrez-Negrín, L.C., Flores-Armenta, M., del Valle, J., García, A., 2017. 2016 Mexico Country Report, IEA Geothermal.

Scott, W.E., Hoblitt, R.P., Torres, R.C., Self, S., Martinez, M.M.L., Nillos, T., 1996. Pyroclastic flows of the June 15, 1991, climactic eruption of Mount Pinatubo. Fire and Mud. Univ. Washington Press, Seattle, pp. 545–570.

Siebe, C., Macías, J.L., Abrams, M.J., Rodríguez, S., Castro, R., Delgado Granados, H., 1995. Quaternary explosive volcanism and pyroclastic deposits in east central Mexico: implications for future hazards. Guideb. Geol. excursions conjunction with Annu. Meet. Geol. Soc. Am. (1995), 1–48 New Orleans, Louisiana, Novemb. 6-9.

Smith, R.L., 1979. Ash-flow magmatism. Geological Society of America Special Papers, pp. 5–28. https://doi.org/10.1130/SPE180-p5.

Smith, R.L., Bailey, R.A., 1968. Resurgent cauldrons. Geol. Soc. Am. Mem., 613–662 https://doi.org/10.1130/MEM116-p613.

Smith, R.L., Shaw, H.R., 1975. Igneous-related geothermal systems. US Geol. Surv. Circ. 726, 58–83.

Sparks, R.S.J., Walker, G.P.L., 1977. The significance of vitric-enriched air-fall ashes associated with crystal-enriched ignimbrites. J. Volcanol. Geotherm. Res. 2, 329–341. https://doi.org/10.1016/0377-0273(77)90019-1.

Suñe-Puchol, I., Aguirre-Díaz, G.J., Dávila-Harris, P., Miggins, D.P., Pedrazzi, D., Costa, A., Ortega-Obregón, C., Lacan, P., Hernández, W., Gutiérrez, E., 2018. The Ilopango caldera complex, El Salvador: origin and early ignimbrite-forming eruptions of a graben/pull-apart caldera structure. J. Volcanol. Geotherm. Res. 371, 1–19. https://doi.org/10.1016/j.jvolgeores.2018.12.004.

Todesco, M., Neri, A., Ongaro, T.E., Papale, P., Rosi, M., 2006. Pyroclastic flow dynamics and hazard in a caldera setting: application to Phlegrean Fields (Italy). Geochemistry, Geophys. Geosystems 7. https://doi.org/10.1029/2006GC001314.

Trolese, M., Cerminara, M., Esposti Ongaro, T., Giordano, G., 2019. The footprint of column collapse regimes on pyroclastic flow temperatures and plume heights. Nat. Commun. 10, 2476. https://doi.org/10.1038/s41467-019-10337-3.

Verma, S.P., Gómez-Arias, E., Andaverde, J., 2011. Thermal sensitivity analysis of emplacement of the magma chamber in Los Humeros caldera, Puebla, Mexico. Int. Geol. Rev. 53, 905–925. https://doi.org/10.1080/00206810903234296.

Viniegra, F., 1965. Geología del macizo de Teziutlán y de la cuenca cenozoica de Veracruz. Boletín la Asoc. Mex. Geólogos Pet. 17, 100–135.

Walker, G.P.L., 1980. The Taupo pumice: product of the most powerful known (ultraplinian) eruption? J. Volcanol. Geotherm. Res. 8, 69–94. https://doi.org/10.1016/0377-0273(80)90008-6.

Willcox, C.P., 2011. Eruptive, Magmatic and Structural Evolution of a Large Explosive Caldera Volcano: Los Humeros, Central Mexico. University of Leicester.

Wilson, C.J.N., Hildreth, W., 1997. The Bishop Tuff: new insights from eruptive stratigraphy. J. Geol. 105, 407–440. https://doi.org/10.1086/515937.

Wilson, C.J.N., Hildreth, W., 2003. Assembling an ignimbrite: mechanical and thermal building blocks in the Bishop Tuff, California. J. Geol. 111, 653–670. https://doi.org/10.1086/378335.

Wilson, C.J.N., Walker, G.P.L., 1982. Ignimbrite depositional facies: the anatomy of a pyroclastic flow. J. Geol. Soc. Lond. 139, 581–592. https://doi.org/10.1144/gsjgs.139.5.0581.

Wilson, C.J.N., Houghton, B.F., Kamp, P.J.J., Mc Williams, M.O., 1995. An exceptionally widespread ignimbrite with implications for pyroclastic flow emplacement. Nature 378, 605–607. https://doi.org/10.1038/378605a0.

Wright, J.V., 1981. The rio caliente ignimbrite: analysis of a compound intraplinian ignimbrite from a Major Late Quaternary Mexican eruption. Bull. Volcanol. 44, 189–212. https://doi.org/10.1007/BF02597704.

Wright, J.V., Walker, G.P.L., 1977. The ignimbrite source problem: significance of a co-ignimbrite lag-fall deposit. Geology 5, 729. https://doi.org/10.1130/0091-7613(1977)5<729:TISPSO>2.0.CO;2.

Yáñez-Garcia, C., García-Durán, S., 1982. Exploración de la región geotérmica Los Humeros–Las Derrumbadas, Estados de Puebla y Veracruz, Comisión Federal de Electricidad (Mexico, D. F).

5.3 Variaciones de facies y permeabilidad de ignimbritas en sistemas geotérmicos activos, caso de estudio de la ignimbrita Xáltipan en el complejo volcánico de Los Humeros.

Artículo: Facies variations and permeability of ignimbrites in active geothermal systems; case of study of the Xáltipan ignimbrite at Los Humeros Volcanic Complex.

Autores: Cavazos-Álvarez, J. A., Carrasco-Núñez, G., Dávila-Harris, P., Peña, D., Jáquez, A., Arteaga, D., (2020).

Revista: Journal of South American Earth Sciences.

DOI: 10.1016/j.jsames.2020.102810

Journal of South American Earth Sciences 104 (2020) 102810

Contents lists available at ScienceDirect

Journal of South American Earth Sciences

journal homepage: www.elsevier.com/locate/jsames

Facies variations and permeability of ignimbrites in active geothermal systems; case study of the Xáltipan ignimbrite at Los Humeros Volcanic Complex

Jaime A. Cavazos-Álvarez[a,*], Gerardo Carrasco-Núñez[a], Pablo Dávila-Harris[b], Daniela Peña[a], Adrián Jáquez[a], Dante Arteaga[a]

[a] *Centro de Geociencias, Universidad Nacional Autónoma de México, Blvd. Juriquilla 3001, Campus UNAM-Juriquilla, Querétaro, 76230, Mexico*
[b] *División de Geociencias Aplicadas, IPICYT, San Luis Potosí, 78216, Mexico*

ARTICLE INFO

Keywords:
Los humeros volcanic complex
Ignimbrites facies
Ignimbrite welding
Porosity-permeability
Secondary mineralization
Intracaldera ignimbrites

ABSTRACT

Ignimbrites' facies are key for interpreting the dynamics of explosive eruptions. Furthermore, they provide evidence of the physicochemical processes that acted during and after their deposition. Nevertheless, ignimbrites commonly present complex facies associations that require an integrative analytical methodology over a robust stratigraphic framework for their proper characterization. This work presents a facies characterization of the caldera-forming Xáltipan ignimbrite at Los Humeros Volcanic Complex, by integrating a combination of petrophysical and geochemical analyses aimed at its outflows (exposed) and intracaldera (buried) deposits. Based on the petrophysical properties, a three-facies association is identified controlled by welding and secondary mineralization effects: (1) The basal facies, characterized in the outflows by highly welded deposits (ranks V-VI), with low porosity (~4–8%), and practically impermeable conditions (<0.01–0.05 mD). In the intracaldera deposits, this facies shows pervasive geothermal-related propylitic mineralization that can reduce porosity up to *ca.* 80%. (2) A middle facies, with moderately welded deposits (ranks III-IV) and porous conditions consisting of a combination of intershard, vesicular, and fracture spaces, partially filled by secondary minerals, which reduce the porosity (6–11.5% in the outflows; 16–28% for the intracaldera), resulting in semi-permeable conditions (6.11–46.38 mD). (3) The upper facies are defined by being not to poorly welded deposits (ranks I-II), and characterized by being highly porous (dominated by intershard spaces) and permeable (310–1557 mD), and barely affected by secondary mineralization. The geochemical results (major and trace element) indicate that the Xáltipan ignimbrite shows a vertical compositional zonation, from rhyolitic (70.9–76.2 wt% SiO_2) in the lower flow unit to rhyolitic-trachydacitic (67–70.7 wt% SiO_2) composition in its upper flow unit. This last unit shows a geochemical affinity with the subsequent pyroclastic deposits. Geochemical analyses of intercalated lavas from well logs also provided evidence of unprecedented breccias formed during the caldera collapse, discarding the existence of previously assumed thick lava flows. Facies correlation, among other well logs, shows that the facies distribution is directly controlled by the ignimbrite thickness. Where the ignimbrite is $>$ 400 m thick, the entire facies association is observed, while when the thickness is $<$ 400 m, the upper and middle facies occurs preferentially. This facies analysis may contribute to the overall model of Los Humeros subsurface stratigraphy, by defining the Xáltipan ignimbrite distribution and its porosity-permeability-based zones, which are of particular interest for geothermal purposes. Finally, this work provides the first example of a caldera-forming ignimbrite that presents analog facies associations between its outflows and intracaldera deposits that may be applied for other ignimbrites worldwide.

1. Introduction

In modern volcanology, the study of ignimbrite facies has become an essential tool to interpret the physicochemical processes involved during explosive eruptions (e.g., eruptive style, magmatic properties), as well as their sedimentation and post-emplacement processes (e.g., current

---

* Corresponding author.
E-mail address: jcavazos@geociencias.unam.mx (J.A. Cavazos-Álvarez).

https://doi.org/10.1016/j.jsames.2020.102810
Received 30 May 2020; Received in revised form 6 August 2020; Accepted 6 August 2020

dynamics, topography, welding, secondary mineralization). Furthermore, particular interest has been paid in the relation among facies, porosity and permeability of ignimbrites, especially for those related with natural reservoirs such as water (Anderson, 1994; Flint and Selker, 2003; Foster et al., 1985), oil and gas (Couves et al., 2016; Purnomo et al., 2008; Sruoga and Rubinstein, 2007; Zheng et al., 2018), waste reservoirs (Bodvarsson et al., 1999; Istok et al., 1994; Neeper and Gilkeson, 1996; Neretnieks, 1980), and geothermal fluids (Arellano et al., 2005; Carranza et al., 2008; Stimac et al., 2004). Nevertheless, ignimbrites commonly present multiple facies that can vary drastically at scales from centimeters to hundreds of meters, and that can occur into single deposits (flow-unit scale) up to large ignimbritic successions. These variations have been extensively reported and interpreted on surficial ignimbrites outflows, where direct observations and sampling of the outcrops allow the definition of constrained facies models that incorporate stratigraphic and spatial information (e.g., Brown and Branney, 2004; Carrasco-Núñez and Branney, 2005; Couves et al., 2016; Scarpati et al., 2015; Valentine et al., 1992; Wilson and Walker, 1982). Complexity increases in subsurface ignimbrites, particularly the intracaldera ignimbrites, where the deposits are not directly observed and have experienced burial effects such as lithostatic pressure, secondary fracturing, and hydrothermal processes. In these cases, facies characterization requires a detailed study of logged samples by a combination of conventional and modern petrologic and petrophysical analyses.

The Los Humeros Volcanic Complex (LHVC) encompasses one of the productive geothermal fields of the country (third up to date) with an installed production of ca. 93 MW (Romo-Jones et al., 2017). Since the '70s, more than 60 exploration wells have been drilled by the Comisión Federal de Electricidad (CFE) of Mexico to survey the geothermal system and therefore enhance electric power production. In the last years, in alliance with CFE, multidisciplinary studies have been done under the CeMIGeo and GEMex projects to enhance the geothermal system's understanding and to upgrade the geothermal productivity. Some of these works comprise the volcanic history of the complex based on its chronostratigraphy (Carrasco-Núñez et al., 2018) and mapping (Carrasco-Núñez et al., 2017a), the architecture of the magmatic plumbing system by using petrologic models (Lucci et al., 2020), characterization of the geothermal system by geophysical and geological studies (Arzate et al., 2018), and structural evolution and configuration of the volcanic complex and geothermal field (Norini et al., 2019, 2015) to mention some. These works have revealed a younger and more complex geothermal system than previously proposed, where the geothermal

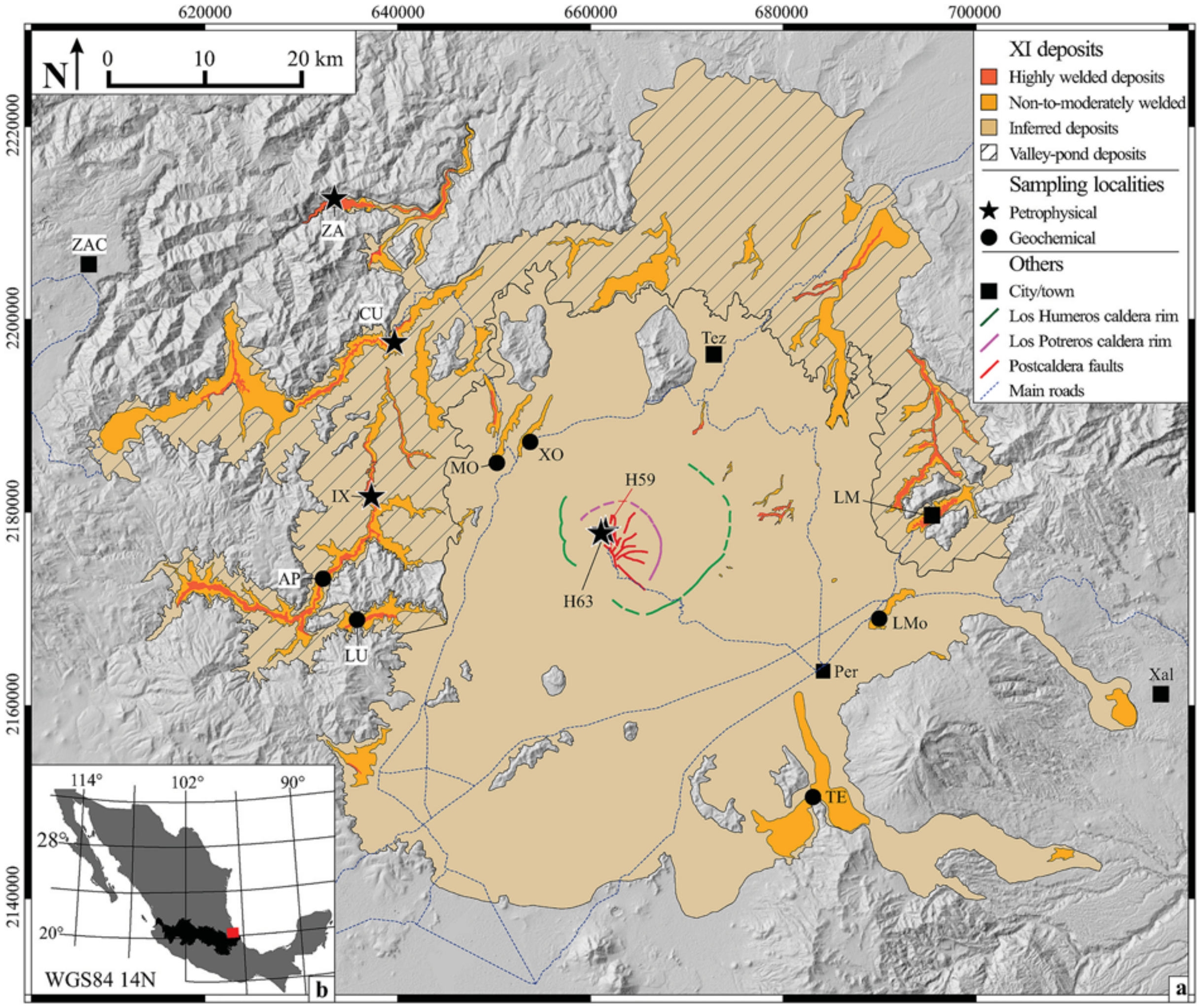

Fig. 1. a) Map showing the distribution of the Xáltipan ignimbrite over a grayscale Digital Elevation Model showing: the selected localities for this study aimed for the petrophysical test are indicated with stars (ZA - Zapotitlán; CU - Cuaximaloyan; IX - Ixtactenango), and the ones for the geochemical tests with circles (XO – Xonocuautla; MO – Morelos; AP – Apulco; LU – La Unión; LMo – Los Molinos; TE – Tenextepec); Los Humeros caldera system (red lines); location of main cities and towns (Zac - Zacatlán de las Manzanas; Tez - Teziultán; Per - Perote; LM – Las Minas; Xal - Xalapa); main roads in dashed blue line. b) Inset showing the location of the Trans-Mexican Volcanic Belt (black area) and the study area at its eastern sector (red square). The maps are plotted over a UTM projection and a WGS84 datum. Modified from Cavazos-Álvarez and Carrasco-Núñez (2019). (For interpretation of the references to color in this figure legend, the reader is referred to the Web version of this article.)

fluids are hosted into the highly fractured andesitic volcanic basement, and sealed by the thick pyroclastic units of the caldera stage which includes the Xáltipan ignimbrite (XI) (Arellano et al., 2000; Cedillo, 1999, 1997; Gutiérrez-Negrín and Izquierdo-Montalvo, 2010; Lorenzo-Pulido, 2008). However, it has been observed that the XI shows important welding and hydrothermal alteration facies variations in the outflows, accompanied by drastic changes in its porosity properties (Cavazos-Álvarez and Carrasco-Núñez, 2017). Therefore, it is also necessary to assess these facies variations for the intracaldera deposits to establish its role in the geothermal field.

The XI at LHVC (Fig. 1) exemplifies a large ignimbrite that deposited as widely exposed surficial outflows with its equivalent intracaldera deposits, which are totally buried into the active Los Humeros geothermal field. Here, the XI has been conventionally referred to as a caprock for the geothermal system (Cedillo, 1999). Since the initial exploration of the LHVC and geothermal field, few works have attempted to present a geologic characterization of this ignimbrite, describing it as a massive, homogeneous, and moderately to non-welded ignimbrite (Ferriz and Mahood, 1984; Willcox, 2011). More recently, the XI's anatomy and stratigraphy have een revised in detail (Cavazos-Álvarez and Carrasco-Núñez, 2019; 2020), revealing that it is highly heterogeneous in its thickness, and present significant lateral and vertical facies heterogeneities. Also, it has been proposed that these facies variations may control its porosity and permeability conditions (Cavazos-Álvarez and Carrasco-Núñez, 2017). Despite the relevance of the XI for understanding the LHVC evolution and its role in the hosted geothermal system, a detailed characterization of its facies is still missing.

In this paper, we present a facies characterization of the XI outflows and intracaldera deposits by applying petrophysical (thin-section petrography, computerized X-ray microtomography, (μCT) and gas pycnometry), and geochemical (major and trace elements) analyses. The analyses were done on sample suites from representative localities, where facies variations are more prone to occur. The results reveal that the XI shows facies variations recorded in its petrophysical and geochemical features, and these variations are similar in both the outflows and intracaldera deposits. Furthermore, the stratigraphy of the intracaldera deposits indicates a continuous ignimbritic deposition with intercalated lithic-rich layers that are now interpreted as breccias deposited during the caldera collapse event. By integrating these results with previously reported well-log data, a more comprehensive facies model of the XI is provided, showing vertical and lateral permeability variations that have important implications for the geothermal system.

2. Geologic background

2.1. Regional setting

The LHVC is a dominantly silicic volcanic center located at the easternmost sector of the Trans-Mexican Volcanic Belt (TMVB) (Fig. 1), a volcanic arc active since the Miocene and formed by the subduction of the Cocos and Rivera plates under the North American plate (Ferrari et al., 2012, and references therein). This complex developed within the Serdán Oriental Basin (SOB), a Pliocene-Holocene closed depression with multiple volcanic structures. These structures include cinder cones, maar craters, domes, and lava flows, surrounded by polygenetic volcanism comprising stratovolcanoes, compound volcanoes and a caldera system, such as the case of the LHVC (Carrasco-Núñez et al., 2007; Negendank et al., 1985; Siebe et al., 1995).

The LHVC rests over a regional basement composed by the Teziutlán massif, a Paleozoic-Mesozoic (246-231 Ma) plutonic and metamorphic complex (Yáñez-García and García-Durán, 1982). This complex is covered by a Mesozoic marine sedimentary succession, highly deformed during the Late-Cretaceous-Eocene orogenic phase forming the Mexican fold and thrust belt (Fitz-Díaz et al., 2018, and references therein), which is cut by Oligocene-Miocene granodiorite and syenite intrusions (Ferriz and Mahood, 1984; Yáñez-García and García-Durán, 1982). These are in turn overlaid by a Miocene-Pleistocene volcanic succession of andesitic composition, followed by the LHVC.

2.2. Geology of the LHVC

The LHVC hosts the largest active caldera system in Mexico (e.g., Carrasco-Nuñez et al., 2017a). Its volcanic evolution records multiple eruptions that can be divided as precaldera, caldera, and postcaldera stages (Carrasco-Núñez et al., 2018). The precaldera stage records predominantly felsic volcanism in the form of rhyolitic domes and lavas located in the western sector of the present Los Humeros caldera's rim. Dating of some of these domes ranges between from 693.0 ± 1.9 ka ($^{40}Ar/^{39}Ar$ in plagioclase; Carrasco-Núñez et al., 2018) to 270 ± 17 ka (U/Th in zircon), and 360 ± 100 ka ($^{40}Ar/^{39}Ar$ in sanidine) and 220 ± 40 ka ($^{40}Ar/^{39}Ar$ in sanidine and K/Ar in whole-rock; Ferriz and Mahood, 1984).

The caldera stage is defined by an intense explosive activity comprising two caldera-forming eruptions and a sequence of Plinian eruptions. The first and leading caldera-forming event occurred 164 ± 4.2 ka (Carrasco-Núñez et al., 2018), forming the voluminous XI (*ca.* 290 km^3 – DRE; Cavazos-Álvarez and Carrasco-Núñez, 2020), and the collapse of the Los Humeros caldera (Ferriz and Mahood, 1984), a sub-circular, 17–18 km in diameter structure (Norini et al., 2019), which hosts the actual geothermal system. A subsequent Plinian phase at 70 ± 23 ka (Carrasco-Núñez et al., 2018) produced a sequence of rhyodacitic pumice fallout layers bounded by paleosols grouped as the Faby tuff, from which no caldera structure has been identified. The caldera stage ended with a second caldera-forming eruption associated with the emplacement of the double compositionally-zoned (rhyodacite-andesite-rhyodacite) intra-Plinian Zaragoza ignimbrite (Carrasco-Núñez and Branney, 2005). This eruption is associated with the collapse of the nested and smaller (9 km in diameter) Los Potreros caldera.

The postcaldera stage comprises a Late Pleistocene resurgent phase and a Holocene bimodal and ring-fracture phase (Carrasco-Núñez et al., 2018). The resurgent phase is marked by felsic volcanism in the central part of the Los Humeros caldera, forming small rhyolitic domes and dacitic pumice fallouts, PDCs, and breccia deposits. The ring-fracture and bimodal phase, representing the youngest volcanic activity of the LVHC, occurred in the north, center, and south sectors of the Los Humeros caldera as effusive basaltic andesite, andesitic, trachyandesitic, and trachytic lava flows along the caldera faults, and as explosive eruptions producing andesitic and rhyodacitic fallout deposits (Dávila-Harris and Carrasco-Núñez, 2014).

2.3. Xáltipan ignimbrite (XI)

Based on previous works (Carrasco-Núñez et al., 2018; Cavazos-Álvarez and Carrasco-Núñez, 2019, 2020; Ferriz and Mahood, 1984; Willcox, 2011) it is possible to refer to the XI as the leading unit of LHVC by several reasons: 1) It records the largest single eruption of LHVC and TMVB, with an aerial extent of *ca.* 4600 km^2 and eruptive magnitude of *ca.* 290 km^3 of dense rock equivalent (DRE) (Cavazos-Álvarez and Carrasco-Núñez, 2019). 2) Its eruption resulted in the collapse of Los Humeros caldera, the main structure of the geothermal system (Ferriz and Mahood, 1984; Willcox, 2011). 3) Its eruption marks the onset of the caldera stage, which continued with two other major explosive eruptions (Carrasco-Núñez et al., 2018). 4) Within the caldera subsurface, it overlies directly the thick, highly fractured, precaldera andesitic succession, where most of the geothermal reservoir is located. Therefore, depending on its physical properties, the XI may serve as a caprock (Arellano et al., 2003; Cedillo, 1999, 1997; Gutiérrez-Negrín and Izquierdo-Montalvo, 2010; Lorenzo-Pulido, 2008), as part of the reservoir unit, or as a combination of both (Carrasco-Núñez et al., 2017b).

2.3.1. General description

The XI has been generally described as a poorly sorted, matrix-supported, white to grey when fresh and pink to orange when altered, trachytic to rhyolitic ignimbrite (67–76.2% SiO_2) that emplaced predominantly in massive lapilli tuff and massive tuff facies (Ferriz and Mahood, 1984; Willcox, 2011).

2.3.2. Architecture and stratigraphy of the XI

The XI displays a radial landform with valley filling-type terminations, as indicated by a recent mapping based on field observations and GIS-tools (Cavazos-Álvarez and Carrasco-Núñez, 2019). The outflows are widely exposed all around the Los Humeros caldera. In the proximal sectors (<30 km), younger LHVC volcanism covers most of the XI, but minor outcrops are reported through road cuts, quarries, and active rivers. At the distal sectors (>30 km from the caldera rim), the ignimbrite ponded into the rugged prevolcanic basement and has been cut by the active rivers (Aliaga-Campuzano, 2017), exposing steep walls of >90 m thick. The original base and top contacts are rarely exposed and are not seen together in any outcrop. Nevertheless, the most recent stratigraphic model reveals that the XI comprises two flow units and two pumice fallout units (Cavazos-Álvarez and Carrasco-Núñez, 2020) (Fig. 2). These units are from bottom to top: 1) a thin (50 cm) basal pumice fallout layer (BPF), which is only exposed near the southern rim of the Los Humeros caldera; 2) a predominant lower flow unit (LFU), exposed in all the outcrops where the ignimbrite has been recognized, and that represents ~95% of the total bulk of the deposit. It must be mentioned that welding exclusively occurs in this unit; 3) a 60 cm thick intermediate pumice fallout (IPF) that thins away through the western sector of the caldera, and; 4) an upper flow unit (UFU) of <12 m thick, which is exposed at the same outcrops of the IPF. Both flow units (LFU and UFU) present similar characteristics at the outcrop scale, except for the welding occurrence only into the LFU. Both are predominantly massive, vitric-rich lapilli-tuffs, with pumice lapilli clasts of similar textures (see section 2.3.1), black obsidian, and lithic clasts.

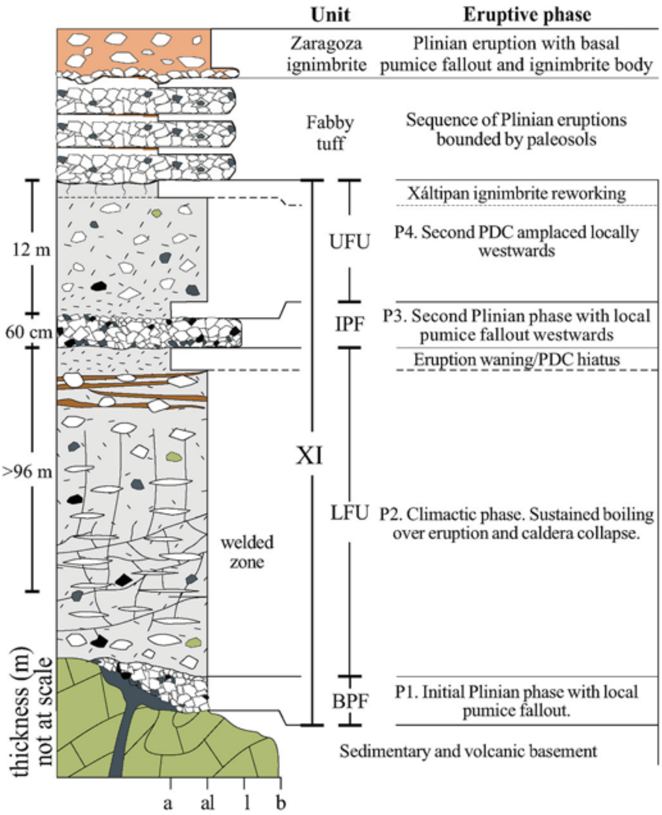

Fig. 2. Simplified composite stratigraphy of the Xáltipan ignimbrite and its relationship with the basement rocks and the overlying Faby tuff and Zaragoza ignimbrite. The units that compose the Xáltipan ignimbrite are shown with a brief interpretation of their eruptive phase (BPF – basal pumice fallout; LFU – lower flow unit; IPF – intermediate pumice fallout; UFU – upper flow unit). Column width corresponds to the dominant grain size (a – ash; al – ash lapilli; l – lapilli; b – blocks). Modified from Cavazos-Álvarez and Carrasco-Núñez (2020).

The intracaldera deposits' stratigraphy has been determined in several well logs (Carrasco-Núñez et al., 2017b). From the logs, it can be observed that the XI exhibits significant thickness variations ranging from 90 to 770 m (Carrasco-Núñez et al., 2017b), which can be interpreted as the result of preferential ponding of the ignimbrite into an irregular pre-eruptive topography and coupled with a differential floor subsidence during the piecemeal-trapdoor collapse of the Los Humeros caldera as proposed by Willcox (2011). The ignimbrite may result in a preferential welding development in the basal levels of the thickest XI deposits. Nevertheless, these phenomena have not been previously quantified, being one of this work's main objectives. It is also observed several intercalations of intermediate to felsic lava layers into the XI, which has been conventionally interpreted as possible lava flows that reach up to *ca.* 100 m thick (Carrasco-Núñez et al., 2017b). Some of these horizons, particularly those of rhyolitic composition, have also been interpreted as the result of the emplacement of a set of relatively small intrusions (domes and cryptodomes) during the postcaldera stage (Urbani et al., 2020).

2.3.3. Welding

In the outflows, welding is restricted to the lower flow unit and ranges from ranks I to VI (Quane and Russell, 2005). Observations through dissected valley-pond type deposits indicate that the XI presents welding zonation, being highly welded facies at the core of the valleys with a gradual welding decrease outwards the external parts of the deposits up to non-welded facies. Here, welding is characterized by pervasive, vertical to curved, columnar jointing (Fig. 3). Welding into the caldera has not been previously quantified by a systematic approach.

2.3.4. Alteration

The XI commonly exhibit hydrothermal mineralization and alteration in its both outflows and intracaldera deposits (Cavazos-Álvarez and Carrasco-Núñez, 2020; del Pilar-Martínez, 2016; Fernández-Maya, 2017; Ferriz and Mahood, 1984; Jáquez-Domínguez, 2018; Willcox, 2011). Glass commonly presents argillic alteration in the non-welded facies, resulting in a characteristic pink to orange coloration of the deposits and the formation of indurated vein nets. On the other hand, the outflows welded facies regularly show secondary microcrystalline quartz precipitation into fractures and vesicles.

Propylitic alteration has been reported for the intracaldera XI based on petrographic descriptions from borehole samples. General quantifications indicate microcrystalline quartz (10%), calcite (5%), pyrite (3%), chlorite (2%), and oxides (2%), which occur replacing matrix and phenocryst, as well as argilization in the form of smectite-illite minerals (Fernández-Maya, 2017; Jáquez-Domínguez, 2018; Martínez-Serrano and Dubois, 1998).

3. Ignimbrites' facies

3.1. Definition

Ignimbrite facies can be defined as the set of physical and compositional characteristics of a part or whole ignimbrite deposit that is distinct from their surroundings and that result from several competing factors acting since the eruption, during sedimentation, and after deposition (e.g., Branney and Kokelaar, 2002; Brown and Branney, 2004; Druitt, 1998; McArthur et al., 1998; McPhie et al., 1993; Quane and Russell, 2005; Wilson and Walker, 1982). Even when the use of facies is strictly descriptive and non-genetic, their identification, along

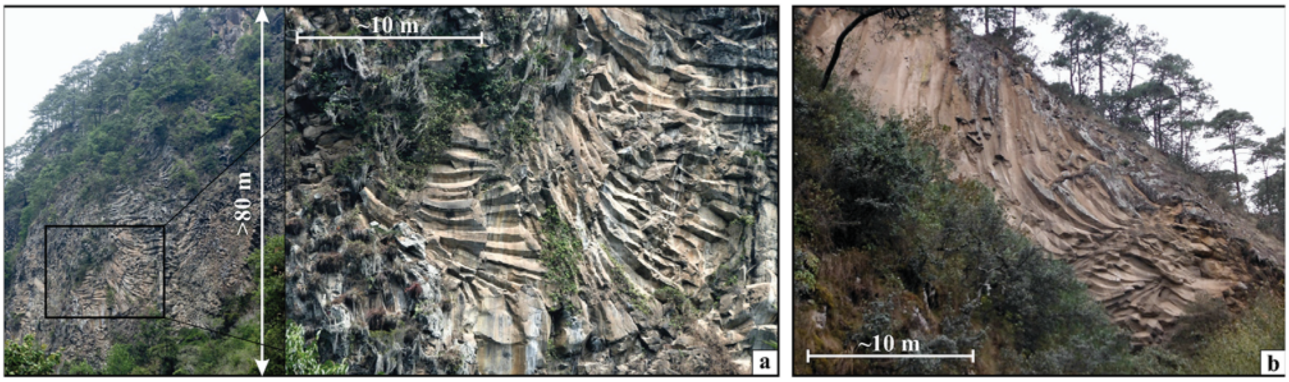

Fig. 3. Photographs showing columnar jointing structure of the Xáltipan ignimbrite. a) Outcrops of the highly welded facies of the ignimbrite in a steep wall at Las Minas locality showing pervasive columnar jointing with an irregular orientation. b) Outcrop near Cuaximaoyan locality showing curved-shaped columnar jointing.

with its corresponding stratigraphy, may provide information about the origin of the deposits and the processes that modify them. However, most ignimbritic deposits exhibit inner facies variations that may be gradational to abrupt, and that can be recorded at a single flow-unit or ignimbrite succession scale. These facies variations can be defined by the petrophysical properties and compositional zonation of the deposits, which are described separately in this section.

3.2. Petrophysical properties

The petrophysical properties describe the relation of the solid fraction of the rock with the porous media. Therefore, the physical properties of an ignimbrite are directly related with its porosity and permeability (Bernard et al., 2007; Bouvet de Maisonneuve et al., 2009; Degruyter et al., 2010; Klug et al., 2002; Klug and Cashman, 1996; Polacci et al., 2014; Rust and Cashman, 2004; Wright et al., 2009). In these studies, it has been proved that porosity and permeability are closely, but non-linearly related, and controlled by primary and secondary processes. As defined by Sruoga and Rubinstein (2007), the primary processes are those that act since the pre-eruptive stage up to the final cooling of the deposit and develop under closed-system conditions; while, secondary processes take place after complete cooling of the deposit in open-system conditions. A complete review of these processes and the associated physical changes are presented in Sruoga and Rubinstein (2007).

3.3. Geochemical properties

Ignimbrites commonly record geochemical variations (or zoning) along with its stratigraphy, which can occur at flow-unit scale up to the entire deposit (Bacon and Druitt, 1988; de Silva, 1991; Giannetti and Luhr, 1983; Hildreth, 1979; Lipman, 1967; Smith and Bailey, 1966; Sumner and Branney, 2002; Wolff and Storey, 1984). These variations result from compositional changes of the erupted magma through time. These processes include withdrawal of a compositionally-stratified (differentiated) magma chamber, magma mixing, injections of compositionally different magmas, and conduits modification during collapse caldera eruptions (e.g., Bacon and Druitt, 1988; Carrasco-Núñez and Branney, 2005; de Silva, 1991; Turner, 1980). Typically, vertical zoning tends to present a felsic to more basic compositions due to the withdrawal of the upper, less dense, and more evolved parts of the magmatic sources (e.g., Bacon and Druitt, 1988; Freundt and Schmincke, 1992). However, more recent studies explain the occurrence of compositionally zoned ignimbrites by invoking to more complex and heterogeneous magmatic systems, where interactions of high-melt zones with silicic crystal mush lenses occur (Bachmann and Bergantz, 2008, 2004; Cashman and Giordano, 2014).

General compositional zoning has been reported for the LHVC by Ferriz and Mahood (1984, 1987), marked by a general trend to more mafic and frequent eruptions through time. They interpret that zoning results from the structural weakening of the magmatic system's host rock during the explosive eruptions of the caldera stage (Xáltipan ignimbrite, Faby tuff, and Zaragoza ignimbrite). This led to an easier outcome of mafic products from the base, tapped by the upper and more silicic levels. Later, Willcox (2011) pointed to a magmatic-controlled process strongly influenced by the rate of replenishment by primitive magma, which explains the less-evolved magmatic trend and the triggering of the caldera-forming eruptions. A more complex magmatic system is invoked based on the compositional double-zonation (rhyodacitic-andesitic-rhyodacitic) reported for the Zaragoza ignimbrite (Carrasco-Núñez and Branney, 2005), which is interpreted to result from the interaction of a hybridized andesitic magma intrusion into a rhyodacitic magma reservoir (Carrasco-Núñez et al., 2012).

4. Methods

The XI facies were identified and classified by integrating field observations and a combination of laboratory analyses from vertically-collected samples suites at selected outflows and intracaldera (geothermal wells) localities. The analyses are divided into petrophysical and geochemical. The petrophysical analyses include petrographic descriptions, μCT imaging, gas pycnometry, and water immersion. The geochemical analyses consist of major and trace element geochemistry only for the outflows deposits, as hydrothermal alteration affects the intracaldera deposits. The criteria for localities selection, sample preparation, and description of each analysis are shown in this section.

4.1. Sampling

The petrophysical and geochemical analyses for the outflows were made at samples of known stratigraphic positions from three localities (Table 1). The petrophysical analyses were made along with the thick (40–70 m) LFU, where welding or induration allowed the extraction of consolidated hand-samples (Fig. 4a–c). Here, the consolidated samples were collected along with their field orientation and later cut into cubes, from which cores (cylinders of 2.54 cm diameter and 2.54–5.08 cm long) and plates were extracted for further μCT and petrographic analyses, respectively (see methodology in Cavazos-Álvarez and Carrasco-Núñez, 2020). In the case of non-consolidated samples, the loose material was collected with no orientation. Geochemical analyses were made on outcrops from six localities where the XI is exposed as not consolidated (see location in Fig. 1) and where fresh, lithic-free pumice could be sampled (Fig. 5). In three from the six localities, only the LFU was sampled (Los Molinos – LMo; Tenextepec – TE; and Apulco –AP); while in the other three, sampling covered the LFU, IPF, and UFU (Xonocuautla –XO; Morelos – MO; and La Unión - LU).

Table 1
Localization and type of analyses done for the selected samples. Coordinate Reference System WGS84.

Type of deposit	Type of analysis	Locality	Coordinates	Samples - depth	Unit	Petrography	μCT	Gas pycnometry	Water immersion	Geochemistry
Outflows	Petrophysical	Ixtactenango (IX)	637,301/ 2,181,638	IXe-0m	LFU	✓	✓	–	✓	–
				IXd-10 m	LFU	✓	✓	✓	–	–
				IXc-20 m	LFU	✓	✓	✓	–	–
				IXb-30 m	LFU	✓	✓	✓	–	–
				IXa-40 m	LFU	✓	✓	✓	–	–
		Cuaximaloyan (CU)	639,637/ 2,198,026	CUd-10 m	LFU	✓	✓	–	✓	–
				CUc-50 m	LFU	✓	✓	✓	–	–
				CUb-50 m	LFU	✓	✓	✓	–	–
				CUa-70 m	LFU	✓	✓	✓	–	–
		Zapotitlán (ZA)	633,415/ 2,212,603	ZAc-0 m	LFU	✓	✓	–	–	–
				ZAb-30 m	LFU	✓	✓	✓	–	–
				ZAa-60 m	LFU	✓	✓	✓	–	–
	Geochemical	Xonocuautla (XO)	653,643/ 2,187,218	Xoc	UFU	–	–	–	–	✓
				XOb	IPF	–	–	–	–	✓
				XOa	LFU	–	–	–	–	✓
		Morelos (MO)	650,278/ 2,185,474	MOc	UFU	–	–	–	–	✓
				MOb	IPF	–	–	–	–	✓
				MOa	LFU	–	–	–	–	✓
		La Unión (LU)	635,440/ 2168759	LUc	UFU	–	–	–	–	✓
				LUa	LFU	–	–	–	–	✓
		Los Molinos (LMo)		LMod	LFU	–	–	–	–	✓
				LMoc	LFU	–	–	–	–	✓
				LMob	LFU	–	–	–	–	✓
				LMoa	LFU	–	–	–	–	✓
		Tenextepex (TE)		TEc	LFU	–	–	–	–	✓
				TEb	LFU	–	–	–	–	✓
				TEa	LFU	–	–	–	–	✓
		Apulco (AP)		APc	LFU	–	–	–	–	✓
				APb	LFU	–	–	–	–	✓
				APa	LFU	–	–	–	–	✓
Intracaldera	Petrophysical and geochemical	H-59	661,574/ 2178239	H59-140	–	✓	✓	–	✓	✓
				H59-260	–	✓	✓	–	✓	✓
				H59-360	–	✓	✓	–	✓	✓
				H59-490	–	✓	✓	–	✓	✓
				H59-580	–	✓	✓	–	✓	✓
				H59-660	–	✓	✓	–	✓	✓
				H59-840	–	✓	✓	–	✓	✓
		H-63	661,155/ 2178053	H63-220	–	✓	✓	–	✓	✓
				H63-380	–	✓	✓	–	✓	✓
				H63-450	–	✓	✓	–	✓	✓
				H63-550	–	✓	✓	–	✓	✓
				H63-710	–	✓	✓	–	✓	✓

Geothermal wells H-59 and H-63 were selected as representative from the intracaldera deposits (Fig. 4b). These wells are located in the geothermal field's productive area and comprise the thickest deposits of the XI (H-59 - 780 m; H-63 - 600 m) (Carrasco-Núñez et al., 2017b). Here, sampling intervals are defined by the well logging process, where samples are obtained as millimetric scale, randomly oriented, chips. Petrophysical and geochemical analyses were done in all sampling intervals, selecting the largest and freshest chips for each sample.

4.2. *Petrography*

Petrographic descriptions were made in all samples to identify and quantify the welding features and secondary mineralization. For this, the non-consolidated samples were resin-impregnated and analyzed by a petrographic microscope. For the consolidated samples, vertical thin-sections were made with the in-field position to observe features such as eutaxitic texture to its maximum extent by assuming a vertical welding mechanism. All the petrographic measurements were supported by using the ImagePro software, making computerized quantifications of the textural features. Special attention was paid in describing the matrix consolidation degree, which refers to the compaction grade between individual glass shards that compose the ignimbrite matrix. Also, pumice oblateness was measured, providing a general approach to the grade of vertical compaction of the sample, by assuming that pumice clasts are isometric objects that show ellipsoidal shapes with a shortened and an elongated axis when compressed. On the other hand, the secondary mineralization was quantified using supervised classification tools over the images (Fig. 6).

4.3. *3D imaging and pore analyses: μCT*

Complete 3-D visualization and textural characterization of the consolidated samples were measured by μCT. Samples were analyzed by an Xradia Versa-510 X-Ray Microcomputarized Tomography System in the University Laboratory of X-Ray Microtomography (LUMIR) at the Centro de Geociencias (CGEO) of the Universidad Nacional Autónoma de Mexico (UNAM). For the outflows' samples, these were mounted in sample holders with their field orientation. An inner space of 1000 × 1000 × 700 μm was rendered at a constant resolution of 14.55 nm/voxel. Each analysis was adjusted according to the intracaldera chips' size and shape, resulting in a variable rendered space and resolution. Further image visualization and analysis (Fig. 7) was made using software AVIZO 2019.4, following the methodology proposed by Cid et al. (2017).

The vesicular porosity was quantified by implementing a filter-based methodology that discriminates the vesicular pores from the total porosity, by assuming that vesicles have a relatively more spherical and smoother shape than the intershard spaces and open cracks. This methodology consists in filtering the total pores by geometrical relations such as size, sphericity, and specific surface. For the outflows' samples,

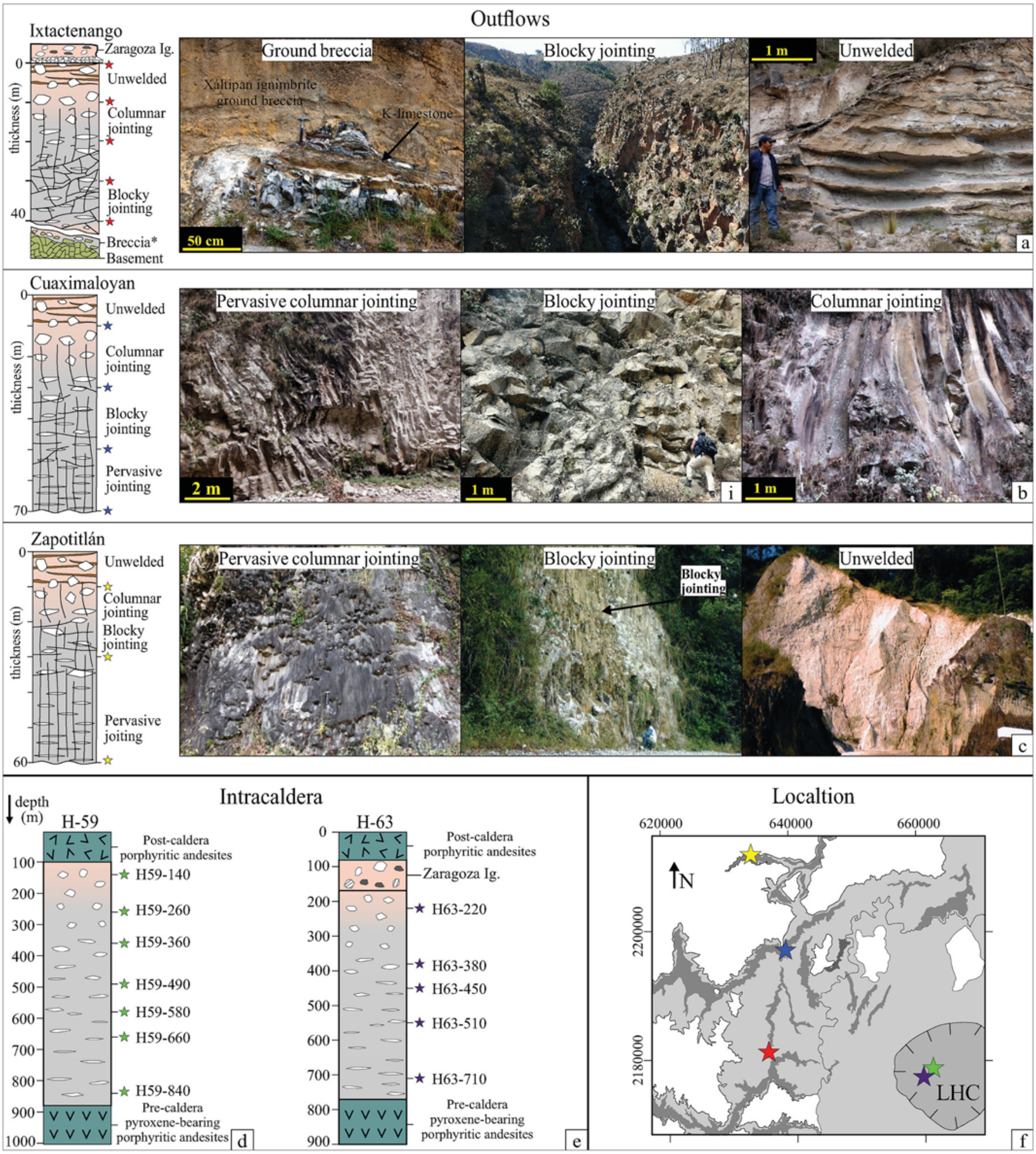

Fig. 4. Location (f) and stratigraphy of the selected outflows' (a–c) and intracaldera localities (d, e), showing the position of the analyzed samples. Photographs showing the welding and alteration variations in the outflows at different stratigraphic levels in the outflows reveal the welding and alteration variations (a–c). Note that in all the outflows the welding variations are gradual, showing from base to top pervasive columnar jointing, blocky jointing, a relatively more spaced columnar jointing, and an uppermost nonwelded facies. The welding features drawn for the intracaldera stratigraphic logs (d–e) are interpretative. A simplified map of part of the LHVC shows the location of the selected sites (f). * Observed in a separate outcrop ~700 m SW from the locality.

we found that the vesicles were accurately segmented by using a pore size >30,815 μm^3, sphericity >0.7, and a specific surface <0.038. While for the intracaldera samples the vesicles were segmented with a size >2063 μm^3, sphericity >0.5, and specific surface >0.2.

4.4. *Gas pycnometry*

Routine porosity and permeability measurements were applied to nine samples from the XI, with different textures or welding levels (Tables 1 and 2). For this, 2.54 cm core plugs with standard lengths were

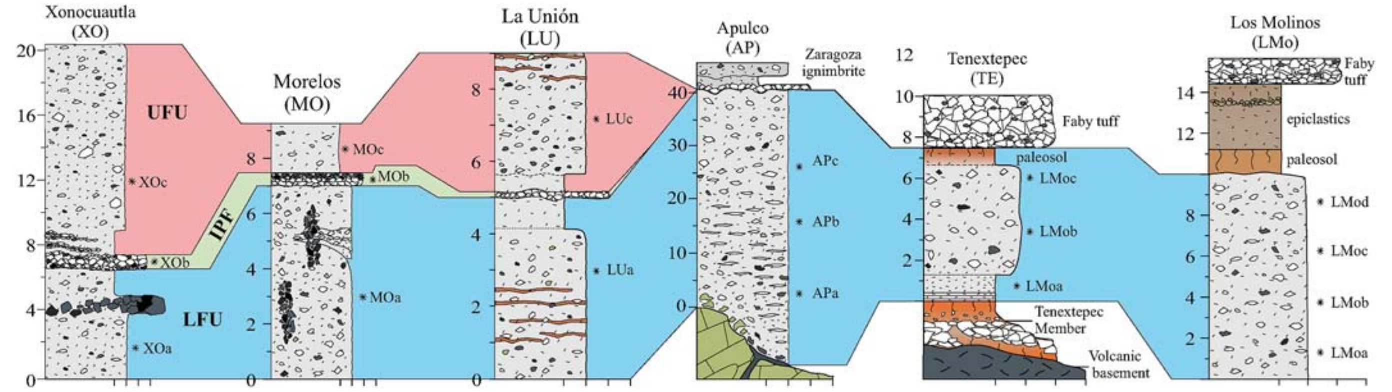

Fig. 5. Correlation of stratigraphic columns of the outflows showing the location and position of samples where the geochemical analyses were done. Note that sampling on the first three columns from left to right covers the LFU, IPF, and UFU, while the three columns at right cover only the LFU. Thickness is not to scale.

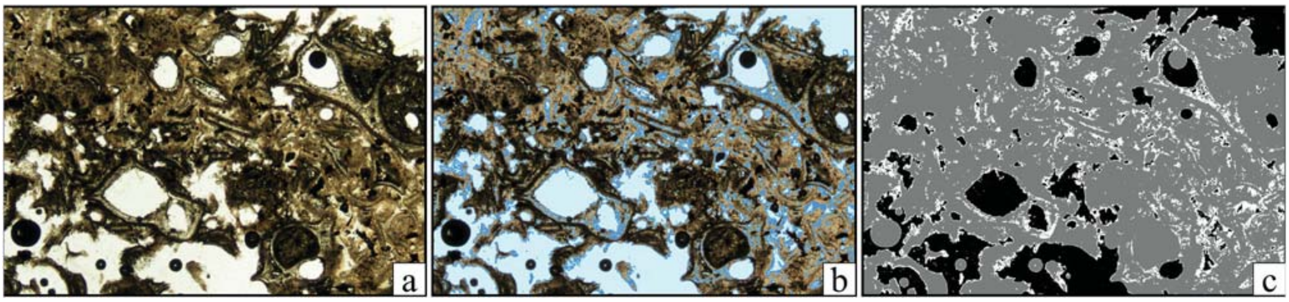

Fig. 6. Photomicrographs of the poorly welded sample (IXc) showing the methodology used to segment the pore fraction and pore-filling minerals. The sample presents a moderately consolidated matrix of slightly adhered and deformed glass shards partially palagonitized. a) Photograph of the unsegmented sample with parallel nicols. b) Combination of the photomicrograph with the segmented pores (white spaces) and secondary minerals (blue). c) Three-component image showing the matrix (grey) pore fraction (black) and secondary minerals (white). (For interpretation of the references to color in this figure legend, the reader is referred to the Web version of this article.)

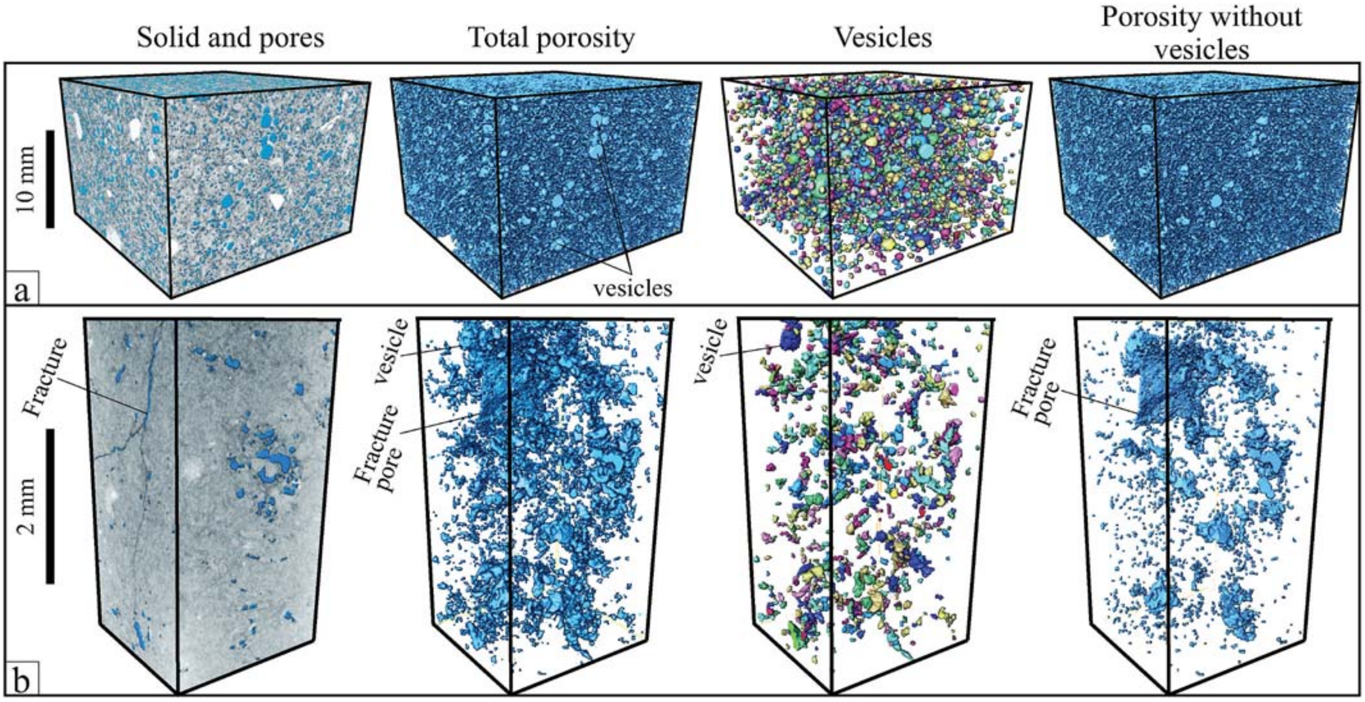

Fig. 7. µCT images showing the total porosity and vesicle segmentation method for outflows (a) and intracaldera (b) samples. From left to right, the images exhibit the relation between the solid (grayscale) pore (blue) fractions; the segmented pore fraction (blue); the separated vesicles, each color representing an isolated pore; the porosity without the vesicles. (For interpretation of the references to color in this figure legend, the reader is referred to the Web version of this article.)

produced at the Applied Geosciences Division, IPICYT (SLP, Mexico). Rock plugs were oven-dried, cleaned, and carefully facetted from the edges. Porosity and density values were determined by routine procedures using a PHI-220 He pycnometer at 240 PSI confining pressure. Gas permeability was measured in an AP-608 automated permeameter-porosimeter on the same core plugs at 500 PSI confining pressures, using the pressure decay method. In both cases, the average value was used.

4.5. Water immersion

Water immersion measurements based on the classical Archimedean principle were applied to samples unsuitable for gas pycnometry experiments to calculate its density. This method was applied for all the intracaldera and unconsolidated outflows' samples. First, the samples were dried and weighted into a high-precision weighing scale; then, the samples were submerged into a graduated test tube, from which the water displacement was measured, representing the sample volume. For the intracaldera samples, at least 20 chips for each logged level were weighted and submerged simultaneously to reduce the observational error. Similarly, for the unconsolidated samples, at least 100 gr of unfractionated material were measured. Finally, the whole-rock density was calculated by dividing the sample weight by its volume.

4.6. Geochemistry: major and trace elements

Sample preparation was made for major and trace elements analyses at the Physical Volcanology Laboratory of the CGEO (UNAM). Major elements were determined by X-ray fluorescence at the Laboratorio Universitario de Geoquímica Isotópica (LUGIS) at the Instituto de Geología (UNAM), following the analytical methodology described in Mori (2007). The trace elements were determined using an Inductively Coupled Plasma Mass Spectrometer (ICP-MS), using a Thermo Series XII, at the Laboratorio de Estudios Isotópicos (LEI) of the CGEO (UNAM) using the procedures described by Lozano-Santa Cruz et al. (1995).

5. Results

5.1. Petrographic features

The ash matrix is mainly composed of platy to cuspate shaped glass shards (87–91 vol %), with a minor content of crystals (1–5 vol %) and lithics (1–8 vol %). Component weighting from the non-consolidated samples indicates that the lapilli fraction consists of pumice (58–81 wt %), basement-derived lithics (9–28 wt %), and black obsidian (4–23 wt %), as a characteristic component. The pumice lapilli is white to grey and mostly aphyric with traces of plagioclase, K-feldspar, biotite, and pyroxene crystals, with minor cases of biotite-rich (~15 vol %) porphyritic pumice clasts. Pumice lapilli shows different textures, but the most characteristic of the XI is bladed to tabular shaped with elongated vesicles that display a woody to silky texture. Pumice also occurs as rounded clasts with round-shaped vesicles. A less common type, which can be found only in the non-welded facies, are grey, highly vesiculated, reticulate-type pumice clasts, even though intermediate textures can be found. The most abundant lapilli-sized lithic clasts are intermediate volcanic rocks from the volcanic basement, but also crystalline, and sedimentary fragments from the basement can be found. Pumice and lithic blocks are scarce but can be rarely found into the lapilli-tuff facies and local lithic breccias and lenses.

5.2. Petrophysical facies

The results from the petrophysical analyses indicate variations along the LFU in all localities (Table 2). The petrophysical variations are observed as changes in the welding grade, and the type and amount of secondary mineralization. For practical purposes, the welding grade is here divided into three types based on the features described by Quane and Russell (2005): the non to poorly welded (ranks I and II), the moderately welded (ranks III-IV), and the highly welded (ranks V and VI) (Table 3). The results are presented individually for outflows and intracaldera localities as follows:

5.2.1. Outflows' petrophysical facies

In the outflows, a general decrease of welding upwards the deposits is observed, while an incipient secondary mineralization is mostly developed in the middle part of the stratigraphy. Based on these variations, we propose three different outflows' facies zones: basal facies, middle facies, and upper facies (Fig. 8a and Table 4).

The outflows' basal facies occurs between 45 and 70 m from the top of the deposit and is represented by the lowermost samples of Ixtactenango and Zapotitlán localities. The samples are light grey color with a highly consolidated texture. A well-developed eutaxitic texture can be observed in thin-section, defined by a highly compacted and foliated matrix composed of partial to totally adhered glass shards. Pumice *fiamme* clasts aligned with the foliation show the highest oblateness ratios ranging from 0.80 to 0.82 (Fig. 9g–i). Pycnometry indicates the lowest effective porosity and permeability values ranging from 3.92 to 8.33% and <0.01 to 0.05 mD, respectively, and the denser samples with 2160 to 2250 kg/m^3. While vesicular porosity is rarely observed at a thin-section, intershard porosity is not observed. On the other hand, open irregular fractures are common and may represent the major pore spaces observed at thin-section scale. The resulting values from all the samples between these depths (45–70 m) indicate highly welded conditions (ranks V-VI). Also, the secondary mineralization is scarce (<1%), and occurs as secondary quartz replacing pumice clasts, and as palagonitization of pumice and glass shards.

The outflows' middle facies occurs between the 25–45 m from the top of the deposit. The samples show a light orange color, with a granular texture that disintegrates when rubbed. The matrix comprises moderately compacted glass shards, poorly foliated, and moderately coalesced (Fig. 9d–f). Individual shards vary in shape from cuspate to bubble walls and show slight to null deformation. Pumice clasts are incipiently foliated with the ash matrix collapsed with oblateness between 0.69 and 0.77. Pycnometry tests indicate that this facies is less welded than the outflows' basal facies, as marked by a higher effective porosity and permeability, ranging from 25 to 32% and 6.11 to 46.38 mD, respectively, and by a lower density ranging from 1720 to 1760 kg/m^3. Therefore, this zone can be classified as moderately welded (ranks III-IV). Microcrystalline quartz occurs as rimming vesicles and filling intershard spaces, reducing primary porosity from 6 to 11.5%.

In all the localities, the outflows' upper facies occurs in the uppermost 25 m. The deposit is completely loose at the outcrop scale, showing a highly porous texture with a characteristic pink to orange coloration and the formation of the nets of subhorizontal veins of partially indurated ash, frequently developing characteristic dish structures with horizontal honeycomb weathering (Fig. 4a). Resin-impregnated thin-sections reveal null to poor adhesion between non-deformed, and non-foliated, bubble wall-shaped glass shards (Fig. 9a–c). Pumice clasts show null to poor deformation. Where deformation is observed, an oblateness of >0.48 ± 0.08 was measured. Gas pycnometry was only made in the poorly consolidated samples at Ixtactenango. The results rendered the highest effective porosity and permeability with values ranging from 49 to 51% and 310.72 to 1557.26 mD, respectively, and the least dense samples ranging from 1210 to 1450 kg/m^3. On the other hand, water immersion was performed in all the non-consolidated samples, resulting in a density range of 1180 to 1420 kg/m^3. Secondary mineralization occurs as palagonitization of the fine ash matrix that fills the intershard spaces as shown in sample Zac (Fig. 9c), and as very fine-grained vapor phase minerals that occur along shard walls (Fig. 9a and b) and in a lesser way by microcrystalline quartz (<1%) precipitated along glass walls.

The normalized vesicular porosity measured by μCT shows a general increase downwards the deposit in all localities. Nevertheless, this

Table 2
Data obtained from petrographic descriptions, micro-CT, He-pycnometry, and water immersion. The results are classified in zones according to the welding grade and type of secondary mineralization.

Type of deposit/Locality		Depth (m)	Sample	Petrography		micro-CT			Gas pycnometry			Water immersion	Welding Rank
				Pumice oblateness	Pore filling by secondary minerals (%)	Porosity (%)	Vesicular Norm (%)	Pore connectivity	Porosity (%)	K Perm (mD)	Density (gr/cm3)	Density (gr/cm3)	
Outflows	Cuaximaloyan	10	CUd	0.55 ± 0.05	2.0	–	–	NA	–	–	–	1420	I
		30	CUc	0.67 ± 0.05	8.0	31.03	5.88	NA	31.03	10.9	1760	–	III
		50	CUb	0.69 ± 0.09	<1	6.86	7.03	NA	6.86	0.047	2210	–	V-VI
		70	CUa	0.80 ± 0.05	<1	8.33	19.19	NA	8.33	0.011	2160	–	V-VI
	Ixtactenango	0	IXe	0.48 ± 0.08	1.0	–	–	NA	–	–		1180	I
		10	IXd	0.50 ± 0.07	4.7	51.90	13.56	NA	51.90	1557.3	1210	–	I
		20	IXc	0.66 ± 0.08	6.8	49.73	30.84	NA	49.73	310.8	1450	–	II
		30	IXb	0.77 ± 0.09	9.7	32.94	51.05	NA	32.94	13.5	1740	–	III
		40	IXa	0.82 ± 0.11	11.5	29.59	71.48	NA	29.59	6.1	1720	–	III
	Zapotitlán	0	ZAc	0.50 ± 0.1	<1	–	–	NA	–	–	–	1250	I
		30	ZAb	0.64 ± 0.08	6.0	25.54	28.62	NA	25.54	46.376	1730	–	III
		60	ZAa	0.81 ± 0.1	<1	3.92	38.15	NA	3.92	0.002	2250	–	V-VI
Intra-caldera	H-59	40	H59-140	–	<1	3.63	7.19	Yes	–	–	–	1556	II
		160	H59-260	–	5.0	5.74	15.29	–	–	–	–	1685	II
		260	H59-360	–	20.1	1.13	2.24	–	–	–	–	1710	III
		390	H59-490	–	24.2	0.48	35.44	–	–	–	–	2032	IV
		480	H59-580	–	11.6	0.80	15.90	–	–	–	–	2080	IV
		560	H59-660	–	32.9	0.19	33.50	–	–	–	–	2240	V
		740	H59-840	–	82.3	2.26	48.57	–	–	–	–	2380	VI
	H-63	50	H63-220	–	<1	9.86	2.49	Yes	–	–	–	1455	II
		210	H63-380	–	<1	3.57	24.19	–	–	–	–	1650	II-III
		280	H63-450	–	28.0	0.36	40.61	–	–	–	–	1788	III
		380	H63-550	–	25.3	1.20	62.99	–	–	–	–	2130	IV-V
		540	H63-710	–	18.5	0.20	11.53	–	–	–	–	2360	VI

Table 3
Petrographic and petrophysical characteristics to define the welding grade in this work. Welding ranks based on the classification scheme from Quane and Russell (2005).

Facies/Ranks*	Ash matrix	Pumice lapilli	Porosity	Density
Non to poorly welded (ranks I-II)	Unconsolidated to incipiently coherent ash matrix. Glass shards loosely packed, randomly orientated (unfoliated), with little to no adhesion, and undeformed. Highly porous with a dominant intershard porosity.	Undeformed and unfractured. Oblateness <0.67	>34	>1350
Moderately welded (ranks III-IV)	Poorly to moderately consolidated ash matrix. Glass shards present slight coalescence and moderate contact area. Individual glass shards are recognized. Spehrical bubble-shaped walls of shards are visible and non to poorly deformed. Evidences of incipient foliation.	Slightly to moderately deformed into *fiamme*, and orientated with foliation. Internal cracks are common. Oblateness 0.67–0.8	34 - 13%	1350–2150
Highly welded (V-VI)	Highly consolidated ash matrix. Glass shards are moderately to strongly adhered. Individual shards hardly recognized with evidences of high plastic deformation. Moderately to well-developed foliation.	Strongly to fully collapsed clasts into *fiamme* and oriented with foliation. In high grade of welding, pumice clasts are hardly recognized. Oblateness >0.8	<13%	>2150

increase is not systematic and occurs in different proportions and rates. The increase in vesicularity is better observed in the Ixtactenango samples, where the transition occurs from the upper to the middle facies. Here the proportion of vesicles ranges from 13.6%, which indicates an intershard dominating porosity at 10 m depth, to 71.5% at 40 m characterized by a vesicle dominating porosity. In the transition from the middle to basal facies, vesicular porosity also increases to a lower extent, as shown by the Cuaximaloyan and Zapotitlán samples, ranging from 5.9 to 19.2% and 28.6–38.2%, respectively. The low proportion of vesicles measured by μCT, absence of intershard spaces, and frequent occurrence of open fractures in the basal facies, indicates that in these samples porosity is dominated by open fractures.

5.2.2. *Intracaldera petrophysical facies*

Based on samples from wells H-59 and H-63, and following the same welding grade classification applied for the outflows' deposits (Table 3) and secondary mineralization measurements, three zones were classified for the intracaldera deposits: basal, middle, and upper facies (Fig. 8b and Table 4).

The intracaldera basal facies occurs between 800 and 510 m depth. The chips are highly consolidated with vitric surface and conchoidal fracturing. A moderately to highly compacted matrix is observed (Fig. 10 f, g, l). Glass shards are hard to distinguish due to vapor phase alteration, but foliation and high adhesion between shards can be observed. Pumice clasts are partial to totally collapsed. Nevertheless, a few pumice clasts were observed, and therefore oblateness could not be determined. μCT porosity was calculated between 0.20 and 2.26%, the lowest porosity value for these deposits. Imaging from μCT also reveals that porosity is composed of a combination of vesicles, intershard, intrapumice, and fracture pores. Density by water immersion was calculated between 2240 and 2380 kg/m^3. These are the denser samples from these deposits. This zone is characterized by irregular and perlitic fractures and partial to full pore filling by secondary minerals, including microcrystalline and polycrystalline quartz, polycrystalline calcite, chlorite and, pyrite, and alteration of glass to oxides, palagonite, and chlorite. Measurements in all the samples from this facies indicate that pore filling quartz and calcite reduce pore spaces from 18.5 to 82.5%

The intracaldera middle facies occurs between the 510 to 240 m depth. The chips present moderate to high consolidation. The matrix presents moderate compaction with moderately deformed glass shards in thin-section, as observed in sample H59-490 (Fig. 10d). Flattened pumice clasts were observed in a few cases (Fig. 10k, sample H63-550). Nevertheless, no oblateness could be measured due to the lack of sufficient clasts. Porosity by μCT was measured between 0.36 and 1.13%. Density by water immersion resulted in 1710 to 2130 to kg/m^3. Irregular fractures are ubiquitous and commonly filled by secondary minerals (Fig. 10d). Secondary minerals are reducing pores between 11.6 and 28%.

The intracaldera upper facies occurs in the uppermost 240 m. The chips show a moderate to poorly consolidated granular texture. At thin-section, the matrix is poorly compacted and highly porous. Glass shards are hard to distinguish due to vapor phase alteration. Nevertheless, no foliation or adhesion between shards was observed. μCT rendered the highest porosity for this type of deposit measured between 3.57 and 9.86%. Porosity is composed of intershard spaces and by matrix and intrapumice vesicles. In the rest of the samples of this zone, porosity is dominated by intershard spaces. Fractures are rarely observed at this zone and are commonly open fractures with evidence of widening by dissolution (Fig. 10b). Density measurements by water immersion resulted in a density ranging from 1445 to 1685 kg/m^3. Secondary mineralization is dominated by glass devitrification to microcrystalline quartz, oxidation of crystals and lithics, and pyrite precipitation. Pore reduction due to secondary mineralization was quantified up to 5%.

The normalized vesicular porosity in both well logs shows a general increase downwards the deposit but slightly decreases in the middle to basal facies transition. The upper facies show the lowest vesicular porosity ranging from 7.2 to 15.3% and 2.5–24.2% for wells H-59 and H-63, respectively. These values increase to its maximum near the 400m depth, resulting in 35.4% and 63% for wells H-59 and H-63, respectively. These values slightly decrease in each well around the 500m depth (middle to basal facies transition), dropped to 15.9, and 11.5% in wells H-59 and H-63, respectively. In this zone, it is also observed the occurrence of open and partially filled fractures (Fig. 10e, l) that may contribute to the total porosity and therefore cause this vesicular porosity decrease. Vesicular porosity increases downwards the deposit, reaching 48.6% as observed in log H-63, and where secondary minerals fill the fractures, as observed in thin-sections (Fig. 10g).

5.3. *Geochemical facies*

In this section, the geochemical data obtained during this work (major and trace elements) are presented for the outflows' deposits by using the TAS diagram and selected discriminant diagrams (Fig. 11) frequently used for ignimbrites in geothermal fields (Bignall et al., 1996). These results are compared with those obtained from previously reported analyses of the XI intracaldera, Faby tuff, and Zaragoza

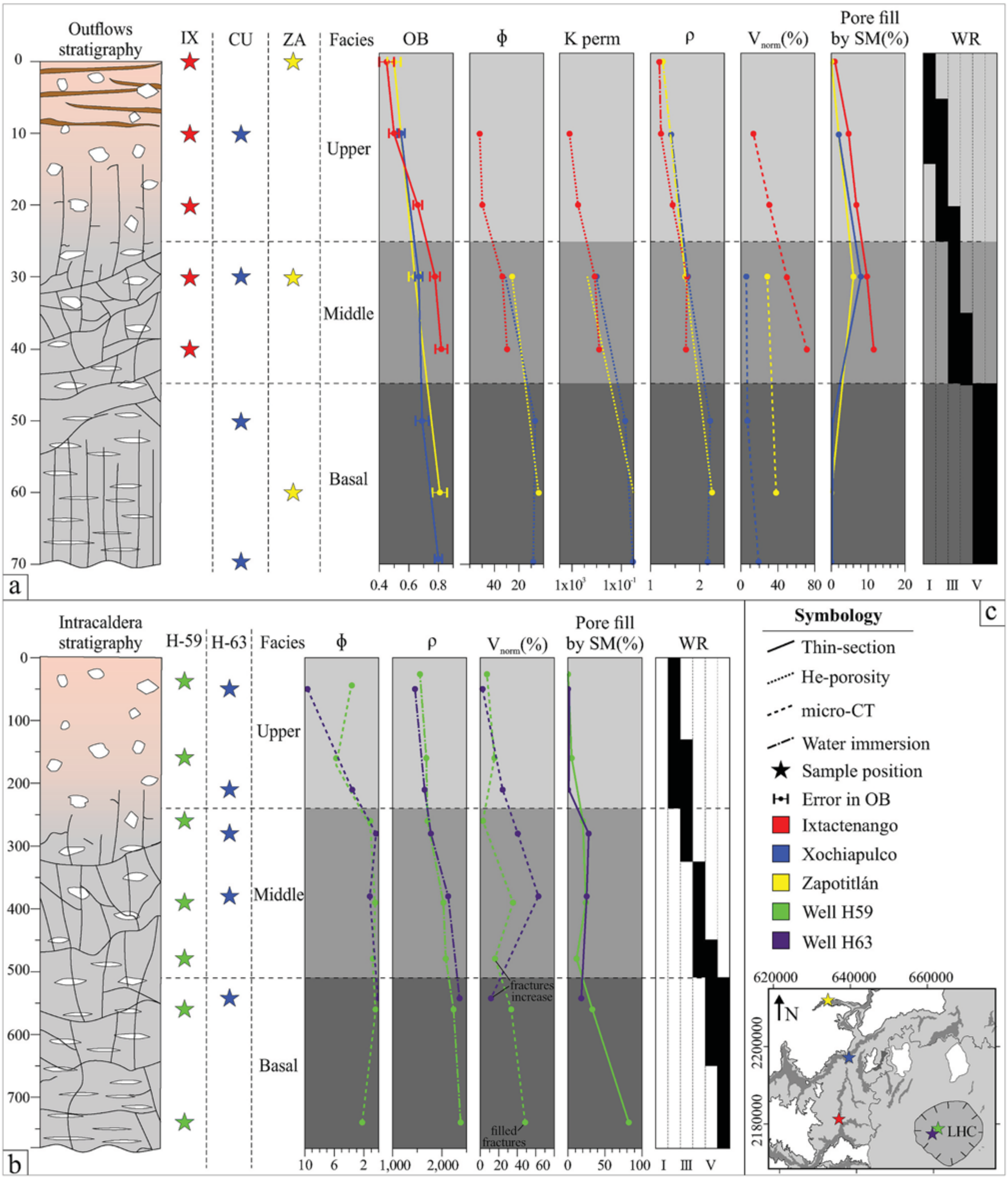

Fig. 8. Physical parameters and facies variations plotted along stratigraphic columns showing the position of the analyzed samples for: a) outflows' deposits, b) intracaldera deposits. Note that for each environment, three facies were proposed (see text for details). The plotted values include oblateness (OB), porosity (ϕ), density (ρ), - Klinkenberg permeability (Kperm), normalized vesiculation (V_{norm}), amount of pore filling by secondary minerals (SM), and welding rank (WR) based on the Quane and Russell (2005), classification scheme. The location of the samples and symbols used are shown in c).

ignimbrite (see Supplementary data 1).

Despite the similarities of both flow units (LFU and UFU), the TAS diagram shows a rhyolitic to trachytic transition upwards the ignimbrite by separating the LFU from the IPF and UFU (Fig. 11a). The LFU is of rhyolitic composition (70.9–76.2 wt% SiO_2), while the IPF and UFU samples lay into between the rhyolite-trachyte fields (67–70.7 wt% SiO_2), and with a general lower alkali content than the LFU. A more variable distribution of the overlying Faby tuff and Zaragoza ignimbrite is observed extending towards more basic compositions. When plotting the intracaldera samples, it was possible to separate two fields with a similar trend of the outflows. For this, the uppermost samples in each well log that showed a slightly more basic composition were separated

Table 4
Summary of the main features used to classify the facies for both environments.

Type of deposit	Facies	Stratigraphic position	Porosity (%)	Density (kg/m^3)	Permeability (mD)	WR	Pore filling by secondary minerals
Outflows	Upper	25–0	49–51	1180–1450	310.72–1557.26	I-II	<1%
	Middle	45–25	25–32	1720–1760	6.11–46.38	III-IV	6–11.5%
	Basal	70–45	3.92–8.33	2160–2250	<0.01–0.05	IV-V	<1%
Intracaldera	Upper	240–0	3.57–9.86	1445–1685	–	I-II	<5%
	Middle	510–240	0.36–1.13	1710–2130	–	III-IV	11.6–28
	Basal	780–510	0.20–2.26	2240–2380	–	IV-V	18.5–82.5

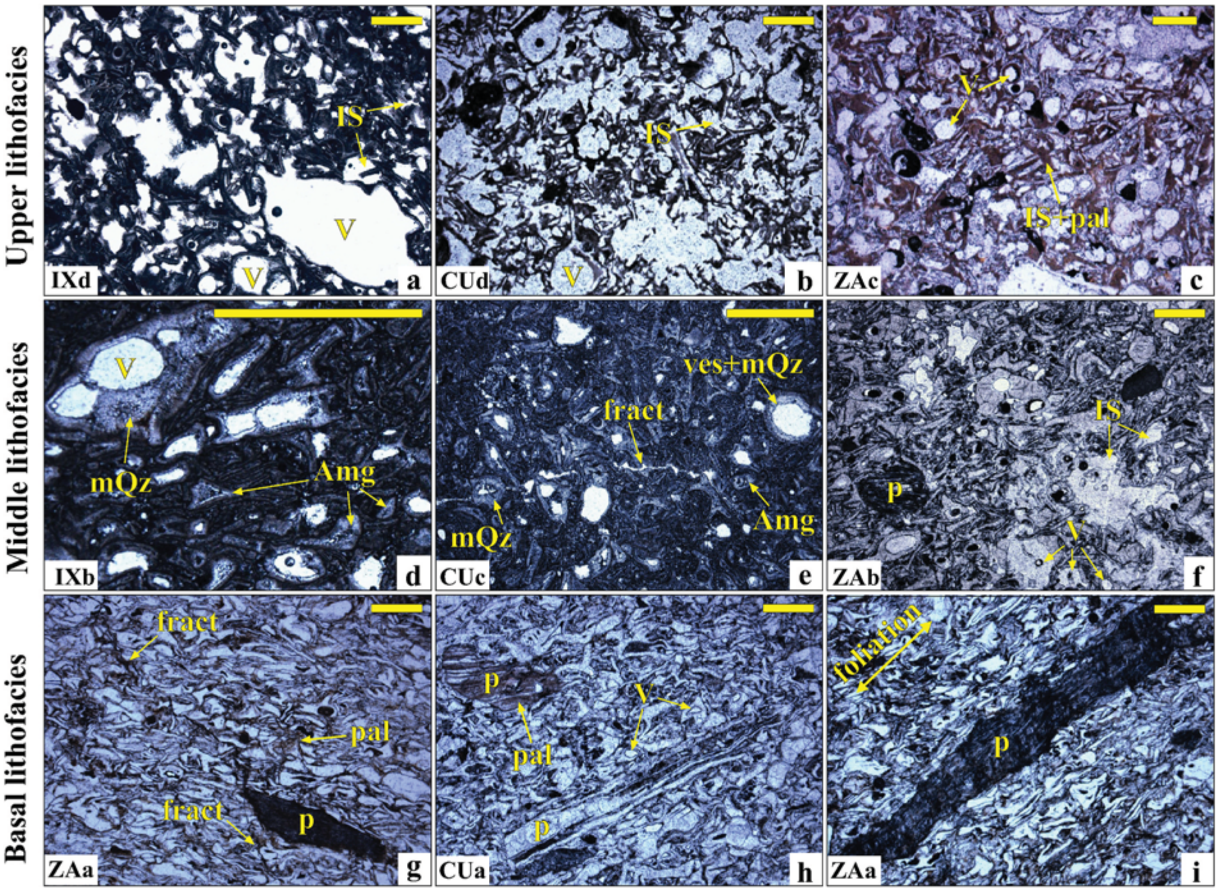

Fig. 9. Photomicrographs of the outflows' samples arranged vertically according to their facies. In the upper facies, the samples present a highly porous, unconsolidated to incipiently coherent ash matrix of loosely packed glass shards randomly orientated (a–c). The middle facies (d–f) includes moderately porous samples composed of moderately consolidated ash matrix that present slight coalescence and moderate contact between glass shards. Samples from the basal facies (g–i) are porous-poor and made of a highly consolidated matrix made of strongly adhered glass shards with a well-developed eutaxitic texture.

and inferred to correspond to the IPF or UFU.

A combination of discrimination diagrams that use immobile elements ratios (Ta/Lu vs. Zr/Yb, Ta/Lu vs. Zr/Y, and Nb/Ta vs. Zr/Lu), also serves to identify the compositional variations of the XI deposits, their relationship with the overlying Faby tuff and Zaragoza ignimbrite, and to invoke a similar behavior for the intracaldera deposits (Fig. 11b–d). A clear difference between the LFU and the IPF-UFU can be observed in all the diagrams. Furthermore, it is observed a gap between the IPF and UFU fields with the Zaragoza ignimbrite and Faby tuff fields (except for Ta/Lu vs. Zr/Yb and Nb/Ta vs. Zr/Lu ratios). Finally, when comparing the outflows' fields with those of the intracaldera, it can be observed that the base and top samples from both types of deposits form well-defined, separated fields, confirming that both the outflows and intracaldera deposits show a vertical geochemical variation.

5.4. *Intercalated lavas: lava flows or lithic breccias?*

Several tens of meter-thick andesitic lava flows have been reported within the XI in some geothermal wells (Carrasco-Núñez et al., 2017b, and references therein). These position of these layers is intriguing, particularly because their thickness and lack of lateral continuity are not compatible with "intracaldera" lavas. Some of the layers of rhyolitic composition have been recently interpreted as small intrusions emplaced during the postcaldera volcanism (Urbani et al., 2020). On the other hand, thin-section analyses from borehole samples indicate that most of these lava bodies are porphyritic andesites, with some exceptions where rhyolitic and sedimentary clasts are observed (e.g., well H-20). These andesite bodies contrast with the highly-viscous, felsic domes and cryptodomes interpreted by Urbani et al. (2020).

We propose an alternative hypothesis in which these layers could represent lithic-rich breccias of local and irregular distribution that formed during the caldera collapse event. To unravel this hypothesis,

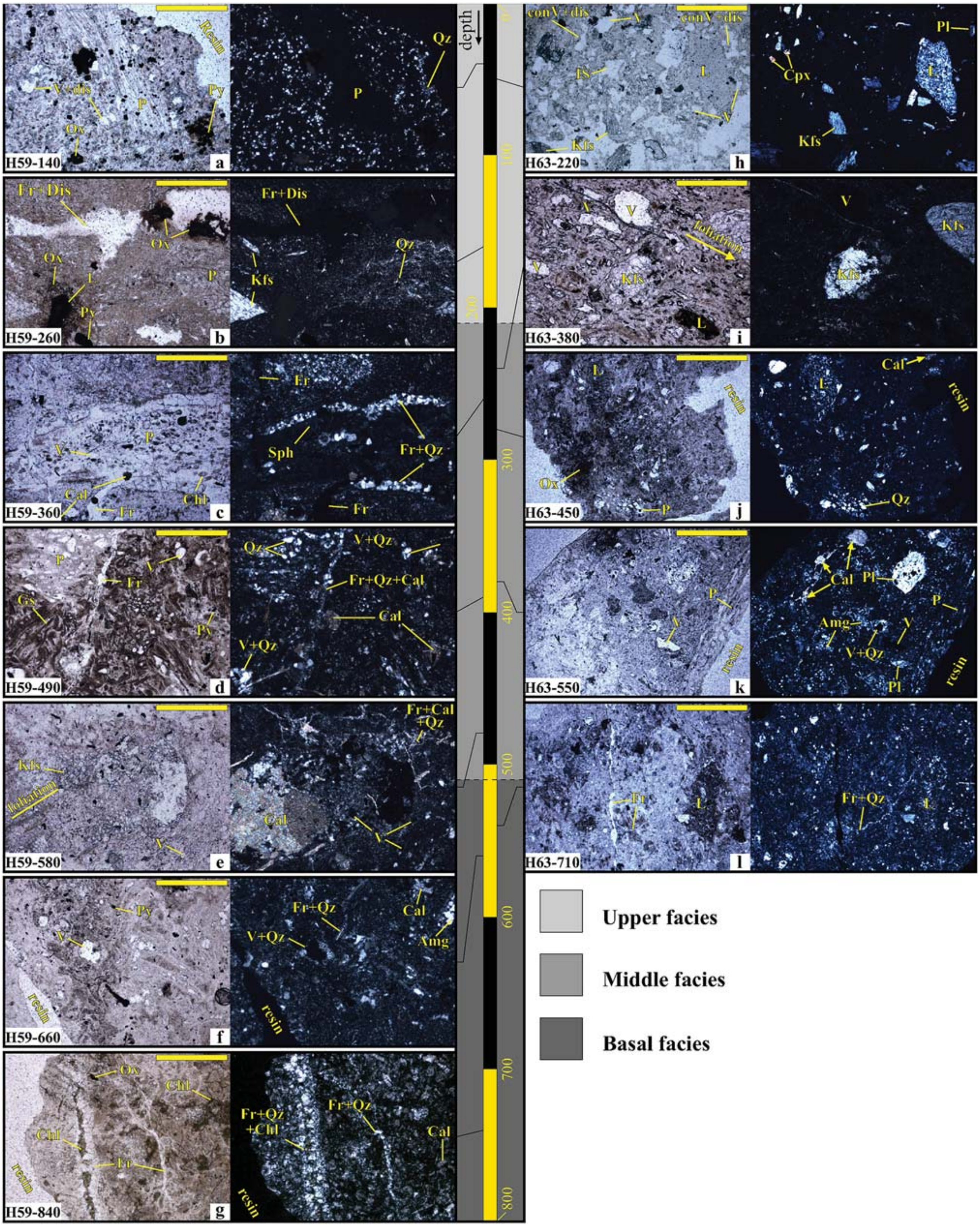

Fig. 10. Photomicrographs of the intracaldera samples vertically arranged according to their logged depth (indicated at the lower left corner of each photo). The same textural features as for the outflows were considered to classify these samples into their corresponding facies. In the upper facies, the samples present a highly porous, unconsolidated to incipiently coherent ash matrix of loosely packed glass shards randomly orientated. The middle facies include moderately porous samples composed of moderately consolidated ash matrix showing slight coalescence and moderate contact between glass shards. Samples from the basal facies are poorly porous and made of a highly consolidated matrix made of strongly adhered glass shards with a well-developed eutaxitic texture.

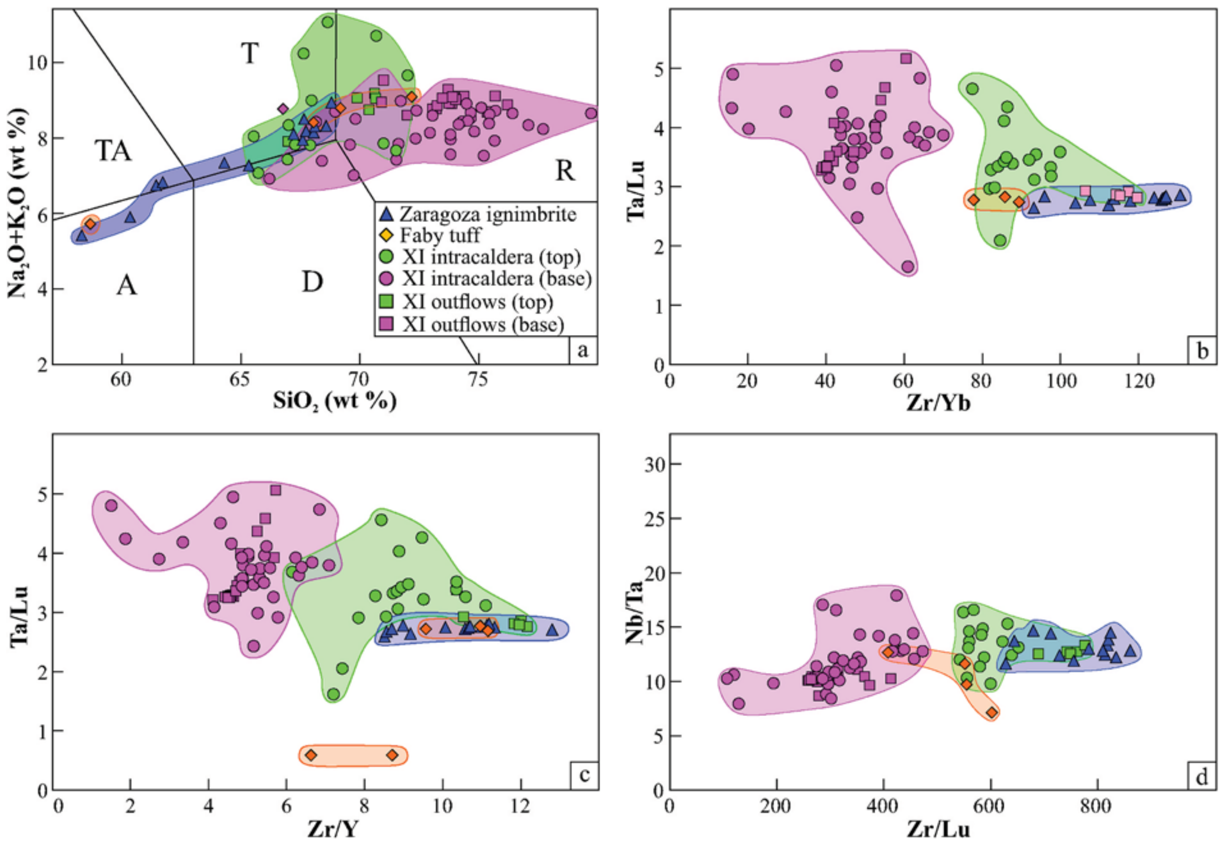

Fig. 11. Plots of the geochemical data using the total alkalis vs. silica (TAS) and Ta/Zr vs. Zr/Yb, Ta/Lu vs. Za/Y, and Nb/Ta vs. Zr/Lu discrimination diagrams. In all the diagrams, the groups of the Xáltipan ignimbrite outflows, Xáltipan ignimbrite intracaldera, Faby tuff, and Zaragoza ignimbrite, are distinguished (see text for more details).

geochemical and petrographic analyses of lava samples from six well logs were performed (see Supplementary data 2). From these analyses, evidence was sought indicating their origins, such as geochemical affinity with other volcanic units (precaldera, syncaldera, or postcaldera), the occurrence of diverse types of lithics at same stratigraphic levels, and fragmentation evidence. To compare the composition of the intercalated lavas with the precaldera and postcaldera lavas, a Zr/Nb vs. Nb/Y discrimination diagram was used. It is observed an almost entirely overlapping of the intracaldera lavas with the precaldera units (and plotting away from the postcaldera lavas or dikes), suggesting a geochemical affinity between these groups. In contrast, the syn-caldera (XI samples) and postcaldera units are different in composition, showing no correlation at all (Fig. 12). Furthermore, petrographic observations from all samples present either lithic heterogeneities (Fig. 13a and b) or pervasive fracturing (Fig. 13c), standard features in lithic breccias that may form as lag and landslide breccias during caldera collapse events (Druitt and Sparks, 1982; Lipman, 1997; Walker, 1985).

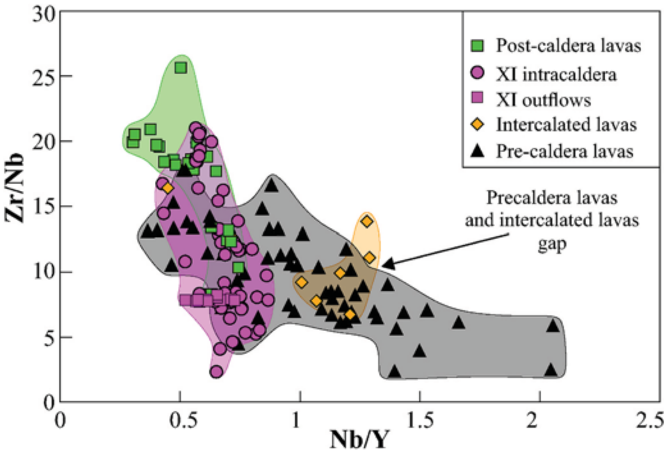

Fig. 12. Zr/Nb vs. Nb/Y discrimination diagram showing the signature of the precaldera lavas, intercalated lavas, postcaldera lavas, and Xáltipan ignimbrite. Note the gap between the intercalated lavas with the precaldera lavas.

6. Facies variations

6.1. Vertical variations

Even if in both environments (outflows and intracaldera), the thickness of the XI differs in one order of magnitude (~70 m for the outflows and ~780 m for the intracaldera), vertical facies variations are observed to behave in similar ways.

The most evident analogy is observed in the welding degree variation, which exhibits a gradual increase downwards the deposits ranging from ranks I to VI. In both types of deposits, the three classified facies match to the same welding ranks, with a basal, middle and upper facies that corresponds to ranks I and II (non to poorly welded), III and IV (moderately welded), and V and VI (highly welded), respectively. Welding-related fracturing is similar for both environments. In the three localities, where the petrophysical analyses were performed, columnar jointing shows a transition in the fracturing upwards, varying from pervasive columnar jointing near the base (30–40 cm spacing between columns at 70 to 55 m from top), passing upwards to blocky jointing (irregular spacing at 55 to 30 m from top), and ending with a more spaced columnar jointing (50–80 cm spacing between columns at 30 to 15 m). Although these variations cannot be seen directly in the

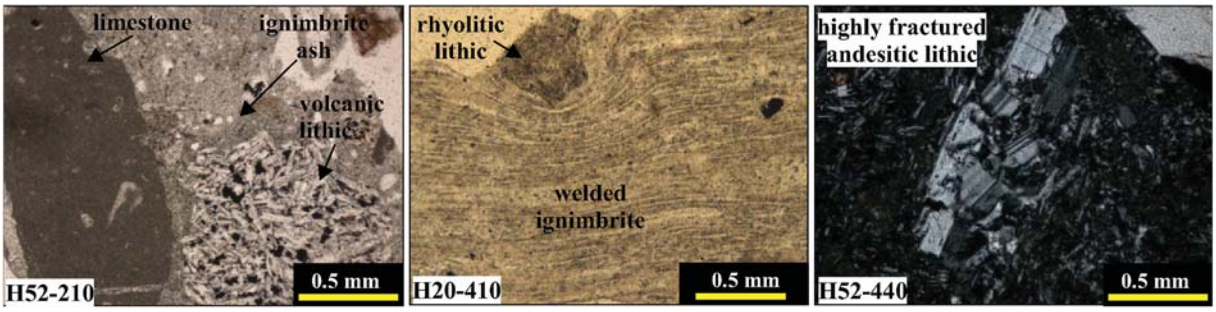

Fig. 13. Photomicrographs showing evidence of breccia deposits that include: heterogeneous lithics (a), rhyolitic lithics into the welded ignimbrite (b), and fracturing of volcanic lithics (c).

intracaldera deposits, it is possible to observe through thin-sections that the intracaldera basal facies show pervasive fracturing filled by secondary minerals (Fig. 10g). We observe that fractures and secondary mineralization decrease through the middle facies, becoming almost negligible in the upper facies. Fractures in the middle and upper facies are partial to not filled by secondary minerals, and, in some cases, they show evidence of dissolution along the crack borders, which may cause the enlargement of the fracture porosity (Fig. 10b), and contribute to the creation of permeable paths.

The welding effect is also observed by examining the total porosity versus the vesicular porosity measured by microCT imaging. In all the outflows and intracaldera deposits here examined, the normalized vesicular porosity increases with depth at the same time that total porosity decreases. This can be explained because when welding occurs, the first reduced pores are the intershard spaces, which results in a relative increase of the vesicular porosity.

Even if secondary mineralization shows vertical changes in both environments, these cannot be adequately correlated because, in the intracaldera deposits, the secondary mineralization is more pronounced, as they are affected by the geothermal system's influence. In this case, secondary mineralization occurs as a propylitic alteration suite that increases gradually downwards the deposits and occurs as microcrystalline quartz, and calcite and as chlorite, pyrite, epidote, and oxides. Under these conditions, secondary mineralization directly affects the deposit's porosity, reducing it up to 82.5% in the basal facies, to 5% in the upper facies. On the other hand, the outflows' deposits show a simpler suite of secondary minerals, composed by microcrystalline quartz and minor amounts of oxides and palagonite along the borders of the glassy material. This suite is more typical of low-temperature hydrothermalism due to magmatic or meteoric water incorporated into the deposit during its cooling. In these cases, porosity is also reduced by secondary minerals, being the middle facies the most affected with a pore reduction of 6–11.5%, while the upper and basal facies does not show significant pore reduction (<1%).

Geochemical results point to a compositional transition varying from rhyolitic near the base (LFU) to trachytic in the last stage of the eruption (IPF and UFU), being this last of similar composition to the subsequent Faby tuff and Zaragoza ignimbrite. This compositional transition of the XI leads to the idea of a compositionally heterogeneous magmatic chamber, and that the eruption may be triggered by the interaction of crystal mush bodies with high-melt zones, as reported for the Zaragoza ignimbrite at 70 ka (Carrasco-Núñez et al., 2012).

The geochemical and petrographic evidence found in the intercalated lavas supports the hypothesis that these layers represent different lithic breccias levels instead of lava flows (Carrasco-Núñez et al., 2017b) or intrusions (Urbani et al., 2020). This evidence includes the positive geochemical correlation of the intercalated lava samples with the precaldera units (Fig. 12), suggesting that these samples may be blocks fragmented and incorporated into the pyroclastic currents that filled the newly-formed Los Humeros caldera. This is also supported by the contrasting geochemical signature of these precaldera lavas with the XI and postcaldera units, suggesting that the former corresponds to a different magmatic stage of the LHVC evolution, possibly to the 1.4–2.6 Ma precaldera volcanism (Carrasco-Núñez et al., 2018). Furthermore, the evidence of fractures that cut crystal and matrix from the lithics suggests that these rocks may have experienced fragmentation, which could occur during the eruption or transport of the PDCs (Fig. 13c). Furthermore, heterogeneous clasts (sedimentary and diverse volcanics) embedded into the XI matrix suggest a mixture of lithics during a breccia-forming process (Fig. 13a and b). These breccias may form by the erosion of the vent or conduit (lag breccias) (Druitt and Sparks, 1982; Walker, 1985) and by the collapse of unstable, inner-caldera walls during caldera subsidence (landslide breccias) (Lipman, 1997).

Along with this evidence, the lag and landslide breccias' hypothesis is conceptually supported by embracing the eruptive history proposed for the outflows by Cavazos-Álvarez and Carrasco-Núñez (2020). This work proposes a practically continuous (with only a brief eruption waning between the two main flow units) eruption and deposition of the ignimbrite, giving no time for the emplacement of tens-of-meters thick lava flows. Also, the existence of these coarse lithic-rich breccias at depth associated to the formation of Los Humeros caldera should not be a surprise, as there are very scarce reports of these deposits in the surficial exposures (Cavazos-Álvarez and Carrasco-Núñez, 2020; Willcox, 2011) and therefore is highly probable that they must be buried, but were not recognized until now.

6.2. Lateral variations

Two correlation profiles, derived from selected well logs, were built to show the lateral variations of the XI facies (Fig. 14). These profiles show that the intracaldera deposits have drastic thickness variations, ranging from 170 m (well H-25) to 780 m (well H-59).

These variations indicate that the XI emplaced over a highly irregular surface, which may be due to two combined factors. 1) An uneven pre-eruptive landscape formed during the LHVC precaldera stage, where the ground was formed mainly by lava fields and multiple rhyolitic domes. 2) Highly marked differential subsidence during the westwards-tilting, trapdoor-piecemeal, caldera collapse model (Norini et al., 2019, 2015; Willcox, 2011).

The XI intracaldera facies association, described in the geothermal wells H-63 and H-59, was identified in the other examined wells by two correlation profiles (Fig. 14). In both profiles, it is observed that the three facies are present in the northwestern sector, where the XI is thicker. On the other hand, through the southern and eastern sectors, where the XI is thinner, the highly-welded zone is not present. This observation suggests that petrophysical facies distribution is controlled by paleotopographic irregularities where the ignimbrite ponded, and where the highly-welded basal facies occurs preferentially in the thickest (>400 m) deposits located into the northwestern sector of the Los Potreros caldera.

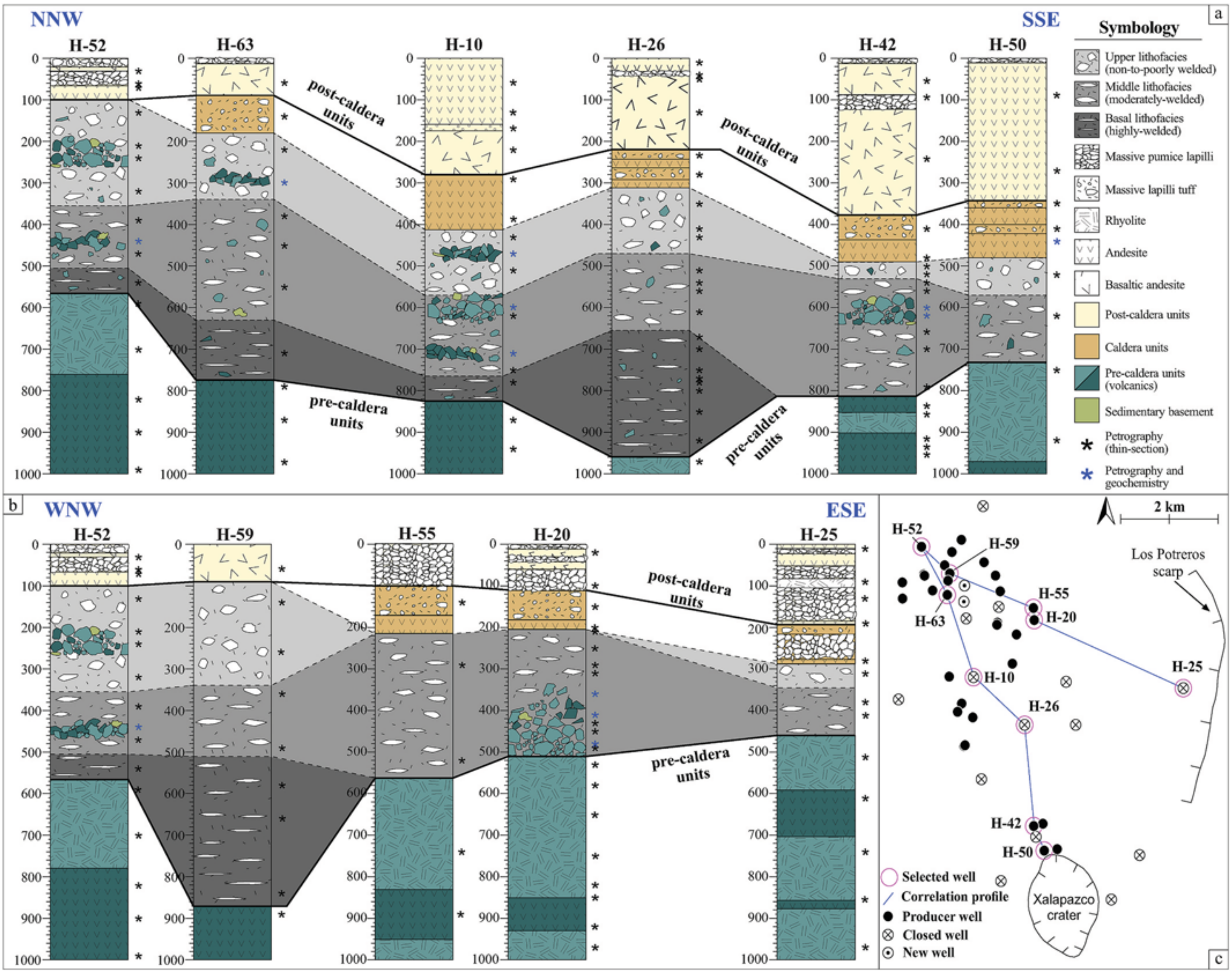

Fig. 14. Two subsurface profiles showing the XI intracaldera deposits and petrophysical facies correlations. a) NWN – SSE profile; b) WNW – ESE profile; c) Sketch map showing the locations of the profiles.

6.3. Implications of the facies variations for the geothermal field

The results of the study show that the facies variations based on the welding of the XI within the caldera are systematic and correlate well with those observed on the outflows' deposits. Vertical variations show a welded basal zone behaving as a low-permeable layer, traditionally regarded as the caprock (aquitard) layer of the LH geothermal system. However, lateral variations indicate that the welding exhibits a heterogeneous lateral distribution strongly controlled by the ignimbrite thickness, where the deposit is > 400 m thick, the complete facies association is more prone to occur. This means that the XI presence is not unequivocally related to the presence of impermeable conditions that may serve as a seal for geothermal fluids. On the contrary, it is observed a strongly variable (vertically and laterally) facies associations that determine the permeable or impermeable conditions, which are in turn, controlled by the thickness of the deposit. Therefore, it is becoming now imperative to identify the type of facies present on the studied samples to better understand the general distribution of the permeable zones favoring the confining conditions required to configure any geothermal reservoir.

7. Conclusions

The XI is an excellent example of a multi-facies ignimbrite showing petrophysical and geochemical zonation that can be recognized in their outflows and their equivalent intracaldera deposits.

Its petrophysical variations are controlled by the welding degree and secondary mineralization. Welding ranges from not-to high welded (ranks I to VI; Quane and Russell, 2005) and shows a systematic increase downwards the deposits, reaching highly-welded (ranks V-VI) conditions. Secondary mineralization is more evident in the intracaldera deposits than the outflows, showing propylitic alteration minerals (quartz, calcite, chlorite, pyrite, oxides, palagonite) associated with the active geothermal system. In both cases (outflows and intracaldera deposits), secondary mineralization occurs as mineral precipitation, and therefore are pore reducing factors.

A three-facies association was identified by analyzing the petrophysical properties in the outflows and intracaldera deposits.

1) The basal facies represents the highest welded deposits (ranks V-VI), where the porosity and permeability show the lowermost values. In this facies, intershard porosity is strongly reduced due to the matrix's welding compaction, causing the closure of permeable paths and leading to porosity dominated by isolated vesicles. Here, gas

pycnometry in the outflows' deposits indicates a practically impermeable media (<0.01–0.05 mD). For the intracaldera basal facies, the porosity is also reduced by pervasive propylitic mineralization related to the geothermal system in addition to the welding effects.

2) The middle facies in both environments is marked by moderate welding (ranks III and IV) with partial pore filling by secondary mineralization. Here, total porosity is controlled by a sum of intershard, vesicular, and fracture spaces, partially filled by secondary mineralization. In both environments, the media is moderately porous and shows semi-permeable conditions (6.11–46.38 mD).
3) The upper facies is defined by the least welded (ranks I and II) and consolidated deposits. Here, porosity is dominated by intershard spaces, and secondary mineralization does not substantially affect the pore fraction. Gas pycnometry in the outflows indicates a highly permeable media (310.72–1557.26 mD).

Geochemical analyses indicate compositional variations in the XI from the LFU (rhyolitic) though the UFU (trachytic-rhyolitic). This compositional zonation may result from high-melt and crystal mush interactions in a highly heterogeneous magma chamber. The ending composition of the XI is similar to those documented for the following eruptions of the caldera stage (Faby tuff and Zaragoza ignimbrite), suggesting that this magma composition remained for a long time (almost 100ky) in the reservoir.

Geochemical and petrographical analyses in lavas intercalated into the XI intracaldera deposits provide evidence that these zones correspond to breccias formed during the caldera collapse event (lag and landslide breccias), instead of lava flows or intrusions.

The XI shows substantial thickness variations into the caldera mainly controlled by the pre-eruptive topography and the irregular and chaotic subsidence during a piecemeal-trapdoor collapse of the Los Humeros caldera. Correlation profiles along well logs from the geothermal field shows a direct relationship of the facies association with the thickness of the deposit. When the thickness is > 400 m, the basal facies developed, and when <400 m, only the middle and upper facies occur. This means that where the XI ponded with >400 m, its base, which has impermeable conditions, may behave as a cap rock for the geothermal system. . However, we observe that these conditions do not have a lateral continuity and therefore, this "caprock" have a restricted distribution depending of the absence of presence of that ignimbrite's welded basal facies.

The similarity between the facies associations from the outflows and intracaldera deposits suggests a positive correlation between the processes that affected their porosity and permeability. This means that the outflows may serve as an analog for the intracaldera deposits and that their study is crucial to understand the conditions within the caldera deposits.

CRediT authorship contribution statement

Jaime A. Cavazos-Álvarez: Conceptualization, Methodology, Investigation, Writing - original draft, Visualization, Supervision. **Gerardo Carrasco-Núñez:** Conceptualization, Writing - review & editing, Funding acquisition. **Pablo Dávila-Harris:** Investigation, Writing - review & editing. **Daniela Peña:** Investigation, Writing - review & editing. **Adrián Jáquez:** Investigation, Writing - review & editing. **Dante Arteaga:** Formal analysis.

Declaration of competing interest

The authors declare that they have no known competing financial interests or personal relationships that could have appeared to influence the work reported in this paper.

Acknowledgments

We acknowledge María Mercedes Zavala, who performed the petrophysical tests, and Juan Vázquez, who helped during the thin-section elaboration. We extend our sincere thanks to Javier Hernández and Francisco Fernández for their help during fieldwork and enriching discussions. We also thank the detailed revision and constructive comments made by two anonymous reviewers and the executive editor Francisco Vega.

Appendix A. Supplementary data

Supplementary data to this article can be found online at https://doi.org/10.1016/j.jsames.2020.102810.

Funding

Primary financing for this project was provided by the GEMEX European Union- Mexico Consortium funded by the Fondo de Sustentabilidad Energética SENER-CONACYT [No. 2015-04-268074], project 4.5. Initial financial support was provided by the Centro Mexicano de Innovación en Energía Geotérmica (CeMIEGeo) Consortium [No. 2007032, Project P05 (México)]. Authors JACA and DPR acknowledge CONACYT for granting scholarships for Ph.D. and Master's studies, respectively. GCN welcomes the PASPA-DGAPA program (UNAM) for support during his sabbatical stay at the University of Roma Tre (Rome, Italy). JAJD is grateful to the Sistema Nacional de Investigadores (SNI) for providing a project assistant grant.

References

Aliaga-Campuzano, M. del P., López-Martínez, R., Dávila-Harris, P., Espinasa-Pereña, R., Espino del Castillo, A., Bernal, J.P., 2017. Timing of speleogenesis of las karmidas cave (Mexico): first description of pseudokarst developed in ignimbrite. Int. J. Speleol 46, 331–343. https://doi.org/10.5038/1827-806X.46.3.2097.

Anderson, L.A., 1994. Water Permeability and Related Rock Properties Measured on Core Samples from the Yucca Mountain GU-3/G-3 and USW G-4 Boreholes.

Arellano, V., García, A., Barragán, R., Izquierdo, G., Aragón, A., Nieva, D., 2003. An updated conceptual model of the Los Humeros geothermal reservoir (Mexico). J. Volcanol. Geotherm. Res. 124, 67–88. https://doi.org/10.1016/S0377-0273(03)00045-3.

Arellano, V.M., García-Gutiérrez, A., Barragán, R.M., Izquierdo, G., Aragón, A., Pizano, A., 2000. A conceptual model of the los Humeros, (Mexico), geothermal reservoir in its natural state. World geotherm. Congr 2000 (15), 2503–2509.

Arellano, V.M., Torres, M.A., Barragán, R.M., 2005. Thermodynamic evolution of the Los Azufres, Mexico, geothermal reservoir from 1982 to 2002. Geothermics. https://doi.org/10.1016/j.geothermics.2005.06.002.

Arzate, J., Corbo-Camargo, F., Carrasco-Núñez, G., Hernández, J., Yutsis, V., 2018. The Los Humeros (Mexico) geothermal field model deduced from new geophysical and geological data. Geothermics 71, 200–211. https://doi.org/10.1016/j.geothermics.2017.09.009.

Bachmann, O., Bergantz, G.W., 2008. Rhyolites and their source mushes across tectonic settings. J. Petrol. https://doi.org/10.1093/petrology/egn068.

Bachmann, O., Bergantz, G.W., 2004. On the origin of crystal-poor rhyolites: extracted from batholithic crystal mushes. J. Petrol. 45, 1565–1582. https://doi.org/10.1093/petrology/egh019.

Bacon, C.R., Druitt, T.H., 1988. Compositional evolution of the zoned calcalkaline magma chamber of Mount Mazama, Crater Lake, Oregon. Contrib. Mineral. Petrol. 98, 224–256. https://doi.org/10.1007/BF00402114.

Bernard, M.L., Zamora, M., Géraud, Y., Boudon, G., 2007. Transport properties of pyroclastic rocks from montagne pelée volcano (Martinique, lesser antilles). J. Geophys. Res. Solid Earth 112, 1–16. https://doi.org/10.1029/2006JB004385.

Bignall, G., Browne, P.R.L., Kyle, P.R., 1996. Geochemical characterisation of hydrothermally altered ignimbrites in active geothermal fields from the central Taupo Volcanic Zone, New Zealand. J. Volcanol. Geotherm. Res. 73, 79–97. https://doi.org/10.1016/0377-0273(96)00015-7.

Bodvarsson, G., Boyle, W., Patterson, R., Williams, D., 1999. Overview of scientific investigations at Yucca Mountain—the potential repository for high-level nuclear waste. J. Contam. Hydrol. 38, 3–24. https://doi.org/10.1016/S0169-7722(99)00009-1.

Bouvet de Maisonneuve, C., Bachmann, O., Burgisser, A., 2009. Characterization of juvenile pyroclasts from the Kos Plateau Tuff (Aegean Arc): insights into the eruptive dynamics of a large rhyolitic eruption. Bull. Volcanol. 71, 643–658. https://doi.org/10.1007/s00445-008-0250-x.

Branney, M.J., Kokelaar, P., 2002. Pyroclastic density currents and the sedimentation of ignimbrites, journal of chemical information and modeling. https://doi.org/10.1017/CBO9781107415324.004.

Brown, R.J., Branney, M.J., 2004. Event-stratigraphy of a caldera-forming ignimbrite eruption on Tenerife: the 273 ka Poris Formation. Bull. Volcanol. 66, 392–416. https://doi.org/10.1007/s00445-003-0321-y.

Carranza, E.J.M., Wibowo, H., Barritt, S.D., Sumintadireja, P., 2008. Spatial data analysis and integration for regional-scale geothermal potential mapping, West Java, Indonesia. Geothermics. https://doi.org/10.1016/j.geothermics.2008.03.003.

Carrasco-Núñez, G., Bernal, J.P., Dávila, P., Jicha, B., Giordano, G., Hernández, J., 2018. Reappraisal of los Humeros volcanic complex by new U/Th zircon and 40Ar/39Ar dating: implications for greater geothermal potential. Geochemistry, geophys. Geosystems 19, 132–149. https://doi.org/10.1002/2017GC007044.

Carrasco-Núñez, G., Branney, M.J., 2005. Progressive assembly of a massive layer of ignimbrite with a normal-to-reverse compositional zoning: the Zaragoza ignimbrite of central Mexico. Bull. Volcanol. 68, 3–20. https://doi.org/10.1007/s00445-005-0416-8.

Carrasco-Núñez, G., Hernández, J., De León, L., Dávila, P., Norini, G., Bernal, J.P., Jicha, B., Navarro, M., López-Quiroz, P., 2017a. Geologic map of los Humeros volcanic complex and geothermal field, eastern Trans-Mexican volcanic belt. Terra Digit 1, 1–11. https://doi.org/10.22201/igg.terradigitalis.2017.2.24.

Carrasco-Núñez, G., López-Martínez, M., Hernández, J., Vargas, V., 2017b. Subsurface stratigraphy and its correlation with the surficial geology at Los Humeros geothermal field, eastern Trans-Mexican Volcanic Belt. Geothermics 67, 1–17. https://doi.org/10.1016/j.geothermics.2017.01.001.

Carrasco-Núñez, G., McCurry, M., Branney, M.J., Norry, M., Willcox, C., 2012. Complex magma mixing, mingling, and withdrawal associated with an intra-Plinian ignimbrite eruption at a large silicic caldera volcano: los Humeros of central Mexico. Bull. Geol. Soc. Am. 124, 1793–1809. https://doi.org/10.1130/B30501.1.

Carrasco-Núñez, G., Ort, M.H., Romero, C., 2007. Evolution and hydrological conditions of a maar volcano (Atexcac crater, Eastern Mexico). J. Volcanol. Geotherm. Res. 159, 179–197. https://doi.org/10.1016/J.JVOLGEORES.2006.07.001.

Cashman, K.V., Giordano, G., 2014. Calderas and magma reservoirs. J. Volcanol. Geotherm. Res. https://doi.org/10.1016/j.jvolgeores.2014.09.007.

Cavazos-Álvarez, J.A., Carrasco-Núñez, G., 2020. Anatomy of the xáltipan ignimbrite at los Humeros volcanic complex; the largest eruption of the Trans-Mexican volcanic belt. J. Volcanol. Geotherm. Res. 392, 106755. https://doi.org/10.1016/j.jvolgeores.2019.106755.

Cavazos-Álvarez, J.A., Carrasco-Núñez, G., 2019. Effective mapping of large ignimbrites by using a GIS-based methodology; case of the Xáltipan ignimbrite from Los Humeros Volcanic Complex. Terra Digit 3, 1–8. https://doi.org/10.22201/igg.25940694.2019.2.65.142.

Cavazos-Álvarez, J.A., Carrasco-Núñez, G., 2017. Vertical and Lateral Lithofacies Variations of a Caldera-Related Ignimbrite and Their Implications in an Active Geothermal System: the Case of Los Humeros Geothermal Field, Mexico. IAVCEI, Portland, Oregon.

Cedillo, F., 1999. Modelo Hidrogeológico de los Yacimientos Geotérmicos de Los Humeros, Pue., México. 8. Geotermia. Revista Mexicana de Geoenergía 15–3, 159–170.

Cedillo, F., 1997. Geología del subsuelo del campo geotérmico de Los Humeros, Pue. Internal Report. Comisión Federal de Electricidad, México, p. 30.

Cid, H.E., Carrasco-Núñez, G., Manea, V.C., 2017. Improved method for effective rock microporosity estimation using X-ray microtomography. Micron 97, 11–21. https://doi.org/10.1016/j.micron.2017.01.003.

Couves, C., Roberts, S., Racey, A., Troth, I., Best, A., 2016. Use of X-ray computed tomography to quantify the petrophysical properties of volcanic rocks: a case study from tenerife, canary islands. J. Pet. Geol. https://doi.org/10.1111/jpg.12629.

Dávila-Harris, P., Carrasco-Núñez, G., 2014. An unusual syn-eruptive bimodal eruption: the Holocene Cuicuiltic Member at Los Humeros caldera, Mexico. J. Volcanol. Geotherm. Res. 271, 24–42. https://doi.org/10.1016/j.jvolgeores.2013.11.020.

de Silva, S.L., 1991. Styles of zoning in central Andean ignimbrites; Insights into magma chamber processes. In: Special Paper of the Geological Society of America, pp. 217–232. https://doi.org/10.1130/SPE265-p217.

Degruyter, W., Burgisser, A., Bachmann, O., Malaspinas, O., 2010. Synchrotron X-ray microtomography and lattice Boltzmann simulations of gas flow through volcanic pumices. Geosphere 6, 470–481. https://doi.org/10.1130/ges00555.1.

del Pilar-Martínez, A., 2016. Caracterización petrográfica y geoquímica de una sección del subsuelo en el campo geotérmico de Los Humeros, Puebla: caso de estudio del pozo H-42.

Druitt, T.H., 1998. Pyroclastic density currents. Geol. Soc. Spec. Publ. https://doi.org/10.1144/GSL.SP.1996.145.01.08.

Druitt, T.H., Sparks, R.S.J., 1982. A proximal ignimbrite breccia facies on santorini, Greece. J. Volcanol. Geotherm. Res. 13, 147–171. https://doi.org/10.1016/0377-0273(82)90025-7.

Fernández-Maya, F.O., 2017. Caracterización petrográfica y geoquímica del pozo H-26 en el campo geotérmico de los Humeros, Puebla. Instituto Tecnológico de Ciudad Madero.

Ferrari, L., Orozco-Esquivel, T., Manea, V., Manea, M., 2012. The dynamic history of the Trans-Mexican Volcanic Belt and the Mexico subduction zone. Tectonophysics 522–523, 122–149. https://doi.org/10.1016/j.tecto.2011.09.018.

Ferriz, H., Mahood, G.A., 1984. Eruption rates and compositional trends at los Humeros caldera, puebla, Mexico. J. Geophys. Res. Solid Earth 89, 8511–8524.

Ferriz, Horacio, Mahood, Gail, 1987. Strong compositional zonation in a silicic magmatic system Los Humeros, Mexican Neovolcanic Belt. Journal of Petrology 28 (1), 171–209. https://doi.org/10.1093/petrology/28.1.171.

Fitz-Díaz, E., Lawton, T.F., Juárez-Arriaga, E., Chávez-Cabello, G., 2018. The Cretaceous-Paleogene Mexican orogen: structure, basin development, magmatism and tectonics. Earth-Science Rev. https://doi.org/10.1016/j.earscirev.2017.03.002.

Flint, L.E., Selker, J.S., 2003. Use of porosity to estimate hydraulic properties of volcanic tuffs. Adv. Water Resour. 26, 561–571. https://doi.org/10.1016/S0309-1708(02)00182-3.

Foster, S.S.D., Ellis, A.T., Losilla-Penon, M., Rodriguez-Estrada, H.V., 1985. Role of Volcanic Tuffs in Ground-Water Regime of Valle Central. Groundwater, Costa Rica. https://doi.org/10.1111/j.1745-6584.1985.tb01959.x.

Freundt, A., Schmincke, H.-U., 1992. Mixing of rhyolite, trachyte and basalt magma erupted from a vertically and laterally zoned reservoir, composite flow P1, Gran Canaria. Contrib. to Mineral. Petrol. Times 112, 1–19. https://doi.org/10.1007/BF00310952.

Giannetti, B., Luhr, J.F., 1983. The white trachytic tuff of roccamonfina volcano (roman region, Italy). Contrib. To mineral. Petrol. Times 84, 235–252. https://doi.org/10.1007/BF00371289.

Gutiérrez-Negrín, L.C.A., Izquierdo-Montalvo, G., 2010. Review and Update of the Main Features of the Los Humeros Geothermal Field, vol. 2010. World Geotherm. Congr, Mexico, pp. 25–29. https://doi.org/10.1016/j.bmc.2011.02.011.

Hildreth, W., 1979. The Bishop Tuff: Evidence for the Origin of Compositional Zonation in Silicic Magma Chambers, pp. 43–76. https://doi.org/10.1130/SPE180-p43.

Istok, J.D., Rautman, C.A., Flint, L.E., Flint, A.L., 1994. Spatial variability in hydrologic properties of a volcanic tuff. Ground Water 32, 751–760. https://doi.org/10.1111/j.1745-6584.1994.tb00916.x.

Jáquez-Domínguez, J.A., 2018. Caracterización petrográfica y geoquímica del pozo H-59 del campo geotérmico Los Humeros, Puebla. Universidad Autónoma de Zacatecas.

Klug, C., Cashman, K.V., 1996. Permeability development in vesiculating magmas: implications for fragmentation. Bull. Volcanol. https://doi.org/10.1007/s004450050128.

Klug, C., Cashman, K.V., Bacon, C., 2002. Structure and physical characteristics of pumice from the climactic eruption of Mount Mazama (Crater Lake). Oregon. Bull. Volcanol 64, 486–501. https://doi.org/10.1007/s00445-002-0230-5.

Lipman, P.W., 1997. Subsidence of ash-flow calderas: relation to caldera size and magma-chamber geometry. Bull. Volcanol. 59, 198–218. https://doi.org/10.1007/s004450050186.

Lipman, P.W., 1967. Mineral and chemical variations within an ash-flow sheet from Aso caldera, Southwestern Japan. Contrib. to Mineral. Petrol. Times 16, 300–327. https://doi.org/10.1007/BF00371528.

Lorenzo-Pulido, 2008. Borehole geophysics and geology of well H-43, los Humeros geothermal field, puebla, méxico. Geothermal Training Programme. Orkustofnun, Grensásvegur, Reykjavík, Iceland.

Lozano-Santa Cruz, R., Verma, S.P., Girón, P., Velasco, F., Morán-Zenteno, D., Viera, F., Chávez, G., 1995. Calibración preliminar de fluorescencia de rayos X para análisis cuantitativo de elementos mayores en rocas ígneas. actas Ina 1, 203–208.

Lucci, F., Carrasco-Núñez, G., Rossetti, F., Theye, T., White, J.C., Urbani, S., Azizi, H., Asahara, Y., Giordano, G., 2020. Anatomy of the magmatic plumbing system of Los Humeros Caldera (Mexico): implications for geothermal systems. Solid Earth 11, 125–159. https://doi.org/10.5194/se-11-125-2020.

Martínez-Serrano, R.G., Dubois, M., 1998. Chemical Variations in Chlorite at the Los Humeros Geothermal System. Clays Clay Miner, Mexico. https://doi.org/10.1346/CCMN.1998.0460602.

McArthur, A.N., Cas, R.A.F., Orton, G.J., 1998. Distribution and significance of crystalline, perlitic and vesicular textures in the Ordovician Garth Tuff (Wales). Bull. Volcanol. 60, 260–285. https://doi.org/10.1007/s004450050232.

McPhie, J., Doyle, M., Allen, S.R., 1993. Volcanic Textures: a Guide to the Interpretation of Textures in Volcanic Rocks.

Mori, L., 2007. Origen del magmatismo miocénico en el sector central de la FVTM y sus implicaciones en la evolución del sistema de subducción mexicano. Cent. Geociencias. Universidad Nacional Autónoma de México.

Neeper, D.A., Gilkeson, R.H., 1996. In: The Influence of Topography, Stratigraphy, and Barometric Venting on the Hydrology of Unsaturated Bandelier Tuff (Jemez Mountains Region).

Negendank, J., Emmermann, R., Krawczyk, R., Mooser, F., Tobschall, H., Werle, D., 1985. Geological and geochemical investigations on the eastern Trans-Mexican volcanic belt. Geofisc. Int. 24, 477–575.

Neretnieks, I., 1980. Diffusion in the rock matrix: an important factor in radionuclide retardation? J. Geophys. Res. Solid Earth 85, 4379–4397. https://doi.org/10.1029/JB085iB08p04379.

Norini, G., Carrasco-Núñez, G., Corbo-Camargo, F., Lermo, J., Rojas, J.H., Castro, C., Bonini, M., Montanari, D., Corti, G., Moratti, G., Piccardi, L., Chavez, G., Zuluaga, M. C., Ramirez, M., Cedillo, F., 2019. The structural architecture of the Los Humeros volcanic complex and geothermal field. J. Volcanol. Geoth. Res. https://doi.org/10.1016/j.jvolgeores.2019.06.010.

Norini, G., Groppelli, G., Sulpizio, R., Carrasco-Núñez, G., Dávila-Harris, P., Pellicioli, C., Zucca, F., De Franco, R., 2015. Structural analysis and thermal remote sensing of the Los Humeros Volcanic Complex: implications for volcano structure and geothermal exploration. J. Volcanol. Geotherm. Res. 301, 221–237. https://doi.org/10.1016/j.jvolgeores.2015.05.014.

Polacci, M., Bouvet de Maisonneuve, C., Giordano, D., Piochi, M., Mancini, L., Degruyter, W., Bachmann, O., 2014. Permeability measurements of campi flegrei pyroclastic products: an example from the campanian ignimbrite and monte nuovo eruptions. J. Volcanol. Geotherm. Res. 272, 16–22. https://doi.org/10.1016/j.jvolgeores.2013.12.002.

Purnomo, E., Ryacudu, R., Sunardi, E., Adhiperdana, B., 2008. In: Paleogene Stratigraphy and Petroleum Potential of Largely Volcanic Play Jatibarang Formation, Onshore Northwest Java Basin, Indonesia. GEO, p. 225.

Quane, S.L., Russell, J.K., 2005. Ranking welding intensity in pyroclastic deposits. Bull. Volcanol. 67, 129–143. https://doi.org/10.1007/s00445-004-0367-5.

Romo-Jones, J.M., Gutiérrez-Negrín, L.C., Flores-Armenta, M., del Valle, J., García, A., 2017. Mexico Country Report. IEA Geothermal, p. 2016.

Rust, A.C., Cashman, K.V., 2004. Permeability of vesicular silicic magma: inertial and hysteresis effects. Earth Planet Sci. Lett. https://doi.org/10.1016/j.epsl.2004.09.025.

Scarpati, C., Sparice, D., Perrotta, A., 2015. Facies variation in the campanian ignimbrite. Rend. Online Soc. Geol. Ital. https://doi.org/10.3301/ROL.2015.20.

Siebe, C., Macías, J.L., Abrams, M.J., Rodríguez, S., Castro, R., Delgado Granados, H., 1995. Quaternary explosive volcanism and pyroclastic deposits in east central Mexico: implications for future hazards. Guideb. In: Geol.. Excursions Conjunction with Annu. Meet. Geol. Soc. Am., pp. 1–48. New Orleans, Louisiana, Novemb. 6-9, 1995.

Smith, R.L., Bailey, R.A., 1966. The Bandelier Tuff: a study of ash-flow eruption cycles from zoned Magma Chambers. Bull. Volcanol. 29, 83–103. https://doi.org/10.1007/BF02597146.

Sruoga, P., Rubinstein, N., 2007. Processes controlling porosity and permeability in volcanic reservoirs from the Austral and Neuquén basins, Argentina. Am. Assoc. Petrol. Geol. Bull. 91, 115–129. https://doi.org/10.1306/08290605173.

Stimac, J.A., Powell, T.S., Golla, G.U., 2004. Porosity and permeability of the Tiwi geothermal field, Philippines, based on continuous and spot core measurements. Geothermics. https://doi.org/10.1016/j.geothermics.2003.03.002.

Sumner, J.M., Branney, M.J., 2002. The emplacement history of a remarkable heterogeneous, chemically zoned, rheomorphic and locally lava-like ignimbrite: 'TL' on Gran Canaria. J. Volcanol. Geotherm. Res. 115, 109–138. https://doi.org/10.1016/S0377-0273(01)00311-0.

Turner, J.S., 1980. A fluid-dynamical model of differentiation and layering in magma chambers. Nature. https://doi.org/10.1038/285213a0.

Urbani, S., Giordano, G., Lucci, F., Rossetti, F., Acocella, V., Carrasco-Núñez, G., 2020. Estimating the depth and evolution of intrusions at resurgent calderas: los Humeros (Mexico). Solid Earth. https://doi.org/10.5194/se-11-527-2020.

Valentine, G.A., Wohletz, K.H., Kieffer, S.W., 1992. Effects of topography on facies and compositional zonation in caldera-related ignimbrites. Geol. Soc. Am. Bull. https://doi.org/10.1130/0016-7606(1992)104<0154:EOTOFA>2.3.CO;2.

Walker, G.P.L., 1985. Origin of Coarse Lithic Breccias Near Ignimbrite Source Vents, vol. 25, pp. 157–171.

Willcox, C.P., 2011. Eruptive, magmatic and structural evolution of a large explosive caldera volcano: los Humeros, Central Mexico. University of Leicester.

Wilson, C.J.N., Walker, G.P.L., 1982. Ignimbrite depositional facies: the anatomy of a pyroclastic flow. J. Geol. Soc. London 139, 581–592. https://doi.org/10.1144/gsjgs.139.5.0581.

Wolff, J.A., Storey, M., 1984. Zoning in highly alkaline magma bodies. Geol. Mag. 121, 563–575. https://doi.org/10.1017/S0016756800030715.

Wright, H.M.N., Cashman, K.V., Gottesfeld, E.H., Roberts, J.J., 2009. Pore structure of volcanic clasts: measurements of permeability and electrical conductivity. Earth Planet Sci. Lett. 280, 93–104. https://doi.org/10.1016/j.epsl.2009.01.023.

Yáñez-García, C., García-Durán, S., 1982. Exploración de la región geotérmica Los Humeros–Las Derrumbadas, Estados de Puebla y Veracruz. Comisión Federal de Electricidad, Mexico (D. F).

Zheng, H., Sun, X., Wang, J., Zhu, D., Zhang, X., 2018. Devitrification pores and their contribution to volcanic reservoirs: a case study in the Hailar Basin, NE China. Mar. Petrol. Geol. 98, 718–732. https://doi.org/10.1016/j.marpetgeo.2018.09.016.

6. Conclusiones

Las conclusiones de esta tesis pueden resumirse en los siguientes tópicos:

Cartografía y arquitectura

La metodología aquí propuesta para el mapeo de la IX resuelve los efectos de enterramiento y erosión, mismos que son comunes en la mayoría de las ignimbritas, por lo que se prevé que esta metodología pueda ser aplicada efectivamente en otros casos.

Las líneas de energía, proyectadas desde el borde de la caldera hacia los depósitos distales de la ignimbrita, apuntan la erupción tuvo un estilo tipo *boiling-over*, marcado por la generación de un gran volumen de CPD a una altura somera (0 a 400 m).

La forma de la ignimbrita provee evidencias del control de la topografía sobre el emplazamiento de las CPD. En la zona proximal (<30 km desde el borde de la caldera) la ignimbrita rellenó y cubrió por completo el campo volcánico pre-caldera del CVLH (con espesores de >150 m), resultando en una distribución radial con una superficie horizontal suavizada. En las facies distales (>30 km) del sector norte del área de estudio, la ignimbrita se encauzó en los valles formados por el basamento altamente deformado, formando potentes depósitos de relleno de valle acoplados a su morfología; mientras que hacia el sur, la ignimbrita remontó grandes barreras topográficas (>500 m), llegando a distancias máximas de 52 km desde el borde de la caldera.

Las secciones geológicas revelan cómo el soldamiento se desarrolló en forma zonificada en los depósitos de relleno de valle. Este zonamiento está definido por un alto grado de soldamiento en el núcleo del valle, el cual disminuye gradualmente hacia las partes externas (zonas de interface ignimbrita-basamento e ignimbrita-atmósfera) hasta presentar condiciones no soldadas.

La cartografía digital, en conjunto con datos de campo y mediciones petrofísicas, indican que la IX tiene un área, volumen y magnitud de *ca.* 4,600 km^2, 340 km^3 (290 km^3 – RDE) y 1.1 $\times 10^{12}$ kg, respectivamente. Estos resultados indican que se trata de una erupción mucho más grande de la previamente reportada (~3,500 km^2 y volumen de 115km^3 de RDE), posicionándola como la mayor erupción explosiva de la FVTM, incluso cuando estos resultados son conservadores ya que no consideran la ceniza co-ignimbrítica.

Estratigrafía e historia eruptiva

El registro estratigráfico de la IX permite reconstruir su historia eruptiva. Se interpreta que la IX es el resultado de una erupción voluminosa y continua que puede ser dividida en cuatro fases eruptivas: La erupción inició con una explosión Pliniana de corta duración y dispersión (fase 1), que depositó la unidad de caída de pómez basal (BPF). La columna eruptiva colapsó y la erupción evolucionó directamente a su fase culminante (fase 2) marcada por un estilo eruptivo tipo *boiling-over*, la cual se asocia con el colapso de la caldera Los Humeros. Durante esta fase se depositó la unidad de flujo inferior (LFU), misma que es la unidad principal de la ignimbrita. Esta fase se ve terminada con un declive de la erupción, un *hiatus* en la generación de CPD. Posteriormente, ocurrió una segunda fase explosiva (fase 3) marcada por la generación de una columna Pliniana en el sector occidental de la caldera recién formada, que formó un depósito de caída (IPF). Esta columna colapsó (fase 4) generando CPD y el emplazamiento de la unidad de flujo superior (UFU).

La estratigrafía del subsuelo del campo geotérmico muestra que la IX tiene un espesor altamente variable. Se interpreta que esta variación del espesor se debe a las irregularidades del terreno volcánico pre-eruptivo, así como a una subsidencia caótica y parcial del terreno durante el colapso de la caldera Los Humeros, lo cual es consistente con el modelo de colapso de dicha caldera, el cual propone que esta colapsó en forma de bisagra (*trapdoor*) y por partes (*piecemeal*).

Las evidencias petrográficas y geoquímicas en muestras de lavas intercaladas en la IX dentro de la caldera indican que estas corresponden a brechas de rezago, y no a flujos de lava como comúnmente se había propuesto. Este hallazgo es importante ya que resuelve la duda sobre la escasez de esos depósitos en la superficie, pero confirma la ocurrencia de los procesos de colapso de la caldera de Los Humeros.

Facies

La IX es un excelente ejemplo de una ignimbrita con múltiples facies que pueden ser abordadas desde sus rasgos petrofísicos y químicos.

Se identificó una asociación de tres facies petrofísicas controladas principalmente por el grado de soldamiento, y en menor grado por mineralización secundaria. Esta asociación de facies está conformada por: 1) la facies basal, caracterizada por ser de alto grado de soldamiento, baja porosidad (dominada por vesículas) y condiciones de impermeabilidad (<0.01 - 0.05 mD) causadas por efectos de soldamiento y reducción de poros por minerales secundarios. 2) La facies intermedia, en donde el soldamiento es moderado y la porosidad es mayor, la cual está conformada por espacios interesquirlas, vesículas y fracturas. En esta facies, la mineralización es un reductor de porosidad importante, no obstante, las condiciones son permeables (6.11 – 46.38 mD). 3) La facies superior, la cual está conformada por depósitos poco a nulamente soldados, y en donde las condiciones de porosidad y permeabilidad son altas (310.72 - 1,557.26 mD) debido al bajo grado de soldamiento y mineralización secundaria.

Los perfiles de correlación de los pozos del campo geotérmico muestran que la asociación de facies petrofísicas está fuertemente controlada por el espesor de la ignimbrita, el cual está estrechamente controlado por la topografía. En donde el espesor es mayor a 400 m, se desarrolla la asociación completa, mientras que donde es menor, se desarrollan solamente las facies intermedia y superior.

Los resultados geoquímicos indican que la ignimbrita presenta un zonamiento composicional que va de riolítico en la base (flujo inferior - LFU), a traquítico-riolítico hacia el cima (depósito de caída intermedio - IPF y flujo superior - UFU). Este zonamiento es asociado a una cámara magmática heterogénea en donde ocurre la interacción de zonas ricas en cristales (*crystal mush*) con zonas ricas en fundido (*high melt* zones). Los elementos mayores y traza de la composición final de la IX son afines con los de las unidades subsecuentes de la etapa de Caldera (toba Faby e ignimbrita Zaragoza), lo que sugiere que esta composición magmática residió durante alrededor de 100 ky.

Aplicación para el sistema geotérmico

La nueva estimación del volumen (*ca.* 290 km^3) de la IX significa que esta deriva de una fuente magmática mucho mayor a la previamente calculada con el volumen precedente (115 km^3), lo que puede ser interpretado como condiciones geotérmicas más favorables que las antes consideradas.

El modelo de facies petrofísicas dentro de la caldera indica que en las zonas donde la IX se confinó en depresiones topográficas y se depositó con un espesor mayor a 400 m, es altamente probable que se hayan desarrollado condiciones impermeables en la base (facies basal) y por lo tanto esta puede servir como un sello para el paso de fluidos hidrotermales.

Finalmente, el hecho de que existe una correlación entre la asociación de facies de los depósitos de flujo y de relleno de la caldera, sugiere que se trata de un sistema análogo. Esto significa que los flujos pueden funcionar como un referente para entender las condiciones de los depósitos de relleno de la caldera, los cuales están involucrados en el funcionamiento del campo geotérmico. Esto hace de la IX un ejemplo sin precedentes de un sistema de facies análogo de depósitos intracaldera y extracaldera que tiene una aplicación directa a un campo geotérmico.

Referencias

Allen, S. R. y Cas, R. A. F. (1998). Lateral variations within coarse co-ignimbrite lithic breccias of the Kos Plateau Tuff, Greece. *Bulletin of Volcanology*. https://doi.org/10.1007/s004450050197

Bachmann, O. y Bergantz, G. W. (2004). On the Origin of Crystal-poor Rhyolites: Extracted from Batholithic Crystal Mushes. *Journal of Petrology*, *45*(8), 1565–1582. https://doi.org/10.1093/petrology/egh019

Bachmann, O. y Bergantz, G. W. (2008). Deciphering magma chamber dynamics from styles of compositional zoning in large silicic ash flow sheets. *Reviews in Mineralogy and Geochemistry*. https://doi.org/10.2138/rmg.2008.69.17

Bacon, C. R. y Druitt, T. H. (1988). Compositional evolution of the zoned calcalkaline magma chamber of Mount Mazama, Crater Lake, Oregon. *Contributions to Mineralogy and Petrology*, *98*(2), 224–256. https://doi.org/10.1007/BF00402114

Bernard, M. L., Zamora, M., Géraud, Y. y Boudon, G. (2007). Transport properties of pyroclastic rocks from Montagne Pelée volcano (Martinique, Lesser Antilles). *Journal of Geophysical Research: Solid Earth*, *112*(5), 1–16. https://doi.org/10.1029/2006JB004385

Best, M. G., Christiansen, E. H. y Gromme, S. (2013). Introduction: The 36-18 Ma southern Great Basin, USA, ignimbrite province and flareup: Swarms of subduction-related supervolcanoes. *Geosphere*, *9*(2), 260–274. https://doi.org/10.1130/GES00870.1

Branney, M. J. y Acocella, V. (2015). Calderas. En *The Encyclopedia of Volcanoes* (Second Edi, pp. 299–315). Elsevier. https://doi.org/10.1016/B978-0-12-385938-9.00016-X

Branney, M. J. y Kokelaar, P. (1992). A reappraisal of ignimbrite emplacement: progressive aggradation and changes from particulate to non-particulate flow during emplacement of high-grade ignimbrite. *Bulletin of Volcanology*, *54*(6), 504–520. https://doi.org/10.1007/BF00301396

Branney, M. J. y Kokelaar, P. (1997). Giant bed from a sustained catastrophic density current flowing over topography: Acatlán ignimbrite, Mexico. *Geology*, *25*(2), 115–118. https://doi.org/10.1130/0091-7613(1997)025<0115:GBFASC>2.3.CO;2

Branney, M. J. y Kokelaar, P. (2002). Pyroclastic Density Currents and the Sedimentation of Ignimbrites. *Geological Society, London*, *27*, 152.

Briggs, R. M., Gifford, M. G., Moyle, A. R., Taylor, S. R., Norman, M. D., Houghton, B. F. y Wilson, C. J. N. (1993). Geochemical zoning and eruptive mixing in ignimbrites from Mangakino volcano, Taupo Volcanic Zone, New Zealand. *Journal of Volcanology and Geothermal Research*, *56*(3), 175–203. https://doi.org/10.1016/0377-0273(93)90016-K

Brown, R. J. y Andrews, G. (2015). Deposits of Pyroclastic Density Currents. En *The Encyclopedia of Volcanoes* (pp. 631–648). Elsevier. https://doi.org/10.1016/B978-0-12-385938-9.00036-5

Brown, R. J. y Branney, M. J. (2004). Event-stratigraphy of a caldera-forming ignimbrite eruption on Tenerife: The 273 ka Poris Formation. *Bulletin of Volcanology*, *66*(5), 392–416. https://doi.org/10.1007/s00445-003-0321-y

Bursik, M. I. y Woods, A. W. (1996). The dynamics and thermodynamics of large ash flows. *Bulletin of Volcanology*. https://doi.org/10.1007/s004450050134

Carrasco-Núñez, G., Bernal, J. P., Dávila, P., Jicha, B., Giordano, G. y Hernández, J. (2018). Reappraisal of Los Humeros Volcanic Complex by New U/Th Zircon and 40Ar/39Ar Dating: Implications for Greater Geothermal Potential. *Geochemistry, Geophysics, Geosystems*, *19*(1), 132–149. https://doi.org/10.1002/2017GC007044

Carrasco-Núñez, G. y Branney, M. J. (2005). Progressive assembly of a massive layer of ignimbrite with a normal-to-reverse compositional zoning: The Zaragoza ignimbrite of central Mexico. *Bulletin of Volcanology*, *68*(1), 3–20. https://doi.org/10.1007/s00445-

005-0416-8

Carrasco-Núñez, G., Hernández, J., De León, L., Dávila-Harris, P., Norini, G., Bernal, J. P., Jicha, B., Navarro, M. y López-Quiroz, P. (2017). Geologic Map of Los Humeros volcanic complex and geothermal field, eastern Trans-Mexican Volcanic Belt Mapa geológico del complejo volcánico Los Humeros y campo geotérmico, sector oriental del Cinturón Volcánico Trans-Mexicano. *Terra Digitalis*, *1*(2), 1–11. https://doi.org/10.22201/igg.terradigitalis.2017.2.24.78

Carrasco-Núñez, G., López-Martínez, M., Hernández, J. y Vargas, V. (2017). Subsurface stratigraphy and its correlation with the surficial geology at Los Humeros geothermal field, eastern Trans-Mexican Volcanic Belt. *Geothermics*, *67*, 1–17. https://doi.org/10.1016/j.geothermics.2017.01.001

Carrasco-Núñez, G., Siebert, L., Díaz-Castellón, R., Vázquez-Selem, L. y Capra, L. (2010). Evolution and hazards of a long-quiescent compound shield-like volcano: Cofre de Perote, Eastern Trans-Mexican Volcanic Belt. *Journal of Volcanology and Geothermal Research*, *197*(1–4), 209–224. https://doi.org/10.1016/j.jvolgeores.2009.08.010

Cashman, K. V. y Giordano, G. (2014). Calderas and magma reservoirs. En *Journal of Volcanology and Geothermal Research* (Vol. 288, pp. 28–45). https://doi.org/10.1016/j.jvolgeores.2014.09.007

Cid, H. E., Carrasco-Núñez, G. y Manea, V. C. (2017). Improved method for effective rock microporosity estimation using X-ray microtomography. *Micron*, *97*, 11–21. https://doi.org/10.1016/j.micron.2017.01.003

Cole, J. W., Milner, D. M. y Spinks, K. D. (2005). Calderas and caldera structures: A review. *Earth-Science Reviews*, *69*(1–2), 1–26. https://doi.org/10.1016/j.earscirev.2004.06.004

Cook, G. W., Wolff, J. A. y Self, S. (2016). Estimating the eruptive volume of a large pyroclastic body: the Otowi Member of the Bandelier Tuff, Valles caldera, New

Mexico. *Bulletin of Volcanology*, *78*(2), 1–11. https://doi.org/10.1007/s00445-016-1000-0

Couves, C., Roberts, S., Racey, A., Troth, I. y Best, A. (2016). Use of X-ray computed tomography to quantify the petrophysical properties of volcanic rocks: A case study from tenerife, canary islands. *Journal of Petroleum Geology*. https://doi.org/10.1111/jpg.12629

Dade, W. B. y Huppert, H. E. (1996). Emplacement of the Taupo ignimbrite by a dilute turbulent flow. *Nature*. https://doi.org/10.1038/381509a0

Dávila-Harris, P. y Carrasco-Núñez, G. (2014). An unusual syn-eruptive bimodal eruption: The Holocene Cuicuiltic Member at Los Humeros caldera, Mexico. *Journal of Volcanology and Geothermal Research*, *271*, 24–42. https://doi.org/10.1016/j.jvolgeores.2013.11.020

Demant, A. (1978). *Características del Eje Neovolcánico Transmexicano y sus problemas de interpretación.* (pp. 172–187). Universidad Nacional Autónoma de México.

Druitt, T. H. (1998). Pyroclastic density currents. *Geological Society, London, Special Publications*, *145*(1), 145–182. https://doi.org/10.1144/GSL.SP.1996.145.01.08

Druitt, T. H. y Bacon, C. R. (1986). Lithic breccia and ignimbrite erupted during the collapse of Crater Lake Caldera, Oregon. *Journal of Volcanology and Geothermal Research*, *29*(1–4), 1–32. https://doi.org/10.1016/0377-0273(86)90038-7

Druitt, T. H. y Sparks, R. S. J. (1982). A proximal ignimbrite breccia facies on santorini , Greece. *Journal of Volcanology and Geothermal Research*, *13*(1–2), 147–171. https://doi.org/10.1016/0377-0273(82)90025-7

Fedele, L., Scarpati, C., Sparice, D., Perrotta, A. y Laiena, F. (2016). A chemostratigraphic study of the Campanian Ignimbrite eruption (Campi Flegrei, Italy): Insights on magma chamber withdrawal and deposit accumulation as revealed by compositionally zoned stratigraphic and facies framework. *Journal of Volcanology and Geothermal Research*, *324*, 105–117. https://doi.org/10.1016/j.jvolgeores.2016.05.019

Ferrari, L., Orozco-Esquivel, T., Manea, V. y Manea, M. (2012). The dynamic history of the Trans-Mexican Volcanic Belt and the Mexico subduction zone. *Tectonophysics*, *522–523*, 122–149. https://doi.org/10.1016/j.tecto.2011.09.018

Ferriz, H. y Mahood, G. A. (1984). Eruption rates and compositional trends at Los Humeros Volcanic Center, Puebla, Mexico. *Journal of Geophysical Research*, *89*(B10), 8511. https://doi.org/10.1029/JB089iB10p08511

Fisher, R. V. (1966). Mechanism of deposition from pyroclastic flows. *American Journal of Science*. https://doi.org/10.2475/ajs.264.5.350

Fitz-Díaz, E., Lawton, T. F., Juárez-Arriaga, E. y Chávez-Cabello, G. (2018). The Cretaceous-Paleogene Mexican orogen: Structure, basin development, magmatism and tectonics. En *Earth-Science Reviews*. https://doi.org/10.1016/j.earscirev.2017.03.002

Flint, L. E. y Selker, J. S. (2003). Use of porosity to estimate hydraulic properties of volcanic tuffs. *Advances in Water Resources*, *26*(5), 561–571. https://doi.org/10.1016/S0309-1708(02)00182-3

Folkes, C. B., Wright, H. M., Cas, R. A. F., de Silva, S. L., Lesti, C. y Viramonte, J. G. (2011). A re-appraisal of the stratigraphy and volcanology of the Cerro Galán volcanic system, NW Argentina. *Bulletin of Volcanology*, *73*(10), 1427–1454. https://doi.org/10.1007/s00445-011-0459-y

Freudnt, A., Wilson, C. J. N. y Carey, S. N. (2000). Ignimbrites and block-and-ash flow deposits. En *Encyclopedia of Volcanoes* (pp. 581–599).

Freundt, A. y Schmincke, H. U. (1986). Emplacement of small-volume pyroclastic flows at Laacher See (East-Eifel, Germany). *Bulletin of Volcanology*. https://doi.org/10.1007/BF01073512

Giordano, G., Mattei, M. y Funiciello, R. (2010). Geological map of the Colli Albani volcano. En R. Funiciello & G. Giordano (Eds.), *The Colli Albani Volcano* (Special Pu, pp. 43–98). Geological Society of London.

Gottsmann, J., Giordano, D. y Dingwell, D. B. (2002). Predicting shear viscosity during volcanic processes at the glass transition: A calorimetric calibration. *Earth and Planetary Science Letters*. https://doi.org/10.1016/S0012-821X(02)00522-8

Grunder, A. y Russell, J. K. (2005). Welding processes in volcanology: Insights from field, experimental, and modeling studies. *Journal of Volcanology and Geothermal Research*. https://doi.org/10.1016/j.jvolgeores.2004.10.010

Gutiérrez-Negrín, L. C. A. y Izquierdo-Montalvo, G. (2010). Review and Update of the Main Features of the Los Humeros Geothermal Field, Mexico. *World Geothermal Congress 2010*, *April*, 25–29. https://doi.org/10.1016/j.bmc.2011.02.011

Iverson, R. M. y Vallance, J. W. (2001). New views of granular mass flows. *Geology*. https://doi.org/10.1130/0091-7613(2001)029<0115:NVOGMF>2.0.CO;2

Langella, A., Di Benedetto, C., Calcaterra, D., Cappelletti, P., D'Amore, M., Di Martire, D., Graziano, S. F., Papa, L. y Langella, A. (2017). The Neapolitan Yellow Tuff: An outstanding example of heterogeneity. *Construction and Building Materials*, *136*, 361–373. https://doi.org/10.1016/j.conbuildmat.2017.01.053

Lipman, P. W. (1976). Caldera-collapse breccias in the western San Juan Mountains, Colorado. *Geological Society of America Bulletin*, *87*(10), 1397. https://doi.org/10.1130/0016-7606(1976)87<1397:CBITWS>2.0.CO;2

Lipman, P. W. (1984). The roots of ash flow calderas in western North America: Windows into the tops of granitic batholiths. *Journal of Geophysical Research*, *89*(B10), 8801. https://doi.org/10.1029/JB089iB10p08801

Lofgren, G. (1971). Experimentally produced devitrification textures in natural rhyolitic glass. *Bulletin of the Geological Society of America*. https://doi.org/10.1130/0016-7606(1971)82[111:EPDTIN]2.0.CO;2

López-Hernández, A. (1995). Estudio Regional Volcánico y Estructural del Campo Geotérmico de Los Humeros, Pue., México. *Revista Mexicana de Geoenergía*, *11*(1), 17–36.

Lozano, R. y Bernal, J. P. (2005). Characterization of a new set of eight geochemical reference materials for XRF major and trace element analysis. *Revista Mexicana de Ciencias Geologicas*.

Marshall, R. R. (1961). Devitrification of natural glass. *Bulletin of the Geological Society of America*. https://doi.org/10.1130/0016-7606(1961)72[1493:DONG]2.0.CO;2

Martí, J., Planagumà, L. l., Geyer, A., Aguirre-Díaz, G., Pedrazzi, D. y Bolós, X. (2017). Basaltic ignimbrites in monogenetic volcanism: the example of La Garrotxa volcanic field. *Bulletin of Volcanology*. https://doi.org/10.1007/s00445-017-1113-0

Mason, B. G., Pyle, D. M. y Oppenheimer, C. (2004). The size and frequency of the largest explosive eruptions on Earth. *Bulletin of Volcanology*, *66*(8), 735–748. https://doi.org/10.1007/s00445-004-0355-9

McPhie, J., Doyle, M. y Allen, S. R. (1993). *Volcanic Textures: a guide to the interpretation of textures in volcanic rocks.*

Miyabuchi, Y. (1999). Deposits associated with the 1990–1995 eruption of Unzen volcano, Japan. *Journal of Volcanology and Geothermal Research*, *89*(1–4), 139–158. https://doi.org/10.1016/S0377-0273(98)00129-2

Mori, L. (2007). Origen del magmatismo miocénico en el sector central de la FVTM y sus implicaciones en la evolución del sistema de subducción mexicano. En *Centro de Geociencias*. Universidad Nacional Autónoma de México.

Negendank, J., Emmermann, R., Krawczyk, R., Mooser, F., Tobschall, H. y Werle, D. (1985). Geological and geochemical investigations on the eastern Trans-Mexican Volcanic Belt. *Geofísica Internacional*, *24*(4), 477–575. file:///C:/Users/Jaime/Documents/CGEO/Bibliografia/Negendank et al, 1985 Geolocical and geochemical investigations on the eastern trans mexican volcanic belt.pdf

Newhall, C. G. y Self, S. (1982). The volcanic explosivity index (VEI) an estimate of explosive magnitude for historical volcanism. *Journal of Geophysical Research*, *87*(C2), 1231. https://doi.org/10.1029/JC087iC02p01231

Porreca, M., Cifelli, F., Soriano, C., Giordano, G., Romano, C., Conticelli, S. y Mattei, M. (2014). Hyaloclastite fragmentation below the glass transition: An example from El Barronal submarine volcanic complex (Spain). *Geology*. https://doi.org/10.1130/G34744.1

Pyle, D. M. (2015). Sizes of Volcanic Eruptions. En *The Encyclopedia of Volcanoes*. https://doi.org/10.1016/b978-0-12-385938-9.00013-4

Quane, S. L. y Russell, J. K. (2005). Ranking welding intensity in pyroclastic deposits. *Bulletin of Volcanology*, *67*(2), 129–143. https://doi.org/10.1007/s00445-004-0367-5

Quane, S. L., Russell, J. K. y Friedlander, E. A. (2009). Time scales of compaction in volcanic systems. *Geology*. https://doi.org/10.1130/G25625A.1

Rampino, M. R. y Self, S. (1993). Climate-volcanism feedback and the toba eruption of ∼74,000 years ago. *Quaternary Research*. https://doi.org/10.1006/qres.1993.1081

Robin, C., Eissen, J.-P. y Monzier, M. (1994). Ignimbrites of basaltic andesite and andesite compositions from Tanna, New Hebrides Arc. *Bulletin of Volcanology*, *56*(1), 10–22. https://doi.org/10.1007/BF00279725

Romo-Jones, J. M., Gutiérrez-Negrín, L. C., Flores-Armenta, M., del Valle, J. y García, A. (2017). 2016 Mexico Country Report. En *IEA Geothermal* (Número April).

Rose, W. I. y Chesner, C. A. (1987). Dispersal of ash in the great Toba eruption, 75 ka. *Geology*, *15*(10), 913. https://doi.org/10.1130/0091-7613(1987)15<913:DOAITG>2.0.CO;2

Rowley, D. P. (1981). Pyroclastic-flow deposits. The 1980 eruptions of Mount St. Helens, Washington. En *US Geol. Surv. Prof. Paper* (Vol. 14, Números 3–4, pp. 396–398). http://ci.nii.ac.jp/naid/10003669884/en/

Sheridan, M. F. (1979). *Emplacement of pyroclastic flows: A review*.

https://doi.org/10.1130/spe180-p125

Siebe, C., Macías, J. L., Abrams, M. J., Rodríguez, S., Castro, R. y Delgado Granados, H. (1995). Quaternary explosive volcanism and pyroclastic deposits in east central Mexico: implications for future hazards. *Guidebook of geological excursions: in conjunction with the Annual Meeting of the Geological Society of America, New Orleans, Louisiana, November 6-9, 1995*, 1–48.

Sparks, R. S. J. (1976). Grain size variations in ignimbrites and implications for the transport of pyroclastic flows. *Sedimentology*, *23*(2), 147–188. https://doi.org/10.1111/j.1365-3091.1976.tb00045.x

Sparks, R. S. J., Self, S. y Walker, G. P. L. (1973). Products of Ignimbrite Eruptions. *Geology*, *1*(3), 115. https://doi.org/10.1130/0091-7613(1973)1<115:POIE>2.0.CO;2

Streck, M. J. y Grunder, A. L. (1995). Crystallization and welding variations in a widespread ignimbrite sheet; the Rattlesnake Tuff, eastern Oregon, USA. *Bulletin of Volcanology*, *57*(3), 151–169. https://doi.org/10.1007/BF00265035

Walker, G. P. L. (1980). The Taupo pumice: Product of the most powerful known (ultraplinian) eruption? *Journal of Volcanology and Geothermal Research*. https://doi.org/10.1016/0377-0273(80)90008-6

Walker, G. P. L. (1985). *Origin of coarse lithic breccias near ignimbrite source vents*. *25*, 157–171.

Walker, G. P. L., Wilson, C. J. N. y Froggatt, P. C. (1981). An ignimbriite veneer deposit: the trail-marker of a pyroclastic flow. *Journal of Volcanology and Geothermal Research*, *9*, 409–421.

Willcox, C. P. (2011). *Eruptive, magmatic and structural evolution of a large explosive caldera volcano: Los Humeros, Central Mexico*. University of Leicester.

Williams, S. N. (1983). Plinian airfall deposits of basaltic composition. *Geology*, *11*(4), 211. https://doi.org/10.1130/0091-7613(1983)11<211:PADOBC>2.0.CO;2

Wilson, C. J. N. y Walker, G. P. L. (1982). Ignimbrite depositional facies: the anatomy of a pyroclastic flow. *Journal of the Geological Society*, *139*(5), 581–592. https://doi.org/10.1144/gsjgs.139.5.0581

Wright, H., Lesti, C., Cas, R. A. F., Porreca, M., Viramonte, J. G., Folkes, C. B. y Giordano, G. (2011). Columnar jointing in vapor-phase-altered, non-welded Cerro Galán Ignimbrite, Paycuqui, Argentina. *Bulletin of Volcanology*, *73*(10), 1567–1582. https://doi.org/10.1007/s00445-011-0524-6

Wright, J. V. y Walker, G. P. L. (1977). The ignimbrite source problem: Significance of a co-ignimbrite lag-fall deposit. *Geology*, *5*(12), 729. https://doi.org/10.1130/0091-7613(1977)5<729:TISPSO>2.0.CO;2

Wright, J. V. y Walker, G. P. L. (1981). Eruption, transport and deposition of ignimbrite: A case study from Mexico. *Journal of Volcanology and Geothermal Research*, *9*(2–3), 111–131. https://doi.org/10.1016/0377-0273(81)90001-9

Yáñez-García, C. y García-Durán, S. (1982). Exploración de la región geotérmica Los Humeros–Las Derrumbadas, Estados de Puebla y Veracruz. En *Comisión Federal de Electricidad*.

Zheng, H., Sun, X., Wang, J., Zhu, D. y Zhang, X. (2018). Devitrification pores and their contribution to volcanic reservoirs: A case study in the Hailar Basin, NE China. *Marine and Petroleum Geology*, *98*, 718–732. https://doi.org/10.1016/j.marpetgeo.2018.09.016